Direct growth of graphene by chemical vapor deposition on silicon carbide and III-nitrides

Roy Dagher

▶ **To cite this version:**

Roy Dagher. Direct growth of graphene by chemical vapor deposition on silicon carbide and III-nitrides. Other [cond-mat.other]. Université Côte d'Azur, 2017. English. NNT : 2017AZUR4068 . tel-01686791

HAL Id: tel-01686791
https://theses.hal.science/tel-01686791

Submitted on 17 Jan 2018

HAL is a multi-disciplinary open access archive for the deposit and dissemination of scientific research documents, whether they are published or not. The documents may come from teaching and research institutions in France or abroad, or from public or private research centers.

L'archive ouverte pluridisciplinaire **HAL**, est destinée au dépôt et à la diffusion de documents scientifiques de niveau recherche, publiés ou non, émanant des établissements d'enseignement et de recherche français ou étrangers, des laboratoires publics ou privés.

UNIVERSITÉ CÔTE D'AZUR

CRHEA

École doctorale : Sciences Fondamentales et Appliquées
Unité de recherche : CNRS-CRHEA UPR10

Thèse de doctorat

Présentée en vue de l'obtention du
grade de docteur en Physique
de
l'UNIVERSITE COTE D'AZUR

par

Roy Dagher

Croissance Directe de Graphène par Dépôt Chimique en Phase Vapeur sur Carbure de Silicium et Nitrures d'éléments III

Direct Growth of Graphene by Chemical Vapor Deposition on Silicon Carbide and III-Nitrides

Dirigée par Yvon CORDIER
Co-encadrée par Adrien MICHON

Soutenue le 22 Septembre 2017
Devant le jury composé de :

Isabelle	BERBEZIER	Directrice de recherche, CNRS-IM2NP	Examinatrice
Yvon	CORDIER	Directeur de recherche, CNRS-CRHEA	Directeur de thèse
Filippo	GIANNAZZO	Chercheur, CNR-IMM	Invité
Bérangère	HYOT	Ingénieure de recherche, CEA-Grenoble	Examinatrice
Adrien	MICHON	Chercheur, CNRS-CRHEA	Encadrant de thèse
Abdelkarim	OUERGHI	Chercheur, CNRS-C2N	Rapporteur
Xavier	WALLART	Directeur de recherche, CNRS-IEMN	Rapporteur

This work is licensed under the Creative Commons Attribution-NonCommercial-NoDerivs 3.0 France License. To view a copy of this license, visit http://creativecommons.org/licenses/by-nc-nd/3.0/fr/ or send a letter to Creative Commons, PO Box 1866, Mountain View, CA 94042, USA.

Cette œuvre est mise à disposition sous licence Attribution - Pas d'Utilisation Commerciale - Pas de Modification 3.0 France. Pour voir une copie de cette licence, visitez http://creativecommons.org/licenses/by-nc-nd/3.0/fr/ ou écrivez à Creative Commons, PO Box 1866, Mountain View, CA 94042, USA.

"...for at the proper time we will reap a harvest if we do not give up."
Galatians 6:9 -The Holy Bible

Acknowledgments

First I would like to express my sincere gratitude to my advisor **Yvon Cordier** for giving me the opportunity to prepare my Ph.D. under his supervision for the last three years. I greatly appreciate his readiness to offer advice, support and guidance whenever needed. I also deeply admire his immense knowledge and true dedication to his work, which was an inspiration to me.

I thank the members of my thesis committee, **Dr. Isabelle Berbezier**, **Dr. Xavier Wallart**, **Dr. Abdelkarim Ouerghi**, **Dr. Bérangère Hyot** and **Dr. Filippo Giannazzo** for devoting their time to read the manuscript and for their insightful comments and remarks.

My sincere and warm gratitude goes to **Adrien Michon**, who has been a great advisor, always generous with his ideas and advice, both on the scientific and personal level, which I truly appreciated. His continuous support, motivation and presence meant a lot to me, especially during the tough times. I deeply acknowledge his constant help and determination to push me forward, making me a better and successful scientist. I truly believe that he is a great scientist and an amazingly good-hearted person. I could not have imagined having a better mentor during my Ph.D.

I would like to cordially thank all the people and collaborations who have participated in the advancements of my Ph.D. project, such as **Benoit Jouault** and **Matthieu Paillet** (Laboratoire Charles Coulomb), who have allowed me to use their Raman spectrometer and provided me with insightful explanation whenever needed. I also acknowledge the help of **Frédéric Georgi** (MINES ParisTech Cemef) and sincerely thank him for his assistance with the X-ray photoemission spectrometer, which has been a key component in the advancement of my project. Thanks also go to **Christian Chatillon** and **Elisabeth Blanquet** (SIMaP) for their motivation to work on my project and for their help in understanding the thermodynamics behind our growth technique. Finally, I would like to acknowledge the help of **Timotée Journot** (Leti CEA) with Raman spectroscopy and the fruitful discussions we had, which made me admire his motivation and thirst for knowledge.

I would also like to warmly thank my colleagues at CRHEA, especially **Sebastien Chenot** for devoting his time and expertise to teach me about clean room processing and for preparing my samples many times. Secondly, I thank **Stéphane Vézian** and **Marc Portail** for their assistance and for the fruitful discussions we had concerning XPS. I also thank **Luan Nguyen** for his help in CVD and SEM. In addition, I am truly grateful for having different opportunities to work with a

lot of people at CRHEA; everyone was friendly and always ready for a discussion, which has made my stay extremely pleasant.

I sincerely thank the administrative team at CRHEA and at the university. In particular, **Anne-Marie Galiana** at CRHEA and the head of the doctoral school **Elisabeth Taffin de Givenchy** for their kindness and constant readiness to offer any help needed concerning paper work.

My warm gratitude goes to my fellow lab mates and friends who have also made my journey fun and enjoyable. In particular, I thank **Rami Khazaka** for his unending advice and great cooking. I thank **Xavier Morard**, **Fadi Haddad** and **Tony Ghorra** for making my stay in Antibes extremely pleasant. I thank **Joe Raad** and **Roni Makdissi** for the special moments we had together. I would also like to thank **Ramy Mantach**, **Samuel Matta**, **Victor F. Arcara** and **Mario Ferraro** for the amazing time we had together and for our extremely interesting discussions, mainly about science-fiction and food, but rarely about Physics. I am truly grateful for having a friend in each one of you.

My heartfelt gratefulness also goes to my family in France, especially **Christianne** and **Sonia**. Your unending love and support meant a lot to me as you have made me feel like home when "home" was so far away. I would also like to thank **Mada**, **May**, **Habib** and **Elias** for their support these last three years.

Special thanks go to my amazing friends in Lebanon, my brothers and sisters in Christ, **Rawad**, **Vanessa**, **Maroun**, **Michel**, **Charbel K.**, **Robert**, **Mireille**, **Nathalie** and entire church group; you are too many to be mentioned, but you know how dear you are to me. I am truly and deeply thankful for your moral and spiritual support.

I also thank, with great affection, my heart and soulmate **Carole** who has been by my sides these last three years. Words cannot describe how dear you are to me; you have been there during my ups and downs, my best moments and my darkest moments, and you were always an amazing support in all times. I am truly grateful for having you by my side and in my life.

My warmest gratitude goes to my beloved parents and sister, **Hala**, **Roger** and **Samia**, ***to whom I dedicate this Ph.D***. Your unconditional and unlimited love and support, not to mention your endless sacrifices have made all this possible and got me where I am today. Thank you!

Finally, this list would not be complete and I would not be sincere if I leave out my dear Savior Jesus Christ. Thank You for the good and the bad moments, and for carrying me through the most stressful situations I have ever faced in my life so far. I would not have done it without You and without my faith in You.

Roy Dagher
22-09-2017

Abstract

Graphene is a two-dimensional material belonging to the family of carbon allotropes, consisting of a stable single atomic layer owing to strong in-plane chemical bonds between carbon atoms. It can be identified as a gapless semiconductor with a linear energy dispersion near the Dirac points, which facilitates ballistic carrier transport. In addition, similarly to any semiconductor, it is possible to control its electrical properties under the influence of an external electric field, resulting in the tuning of its carrier density and doping type, i.e. electrons or holes.

Graphene can be elaborated by different techniques and approaches. In this present work, we have considered the direct growth on silicon carbide (SiC) by chemical vapor deposition (CVD) with an external carbon source. This approach which has started to be developed in our laboratory since 2010 is very promising since it allows to control the graphene properties by manipulating the growth parameters. Our objective in this manuscript is to give further insights into this growth technique and to study its potential for the growth of graphene. For this purpose, we have discussed in details different aspects of the growth, starting with thermodynamic simulations to understand the chemistry behind our distinct growth approach. We have also investigated the influence of the different growth parameters, such as the growth time, the propane flow rate and other parameters on the growth of graphene and its properties. However, we mainly focused on two major factors: the hydrogen amount in the gas mixture, especially since the growth is carried out under hydrogen and argon, and the substrate's miscut angle.

Our investigations revealed that the graphene structure can be altered depending on the hydrogen percentage in the gas mixture considered for the growth. For low hydrogen percentage, the graphene growth is associated with a $(6\sqrt{3}\times6\sqrt{3})$ interface reconstruction, whereas for high hydrogen percentage, the graphene layer is dominated by in-plane rotational disorder. These observations are related to the hydrogen intercalation at the interface between the graphene layer and the SiC substrate, which can allow or prohibit the formation of the $(6\sqrt{3}\times6\sqrt{3})$ interface reconstruction as we have discussed thoroughly in this manuscript. The presence of two graphene structures was expected to impact the strain within the graphene layer. For this reason, we have discussed in details the origins of the strain in graphene and attempted to correlate the hydrogen intercalation at the interface to the strain amount. Furthermore, the substrate's miscut angle was also found to have a direct influence on the growth of graphene, mainly affecting the morphology but also the strain within the graphene layer. In light of the different studies and results, we were able to combine the ideal growth parameters to produce state-of-the art graphene, while demonstrating the possibility of tuning its electrical properties with the growth conditions.

Abstract

In a second part of this work, we extended our study to the growth of graphene on III-nitrides semiconductors. We have considered substrates and templates such as bulk aluminum nitride (AlN), AlN/SiC and AlN/sapphire, which opens new opportunities for innovative applications. The growth of graphene was preceded by an annealing study on the different AlN substrates, in an attempt to enhance their surface quality, but also to test their stability at the temperatures necessary for the growth of graphene. Although the AlN film was found to be unable to withstand the high temperature in some cases, an enhancement of the crystalline quality was detected, attributed to the annealing effect. The growth of graphene on such substrates and templates seems promising but challenging. Few points require improvements, such as the presence of defects and non-uniformity in the deposited graphene. Finally, we considered the growth of AlN with molecular beam epitaxy (MBE) on graphene on SiC substrates, which has also brought encouraging results.

Key words: *graphene, silicon carbide, chemical vapor deposition, direct growth, hydrogen, III-nitrides, aluminum nitride.*

Résumé

Titre de la thèse : Croissance directe de graphène par dépôt chimique en phase vapeur sur carbure de silicium et nitrures d'éléments III.

Le graphène est un matériau bidimensionnel appartenant à la famille des allotropes du carbone. Il consiste en une couche atomique restant stable grâce à des liaisons chimiques fortes dans le plan entre les atomes de carbone. C'est un semi-conducteur sans bande interdite (gap) avec une dispersion d'énergie linéaire près des points de Dirac, ce qui facilite le transport balistique des porteurs de charge. De plus, tout comme n'importe quel semi-conducteur, il est possible de contrôler ses propriétés électriques sous l'influence d'un champ électrique externe, ce qui permet de modifier la densité de porteurs et leur type (électrons ou trous).

Le graphène peut être élaboré par différentes techniques, mais nous avons considéré la croissance directe sur le carbure de silicium (SiC) par dépôt chimique en phase vapeur (CVD) avec une source de carbone externe, technique développée dans notre laboratoire depuis 2010. Cette approche est attrayante car elle permet de contrôler les propriétés du graphène en modifiant les paramètres de croissance. Notre objectif dans ce manuscrit est de donner une idée plus approfondie de cette technique de croissance et d'étudier son potentiel pour la croissance du graphène. À cette fin, nous avons discuté en détail de différents aspects de la croissance, en commençant par des simulations thermodynamiques pour comprendre la chimie gouvernant cette méthode. Nous avons également étudié l'influence des différents paramètres de croissance sur la formation du graphène et sur ses propriétés, tels que le temps de croissance, le débit de propane et d'autres paramètres. Cependant, nous nous sommes principalement concentrés sur deux paramètres majeurs: la quantité d'hydrogène dans le mélange gazeux, surtout que la croissance se fait sous hydrogène et argon, et la désorientation du substrat.

Nos recherches ont révélé que la structure du graphène peut être modifiée en fonction de la proportion de l'hydrogène dans le mélange des gaz utilisé pour la croissance. Pour une faible proportion d'hydrogène, la croissance du graphène est associée à une reconstruction d'interface de ($6\sqrt{3}\times6\sqrt{3}$), alors que pour une proportion élevée d'hydrogène, la couche de graphène est désordonnée dans le plan. Ces observations sont liées à l'intercalation de l'hydrogène à l'interface entre la couche de graphène et le substrat SiC, ce qui peut favoriser ou interdire la formation de la reconstruction ($6\sqrt{3}\times6\sqrt{3}$) comme nous l'avons discuté dans le manuscrit. On s'attend à ce que la présence des deux structures de graphène ait un effet sur la contrainte dans la couche de graphène. Pour cette raison, nous avons discuté en détail les origines de la contrainte dans le graphène et tenté de corréler l'intercalation de l'hydrogène à l'interface avec la contrainte.

Aussi, nous avons montré que l'angle de désorientation du substrat a une influence directe sur la croissance du graphène, affectant principalement la morphologie mais également la contrainte dans la couche du graphène. Enfin, nous avons pu produire du graphène de haute qualité, tout en démontrant la possibilité de contrôler ses propriétés électriques avec les conditions de croissance.

Dans la deuxième partie de ce travail, nous avons étendu notre étude à la croissance du graphène sur les semi-conducteurs de type nitrures d'éléments III et en particulier le nitrure d'aluminium (AlN) massif ainsi que des couches hétéroépitaxiées d'AlN/SiC et AlN/Saphir, ce qui ouvre de nouvelles opportunités pour des applications innovantes. La croissance du graphène a été précédée d'une étude de recuit sur les différents échantillons d'AlN, dans le but d'améliorer leur qualité de surface, mais aussi pour tester leur stabilité à la température nécessaire pour la croissance du graphène. Bien que le film d'AlN ait été incapable de résister à la température élevée dans certains cas, une amélioration de la qualité cristalline a été détectée, attribuée à l'effet de recuit. La croissance du graphène sur de tels substrats semble encourageante mais quelques points nécessitent des améliorations, tels que la réduction du nombre de défauts dans AlN et l'uniformité du graphène déposé. Enfin, nous avons considéré la croissance par épitaxie sous jets moléculaires (EJM) de l'AlN sur du graphène sur SiC, qui a également apporté des premiers résultats encourageants.

Mots-clés: *graphène, carbure de silicium, dépôt chimique en phase vapeur, croissance directe, hydrogène, nitrures d'éléments III, nitrure d'aluminium.*

Résumé substantiel (Extended abstract in French)

Le graphène est un matériau bidimensionnel appartenant à la famille des allotropes du carbone. Il consiste en une couche atomique restant stable grâce à des liaisons chimiques fortes dans le plan entre les atomes de carbone. C'est un semi-conducteur sans bande interdite (gap) avec une dispersion d'énergie linéaire près des points de Dirac, ce qui favorise le transport balistique des porteurs de charge. De plus, tout comme n'importe quel semi-conducteur, il est possible de contrôler ses propriétés électriques sous l'influence d'un champ électrique externe, ce qui permet de modifier la densité de porteurs et leur type (électrons ou trous).

Le graphène a été décrit théoriquement en tant que monocouche de graphite dans les années 50 [1] et des premières couches de graphène ont été produites à partir des années 1970 [2]. Toutefois, le graphène n'a commencé à susciter l'intérêt des chercheurs qu'à partir du travail de Noveselov et Geim en 2004 [3] mettant en évidence ses propriétés remarquables. Pour ce faire, ils ont utilisé du graphène exfolié mécaniquement à partir du graphite, puis ont appliqué des techniques de salle blanche pour préparer des dispositifs électriques. Cette technique est simple et efficace, mais limitée à la recherche fondamentale en raison du caractère artisanal de la méthode. D'autres techniques ont été développées pour préparer du graphène à plus grande échelle. L'une des techniques les plus courantes aujourd'hui est la graphitisation des substrats en carbure de silicium (SiC) par sublimation du silicium [4] permettant la croissance de graphène sur tout le substrat de SiC tout en obtenant des mobilités élevées (jusqu'à 27 000 $cm^2/V.s$ à 4 K [5]). Cette technique est largement étudiée aujourd'hui, avec pour premier avantage de ne pas nécessiter d'étape de transfert sur un substrat isolant, permettant ainsi la réalisation de transistors haute fréquence [6] sur SiC. D'autres techniques ont émergé pour la croissance du graphène, comme le dépôt chimique en phase vapeur (CVD) sur du métal [7–9] avec une source de carbone externe, qui permet, aujourd'hui une production sur de larges surfaces [10]. Ces études ont inspiré de nouvelles méthodes pour obtenir du graphène sur SiC par croissance directe à partir d'une source de carbone externe, en ultravide (UHV) dans un réacteur à épitaxie par jets moléculaire (EJM) [11] ou dans une atmosphère d'argon avec un réacteur CVD [12,13].

Dans cette thèse, nous nous sommes concentrés sur l'étude de la croissance directe du graphène sur SiC par CVD afin de mieux comprendre et maîtriser cette technique de croissance originale et d'étudier son potentiel pour la croissance de graphene. Pour cette raison, nous avons discuté de différents aspects de la croissance, en commençant par des simulations thermodynamiques permettant de comprendre la chimie gouvernant cette méthode de croissance. Nous avons également effectué des études expérimentales de recuit du SiC sous H_2 et H_2 + Ar, en plus des simulations thermodynamiques; ceci nous a permis de conclure que pour le recuit sous H_2, il n'est pas possible de considérer que le mécanisme de croissance repose sur la sublimation de silicium à partir du SiC car ce dernier produit des espèces à base de carbone dans la phase gazeuse en beaucoup plus grand nombre que les espèces à base de silicium. Au contraire, lors du recuit de SiC sous argon, le SiC se décompose principalement en espèces à base de silicium, ce qui entraîne un excès de carbone à la surface et forme du graphène. Par conséquent, en présence d'hydrogène, dans une atmosphère H_2 + Ar par exemple, le propane est nécessaire comme source principale de carbone pour la croissance du graphène.

Après l'étude thermodynamique, nous avons exploré les différents paramètres de croissance afin de comprendre leur rôle dans la croissance du graphène et leur influence sur ses propriétés. Nous avons par exemple étudié les effets de la durée de la croissance et du débit de propane sur le dépôt de graphène. En augmentant ces paramètres, l'épaisseur du graphene déposée augmente aussi. Nous avons également étudié l'effet de la température de croissance qui affecte la morphologie, le nombre de couches et la structure de la couche de graphène. Un autre paramètre intéressant est la quantité d'hydrogène dans le mélange de gaz, qui a des effets importants sur la croissance du graphène, la morphologie et la structure en particulier. Pour comprendre le rôle de l'hydrogène dans la croissance, nous avons mené une étude approfondie basée sur la microscopie à force atomique (AFM), la diffraction des électrons à faibles énergies (LEED), la spectroscopie Raman et la spectroscopie de photoélectrons générés par rayons-X (XPS). Pour une faible teneur en hydrogène dans le mélange gazeux (entre 9% et 33%) utilisé pour la croissance, le graphène est associé à une reconstruction $(6\sqrt{3}\times6\sqrt{3})$-R30° de l'interface graphène/SiC, considérée comme une couche tampon. En revanche, pour une quantité élevée d'hydrogène dans le mélange gazeux (75% et 100%), aucune couche tampon n'est détectée et la couche du graphène se développe en domaines désorientés dans le plan. L'origine de ce comportement est liée à l'intercalation de l'hydrogène à l'interface entre la couche du graphène et le SiC. En effet, pour un faible pourcentage d'hydrogène, la couche tampon partage des liaisons avec le substrat, mais pour un pourcentage élevé d'hydrogène, celui-ci sature les liaisons pendantes à la surface du substrat et limite la formation de liaisons avec la première couche de carbone déposée. Sur la base d'études antérieures et de la littérature, nous nous attendions à ce que le graphène présente différents états de contrainte pour ces deux structures. Nous avions l'intention d'étudier le rôle de l'hydrogène sur la contrainte en nous basant sur la spectroscopie Raman, mais malheureusement, les variations de contrainte observées étaient principalement dues à des non-uniformités d'épaisseur, ce qui a rendu l'étude compliquée.

Nous nous sommes également intéressés à l'influence de la désorientation du substrat (offcut) sur la croissance du graphène, paramètre rarement discuté dans la littérature, mais qui a finalement une influence directe sur la croissance, comme nous l'avons démontré dans le manuscrit. Pour cette étude, nous avons fait croître du graphène sur des substrats ayant différents angles d'offcut. La croissance du graphène sur le substrat de 0,05°-off semblait difficile et non uniforme. Au contraire, la croissance de graphène sur les substrats avec des offcuts de 0,2, 1 et 4° est apparue plus aisée et produit un graphène plus uniforme. La seule différence que nous avons observée est l'augmentation du nombre de couches pour les substrats d'offcuts croissants. La spectroscopie Raman a révélé une augmentation de la contrainte pour les offcuts les plus importants, ce qui a été attribué en partie à une augmentation de la densité des marches et en partie à l'augmentation d'épaisseur.

Enfin, nous avons combiné les différents paramètres de croissance pour produire un graphène uniforme sur un substrat SiC à grande échelle avec une mobilité élevée des porteurs de charge, d'environ 1700 $cm^2/V.s$ à 300 K. Nous avons également démontré la possibilité d'avoir différents types de porteurs (électrons ou trous) en fonction des paramètres de croissance, ce qui peut étendre largement la gamme d'applications pour notre graphène.

L'utilisation d'une source de carbone externe nous a permis d'étendre la croissance du graphène aux surfaces de nitrures d'éléments III telles que celles du nitrure d'aluminium (AlN) massif ainsi que des couches hétéroépitaxiées d'AlN/SiC et AlN/Saphir par EJM. Avant la croissance du graphène, nous avons mené des études reposant sur le recuit des différents substrats pour en améliorer la qualité et évaluer leur comportement à la température requise pour la croissance du graphène. Nous avons réussi à améliorer la qualité de la surface de la face Al de l'AlN massif, mais ce n'était pas le cas pour toutes les couches d'AlN préparées sur SiC et saphir. En particulier, les couches d'AlN sur saphir se dégradaient à haute température. Cependant, les recuits à haute température ont eu un effet bénéfique sur la qualité cristalline des films AlN préparés sur saphir. La croissance du graphène a été mise en évidence sur tous les substrats d'AlN en se basant sur l'AFM, l'XPS, le LEED et la spectroscopie Raman. Cependant, la couche de graphène présentait des défauts et du désordre dans certains cas. La croissance s'est révélée favorisée sur la face azote d'AlN massif par rapport à la face Al des mêmes substrats ainsi que sur des couches d'AlN plus fines sur SiC et préalablement traités par recuit. Nous avons également tenté de faire croître du graphène sur des couches d'AlGaN préparés sur saphir par EJM. Nous suspectons le dépôt d'une phase graphitique, identifiée par AFM et XPS, mais nous soupçonnons que le film d'AlGaN a été modifié par les tentatives de croissance du graphène, puisque nous avons détecté la formation d'oxyde d'aluminium et une diminution de la teneur en gallium par XPS. Enfin, nous avons envisagé une autre voie pour combiner le graphène et l'AlN, en faisant croitre de l'AlN par EJM sur du graphène préalablement obtenu sur SiC. Les premiers résultats, mettent en évidence la croissance d'AlN par des observations RHEED et AFM et semblent encourageants, même si pour l'heure, l'AlN présente du désordre dans le plan de croissance. Par ailleurs, la couche

du graphène s'est révélée intacte après la croissance d'AlN d'après des mesures par spectroscopie Raman.

En conclusion, notre contribution a permis de mieux comprendre cette technique de croissance originale et permettra d'autres développements à l'avenir. Maintenant que nous comprenons le rôle des différents paramètres de croissance, nous pouvons anticiper le comportement de la croissance et l'améliorer davantage. Le bénéfice de cette technique est qu'elle s'appuie sur la source de carbone externe, ce qui permet de faire croitre du graphène directement sur le substrat d'intérêt pour différentes applications, par exemple sur SiC ou AlN pour l'électronique de puissance ou les transistors à effet de champ avec AlN comme grille. Nous souhaitons également combiner le graphène avec de l'AlGaN pour les applications HEMT, mais la tâche semble difficile puisque la couche d'AlGaN n'est pas stable à haute température. Des travaux sont encore en cours pour améliorer ce travail et pour le compléter avec des mesures électriques pour évaluer les propriétés du graphène préparé sur nitrures d'éléments III. D'autre part, nous pouvons également essayer d'optimiser la croissance d'AlN sur le graphène sur SiC pour des applications similaires telles que des transistors avec une grille supérieure.

Enfin, j'aimerais ajouter que ce travail a non seulement contribué aux progrès de la recherche sur la technique de croissance directe, mais a également contribué aux progrès de la recherche dans différents domaines grâce à différents projets et collaborations, où nous avons fourni des échantillons de graphène pour de nombreux objectifs tels que les études de métrologie, la croissance de GaN sur le graphène, l'étude des îlots du graphène, l'étude des propriétés thermiques du graphène, la croissance du silicène sur le graphène et d'autres projets.

Mots-clés: *graphène, carbure de silicium, dépôt chimique en phase vapeur, croissance directe, hydrogène, nitrures d'éléments III, nitrure d'aluminium.*

Table of Contents

Abstract 7

Résumé 9

Résumé substantiel (Extended abstract in French) 11

Introduction 19

Chapter 1 23

Fundamentals and techniques 23

1.1. Graphene: Fundamentals and applications 23

1.2. Graphene elaboration techniques 29

1.2.1. Mechanical exfoliation and other related techniques 29

1.2.2. Graphene growth by Si sublimation from SiC 32

1.2.3. Graphene elaboration on metal 36

1.2.4. Growth of graphene on SiC from an external carbon source in UHV or in argon atmosphere 41

1.2.5. Discussion and conclusion 43

1.3. Graphene on SiC: Structure and polarity 46

1.3.1. Graphene growth on the Si-face of SiC 46

1.3.2. Graphene growth on the C-face of SiC 48

1.4. State of the art CVD of graphene on SiC under H_2 51

1.5. General conclusion 56

Chapter 2 59

Experimental methods 59

2.1. Chemical vapor deposition (CVD) 59

2.2. Experimental details 61

2.3. General observations an characterization 63

2.3.1. Topographic characterization 63

2.3.2. Scanning electron microscopy (SEM) 65

2.3.3. X-ray photoemission spectroscopy (XPS) 66

2.3.4. Raman spectroscopy 70

2.3.5. Low-energy electron diffraction (LEED) 75

2.3.6. Device processing and electrical measurements 80

2.4. General conclusion 83
Chapter 3 85
Graphene CVD on silicon carbide 85
3.1. Direct growth under H_2: A Thermodynamic approach 85
3.1.1. Si sublimation attempts under H_2 or argon 86
3.1.2. Thermodynamics and FactSage 91
3.1.3. Graphene on SiC through Thermodynamic calculations 92
3.1.3.1. Hydrogen-argon atmosphere 92
3.1.3.2. Argon atmosphere 97
3.1.4. Discussion and conclusion 99
3.2. Influence of the growth parameters 102
3.2.1. Growth time and propane flow rate 102
3.2.2. Growth temperature 109
3.2.3. Hydrogen amount in the gas mixture 113
3.2.3.1. First observations 113
3.2.3.2. Interface control: discussion and conclusion 118
3.2.3.3. XPS study: sample-set 2 120
3.2.4. Substrate's miscut angle 123
3.2.4.1. 17% H_2 at 1550°C 123
3.2.4.2. 100% H_2 at 1450°C 126
3.2.4.3. Discussion and conclusion 128
3.3. Strain in graphene on SiC: a Raman spectroscopy study 130
3.3.1. Origins of strain in graphene 130
3.3.2. H_2 influence on strain 133
3.3.3. Substrate's miscut angle influence on strain 136
3.3.3.1. Growth with 17% of H_2 136
3.3.3.2. Growth with 100% H_2 138
3.3.4. Discussion and conclusion 139
3.4. Optimized growths and performances 145
3.5. General conclusion 152
Chapter 4 155
Graphene and III-nitrides 155

4.1. Experimental details 155
4.1.1. Nitrides templates and substrates 156
4.1.2. Nitrides annealing and graphene growth 157
4.2. Bulk AlN: annealing and graphene growth 159
4.2.1. Annealing of the Al-face of bulk AlN 159
4.2.2. Annealing of the N-face of bulk AlN 161
4.2.3. Graphene growth on bulk AlN 163
4.2.4. Conclusion 167
4.3. AlN templates on SiC (0001) 169
4.3.1. AlN/SiC templates annealing 169
4.3.2. Graphene growth on AlN/SiC templates 171
4.3.3. Conclusion 179
4.4. AlN templates on sapphire (0001) 181
4.4.1. AlN/sapphire templates annealing 181
4.4.1.1. Annealing effect on the morphology 181
4.4.1.2. Annealing effect on the crystallinity 183
4.4.2. Conclusion on the annealing of AlN/sapphire templates 186
4.4.3. Graphene growth on AlN/sapphire templates 187
4.4.4. Conclusion on the graphene growth on AlN/sapphire templates 189
4.5. Graphene growth on AlGaN templates 190
4.6. AlN growth attempt on graphene/SiC 196
4.7. General conclusion 201
Summary & perspectives 205
Appendix A 209
Double resonance, D, D' and disorder 209
2D-peak and thickness 210
References 211

Introduction

Nowadays, technology has become a foremost part of everyday life, owing to the major breakthroughs in science during the last fifty years, starting with the development of the personal computer in the 70s to the number of inventions surfacing every day such as flexible electronics, 3D printing, smart watches etc… The late-20^{th} century and the beginning of the 21^{st} century were the dawn of scientific strides where major companies and research teams devoted their efforts to find the next $E = mc^2$ to change the way we live by making the daily life easier. Behind these innovations rest brilliant minds and great skills in advanced computer programing and product marketing, but it is without any doubt safe to say that it would not have been possible without a simultaneous advancement in semiconductor technology, especially since the consumer today is looking for technologies and devices that are faster, thinner, lighter and enduring. This is what motivates material and semiconductor scientists to step up and concentrate their research on improving and understanding the existing materials, and also on finding new and innovative materials for the sake of fundamental research and also to meet the consumer's needs. It is indisputable that graphene falls in this last category of groundbreaking materials, brought to light by two Russian scientists in 2004, Andre Geim and Konstantin Novoselov, at the University of Manchester, where they were investigating the electrical properties of graphite flakes when they decided to make it thinner with the simplest technique of using regular scotch tape. The discovery of graphene was the birth of the 2D materials research and a new concept for device fabrication by stacking different 2D materials on top of each other.

Graphene is a two-dimensional material and one of the carbon allotropes consisting of a stable single atomic layer owing to strong in-plane bonding between atoms. It is a gapless semiconductor presenting a linear energy dispersion near the Dirac points, making it the host of charge carriers acting like massless relativistic particles. In addition, being a semiconductor, graphene exhibits a pronounced field effect allowing the continuous tuning of its carrier density and switching between electrons and holes as charge carriers under the influence of an external electric field [3]. These exceptional qualities of graphene are behind its peculiar electronic properties and its extremely high mobility, reaching 200 000 $cm^2/V.s$ at 5 K, demonstrated on suspended single-layer graphene [14] and allowing ballistic electron transport. The different remarkable properties of graphene extend to excellent optical transparency, chemical stability and noticeable thermal conductivity, which attracted a lot of interest for different fields such as electronics, optoelectronics and photonics, even bioapplications [15].

Of course, if graphene is considered for commercial uses, a large scale mass production is crucial for such a task. It was then normal that the work of Novoselov and Geim in 2004 would launch a gold rush for the production of graphene at a large scale. One of the most common technique today is the graphitization of silicon carbide (SiC) substrates by silicon sublimation [4], which was found to be promising and allowing the growth of graphene on the full SiC wafer, while achieving a high mobility of 27 000 cm^2/V.s at 4 K [5]. C. Berger et al. [4,5] have proven that the novel electrical properties of graphene can also be achieved for epitaxial graphene on an SiC substrate, even though the mobility is reduced compared to suspended graphene. It was the work of C. Berger et al. that shed the light on SiC graphitization, but graphene on SiC was known since 1975 [2], also achieved by annealing the SiC substrate and identified at that time to be a monolayer of graphite. This technique is widely studied today, with interesting advantages, since there is no need to detach the graphene from the SiC substrate as it can already be employed for applications, e.g. for high-frequency transistors [6]. Other techniques emerged for the growth of graphene, such as catalytic chemical vapor deposition (CVD) on metal [7–9] with an external carbon source, which resulted, after intensive research, in large scale production [10]. These studies inspired new procedures for growing graphene on SiC by direct growth from an external carbon source with different approaches: in a molecular beam epitaxy (MBE) reactor [11] or CVD reactor [13] under different environments such as ultra-high vacuum (UHV) [16] or argon atmosphere [12,13].

All these growth techniques present encouraging results but also limitations, and the growth of graphene has yet to be optimized. The interest in graphene continues to grow and improvements are still being conducted, especially since epitaxial graphene does not present the same outstanding electrical properties as suspended graphene. Therefore, before considering graphene for commercial uses, fundamental research is still necessary to enhance the epitaxial graphene's properties. This is where the work of this thesis fits in; in particular, for epitaxial graphene on SiC.

The Direct growth of graphene on SiC from an external carbon source in a CVD reactor has been the main focus of many research groups since 2010. Their efforts brought promising results, but still until this day, few imperfections and unexplained behaviors still surface, such as reduced mobility, defects in the graphene layer, non-uniform growth etc… Some studies considered the growth under an argon atmosphere [12,13], but our research team has demonstrated that the growth under a hydrogen atmosphere allows a better control of the graphene growth and properties [17,18]. It gets even more interesting when combining both hydrogen and argon in a CVD growth of graphene, which resulted in promising electronic properties and high carrier mobility [19] with the ability to tune these properties by changing the growth parameters. It has also allowed to establish a new state-of-the-art graphene-based quantum Hall resistance standards, surpassing the GaAs counterparts in terms of cryomagnetic conditions [20,21]. In the light of these results, it seems that the key to enhance the epitaxial graphene's properties is to master the growth and understand the role of the different growth parameters, especially since detailed studies of this graphene growth method are still lacking.

The work of this thesis aims to fill this gap by providing thorough discussions on the CVD direct growth technique and on the properties of the graphene films grown by this method while investigating the effects of the different growth parameters. We will consider topics that are rarely mentioned in the literature such as the strain within the epitaxial graphene layer and the substrate's miscut angle and its influence on the graphene growth. To complete the study, we even conducted thermodynamic calculations to address matters that are still not clear. Our intention is to shed the light on this growth technique and the process of preparing state-of-the-art graphene on silicon carbide.

Finally, this technique was not limited to SiC substrates, since it relies mainly on the growth from the external carbon source. Therefore, it would be unfortunate if we do not invest in this major advantage to extend the growth of graphene to other semiconductors. Hence, our second contribution focuses on the growth of graphene on aluminum nitride (AlN) and related materials. This opens new paths for innovative applications combining both graphene and nitrides into one market, especially since both materials are hot topics today with a lot of prospective. In fact, one can already find in the literature integrated graphene with nitrides as a transparent electrode [10,22] or as a contact for GaN based devices [23]. However, in these studies graphene was first grown on metal by CVD then transferred to the nitride surface. In our work, we will demonstrate the possibility of directly growing graphene on the nitride substrate by adapting our growth process, initially optimized on SiC. In addition, since we consider unprepared AlN substrates and AlN templates, we conducted annealing studies to investigate the influence of high temperature annealing on the morphology and structure of AlN as a preliminary study before the growth of graphene.

The manuscript is divided into four chapters. Each chapter is preceded by a small introductory paragraph to emphasize the major points that will be discusses. We present in the following the structure of this manuscript and the headlines of each chapter.

Chapter 1 presents the attractive properties of graphene in a first part and its integration in different applications and fields. Then we go through the different elaboration techniques of graphene while highlighting their advantages and limitations. After that we narrow down our discussion to focus on graphene on SiC and the growth dependence on the SiC polarity. Finally, we present the different contributions of our research team to the graphene growth on SiC since 2010 until the start of this thesis.

Chapter 2 describes the CVD experimental setup and the growth technique we employed in the frame of this work. Later on, we demonstrate how to properly characterize graphene on SiC with different characterization techniques while describing briefly the physical premises underlying each technique.

Chapter 3 covers different aspects of the growth of graphene on SiC, starting with thermodynamic simulations to shed the light on the main contributors to the growth and to point out major differences between our approach and the Si sublimation technique. Afterwards, the

chapter goes through the different growth parameters and their influence on the growth of graphene, such as the growth time, the growth temperature, the hydrogen amount in the gas mixture and the substrate's miscut angle. We then present a review on the origins of strain within graphene grown on SiC, followed by a detailed study of the influence of few growth parameters on that strain. Finally, we combine together the ideal growth parameters to prepare optimized graphene on SiC on a large scale, relative to the size of our reactor.

Chapter 4 extends the growth of graphene from SiC to AlN and related materials. Different substrates and templates were considered for this particular study: bulk AlN, AlN templates on SiC and sapphire and AlGaN templates on sapphire. The chapter also gives details on annealing studies carried out on the different substrates as a surface preparation method and as a graphene pre-growth step. After that, the graphene direct growth by CVD on the different substrates is investigated and the quality of the growth is evaluated on the basis AFM, LEED, XPS and Raman spectroscopy measurements.

Finally, we summarize the results in a general conclusion while proposing future perspectives beyond this work.

Chapter 1

Fundamentals and techniques

This chapter will first present an overview on the peculiar properties of graphene and its integration into many scientific fields. Then we propose a description of the different elaboration techniques developed to obtain graphene. Our intention is to emphasize the major advancements in graphene elaboration techniques and applications reported in the literature for the last decade. Finally, we present the state of the art in the field of graphene on SiC.

1.1. Graphene: Fundamentals and applications

Graphene is a two dimensional allotrope and phase of carbon, consisting of carbon atoms bound together in a honeycomb structure (Fig. 1.1(a)). It can be considered as the building block of all graphitic forms: for example a graphene layer can be rolled up into one dimensional carbon nanotube or stacked on top of other graphene layers to form three-dimensional graphite. The elementary unit cell contains two atoms A and B, each corresponding to a different sublattice of equivalent atoms, represented by the shaded shape in Fig. 1.1(a), and connected with in-plane lattice vectors **a** and **b**.

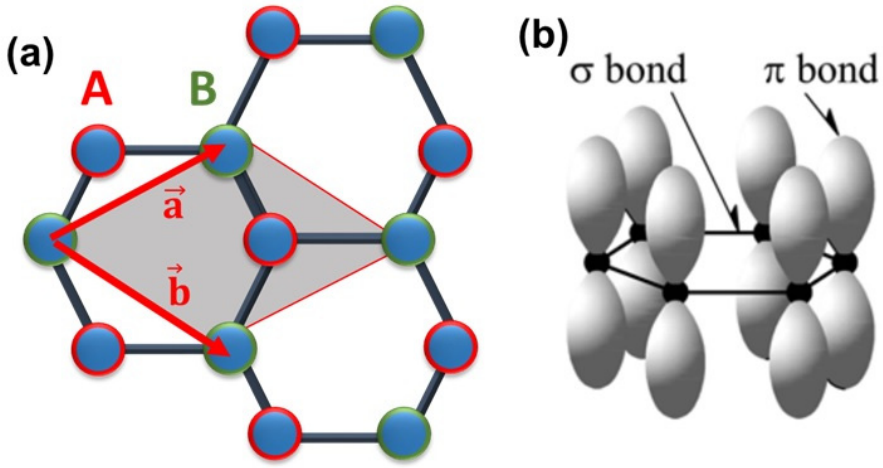

Figure 1.1: ***(a)*** *Honeycomb lattice structure of graphene.* ***(b)*** *Schematic representation of the in-plane σ-bands and out-of-plane π-bands [27].*

The lattice parameter of graphene is considered to be 2.46 Å, corresponding to a C-C bond length of 1.42 Å, based on diffraction measurements in graphite [24]. However, when discussing certain aspects of graphene such as strain, one needs to establish more accurately its lattice parameter, which is still subjected to debate since different values can be found in the literature. If we consider the in-plane lattice parameter of graphite, we can find values ranging between 2.456 Å [25], 2.4589 Å [26] and 2.464 Å [24], corresponding to a discrepancy of 0.32%. This inconsistency could be originating from the different graphites considered for the different studies, from natural disordered turbostratic graphite to synthetic highly-oriented pyrolytic graphite (HOPG). This can be an important issue when predicting the strain value for epitaxial graphene since this lack of accuracy on the lattice parameters may be comparable or larger than the strain itself.

Each carbon atom of graphene shares three out of four valence electrons: one 2s-electron and two 2p-electrons (p_x, p_y), forming three sp^2-hybridized planar orbitals connected to the three neighboring carbon atoms via strong in-plane σ-bonds. These bonds are responsible for the extreme mechanical strength of graphene films. The fourth valence electron is the out-of-plane $2p_z$-electron which gives rise to the π-orbital, responsible for the electrical conductivity in graphene and the interlayer coupling in graphite [27], see Fig. 1.1(b). P. Wallace was the first to calculate the electronic band structure of graphene in 1947 [1]. We present in Fig. 1.2(a) an *ab initio* calculation of a single isolated graphene sheet band structure, taken from reference [28]. The valence band consists of three σ-bands and one π-band. The valence band (π) and the conduction band (π*) meet only at the specific K and K' points of the graphene Brillouin zone, known as the Dirac points. In Fig. 1.2(b) we show a 3D illustration of the band structure in the vicinity of the K and K' points revealing the Dirac cones, taken from reference [29]. As we can see, graphene is a gapless material presenting a spectrum similar to the Dirac spectrum for massless fermions [30–32]. This behavior is a consequence of the graphene crystal structure, consisting of two equivalent sublattices. The electron hopping between sublattices interact with the periodic potential of the

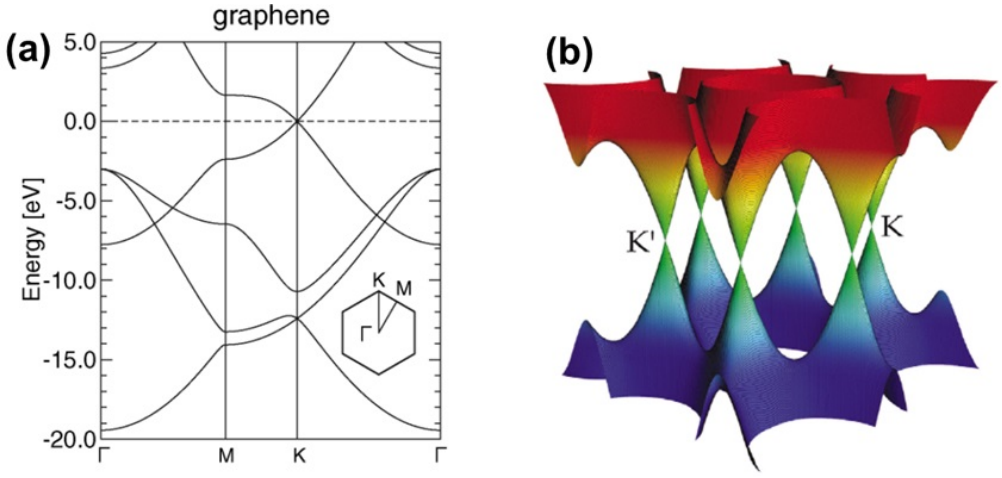

Figure 1.2: (a) *ab initio calculation of the band structure of graphene [28].* ***(b)*** *3D illustration of the band structure [29].*

graphene honeycomb lattice activating new quasi-particles described by the Dirac equation instead of the usual Shrödinger equation [30,31]. The energy dispersion near the Dirac points is linear $E=\hbar k v_F$, where v_F is the Fermi velocity and k is the 2D-wave vector relative to one of the K points. This linear dispersion clearly shows that electrons will act as massless relativistic particles.

Over the years, graphene was found to present exceptional electronic properties, it is a gapless semi-metal, but it also presents the ability to host an electric field effect and the possibility of tuning its charge carrier density between electron and hole 2D gases, by controlling the Fermi level [3–5,32], see Fig. 1.3(a) taken from [33] . Graphene also exhibits a robust quantum Hall effect (QHE) even at room temperatures [34,35], see Fig. 1.3(b) taken from [35].

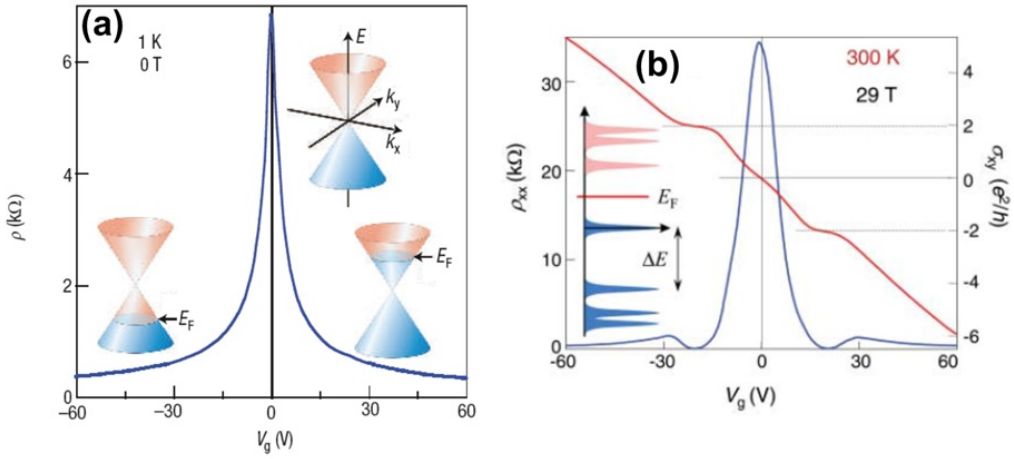

Figure 1.3: (a) *Electric field effect in exfoliated single-layer graphene, indicating a change in the position of the Fermi energy with the gate voltage [33].* ***(b)*** *Resistivity and conductivity as a function of gate voltage showing room temperature QHE in graphene [35*].

So far we have discussed the band structure of a single-layer isolated graphene. However, studies have shown that the band structure depends on the number of layers and on the stacking sequence [28,36,37]. Each new layer adds another two π-bands to the existing band structure, due to the splitting of the π-bands whenever a layer is added. In contrast, the σ-bands are not affected [28]. In Fig. 1.4, we present band structure calculations for graphene layers between 1 and 4, for two different sequences: either Bernal stacking (ABAB…) or rhombohedral (ABCABC…) [37]. Contrary to monolayer-graphene, bilayer-graphene presents parabolic bands [38,39]. In addition, it was found, both theoretically [37–39] and experimentally [40–42], that applying an external bias voltage across the two layers will induce an opening in the gap between the valence band and the conduction band, thus making bilayer-graphene insulating see Fig. 1.4 (bottom panel), taken from reference [37]. It is worth mentioning that few studies have reported that multilayers of graphene with rotational stacking disorder will act as decoupled layers i.e. the linear dispersion relation characteristic of monolayer-graphene is still maintained even for several layers [43,44].

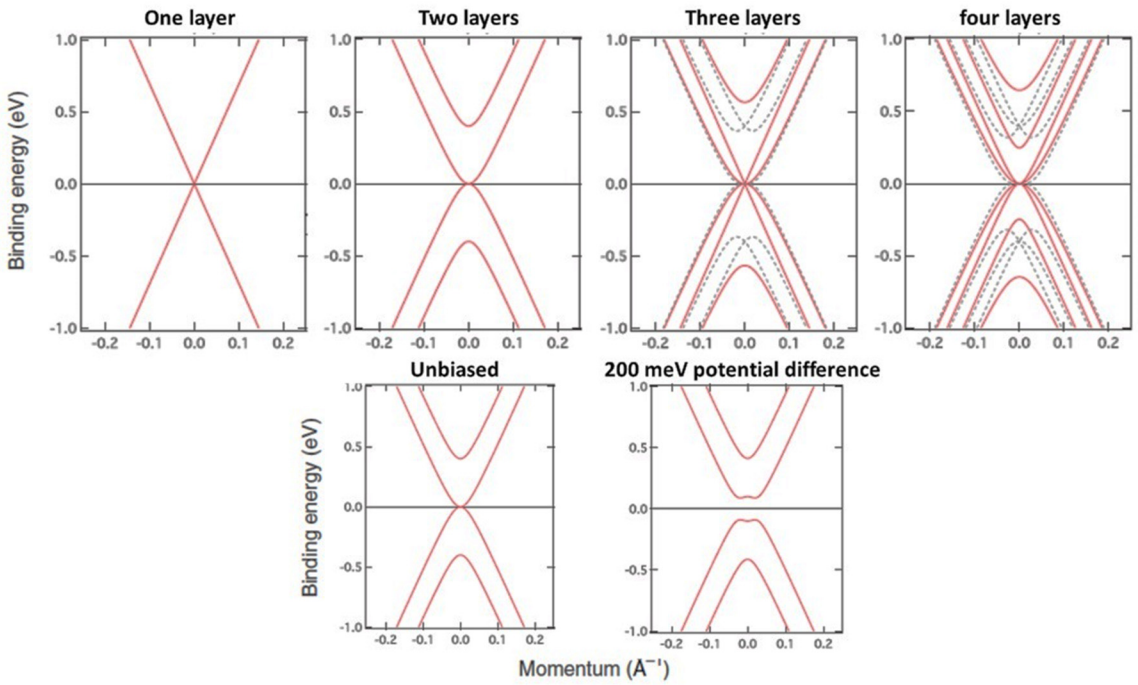

Figure 1.4: *Upper plane displaying the band structure for unbiased one to four layers of graphene with two stacking sequence: Bernal stacking (solid line) and rhombohedral (dashed lines). Bottom plane showing the band structure of unbiased bilayers and biased with 200 meV potential difference across the films [37].*

Owing to its exceptional electrical properties, graphene can be attractive for a lot of electronic and optoelectronic applications. Its unique properties also include an excellent transmittance of ~98% of white light for a single graphene layer [45] and a low sheet resistance down to 30 Ω/□ for multilayers stacked together [10], making it an interesting substitute for indium tin oxide (ITO), and a great candidate for optoelectronics such as touch screens and organic light emitting diodes (OLED) [10,46,47]. It is worth noting that the conventional ITO still presents slightly better characteristics than graphene in some cases, but graphene surpasses ITO when it comes to mechanical flexibility and chemical durability. In fact, we already find some studies that have invested in these latter properties of graphene for flexible electronic devices [46,48]. In addition for the electronics, graphene can be of great interest for photonic applications. Graphene is capable of absorbing white light: absorption of 2.3% per layer, which means that the absorption increases when adding more graphene layers [45]. The optical absorption is not only limited to white light, it also ranges from ultraviolet to THz, unlike semiconductor photodetectors who are limited in their spectral-width detection, but without exceeding 3% of absorption per graphene layer [45,49–51]. It also surpasses other semiconductors in high-speed data communication, due to its high carrier mobility enabling a fast extraction of photo-generated carriers, thus allowing a photo-response up to 40 GHz and a high bandwidth reaching 640 GHz [52], which is comparable to traditional photodetectors [53]. Due to this fast response and wide spectral range, the progress in graphene did not stop here. It was extended to other photonic applications such as Mode-lock

lasers [34,49], optical modulator [54,55], solar cells [56,57] etc… We show in Fig. 1.5 some of the applications for graphene.

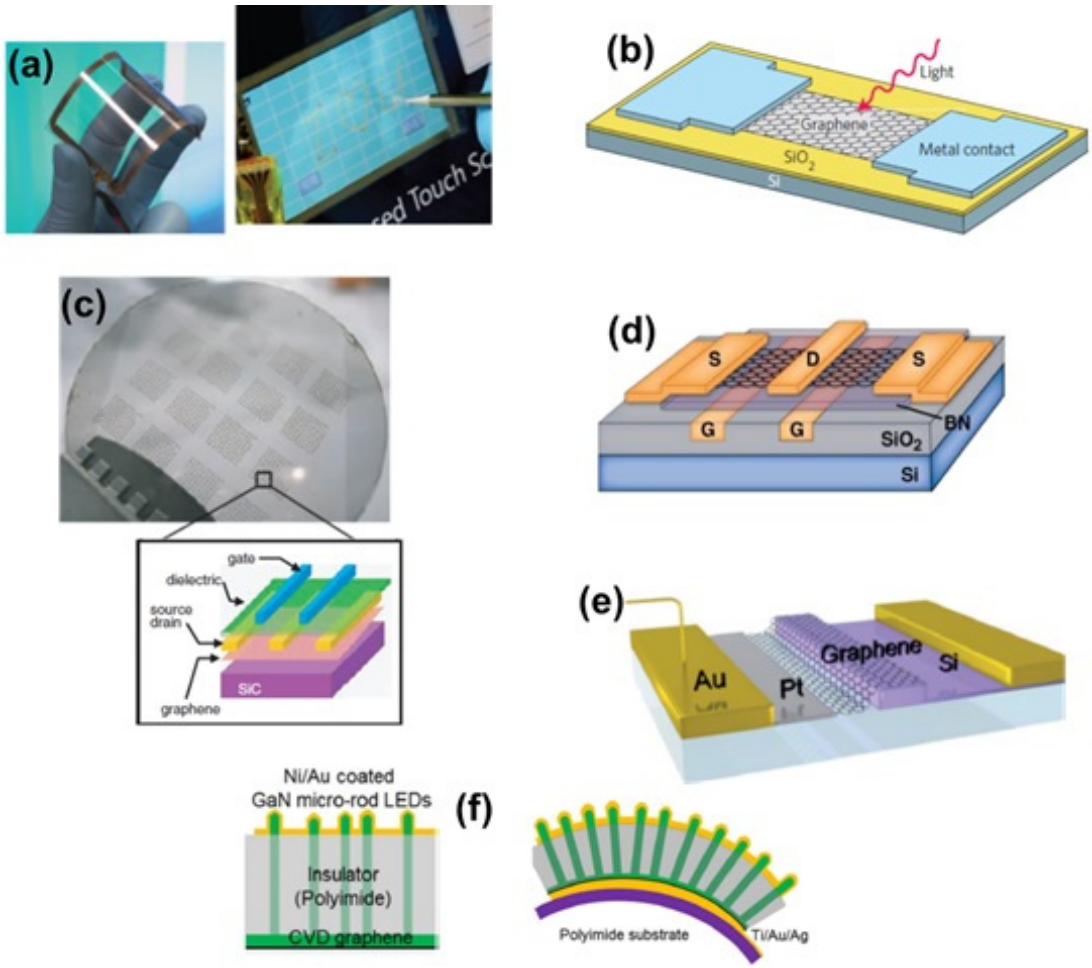

Figure 1.5: *Graphene applications.* ***(a)*** *Graphene for touch screens* [10]. ***(b)*** *Schematic representation of graphene in a photodetector* [47]. ***(c)*** *Wafer-scale graphene on SiC for field effect transistors* [6]. ***(d)*** *Graphene FET with BN as the dielectric* [58]. ***(e)*** *Schematic illustration of Graphene on Si waveguide as optical modulator* [55]. ***(f)*** *Graphene combined with GaN rods for flexible LEDs* [48].

Another remarkable use for graphene is the development of the universal resistance standards based on the quantum Hall Effect. The precision of Hall Effect quantization for graphene grown on the Si-terminated SiC substrates has by far outperformed the traditionally used GaAs heterostructures [20,21,59] and is today employed by several metrology facilities. Graphene had also been used for high-frequency transistors [6], presenting interesting features like a cut-off frequency as high as 300 GHz [60], with the ability of increasing it to 1 THz at a channel length of 100 nm [61]. Still, it has failed to surpass existing technologies based on III-V materials or silicon high-frequency transistors. But instead of competing with an already established market, a wiser approach would be to combine graphene with III-V materials in an attempt to enhance the

device's performance. Efforts have targeted the introduction of graphene to III-V materials, for example gallium or aluminum nitride-based devices (GaN or AlN) [22,23] or boron nitride (BN) [58,62,63]. Other studies considered opening a band gap in graphene, by patterning graphene nanoribbons [64,65] or chemically modifying graphene [66,67]. Although, results seem promising, they still need to be improved. Besides, graphene can always be used for thermal dissipation in integrated circuits owing to its impressive thermal properties [68]. Finally, one can find other applications for graphene in different domains, even in conductive paints and ink, depending on the elaboration process.

1.2. Graphene elaboration techniques

Now that we have shed the light on the basic properties of graphene, and its outstanding performances in many major fields, it seems essential to discuss the different graphene elaboration techniques since its quality and performance is strongly related to the production process. We will consider in the next part main elaboration techniques allowing to obtain graphene with good electronic properties, focusing also on their benefits and limitations.

1.2.1. Mechanical exfoliation and other related techniques

This method is considered a milestone in the history of elaborating graphene, as it is today the most known technique owing to the work of K. Novoselov, A. Geim et al. [3] reported in 2004, which unraveled an innovative approach to prepare few-layer graphene (FLG). The method is not only groundbreaking in its simplicity but also in unveiling the exceptional electrical properties of graphene. They were able to demonstrate that an FLG film can host either an electron gas or a hole gas by changing the gate voltage.

One of the procedures to prepare graphene films is described by Novoselov et al. [69] starting with platelets of highly-oriented pyrolytic graphite (HOPG). To better visualize this process, a schematic view is presented in Fig. 1.6. The HOPG is etched with O_2 plasma to create squared mesas of different sizes, 20 µm to 2 mm wide and 5 µm deep. It is then pressed against a photoresist on a glass substrate, followed by a bake to well attach the mesas to the photoresist layer. Subsequently, the mesas are cleaved-off from the rest of the HOPG sample. After that, using scotch tape, flakes of graphite are repeatedly peeled-off from the mesas, to leave few thin flakes trapped in the photoresist. The photoresist is then removed in acetone, releasing the graphite flakes in the solution. Silicon (Si) wafers covered with 300 nm of SiO_2 are then dipped in the solution, then washed in water and propanol. By simply dipping the Si wafers in the solution, the thin

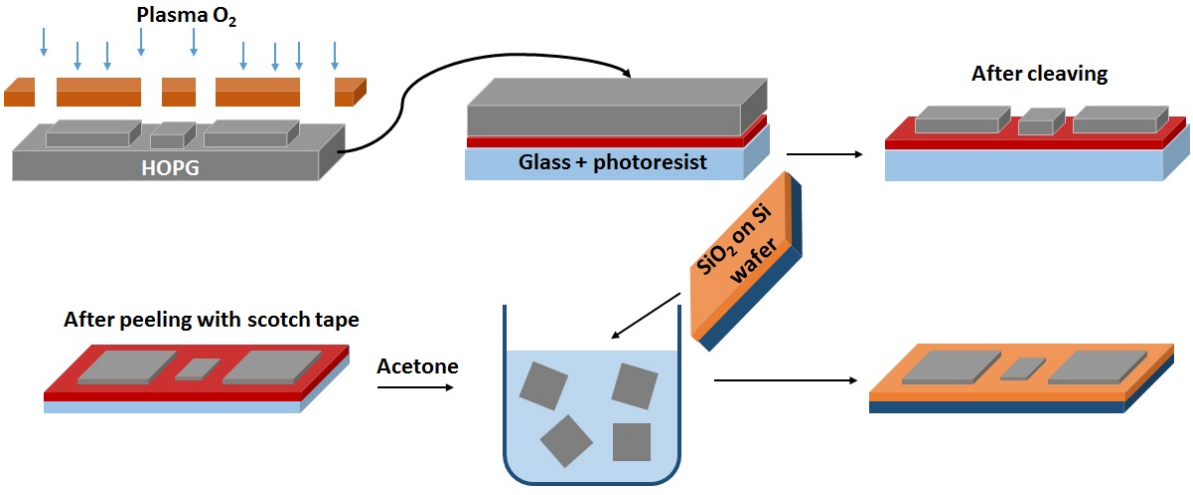

Figure 1.6: *Schematic representation of the graphene mechanical exfoliation process.*

graphite flakes get attached to the wafer's surface, first due to capillary forces then to Van der Waals forces after drying-out the sample.

To detect the graphitic films, an optical microscope can be used, even if they are transparent to visible light, it is possible to detect them on a SiO_2 substrate because of color interferences. A 300 nm SiO_2 wafer appears violet-blue (depending on the microscope), but when adding graphite films, it will shift to blue (see Fig. 1.7(a) taken form reference [69]). However, the interference shift is no longer noticeable for films thinner than 1.5 nm. In this case, scanning electron microscopy (SEM) is very useful to evaluate single and few layers of graphene. As we can see in Fig. 1.7(b), a single layer gives a different contrast than for thicker films. Therefore, Noveselov et al. [3] were able to separate single-layer graphene from few-layer graphene using SEM and atomic force microscopy (AFM). However, they were unable to evaluate exactly the number of graphene layers for the prepared devices since the AFM tip can damage the films. Nevertheless, other techniques can be used today to evaluate the number of layers such as Raman spectroscopy.

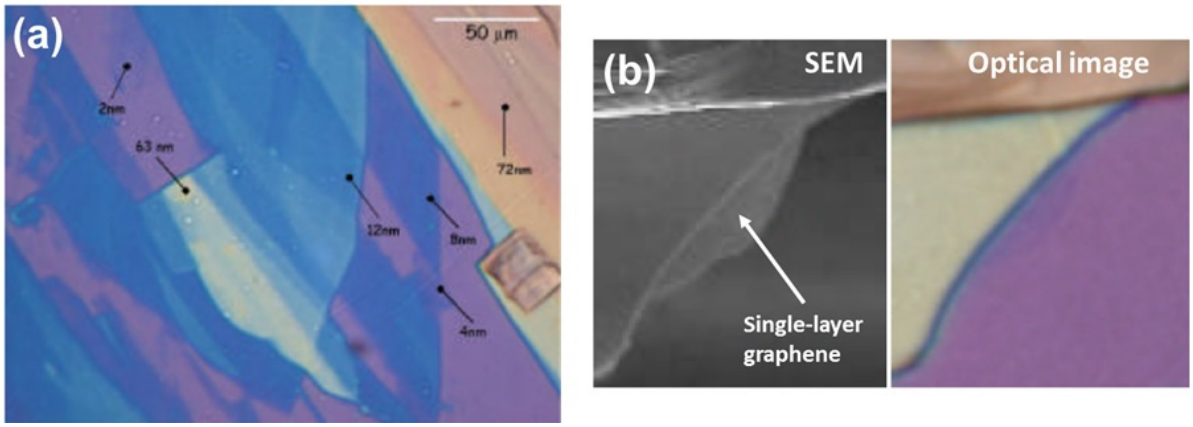

Figure 1.7: (a) *Optical image of the graphene films on the SiO_2 substrate.* ***(b)*** *Left image: SEM view of a single-layer graphene among thicker layers. Right image: the corresponding optical image [69].*

The mechanical exfoliation technique seems very attractive, allowing the production of suspended graphene, unspoiled by the elaboration process. But for obvious reasons, this technique cannot be employed for industrial purposes and it remains for research only, allowing the access to the fundamental properties of graphene and other 2D materials in a simple way. Unless research finds a new technique to exfoliate graphene, the sample size remains around few mm. Despite this drawback, this technique has revealed the amazing 2D electron (or hole) gas behavior within a graphene sheet [3,4], with the ability to tune this behavior similar to field-effect transistors, which was an unprecedented demonstration in atomically-thin 2D materials. This simple technique is still widely used today, and even extended to other 2D materials to explore new territories and new innovative devices, such as boron nitride (BN), molybdenum sulfide (MoS_2), tungsten diselenide (WSe_2), tungsten sulfide (WS_2), etc…[70]. Many studies suggested original devices based on 2D

materials mechanically exfoliated and assembled together [70,71]. We show an example in Fig. 1.8 of a light emitting diode heterostructure consisting of mechanically exfoliated BN, graphene and WS_2, taken from reference [71]. Encapsulating graphene can be very appealing, for example encapsulated graphene with BN layers revealed substantial carrier mobility (all layers created by the exfoliation technique), where Hall bars of few tens of nanometers in width and few microns in length were prepared, giving rise to carrier mobility exceeding 1×10^5 $cm^2/V.s$ at 300 K for both electron- and hole-doping [62].

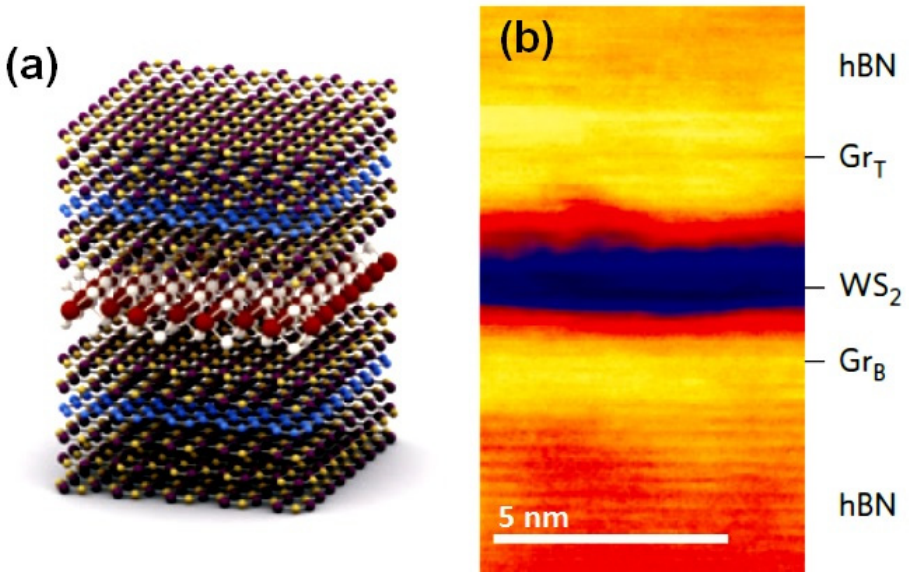

Figure 1.8: ***(a)*** *Schematic illustration of the BN/Gr/WS_2/Gr/BN heterostructure.* ***(b)*** *Cross-sectional bright-field Scanning-TEM image of this type of structure. Gr_T and Gr_B refer to the top and bottom graphene layer respectively [71].*

Two related methods have been developed: liquid-phase chemical exfoliation [72,73] and graphite oxide exfoliation [74,75]. We will discuss briefly these two techniques, starting with the first one. Powder graphite is poured into solvents such as N-methylpyrrolidone (NMP), known to have Van der Waals interactions with graphite. The solution is placed in an ultrasonic bath and centrifuged for 90 minutes. This process separates the graphite platelets into few- and mono-layer graphene flakes. For characterization, the graphene flakes can be deposited onto other substrates by spray-coating or by dropping small quantities with a pipette. After deposition, sample drying can be carried out in vacuum or in gas atmosphere at room temperature or at 400°C for 4 hours to remove any traces of solvents. Combined investigations with Raman spectroscopy, X-ray photoemission spectroscopy (XPS) and transmission electron microscopy (TEM) reveal the presence of multilayers and monolayers [73]. Traces of residual solvent can be identified, but the overall structural quality of graphene is good.

The second exfoliation technique starts by oxidizing graphite with oxidizing agents such as sulfuric acid, nitric acid and potassium chlorate for more than 90 hours. This step will introduce

oxygen into the graphite structure, creating bonds such as C-O-C, C-OH and -COOH which will increase the separation between the graphite layers [74,75]. After that, the oxidized graphite is placed in an aqueous solution and exposed to ultrasounds in order to separate the oxidized graphene layers. The solution can be processed by centrifugation and deposited on any substrate, then treated chemically or thermally to remove the oxygen. Another approach can be used to exfoliate and remove the oxygen simultaneously by rapidly heating the graphite oxide [75]. The heating process will separate the graphite into individual graphene sheets by releasing CO_2 gas. The flakes can be then dispersed in NMP for characterization. These two techniques can be very appealing for certain applications, allowing the production of important quantities of graphene in solutions. However, the size and number of graphene layers does not seem well controlled, in addition to contamination or unintentional doping from the solvents used. These setbacks limit the application of this technique but still it can be very attractive for emerging markets e.g. for graphene ink or paint, or also for conductive coatings and layers [15].

In summary, in 2004 Novoselov and Geim reported an innovative technique to prepare few layers of graphene starting with graphite. The procedure starts first with a preparation of the graphite substrate with O_2 plasma etching, then with simple scotch tape one can peel-off many layers, leaving behind few graphene layers embedded in a polymer. The graphene layers can then be transferred to a SiO_2/Si wafer followed by investigations with optical microscopy, SEM and AFM to determine the number of layers. Transistors made with the as-grown graphene revealed its exceptional electrical properties of ballistic transport and the possibility of tuning the charge carrier concentration with an external gate voltage. Although this approach is very innovative, allowing to produce suspended pristine graphene, it is limited to research due to the small sample size. However, it has inspired new devices based on 2D-material heterostructures. It also led to related techniques such as liquid phase exfoliation and graphite oxide exfoliation, which support a different but interesting market: graphene ink and conductive coatings.

1.2.2. Graphene growth by Si sublimation from SiC

Among the known techniques to obtain graphene, the SiC thermal decomposition technique is also very common today. It relies on the fact that silicon atoms are more volatile than carbon atoms. By heating the substrate under proper conditions, it will release silicon atoms, leaving behind carbon atoms, which will form the graphene layer. The work of Berger et al. [4] in 2004 can also be considered today a landmark in graphene history, even though the graphitization of SiC by Si sublimation was already known since the 1970s.

Early studies [2,76,77], between 1975 and 2002, have shown that annealing an SiC substrate for 10 to 20 minutes under ultra-high vacuum (UHV) conditions results in the formation of graphite layers. The evaporation of silicon even starts at 800°C [2]. Thorough investigations were reported by the same team between 1998 and 2002 [76–78], on the basis of low-energy electron diffraction (LEED), concerning the SiC surface reconstructions as a function of the

sublimation temperature. It was found that the Si-face of hexagonal SiC (also named SiC (0001)) [76] undergoes two reconstructions between 1050 and 1250°C under UHV: ($\sqrt{3}\times\sqrt{3}$)-R30° and ($6\sqrt{3}\times6\sqrt{3}$)-R30°, which is a C-rich phase. Increasing the temperature to 1400°C activates the formation of graphite. In contrast, the growth mechanism is not the same on the C-face or SiC (000-1) [78], where no signs of the ($\sqrt{3}\times\sqrt{3}$)-R30° surface reconstruction appear, but instead a (2×2) reconstruction takes place and the graphite signature is detected at 1100°C. The formation of graphite is confirmed with angle-resolved inverse photoemission spectroscopy (KRIPES). In addition, as identified by LEED and photoemission spectroscopy (KRIPES and Auger spectroscopy) [2,76], the number of graphite layers can be controlled with the temperature. Also, the graphite layer was found to be monocrystalline on the Si-face and polycrystalline on the C-face associated with diffraction rings observed in LEED patterns. These studies were later completed with scanning tunneling microscopy (STM) and grazing-incidence X-ray diffraction (GIXRD) investigations of the first stages of the graphite formation [77].

Although these achievements seem complete and original, they lack information concerning the electrical properties of the graphite layers, which would have emphasized their work at that time. It was not before 2004, when C. Berger et al. [4] adopted this technique of Si sublimation to prepare thin graphite films on 6H-SiC (0001), and detected the 2D electron gas behavior by processing a field-effect transistor with the grown graphite layers. This behavior was confirmed the same year by Novoselov et al. [3]. After that, these breakthroughs initiated many studies concentrated on the growth of graphene on SiC by Si sublimation, either on the Si-face [79,80] or the C-face of SiC [5,81,82]. We present topographic images of graphene on the Si-face and the C-face of SiC in Fig. 1.9(a) and Fig. 1.9(b, c) respectively, taken from references [79,81,82]. The growth on the C-face seems associated with wrinkles up to 10 nm-high and 40 nm-wide [81,82], depending on the growth temperature.

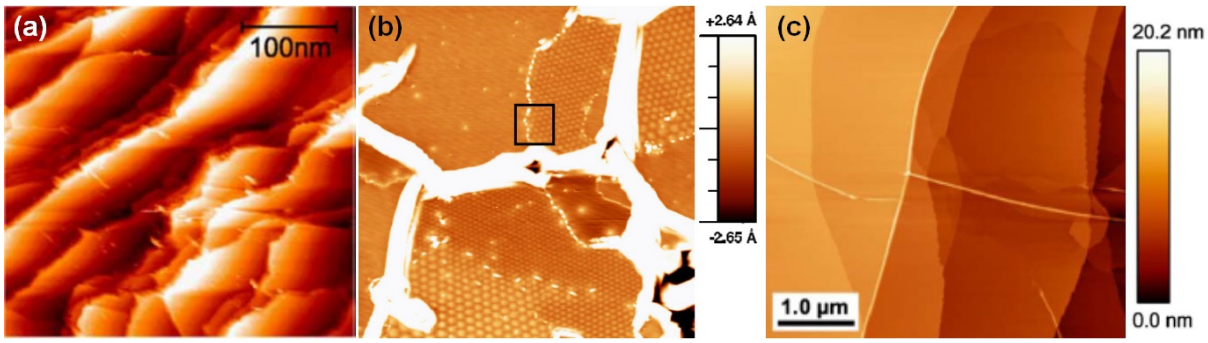

Figure 1.9: *STM topographic images of graphene on SiC.* ***(a)*** *370×350 nm^2-area of graphene on 4H-SiC (0001) [79].* ***(b)*** *150×150 nm^2-region of graphene on 6H-SiC (000-1) presenting wrinkles 0.5 to 2 nm-high (sample grown at 1150°C) [81].* ***(c)*** *5×5µm^2-region of graphene on 4H-SiC (000-1) showing wrinkles 5 to 10 nm high (sample grown at 1500°C) [82].*

So far we discussed results of graphene growth on SiC by Si sublimation under UHV. Other studies suggested that graphene growth by Si sublimation produces better quality graphene under an argon atmosphere, instead of UHV [80]. In this case, the growth needs to be done under higher temperatures (1650°C) compared to UHV temperature (1280°C) for the same growth time. In Fig. 1.10, we present AFM images comparing the two different growths, and Raman spectroscopy evaluating the quality of each graphene layer [80]. The difference in contrast in Fig. 1.10(a) is due to a local non-uniformity in the layer thickness. Raman spectroscopy in Fig. 1.10(c) reveals an important D peak for the sample grown under UHV. The D peak is a defect-induced peak, attesting for the lower graphene quality of the UHV-grown sample.

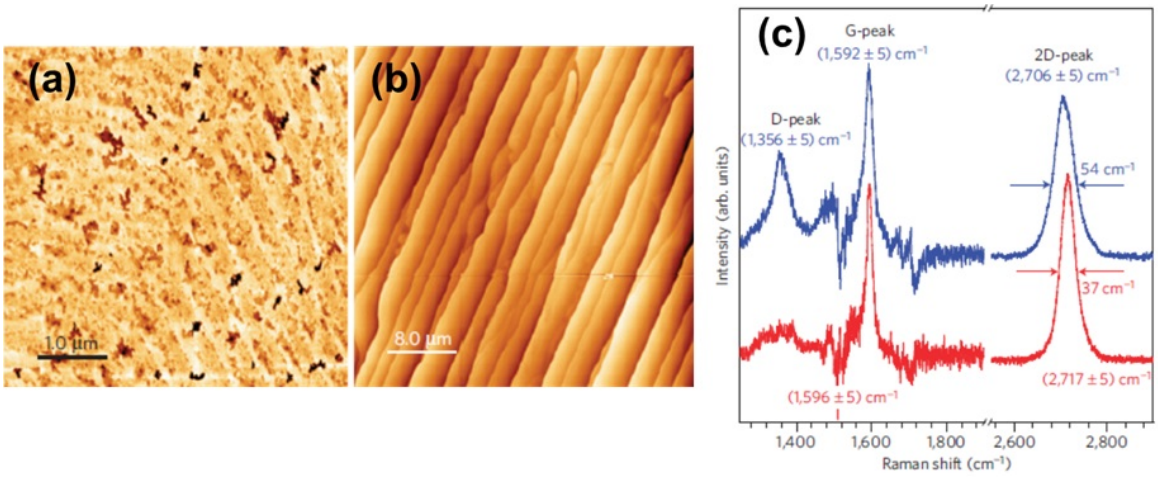

Figure 1.10: *AFM images of graphene grown for 15 min under* ***(a)*** *UHV at 1280°C and* ***(b)*** *900 mbars of argon at 1650°C.* ***(c)*** *Raman spectra of argon-grown graphene (red curve) and UHV-grown graphene (blue curve) [80].*

The Si sublimation approach not only provides a full wafer graphene growth with promising electrical properties, it also precludes the need for transferring the graphene layer, since SiC is a semiconductor and already integrated in many electronic applications, mainly high-power electronics and as a substrate for GaN-based high frequency electronics. First studies by Berger et al. in 2004 [4] succeeded on gating multi-layer graphene, even though the resistance modulation was poor (2%). The graphene layers were found to be n-doped with a carrier mobility of 1100 $cm^2/V.s$, as measured at 4 K. Further studies by the same team, have shown that nano-patterned structures of graphene exhibit charge carrier confinement [5]. They employed e-beam lithography to create Hall bars on single-layer graphene ribbons, 500 nm wide and 6µm long, previously grown on the C-face of a 4H-SiC substrate. The nanostructure leads to the confinement of the charge carriers, resulting in a mobility of 27 000 $cm^2/V.s$ at 4 K. Despite these few advantages, some downsides appear as well, the carrier mobility for graphene grown on SiC (0001) by this technique seems not so important, around 900 $cm^2/V.s$ at 300 K [80]. This drawback has led to concentrated efforts on finding ways to enhance the mobility, such as a post-growth annealing under H_2 [83,84] or creating patterned nanoribbons out of the grown graphene layer on SiC (0001) [85], which adds an extra step to the whole graphene production process. The post-growth annealing under H_2 aims

to introduce hydrogen at the interface between graphene and the substrate to achieve "quasi free-standing" graphene [84,86]. We will describe in details this process in **part 1.3.1**. This approach has been proven to be reliable, since it has led to the achievement of a carrier mobility reaching 11 000 $cm^2/V.s$ at 0.3 K for graphene grown on the Si-face of SiC by Si sublimation [84].

Another disadvantage rises from the fact that graphene grows from the substrate itself, which makes this method limited to SiC substrates, and to our knowledge only few studies have been developed to detach graphene from the SiC substrate [87,88]. In addition, it was found difficult to achieve a single layer of graphene on both the Si-face and the C-face. For SiC (0001) multilayers seem to appear at step edges as we can see in the low-energy electron microscopy (LEEM) image in Fig. 1.11(a), taken from reference [80]. The difference in contrast we see attests for the deposition of extra layers at step edges. Concerning the growth on SiC (000-1) it was found that it is challenging to achieve less than 3 to 4 monolayers (MLs) [89,90].

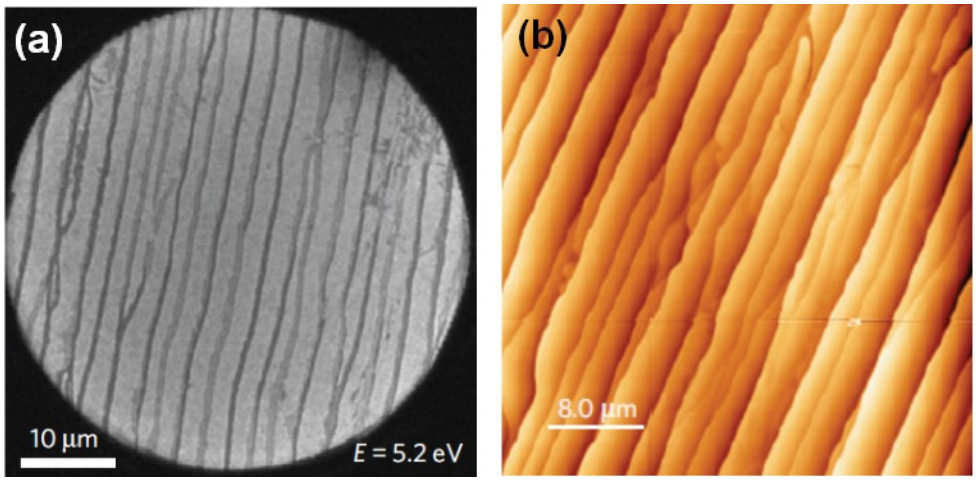

Figure 1.11: (a) *LEEM image of graphene grown under argon at 1650°C, the darkest regions correspond to bilayers and trilayers of graphene.* ***(b)*** *Corresponding AFM image [80].*

To conclude, the Si sublimation technique goes back to the 1970s, when SiC annealing led to the formation of graphite layers, detected on the basis of LEED and photoemission spectroscopy. Studies made just before 2004 have investigated in details the growth stages of graphite by looking at the SiC surface reconstructions. This elaboration technique was later adopted to demonstrate the 2D electron behavior in graphene grown on SiC, the same year of the discovery of Novoselov and Geim. After that, research concentrated on developing and enhancing this technique, by considering other approaches such as Si sublimation under atmospheric pressure of argon instead of UHV, which seemed better but required higher annealing temperatures. This technique seems promising allowing full scale growth, yet few drawbacks appear such as the limitation to SiC substrates, low carrier mobility compared to the exfoliation technique and difficulty to grow a single graphene layer.

1.2.3. Graphene elaboration on metal

Graphene elaboration on metal is today a large scientific community. Also started to surface around the year 2004, after which advancements happened very quickly, where major developments came to light in 2007 and 2008. By 2010, graphene elaboration on metal took a major leap towards large-surface graphene samples where 30-inch graphene roll was produced, after being initially grown on metal by CVD [10]. Despite this fast advancement in this area, the idea behind graphite/graphene formation on metal goes way back before the mechanical exfoliation to the 1970s. However, back then the main objective was not to grow or form graphite on metal, but rather study the impurity segregation (in this case carbon impurity) from the metallic substrate to the surface, upon annealing. Their main concern was the contamination of the surface when annealing at sufficiently high temperatures due to the diffusion of impurities from the substrate itself. Yet, we cannot pass by these discoveries without giving them credit, especially since this segregation technique was later adopted to grow graphene on metal.

Among these first studies, we will discuss briefly some segregation studies published in 1970 [91] and 1974 [92] on nickel Ni (100) and Ni (111) respectively. The experiments were carried out under UHV in standard LEED chambers equipped with heating filaments at the back of the sample holder. After annealing, Auger spectroscopy was used to detect impurities, and LEED to examine any structural changes at the surface. In the case of the Ni (111) [92], Auger peak analysis and LEED observations led to the following conclusion: an annealing up to 907°C, will lead to what is believed to be a "single layer of graphite". But this process is reversible, after an annealing above 907°C, the carbon will be dissolved back into the nickel substrate. For information, the Auger observations were taken at the annealing temperature and at room temperature, followed by LEED measurements at room temperature. LEED observations reveal ring-like patterns, which are attributed to a graphitic phase. Another interesting work of graphite formation on platinum (Pt) was reported in 1975 [93]. In this case, carbon was deliberately deposited on the Pt surface, in an attempt to study the carbon/metal interface. The growth chamber is again a LEED chamber maintained under UHV. The samples are heated between 300 and 810°C under 5 to 600 Langmuir (L) of ethylene and a total pressure of 10^{-8} mbar. They are monitored with LEED during the growth. Graphitic rings are detected and the deposition is estimated to be around 0.6 nm. This study is later completed with STM investigations in 1992 [94], which uncovered the morphology of the deposited graphite, and correlates to previous findings by presenting the honeycomb lattice of graphite. In this study, the growth chamber is saturated with 5 L of ethylene at room temperature, which subsequently decomposes when heating up to 500°C. This approach led to the appearance of graphitic islands at 627°C, and more continuous films at 797 and 957°C, see Fig. 1.12, taken from reference [94]. At 627°C, islands appear on the step terraces, with diameters between 2 and 3 nm. Increasing the annealing temperature, leads to the accumulation of graphite, leaving some large islands at the terraces, but also complete layers at step edges. Finally, STM observations have allowed them to conclude that a "single layer of graphite" has formed.

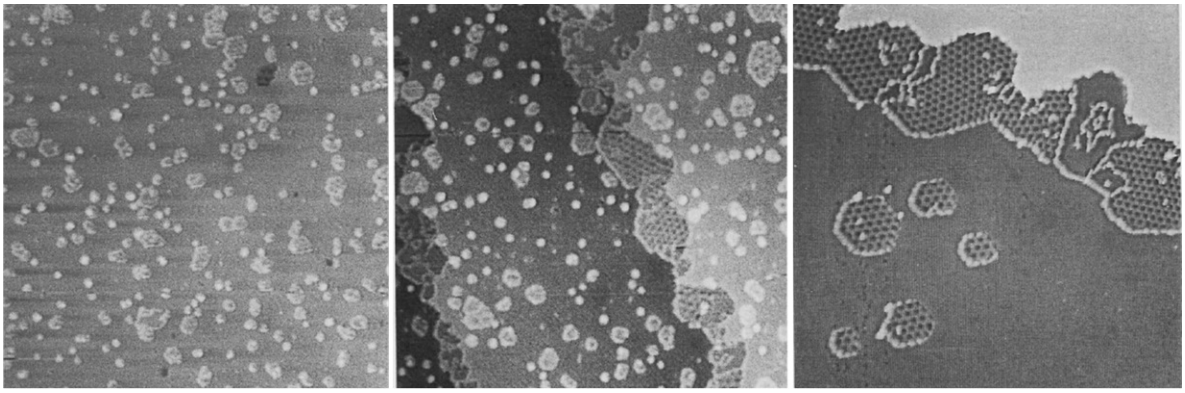

Figure 1.12: *100×100 nm² STM images of graphite on Pt steps at different annealing temperatures, taken at room temperature. From left to right, annealing temperatures: 627, 797 and 957°C respectively [94].*

It seems only fair to consider these studies as the foundation to future growth of graphene on metal. Yet, the influence of their contributions was not emphasized before the breakthrough of Novoselov and Geim in 2004 [3]. After this date, research began to target a more controlled deposition of uniform graphene films on metallic substrates, not to mention the transfer from metallic surface to an insulating surface for applications.

We will not mention all the studies done, the procedure is more or less the same, consisting in exposing the metal to a hydrocarbon under UHV with temperatures around 1000°C. Around and after 2004, studies were extended to different metallic surfaces in attempts to enhance the graphene quality, for example on iridium Ir (111) [95], platinum Pt (111) [96] and ruthenium Ru(0001) [97]. This latter study on Ru (0001) done in 2007 [97] is particularly interesting, since it relies only on the segregation of carbon from the substrate itself, without any external carbon source. The annealing is done under UHV at temperatures ranging from 730 to 1500°C, from 90 to 120 seconds. In Fig. 1.13, we display STM images of the as-grown graphene for two different annealing temperatures [97]. Fig. 1.13(a) exhibits incomplete graphene layer, but Fig. 1.13(b) presents a continuous graphene layer across the steps. What is more interesting is that in this case, LEED patterns presented well-ordered graphene spots, instead of the usual graphitic rings. Other promising results appeared on Ir (111) [98] in 2008, but this time in a low-pressure CVD reactor, which is a more user-friendly technique different from the UHV systems used before 2004. The substrate was exposed to ethylene at different temperatures ranging from 850 to 1050°C, which was the best temperature for the growth where a continuous graphene layer was deposited, as we can see in Fig. 1.13(c), taken from reference [98].

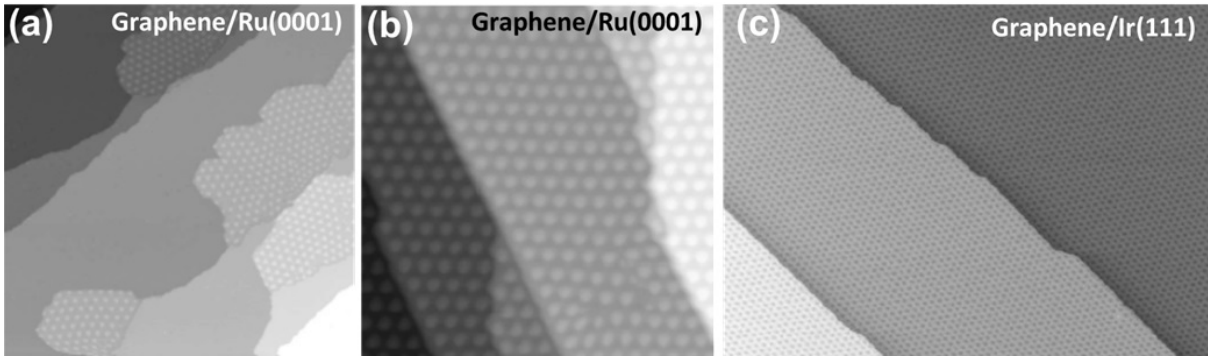

Figure 1.13: *STM images recorded after annealing at different temperatures.* ***(a)*** *100×100 nm² STM view of the annealed ruthenium at 730°C for 120 s.* ***(b)*** *50×50 nm2 view of the annealed ruthenium at 1200°C for 90 s [97].* ***(c)*** *125×250 nm² image of the grown graphene on iridium at 1050°C [98].*

So far the growth of graphene on metal seems promising, yet of little interest in the electronic industry. However, progress spread quickly and different studies emerged proposing innovative methods to detach the graphene from the metal substrate [8–10,46]. They rely mainly on the segregation technique, by exposing polycrystalline nickel or copper substrates to a hydrocarbon (CH_4). The process is carried out in CVD reactors, under atmospheric pressures of argon and H_2 and at high temperature (usually around 1000°C), sufficient to instigate the carbon diffusion into the metallic substrate. This step is then followed by a medium-rate cooling (~10°C/s) leading to the formation of a thin graphene layer at the metallic surface. It is crucial to control the cooling rate, in order to control the graphene thickness and quality [9]. The growth process is summarized in Fig. 1.14.

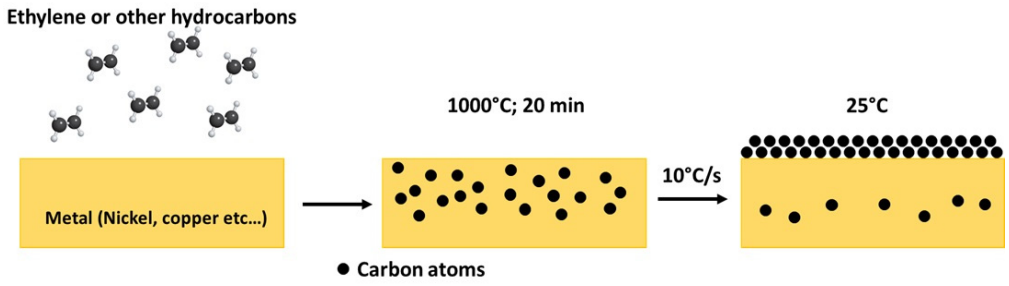

Figure 1.14: *Growth procedure of graphene on metal.*

After the graphene formation, a PMMA layer is spin-coated on the graphene/metal structure, or in some other cases polymerized siloxanes are used, followed by a chemical etching of the metallic substrate ($FeCl_3$, HNO_3 or other acids). The PMMA/graphene can then be deposited on any substrate suitable for applications and then the PMMA is removed by proper means. We present this procedure in Fig. 1.15.

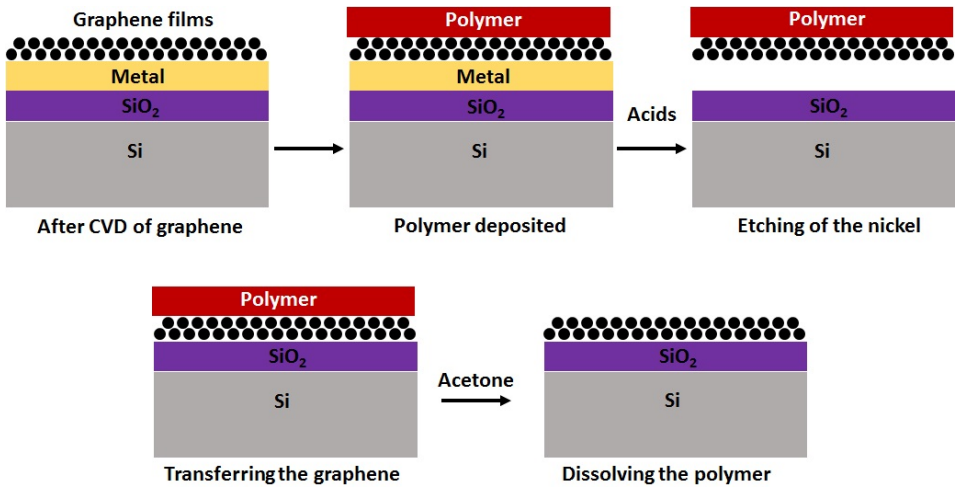

Figure 1.15: *Transfer process of the grown graphene on metal to another substrate.*

Now that we have described this technique we will discuss its advantages and limitations. The main advantage of this technique is the ability to transfer the graphene layers to any arbitrary substrate with different sizes, since the size of the graphene sample is limited by the size of the growth chamber. Some studies considered iridium as a host for the graphene deposition, however other studies proved that it can be possible to use polycrystalline nickel or copper, which is a lot cheaper, and can be prepared by simple physical vapor deposition. Bae et al. [10] considered copper for their study and demonstrated the possibility to produce large area graphene films with widths up to 30 inches. Both Bae et al. [10] and Kim et al. [46] reported impressive results of sheet resistance and charge carrier mobility of graphene films, initially grown on copper [10] and nickel [46], then transferred to SiO_2/Si substrates or Polyethylene terephthalate (PET) substrates. Their main objective was to create graphene electrodes consisting of multilayers stacked together. The lowest sheet resistance for assembled films of graphene, initially grown on copper (resp. nickel) was found to be around 30 Ω/□ (resp. 280 Ω/□). Charge mobility recorded on a single layer of graphene at 295 K is around 5100 cm^2/V.s for graphene films grown on copper, and 3700 cm^2/V.s for graphene films grown on nickel. Further investigations revealed that the sheet resistance decreases for an increasing number of graphene films, but in this case the optical transmittance is reduced. A fair compromise between the transmittance and sheet resistance has to be done, depending on the application. This technique is widely used today and is being developed to produce graphene as a substitute for ITO [10]. Even though multilayer graphene is required to achieve low sheet resistance compared to ITO, the transmittance of the visible spectrum is thought to be better in graphene than in ITO [10,22]. In addition, graphene can withstand a lot more strain than ITO [10]. The carrier mobility in the as-grown graphene is variable across the literature, studies report a carrier mobility between 3000 and 5000 cm^2/V.s at 300 K [10,46,99].

A recent study [100], considered a new approach to detach the graphene from the metal. Graphene flakes with width up to 500 µm were grown by CVD on copper, then instead of covering graphene directly with a polymer, exfoliated h-BN was brought into mechanical contact with the

graphene flake. The heterostructure polymer/h-BN/graphene was then peeled-off from the metal, due to the strong BN-graphene interactions. After that, the structure was transferred on SiO_2/Si substrate. The carrier mobility measured for the encapsulated graphene reaches 1×10^5 cm^2/V.s at 300 K for both holes and electrons. Although this approach seems innovative, it is still limited to the size of the exfoliated BN flake.

Despite these promising achievements, few drawbacks can arise. The process can be more or less expensive depending on the metal used, especially since the metal needs to be sacrificed each time. The quality and the number of layers seem very dependent on the roughness and initial state of the metallic substrate as some studies have mentioned [8,9]. The initial substrate is a polycrystalline metal, for example Reina et al. [8] used polycrystalline nickel deposited on SiO_2/Si substrates. The substrate is annealed before the CVD growth of graphene, revealing grain sizes ranging between 1 and 20 µm. Consequently, as it has been reported, 1 to 2 graphene layers are detected on the nickel grain, but more graphene layers are found at the grain boundaries. Fig. 1.16(a) presents an optical image of graphene reported to a SiO_2/Si substrate, taken from reference [8]. The color fluctuations emanate from the variation in the number of graphene layers due to light interferences on the SiO_2 layer. Overall, between 1 and 12 layers are detected by correlating this optical image with AFM and TEM. Same for the study presented by Kim et al. [46] different graphene layers were detected (see Fig. 1.16(b)). The uniformity of the graphene layers can be more or less controlled by changing few growth parameters, such as the growth time and the nickel thickness, but it is not completely optimized. As previously mentioned, the optical transmittance and sheet resistance depend immensely on the number of graphene layers. Non-uniformity of this parameter will lead to other non-uniformities in any prepared device. Bae et al. [10] also mentioned this issue, but in their case, copper films were heated enough to increase the grain sizes up to 100 µm, resolving to some extent the problem, but still some non-uniformities can be detected as we can see in the TEM and AFM images in Fig. 16(c, d), taken from reference [10]. We can also see some cracks and ripples in the AFM image. But this is not the end, as some studies failed to mention, early studies identified with LEED the polycrystalline nature of graphene grown on metal [91,95,96]. The polycrystalline nature and the un-controlled uniformity can be major drawbacks for this technique.

To summarize, graphene growth on metal is also as old as the Si sublimation technique, but first objectives were concerning the impurity segregation upon metal annealing under UHV. These first studies are very important since they later inspired the growth of graphene on metal in UHV but also in CVD systems. Different metallic substrates were considered, such as expensive iridium or cheap polycrystalline nickel. After 2004, efforts concentrated and succeeded on finding ways to detach the graphene layer from the metallic substrate, by sacrificing the metal. Many achievements were reported in this area, such as large scale graphene production, high carrier mobility and low sheet resistance. In contrast, few points need to be improved, such as the crystallinity of the graphene layer and the non-uniform thickness, depending on the metallic substrate.

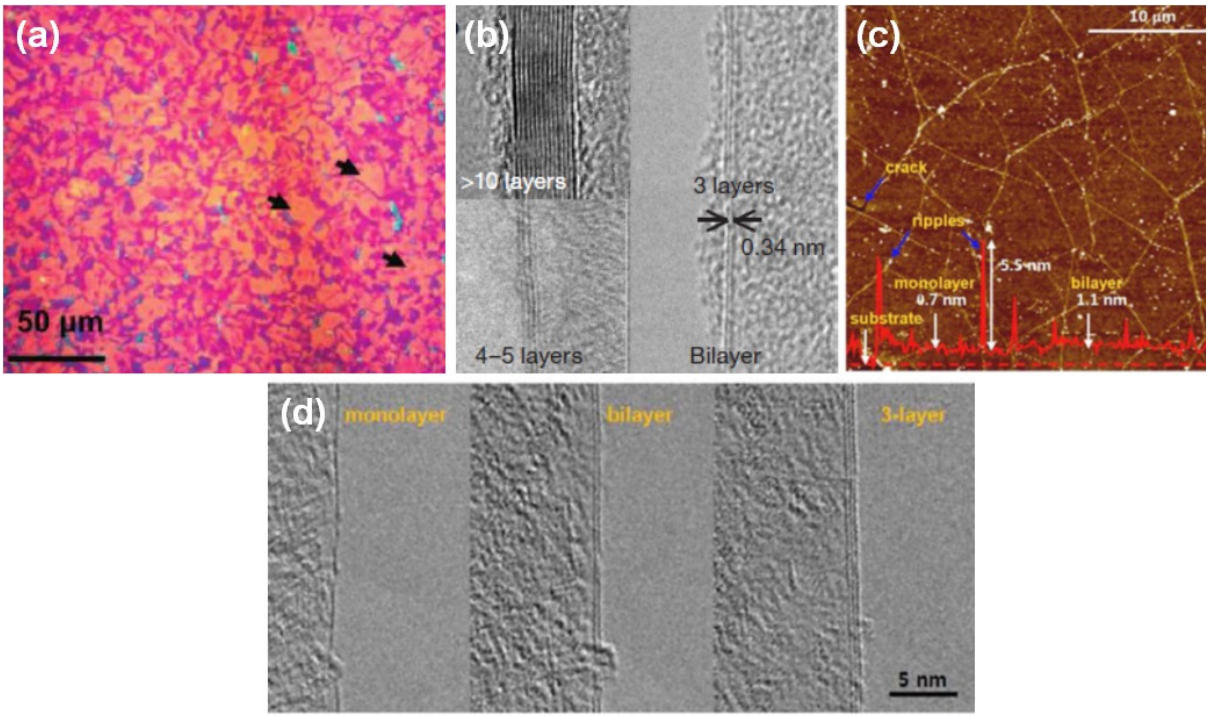

Figure 1.16: ***(a)*** *Optical image of graphene transferred on SiO_2/Si substrate. Arrows indicate large grains, where the number of graphene layers is assumed to be 1 and 2 [8].* ***(b)*** *Cross-section TEM image showing the variety of the number of layers [46].* ***(c)*** *and* ***(d)*** *AFM and cross-section TEM images presenting different layers of graphene, in addition to ripples and cracks on the AFM image [10].*

1.2.4. Growth of graphene on SiC from an external carbon source in UHV or in argon atmosphere

Initially, SiC was employed for the growth of graphene by Si sublimation, a technique known before 2004. While some studies tried to improve the Si sublimation method, especially after 2004, others proposed a new approach to grow graphene on SiC. Instead of considering the SiC substrate as the source of carbon, one can rely on an external carbon source to grow graphene, a method we name direct growth. These studies started to appear around 2009, claiming that this approach would help in reducing the growth temperature under UHV [11,16] compared to the Si sublimation technique. The growth can be carried out by MBE i.e. under UHV conditions, while the source of carbon can be the thermal decomposition of graphite filaments. The growth temperature can be reduced to 950°C, but the growth time is around 30 minutes [16]. For a slightly higher temperature (1050°C) the growth can be achieved within 3 to 4 minutes [11]. We present in Fig. 1.17(a) an AFM image of graphene grown on SiC (0001) by MBE taken from reference [11].

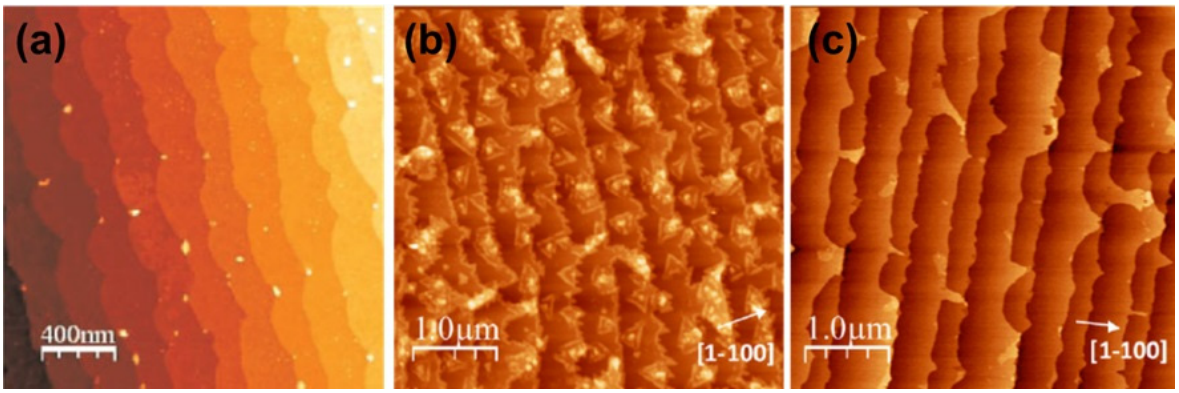

Figure 1.17: ***(a)*** *AFM image of graphene grown on 6H-SiC(0001) at 1050°C under UHV for 3 min [11].* ***(b)*** *and* ***(c)*** *graphene grown at 1300°C for 30 min under argon atmosphere of* ***(b)*** *100 mbars and* ***(c)*** *700 mbars [101].*

Other approaches can be considered such as the growth by CVD, which relies on higher growth pressures of argon, with propane (C_3H_8) as the carbon source [12,13,101]. The direct growth under argon was first suggested in 2010 by Hwang et al. [12], who succeeded on growing graphene on sapphire and on SiC (000-1) at 800 mbars and temperatures between 1350 and 1650°C. For temperatures around 1350 and 1450°C, the process requires a longer growth time (5-15 minutes). For a temperature as low as 1300°C, a 45-minute growth is required to achieve a continuous graphene layer [101]. We can notice one of the advantages of this technique compared to the Si sublimation process i.e. the lower growth temperature which is around 1350°C for CVD instead of 1650°C for 15 minutes of annealing under 1 bar of argon [80]. Other growth parameters need to be well controlled for good quality graphene. A CVD growth of graphene on SiC under argon demonstrated that the quality of the graphene presents a strong dependence on the growth pressure, with higher pressures promoting smoother surfaces and smaller sheet resistances [101]. We show in Fig. 1.17(b) and (c), the morphology dependence on the growth pressure [101]. At 100 mbars (Fig. 1.17(b)) clusters appear on the surface, but the morphology becomes smoother and more uniform at 700 mbars (Fig. 1.17(c)). Further investigations done by Strupinski et al. [13] revealed that the Si sublimation can be inhibited even under pressures as low as 20 mbars and temperatures as high as 1600°C in a CVD system. This is achieved by controlling the partial pressure of argon in a way to control the thickness of the boundary layer of the gas phase in the vicinity of the surface. For example with the right growth conditions, one can have an argon boundary layer thick enough to stop the silicon atoms from evaporating to the gas phase, but thin enough to allow the diffusion of propane to the substrate. This way the graphene layer is grown from the external carbon source and not from the substrate.

In summary, we have shown the wide range of growth parameters employed to obtain epitaxial graphene on SiC with an external carbon source. Such direct growth can be achieved under UHV systems such as MBE reactors or under argon in CVD reactors, at temperatures as low as 1300°C. However, some growth parameters are improved at the expense of other parameters. For example, reducing the growth temperature, or increasing the total pressure requires a longer

growth process reaching 45 minutes. It was also reported that a higher growth pressure is better for the graphene quality in terms of morphology and electrical properties. This technique was also proven capable on achieving wafer-scale deposition [102] similar to the Si sublimation technique. But unlike the Si sublimation method, direct growth is not limited to the SiC substrate, since it was extended to sapphire and aluminum nitride (AlN) as we will see in the following paragraphs. In addition electrical measurements revealed carrier mobility as high as 1800 $cm^2/V.s$ at 300 K [13].

1.2.5. Discussion and conclusion

We have discussed previously the most common techniques used today to elaborate graphene. One can find other techniques in the literature, which are less known or less effective. In this paragraph we will discuss the interest of each technique despite its limitations, as presented in table 1.1 at the end of this part. We also summarize in table 1.2 the typical graphene elaboration parameters or growth conditions for the different techniques that we presented so far.

Although the mechanical exfoliation technique has been a landmark in the history of graphene, it is limited to research due to the small sample size, even though we cannot disregard what this approach brought to the science community. It unveiled the exceptional properties of graphene and allowed the detection of ballistic transport in graphene layers by achieving a carrier mobility of 100 000 $cm^2/V.s$ at 300 K [62]. This carrier mobility was recorded for encapsulated graphene in BN layers, also achieved by exfoliation. This method has inspired new assemblies of 2D materials and a new vision for electronic devices, based on 2D-material heterostructures. We also believe that this technique was the spark which unleashed advancements in other areas such as graphene growth by Si sublimation and graphene growth on metal.

Many achievements were reported for graphene on metal, which relies mainly on CVD systems. Polycrystalline nickel or copper were found to be the best hosts for graphene deposition, since they can be easily prepared and etched in order to release the graphene layer. Studies have developed exhaustive procedures for the production of graphene layers starting with the deposition step and achieving the preparation of 30-inch rolls of graphene [10]. With this process, many layers can be stacked together on any arbitrary substrate for any application. Even electronic devices were demonstrated based on the as-grown graphene with carrier mobility ranging between 3000 and 5000 $cm^2/V.s$ at 300 K [10,46]. Despite these promising results, some parameters need to be improved, such as the quality of the graphene consisting of ripples, cracks, non-uniform thickness and even polycrystalline deposition in some cases.

Concerning the Si sublimation method, it was also a milestone in graphene history, since it contributed to the knowledge of the graphene electronic behavior, even if it is not suspended but on SiC. In fact, a study was published in the same year as the work of Novoselov in 2004 [3], attesting for a 2D electron gas behavior in graphene grown on SiC by Si sublimation [4]. This technique allows a wafer-scale deposition on SiC, which is a material already integrated in power electronics with rather large wafers (4” and soon 6”). It has also revealed ballistic transport in nano-patterned graphene, on the Si-face and on the C-face [5,85]. On the other hand, the

sublimation method is still limited to SiC and the carrier mobility in a continuous graphene layer on the Si-face is not so important (around 900 $cm^2/V.s$ at 300 K [80]). A post-growth annealing under H_2 is needed to enhance the mobility (11 000 $cm^2/V.s$ at 0.3 K) [84].

This technique is overall very promising but whether it is better than the direct growth from an external carbon source or not is still questionable. Strupinski et al. [13] have demonstrated that graphene prepared by Si-sublimation is under more compressive strain than graphene prepared by CVD on SiC. The reason they proposed is the different growth mechanism in the two cases: for the Si sublimation the growth starts in an arbitrary way at step edges and at defects such as dislocations, but for CVD graphene, the nucleation seems correlated with the atomic steps of SiC, allowing "step-flow" epitaxy. They also claim that the number of layers can be better controlled with direct growth CVD. They also reported higher carrier mobility on SiC (0001) reaching 1800 $cm^2/V.s$ at 300 K, reflecting the better quality of CVD graphene. Regardless of these observations, the direct growth techniques still holds few advantages compared to the Si sublimation, such as the lower growth temperature around 1300°C [12,101] instead of 1650°C [80] at atmospheric argon pressures. In addition, since it depends mainly on the external carbon source, it was extended to other substrates. For example sapphire [12], AlN/Si(111) templates [103], bulk AlN and AlN/SiC templates [104], creating new opportunities and new markets for graphene in optoelectronics. Finally, it has also inspired a new approach for CVD which is CVD under H_2, leading to enhanced carrier mobility ranging between 1200 and 4400 $cm^2/V.s$ at 300 K [13,19]. This new approach will be the main subject of **part 1.4**.

We present in table 1.1 the highest values of carrier mobility we found in the literature for each graphene elaboration technique. We also present the main drawbacks but not all of them. Note that the sample size for the CVD methods depends on the reactors size. One can notice that the different elaboration techniques demonstrated promising results, but also some disadvantages. Our intention is not to derogate the growth techniques, but simply to point out their characteristics and limitations.

Table 1. 1: *Graphene elaborations techniques and there characteristics*

Method	Sample size	Charge Carrier mobility ($cm^2/V.s$)	Drawbacks	Applications
Exfoliation	~1 mm	~1×10^5 at 300 K	Limited in size	Research
CVD (metal)	~1000 mm	Mostly 5×10^3 at 300 K	Polycrystalline and non-uniform	All kinds of electronics
Si sublimation	Wafer-scale	~2.7×10^4 at 4 K (C-face) and 1.1×10^4 at 0.3 K (Si-face)	High temperature, non-uniform thickness	High-frequency and power electronics
CVD (SiC)	Wafer-scale	~5×10^3 at 300 K		

Table 1. 2: *General graphene elaboration parameters for the different techniques.*

Method	Temperature	Atmosphere	Process duration/Growth time	Special requirements
Exfoliation	Room temperature	Room atmosphere	>60 min	Clean room procedures
CVD (metal)	~1000°C	UHV or atmospheric pressure of argon + H_2	20 min	Clean room; metal solvents
Si sublimation	~1200°C or 1750°C	UHV or atmospheric pressure of argon	>15 min	High-temperature systems
CVD (SiC)	1350°C	Atmospheric pressure of argon	15 to 45 min	External carbon source

1.3. Graphene on SiC: Structure and polarity

We have mentioned previously in **part 1.2.2** some of the different observations made for graphene grown on the Si-face and the C-face of SiC, in terms of morphology, crystallinity and electrical properties. These differences emanate from the different graphene growth mechanisms on the two SiC polarities. We will discuss in this part, the graphene's growth mechanism on both of the SiC faces and its influence on the graphene properties.

1.3.1. Graphene growth on the Si-face of SiC

Regardless of the growth technique, whether it is by Si sublimation or from an external carbon source in UHV or argon atmosphere, the graphene formation on SiC (0001) was found to be associated with the growth of a buffer layer. Early studies [2,76] have identified this layer as a C-rich surface reconstruction of the SiC substrate when annealed at sufficiently high temperatures. Annealing at 1050°C under UHV resulted in a SiC ($\sqrt{3}\times\sqrt{3}$) surface reconstruction oriented at a 30°-angle with respect to the substrate [76]. Increasing the temperature to 1150 and 1250°C led to a ($6\sqrt{3}\times6\sqrt{3}$)-R30° SiC surface reconstruction (hereafter referred to as "$6\sqrt{3}$"), also known as the buffer layer.

Many studies have since concentrated efforts on this surface reconstruction to identify its nature because it was believed that it has an important effect on the graphene properties [16,27,105,106]. In particular, Emtsev et al. [105] were able to define the structural and electrical properties of this buffer layer on the basis of angle-resolved photoemission (ARPES) and X-ray photoemission spectroscopy (XPS) in addition to LEED measurements. The valence band of the $6\sqrt{3}$ structure was found to exhibit graphene-like σ-bands which implies that the atomic arrangement and the C-C bond length within the $6\sqrt{3}$ buffer layer are identical to those in graphene. On the other hand the $6\sqrt{3}$ structure failed to present graphene-like π-bands, revealing the nonmetallic nature of the buffer layer, which can be ascribed to strong covalent coupling to the substrate. This deduction is confirmed with XPS by examining the C1s spectrum of the buffer layer [105].

As we present in Fig. 1.18(a) (from reference [105]), the XPS spectrum can be fitted with three peaks, one at lower energies (~283 eV) attributed to the SiC substrate and two components at higher energies, S1 at ~ 284.75 eV and S2 at ~ 285.55 eV, with an area ratio S1/S2 of 0.5. The presence of two peaks for the buffer layer reflects the presence of two types of atomic bonds i.e. some C atoms of the buffer layer bond to the substrate. By considering that the area density of C atoms in graphene is three times the area density of Si atoms on the SiC (0001) surface, and the ratio S1/S2 to be 0.5, it is possible to conclude that the S1 component ensues from one-third of C atoms, within the buffer layer, interacting with the Si dangling bonds of the substrate. The two-thirds which are left are bound together and give rise to the S2 component. In other words, the buffer layer is a mix of sp^2- hybridized C atoms (similar to graphene) and 33% of sp^3-hybridized C atoms, each one of them bound to other three C atoms from the buffer layer and one Si atom

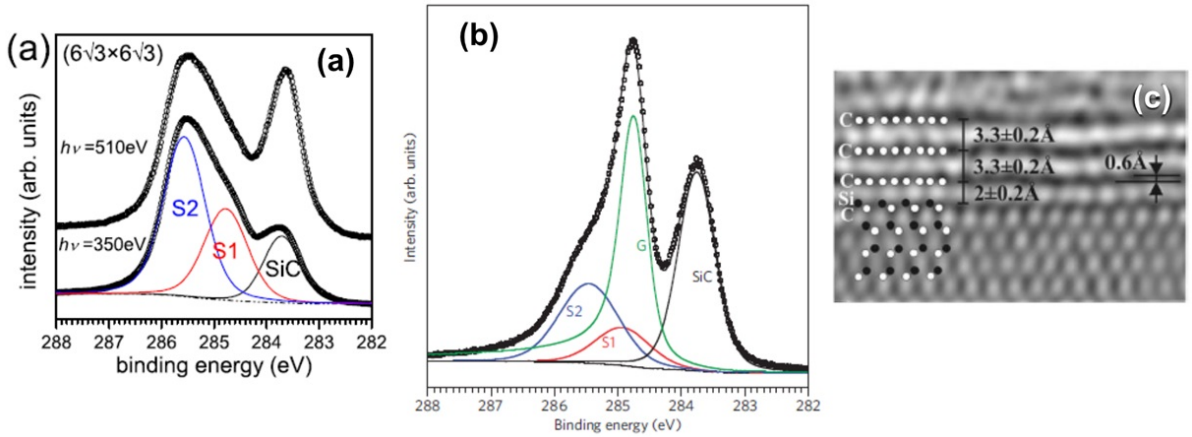

Figure 1.18: *C1s core-level of* ***(a)*** *the 6√3 structure and [105]* ***(b)*** *graphene on the 6√3 structure grown on SiC(0001) [80].* ***(c)*** *TEM image of three layers and the 6√3 structure grown on SiC(0001) [110].*

belonging to the substrate. However this does not mean that each C atom from the buffer layer has a Si atom directly beneath it, but because of the flexibility in bond angle and bond length of the Si atoms, the Si-C bonds can be achieved [107–109]. On a side note, the graphene peak is shown in another study to be close to the S1 component, see Fig. 1.18(b) taken from reference [80]. Finally, Emtsev et al. were able to conclude that the 6√3 structure corresponds to a graphene (13×13) unit cell [105]. In addition, the buffer layer and the subsequent graphene layer are rotated by a 30°-angle with respect to the substrate. TEM observations further confirm the presence of bonds between the buffer layer and the substrate. As we present in Fig. 1.18(c), taken from reference [110], the distance between the buffer layer and the substrate is 0.2 nm, which is close to the Si-C bond length (0.189 nm) in SiC, whereas the distance between the buffer layer and the first graphene sheet is 0.33 nm.

Few studies have attempted to reduce the effects of the buffer layer, mainly by a post-growth annealing with H_2 as we have previously mentioned. The post-growth annealing with H_2 aims to intercalate hydrogen at the interface between graphene and the substrate [84,86]. We illustrate in Fig. 1.19 the hydrogen intercalation process. At first, before the graphene growth, the topmost SiC (0001) layer is silicon-terminated where few or all of the silicon atoms have dangling bonds. When growing graphene by Si sublimation or by other means on the Si-face of SiC, first a buffer layer is grown, which shares covalent bonds with the substrate by bonding with few of the Si dangling bonds as we show in Fig. 1.19(a). Annealing this latter sample under H_2 at atmospheric pressures and temperatures around 700°C will introduce hydrogen at the interface, which will bond with the silicon atoms of the substrate and replace any bonds between the substrate and the buffer layer, thus transforming the buffer layer into a quasi "free-standing" graphene layer, see Fig. 1.19(b). However, this hydrogen intercalation process is reversible: if we anneal a hydrogenated sample at temperatures around 700°C under UHV[111], Si-H bonds will break and

hydrogen will desorb, which will allow the graphene layer to bond back with the substrate and form again a buffer layer [86,111].

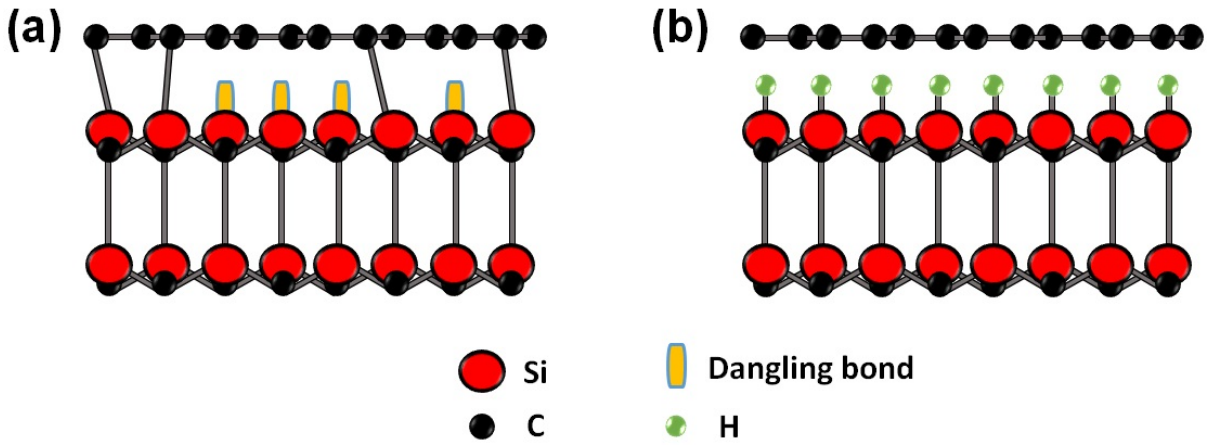

Figure 1.19: *Side view model of the Si-face of SiC, showing in* ***(a)*** *the 6√3 buffer layer with few Si dangling bonds and* ***(b)*** *the hydrogenated interface.*

1.3.2. Graphene growth on the C-face of SiC

On the other hand, the growth on the C-face of SiC (SiC (000-1) is completely different. The process starts with an annealing at temperatures around 900°C under a silicon flow to remove surface oxides, leading to a (3×3) reconstructed Si-rich surface. Increasing the temperature to 1050 and 1100°C leads to a (2×2) reconstruction and smeared elongated shapes [78]. For higher temperatures, the (2×2) reconstruction is weakened and the elongated shapes are more intense and form diffraction rings [2,78]. No (√3×√3)-R30° reconstruction was observed [2,78,105]. In addition, ARPES measurements [105] show no changes to the σ- and π-bands similar to those observed in the 6√3 case, which suggests a weak coupling with the substrate. Furthermore, ARPES and LEED observations reveal the presence of highly disoriented domains with respect to each other, even for a coverage of 0.3 monolayer. This means that from the beginning of the growth, graphene domains are rotated. The absence of the strong interaction between the first graphene layer and the substrate is confirmed with XPS. By examining the C1s core-level, only two components appear, one for the SiC substrate around 282 eV, and another for the graphene sheets around 284 eV (see Fig. 1.20(a) taken from reference [105]). The reason behind this weak bonding with the substrate could be related to the C atoms dangling bonds. In fact, the C-face presents a stronger inward relaxation of the outermost C atoms compared to the Si-face, along with shorter dangling bonds and a maximum of dangling bonds within the surface plane [109]. Other studies also corroborate the absence of bonds at the interface, but instead they report an amorphous mix of Si and C atoms on the basis of TEM observations and fast Fourrier transform (FFT) analysis [90]. TEM measurements even show an increase in the interface layer thickness with the sublimation temperature (see Fig. 1.20(b-d) taken from reference [90]). Presumably, this weak coupling with the substrate can be accounted for the rotational disorder within the nucleating

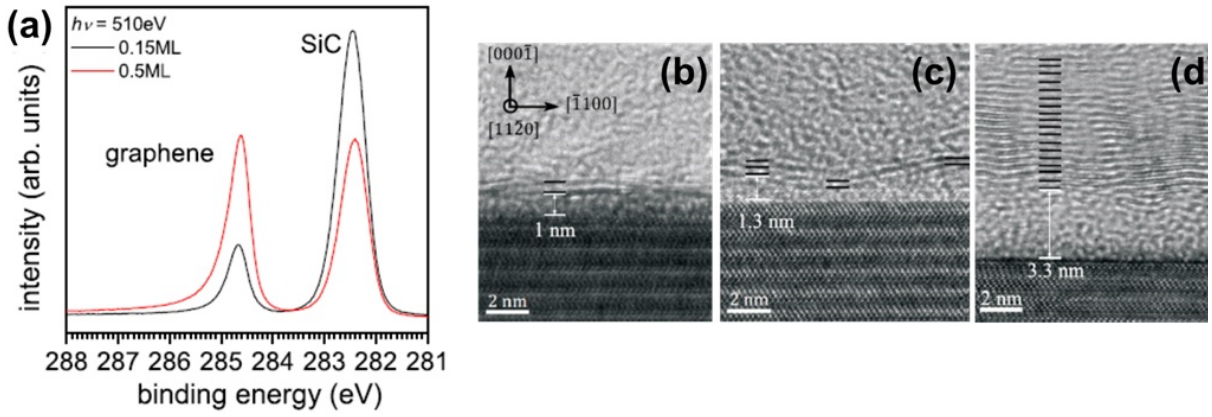

Figure 1.20: (a) *C1s core-level of graphene on SiC (000-1) [105].* ***(b)*** *to* ***(d)****: Graphene grown under argon atmosphere on SiC (000-1) at different temperatures:* ***(b)*** *1800°C* ***(c)*** *1900°C* ***(d)*** *2000°C [90].*

graphene layer. Extensive investigations [27,43,112] reveal that also stacking faults occur between the graphene films, which means that adjacent graphene layers can be rotated with respect to each other, and fail to follow a Bernal AB stacking, typical for graphite. These stacking faults will cause an interference between the π*-states of two graphene planes, inducing an expansion in the inter-layer spacing, larger than that for the expected AB stacking [112]. Accordingly, the graphene layers will act as electrically decoupled graphene sheets. For this same reason studies claim that multilayer-graphene grown on SiC (000-1) behave as a single layer [43], since their band structure is nearly identical to isolated graphene. Another characteristic of the C-face is the observation of surface wrinkles (see Fig. 1.19). In most cases, these features are only observed on the C-face and attributed to a strain relaxation mechanism. We will come back to this point in **chapter 3** in which the strain in the epitaxial graphene layer will be more discussed. However it is worth noting that few studies have also reported wrinkles on the Si-face under special hydrogenated elaboration conditions [17,18], but also under UHV at relatively high temperatures (1300-1400°C) [113].

So far we have discussed the growth of graphene on both of the SiC faces, but we cannot say whether the Si-face or the C-face is better for the growth because this subject is still debatable today. Some consider that the C-face is more promising, since high electron mobility was demonstrated (27 000 cm^2/V.s at 4 K) [5] compared to the lower carrier mobility on the Si-face (11 000 cm^2/V.s at 0.3 K after a post-growth treatment) [84]. However, both polarities present different disadvantages: the C-face exhibits graphene with in-plane rotational disorder and up to 10 nm high wrinkles [78,82], which could affect the electrical properties for devices at the micrometer scale, or also cause non-uniformities in the electrical properties on the wafer-scale. In addition, the growth rate on the C-face is known to be faster than on the Si-face, since the nucleation process on the C-face is believed to start at screw dislocations by forming thick graphene islands (up to 5 MLs), leading to different thicknesses across the substrate [89,114] and making it challenging to achieve 1 to 2 graphene layers on the C-face, whether by Si sublimation [90] or CVD [12]. On the other hand, the growth on the Si-face is associated with a buffer layer,

not exhibiting graphene-like properties, which some scholars blame for the reduced carrier mobility in graphene grown on the Si-face. In addition, the growth on the Si-face is usually accompanied with multi-layer deposition at the step edges, under Si sublimation conditions [80,115], yet we believe that this lack of uniformity can be better mastered in CVD direct growth.

In summary, in order to understand the difference between graphene grown on the Si-face and on the C-face of SiC we had to emphasize the role of the interface between the graphene layer and the SiC substrate, which has a substantial effect on the graphene's properties. The growth on the Si-face of SiC is associated with the presence of a buffer layer sharing covalent bonds with the substrate. This buffer layer is a surface reconstruction of $(6\sqrt{3}\times6\sqrt{3})$-R30° with respect to the substrate which undergoes further coverage with graphene sheets. It can be detected with LEED, XPS and TEM. ARPES measurements [105] have shown that this layer does not present a graphene-like electronic structure, uncovering its nonmetallic nature. On the other hand, no covalent bonds with the substrate were attested for in the case of the C-face, but instead an amorphous mix of Si and C atoms was detected at the interface [110]. The growth on this latter face is associated with in-plane rotational disorder and rotational stacking faults, which give rise to electrically decoupled adjacent graphene layers. However, charge transfer is suspected to occur from the substrate to the graphene layers, even in the case of the C-face growth [43,105], which can be detrimental for the charge carrier mobility if the charge transfer becomes important, possibly because of interactions between the charge carriers. On the other hand, the $6\sqrt{3}$ buffer layer is expected to have even a worst effect on the carrier mobility. Varchon et al. [36] assume that in this latter case, interface electronic states interact with the graphene states, thus explaining the reduced mobility for the Si-face compared to the C-face. Consequently, some studies attempted to inhibit the effects of the buffer layer with a post-growth treatment by annealing the graphene sample under H_2. This will lead to hydrogen intercalation at the interface and decouple the buffer layer from the substrate, making it a graphene layer [84,86]. Other approaches can be considered, instead of a post-growth hydrogen-treatment, the same effects can be achieved by conducting the growth under hydrogen atmospheres in a CVD reactor. This approach has been developed starting from 2010 before this present work and it was found to be very reliable. We will present the state of the art of this technique in the next paragraph, along with all the achievements it added to the growth of graphene on SiC.

1.4. State of the art CVD of graphene on SiC under H_2

Even though the popular technique to grow graphene on SiC was Si sublimation after 2004, other approaches emerged considering epitaxy from an external carbon source. Some studies considered MBE under UHV [11,16], others relied on CVD with a carbon source under atmospheric pressures of argon [12,13]. At the same time around 2010, it was demonstrated in our laboratory that graphene can be grown in a propane-hydrogen atmosphere on the Si-face of SiC. In particular, the growth was carried out on 6H-SiC (0001) and on 3C-SiC/Si (111) templates [17]. This approach allowed to reduce the growth time to 5 minutes at 1350°C and 200 mbars. However, an unexpected observation was made: the as-grown graphene on the Si-face under the mentioned conditions exhibited in-plane rotational disorder (IRD) observed with LEED, along with wrinkles appearing at the surface (see Fig. 1.21 taken from reference [17]). These observations (the IRD and the wrinkles) are usually associated to the growth of graphene on the C-face [81,82].

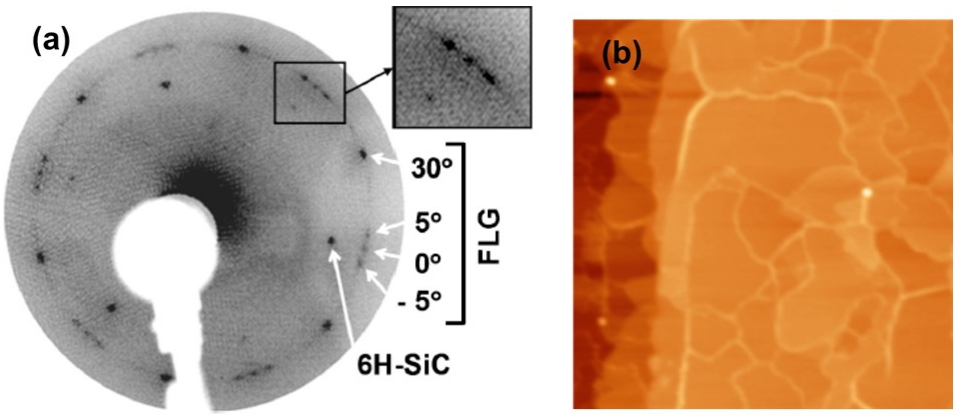

Figure 1.21: *Graphene grown on SiC (0001) at 1350°C and 200 mbars of H_2 + C_3H_8, for 5 min.* ***(a)*** *LEED pattern showing IRD and* ***(b)*** *AFM image (650×650 nm^2) presenting wrinkles [17].*

The reason behind this behavior was attributed to the saturation of the surface dangling bonds with hydrogen, inhibiting the first deposited carbon layer to bond with the substrate. In addition, unlike the growth on the C-face, the propane-hydrogen growth permits a better control of the graphene thickness by changing the propane flow. As a result, it is possible to achieve FLG thicknesses ranging between 1.5 and 6.4 monolayers (MLs). We show in Fig. 1.22(a) the C1s core-level intensity as a function of the propane flow rate [17]. The sp^2 peak (graphene peak) intensity reflects the thickness of the epitaxial graphene. Therefore, increasing the propane flow rate induces an increase in the graphene thickness.

At the same time, our research group attempted to grow graphene under propane-argon atmosphere without any hydrogen, again on 6H-SiC (0001) and 3C-SiC/Si (111) [101,102]. The process is slower requiring at least 30 minutes of growth and in this case the ($6\sqrt{3}\times6\sqrt{3}$) buffer layer is detected with LEED and XPS. The quality of the graphene presents a strong dependence

on the growth pressure, where higher pressures promote smoother surfaces and smaller electrical sheet resistance. In addition, it allows a wafer-scale growth with noticeable uniformity over the 2'' substrate, as we present in Fig. 1.22(b) [102]. The C1s(sp^2)/C1s(SiC) ratio is linked directly to the thickness of the graphene layer [79]. As we can see, the thickness is more or the less the same across the wafer.

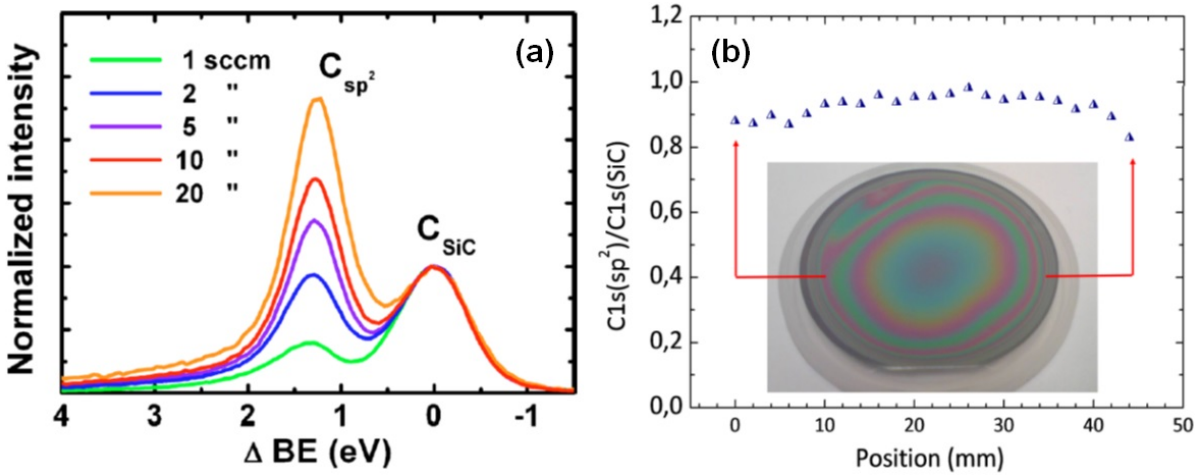

Figure 1.22: ***(a)*** *C1s core-level spectra for different propane flows, grown under 200 mbars H_2 at 1350°C for 5 min on 6H-SiC (0001) [17].* ***(b)*** *sp^2/SiC intensity ratio taken from different positions on the 2'' 3C-SiC wafer after graphene growth at 600 mbars of Ar at 1300°C for 30 min [102].*

The propane-argon growth seems promising, but the propane-hydrogen approach holds the advantage of shorter growth times i.e. 5 minutes [17]. Further investigations revealed the dependence of this latter technique on the growth temperature and pressure, unveiling another interest of this approach [18,116,117]. For the same mixture of propane and hydrogen, changing the pressure and temperature will yield the exact control of the graphene structure. In other words, graphene can be grown with IRD or with the 6√3 structure on the Si-face depending on the temperature-pressure conditions. Fig. 1.23 displays the wide range of the growth conditions with the different graphene structures [18]. We also show two examples of growth with the IRD or 6√3 structure in Fig. 1.24.

As we can see in Fig. 1.23, the IRD structure expands for a wide range of conditions: between 200 and 800 mbars, and between 1100 and 1550°C, whereas the 6√3 structure appears for high temperatures between 1350 and 1650°C with pressures below 200 mbars. Fig. 1.24 (a) of the sample grown at 1550°C and 100 mbars displays no wrinkles at the surface, and the corresponding LEED image (Fig. 1.24(c)) exhibits the 6√3 structure indicated by blue circles, taken from reference [18]. Fig. 1.24(b) of the sample grown at 1350°C and 800 mbars presents wrinkles with IRD in the corresponding LEED pattern (Fig 1.24(d)), indicated with red arrows. We believe that the ability of controlling the structure rises from the influence of the pressure and temperature on the intercalation of hydrogen at the interface between graphene and SiC. Despite

the appeal of this aspect, we are limited to 200 mbars to obtain the 6√3 structure and we know that the graphene quality is better at higher pressures, but with these H_2-rich growth conditions, the price to pay is in-plane rotational disorder and wrinkles at high pressures. Besides, the mobility recorded for such samples is below 500 $cm^2/V.s$ at 2 K [117], whether for samples grown at 800 mbars but with IRD, or at 100 mbars with the 6√3 structure. Therefore, modifying the conditions seems crucial to grow graphene at a high pressures but without the IRD.

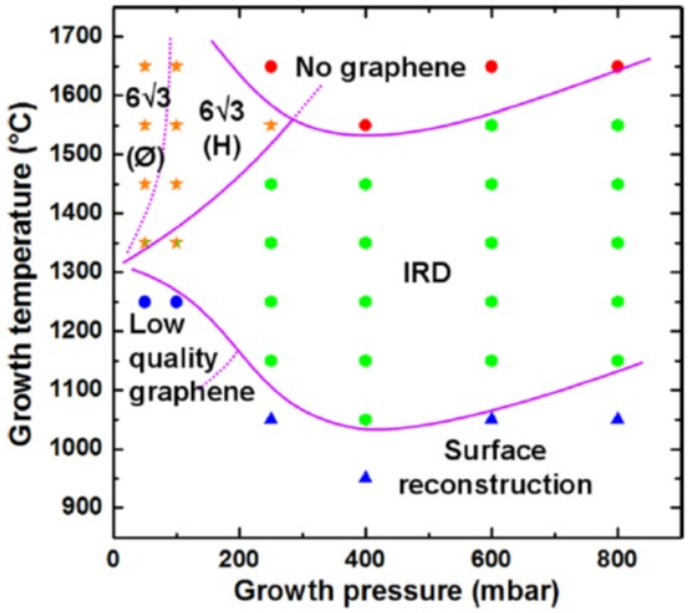

Figure 1.24: *Graphene structure deduced from LEED for the different pressures and growth temperatures, with 20 slm of H_2, 5 sccm of propane for 5 minutes [18].*

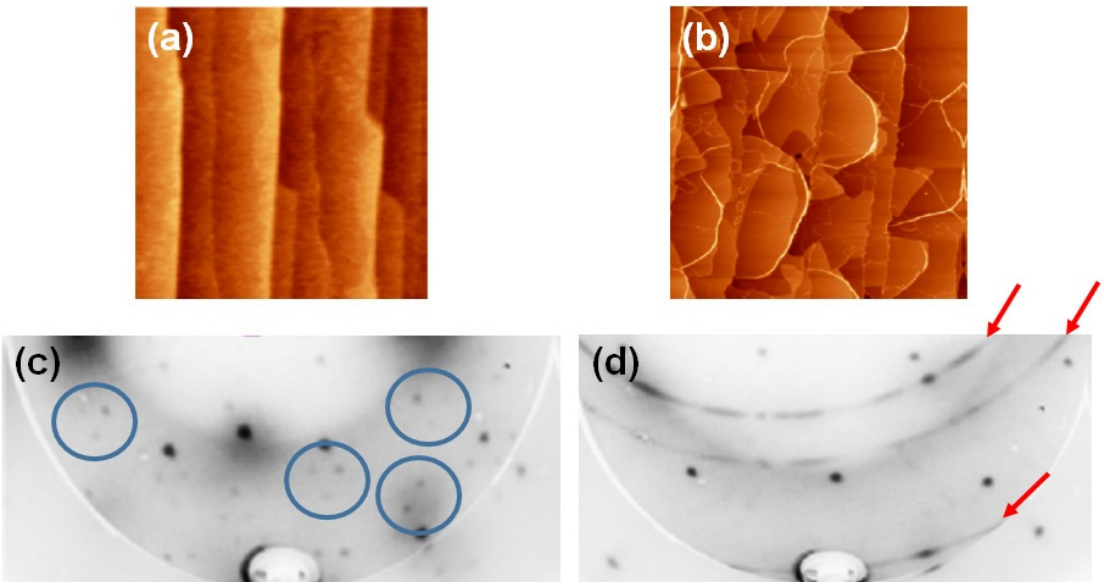

Figure 1.23: *1×1 μm^2 AFM images (z-scale = 2.5 nm) of graphene grown at **(a)** 1550°C, 100 mbars, **(b)** 1350°C, 800 mbars and their corresponding LEED images in **(c)** and **(d)** [18].*

So far we have mentioned studies on 6H-SiC and 3C-SiC. We will focus in the following on 6H-SiC (0001). We have also distinguished the growth under argon and the growth under hydrogen. However, it was demonstrated that combining both gases could lead to good results, with the same effects as those observed in Fig. 1.23. In fact, instead of changing the pressure and temperature, one can fix these parameters and only change the hydrogen amount in the hydrogen-argon mixture. This will also allow to alternate between the two structures of IRD and $6\sqrt{3}$ [118], but also to increase the pressure to 800 mbars for the $6\sqrt{3}$ case. An exhaustive study was conducted on the as-grown graphene uncovering the enhanced electrical properties of the graphene sheets produced by this method [19]. Controlling the hydrogen amount and the temperature will not only influence the structure but it will also allow the tuning of the electrical properties of graphene. Jabakhanji et al. [19] reported that a high temperature growth (1550°C) under 23% of H_2 in the gas mixture is very likely to produce n-type graphene. In contrast, a reduced temperature (1450°C) is more likely to produce p-type graphene. They were able to achieve "quasi-freestanding" single layer of graphene at 1450°C, 28% of H_2 and a growth time of only 1 minutes. The as-grown graphene recorded a hole mobility of 4400 $cm^2/V.s$ at 300 K, which is far more important than the usual carrier mobility reported on the Si-face [4,80]. Graphene is referred to as "quasi-freestanding" because it is believed that for a particular amount of hydrogen, some of the dangling bonds will be saturated, but at the same time the buffer layer will still be present forcing graphene to be ordered, leading to enhanced carrier mobility. Finally, graphene obtained by this same technique achieved remarkable results in quantum hall resistance standards owing to its novel electrical properties [20,21]. The resistance precision attained by the graphene sample surpassed that of the conventionally used GaAs devices in terms of cryomagnetic conditions. This was demonstrated on graphene grown on SiC by CVD and covered with a photoresist just after the metallic contacts deposition [20].

In conclusion, CVD direct growth under hydrogen atmospheres seems to be more promising than the Si sublimation technique or the growth under argon. It promotes a shorter growth time, around 5 minutes, and a better control of the graphene thickness. It also influences directly the interface between the graphene layer and the substrate, allowing to control the graphene structure on the Si-face. Therefore, instead of growing graphene by Si sublimation and then doing a post-growth annealing under H_2, one can directly grow graphene in a hydrogen atmosphere and have the same outcome, which is a hydrogenated interface. However, it presents some limitations in the growth pressure and the electrical properties. Adding argon to the hydrogen mixture allows to increase the growth pressure and successfully leads to enhanced results, especially in the electrical properties, opening new ways to tune the graphene doping and carrier mobility. It also leads to new achievements in the metrology of the resistance. Despite the attractive results of this latter approach, detailed studies of the growth mechanism and the graphene quality are still deficient. This will be the main subject of **chapter 3**.

The growth of graphene was not limited to SiC but it was also extended to AlN/Si (111) templates [103], in order to create new opportunities for graphene devices within the III-nitrides

market. The growth of graphene was carried out in the CVD reactor at 800 mbars, under 50% of H_2 and 50% of N_2, at temperatures ranging between 1150 and 1350°C i.e. below the melting point of silicon. The samples were exposed to 6 minutes of 17 sccm of propane for the graphene epitaxy. First results were successful and graphene deposition was identified with LEED, AFM and Raman spectroscopy. LEED patterns showed diffraction rings associated with a graphitic deposition, in addition to wrinkles observed with AFM, as we can see in Fig. 1.25(a, b), taken from reference [103]. Raman spectroscopy revealed the graphene signature i.e. the G and 2D modes for all the grown samples [119], see Fig. 1.25(c). We also see defect-induced peaks, such as the D, D' and D+D' peaks [120,121]. Raman spectroscopy attests that the best sample is the one grown at 1350°C, with crystallites size of 30 nm, probably limited by those of AlN. These fruitful first results are very encouraging, but further studies are required to establish a good integration between graphene and III-nitrides electronics. **Chapter 4** will cover recent achievements in this field.

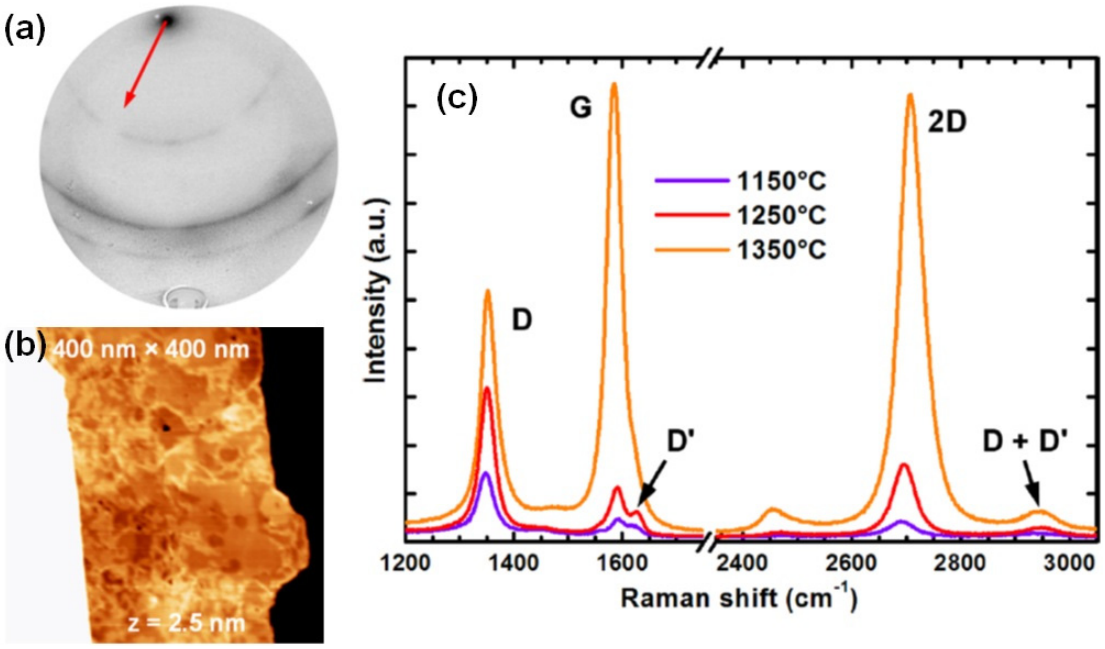

Figure 1.25: ***(a)*** *LEED pattern of the as-grown graphene on AlN templates. The red arrow indicates the* $[11\bar{2}0]$ *direction.* ***(b)*** *Corresponding AFM image showing wrinkles with small domains.* ***(c)*** *Raman spectra for the three growth temperatures presenting the graphene signature for all the samples [103].*

1.5. General conclusion

Graphene is a two-dimensional gapless material with very distinctive electrical properties due to its honeycomb lattice structure. Electrons in graphene obey the Dirac equation for massless fermions, mainly because of its unique hexagonal structure. Therefore, the energy dispersion near the Dirac points is linear for a single isolated graphene layer. On the other hand, studies have shown that the band structure is subjected to changes with increasing number of layers, which allows to open a bandgap in bilayer graphene. Graphene allows also the tuning of its charge carrier density with an external voltage. All these exceptional qualities along with excellent optical transparency, chemical stability and pronounced thermal conductivity have made graphene very attractive for different applications in electronics, optoelectronics and photonics.

We also presented the most recognized graphene elaboration techniques, starting with mechanical exfoliation. This technique is very interesting allowing the production of high quality graphene, unspoiled by the elaboration process and preserving a high carrier mobility. However, its drawback is the graphene size which limits it for research purposes only. Large scale production is possible with CVD on metal and very promising, despite few issues in the graphene quality regarding the crystallinity and the uniformity. Nevertheless, very low sheet resistance and high carrier mobility were recorded for graphene produced by this technique. Wafer-scale graphene growth can be achieved with thermal decomposition of SiC substrates or by CVD under argon (or MBE under UHV) with an external carbon source. We believe that this latter approach can be more interesting as it allows to grow graphene at lower temperatures compared to the Si sublimation technique. And since it relies on the external carbon source it can be extended to other substrates than SiC. In addition, some studies argue that CVD graphene is better than Si sublimation graphene, in terms of strain, electrical properties and homogeneity. Graphene on SiC is today widely used, the graphene/SiC heterostructure can be very promising for high-power and high-frequency transistors, in addition to a great interest for the metrology community. Yet, some imperfections still remain related to the structure of graphene and the SiC polarity.

Extensive studies have shown that graphene growth on both the SiC polarities is completely different. The growth on the Si-face of SiC is associated with a $(6\sqrt{3}\times6\sqrt{3})$-R30° surface reconstruction known as a buffer layer, which shares covalent bonds with the substrate. This buffer layer was found to behave in a different way than graphene and was considered to be the number one suspect for the reduced carrier mobility, compared to what is reported for the C-face. However, studies suggested few solutions to this problem such as a post-growth annealing under H_2, which will hydrogenate the interface by replacing the shared covalent bonds between the substrate and the buffer layer with Si-H bonds, resulting in quasi free-standing graphene. In contrast, the C-face does not seem to instigate a buffer layer, but instead rotational stacking disorder is observed. Not necessarily a down point, since it is believed to be the reason why multilayer-graphene acts as a stack of isolated graphene layers.

Last but not least, we have presented a new approach of graphene growth under H_2 atmosphere in CVD systems, which was developed in the last few years before this present work. This technique allows to control the graphene structure on the Si-face and to switch between the $6\sqrt{3}$ buffer layer and the IRD structure, by controlling the temperature and pressure and influencing the hydrogen intercalation at the interface. We believe that this technique can be an alternative to the post-growth annealing after the growth of graphene by Si sublimation, since the hydrogenation of the interface occurs during growth. Further investigations revealed that adding argon to the hydrogen atmosphere modifies the growth conditions and enhances the electrical properties. It also led to new achievements in the metrology of the resistance by producing graphene devices outperforming the conventionally used devices. Despite these recent achievements, little is known about this approach, hence it will be a major part of this present work. Finally, it has also been demonstrated that graphene can be grown on AlN on Si templates by CVD with propane. First results are very promising, but more investigations are required for a better graphene quality and a better integration of graphene with nitrides. This will be the second major part of this work.

Chapter 2

Experimental methods

In this chapter we will present our chemical vapor deposition (CVD) experimental set and the experimental details of graphene growth on SiC. We will also show how to characterize a graphene sample on the basis of different structural techniques (AFM, SEM, and LEED), spectroscopy methods (XPS and Raman spectroscopy) and electrical measurements (Van der Pauw and Hall Effect).

2.1. Chemical vapor deposition (CVD)

In the present study, all the growth-related procedures were carried out in a hot wall horizontal CVD reactor, presented in Fig. 2.1. The reactor is a home-made furnace initially designed for the homoepitaxy of 4H-SiC and the heteroepitaxy of 3C-SiC templates on Si [122]. It was later extended to other uses, such as the growth of graphene and less frequently for high temperature annealing of III-V materials [123]. A horizontal, double-wall, water cooled cylinder forms the external part of the furnace, but the growth takes place in a rectangular graphite tube designed for two-inch wafers, known as the liner. The heating is performed using two graphite resistors placed above and below the graphite tube, as we can see in Fig. 2.1. The internal parts of the tube can be changed depending on the growth to avoid any contamination from the different materials used such as SiC or III-V materials. All the parts inside the reactor are made of pure refractory and inert materials, in principle having very low vapor pressure at the working temperatures. For this reason, the reactor can sustain temperatures as high as 2000°C for low pressure conditions. It is also equipped with a standard primary pump, in addition to a pressure gauge and a butterfly valve, which allows the control of the pressure within the reactor. The operating pressure ranges between 10 mbars and 1 bar, and can be reduced to 10^{-2} mbars if no gases are introduced. The sample undergoes a laminar flow of gases introduced by a gas line directly connected to the inner part of the liner. This line is for the carrier gases and the precursor, while another line is installed between the tube and the external parts of the reactor, for the secondary gases to cool down the resistors, mainly neutral gases but also hydrogen.

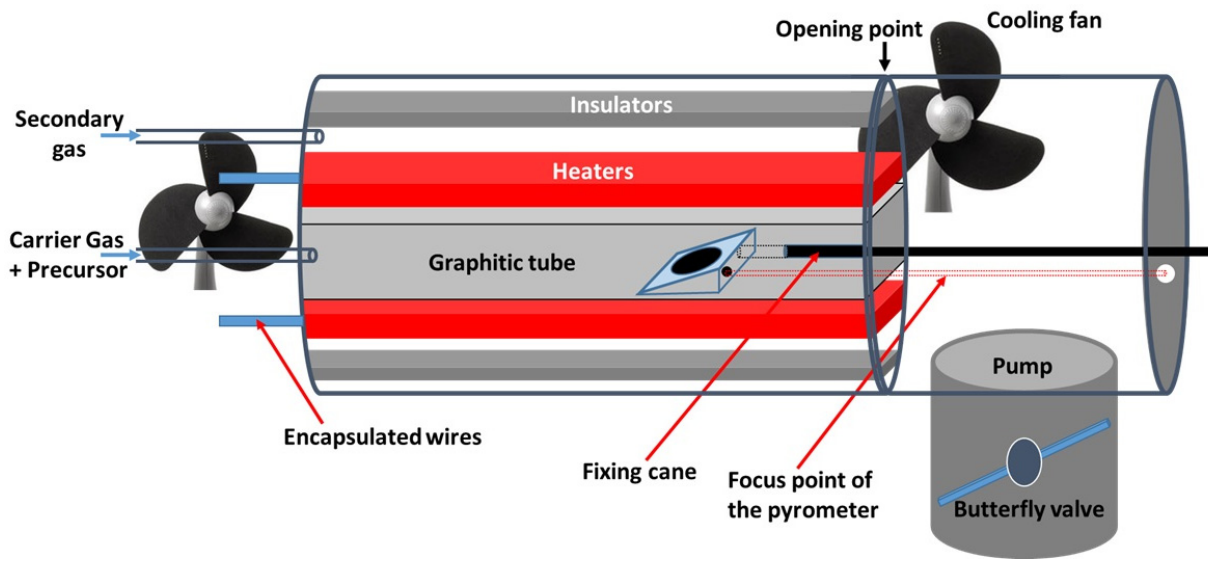

Figure 2.1: *Schematic illustration of the reactor seen from the side.*

The temperature is monitored with a pyrometer focused on the substrate holder, directly beneath the sample, with an estimated error of the order of ± 20°C. Note that the pyrometer cannot monitor temperatures below 800°C. In addition to the water cooling, cooling fans are added at the opening point of the reactor and where the conductive wires are placed. The sample can be placed on a rotating holder, however in this particular study no rotation was applied. The sample holder we employed was inclined with respect to the horizontal to ensure a uniform deposition over the sample. It is fixed with a fixing arm, which also allows to control the position inside the reactor. However, we rarely change this parameter as it is already optimized. The operating conditions tolerated by this system are summarized in table 2.1.

Table 2. 1: *Operating conditions of the CVD reactor*

Temperature	Pressure	Primary gas line	Secondary gas line
800°C-1700°C	10^{-2} mbars - 1 bar	H_2, Argon, N_2, C_3H_8, SiH_4, HCl	H_2, Argon

2.2. Experimental details

The starting point of the present work was the growth of graphene on SiC, but we also extended our work to the growth of graphene on III-V materials. However, our focus in this part will only be on SiC since our objective at this point is to show the operating conditions that we have adopted for the growth of graphene and the performance of the reactor. We will also present the characterization methods we employed for evaluating the growth, along with a brief description of the theoretical background behind each technique we used. For reasons of simplicity and clearness, our approach will be wide-ranging in this part, as more details concerning the outcome of each implemented recipe are presented in the corresponding chapter: **Chapter 3** for graphene on SiC and **Chapter 4** for III-nitrides.

The silicon carbide substrates of choice were mainly 6H-SiC but also 4H-SiC, provided by Tankeblue [124] and Xiamen [125]. However, most of our work was done on Tankeblue, consequently, the SiC substrate in the following is by default from Tankeblue unless when we mention that it is from Xiamen. The substrates are 2 to 4'' in diameter with a preferred thickness around 350 µm to ease the cleaving into pieces. They are n-doped with a resistivity smaller than 0.2 Ω.cm, or Semi-insulating with a resistivity greater than 10^5 Ω.cm, depending on the application. The miscut angle is usually around 0.2° or smaller than 1°, but in few cases 4°-off substrates were used. Unfortunately, the manufacturers specify an inaccuracy on the miscut angle around 0.5°, which makes it difficult to have the same miscut angle on different substrates or between orders. They are chemo-mechanically polished and exhibit a full width at half maximum (FWHM) smaller than 30 arc sec verified with X-ray diffraction. All the work presented in this study was performed on the Si-face of the SiC substrates. The samples are overall cleaved into 5×5 mm^2, but occasionally we do the growth on 10×10 mm^2 or ¼ of a 2'' substrate for uniformity check and other applications.

Graphene epitaxy is usually carried out at temperatures extending between 1350 and 1650°C and pressures ranging between 200 and 900 mbars. A mixture of hydrogen and argon is used as the carrier gas and propane as the precursor. The total carrier gas pressure is fixed to 12 slm (standard liters per minute). The samples are in general exposed to 5 sccm (standard cubic centimeters per minute) of propane for 1 to 20 minutes. Since we are using a mixture of hydrogen and argon throughout this whole study, whenever we mention that we have x% of H_2, we imply that 100-x% is of argon. The secondary gases are introduced with a flow around 2 slm, either argon or a mixture of argon and hydrogen.

In this part, we introduce a wide range of growth conditions as the choice depends on the application and the desired outcome. We present in table 2.2 two of our most used and typical growth conditions, but we will discuss in more details the outcome behind each recipe in **chapter 3**. We illustrate in Fig. 2.2 the growth process: first the temperature is increased under the carrier gas, after having reached the growth pressure. When the growth temperature is reached, the sample is kept under the carrier gas without propane for 2 to 5 minutes. This step, is referred to as the pre-

growth annealing, allows to stabilize the growth temperature while preparing the surface for the growth. After the annealing step, propane is added to the carrier gas for a certain growth time, before it is cut-off, leaving the sample under the carrier gases to cool down for 20 minutes, with an initial cooling rate about 4°C/s. The whole process takes between 35 and 50 minutes depending on the growth time.

Table 2. 2: *Two standard recipes for graphene growth on SiC depending on the application.*

Recipe n°	Temperature (°C)	Pressure (mbars)	H_2 (%)	C_3H_8 (sccm)	Time (min)
I	1450	800	100	5	5
II	1550	800	17-25	5	5

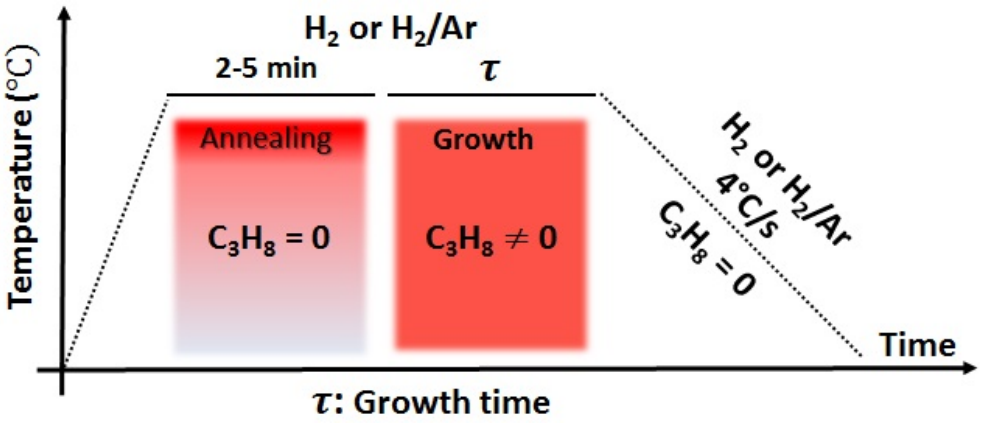

Figure 2.2: *Schematic representation of the growth process of graphene on SiC.*

2.3. General observations an characterization

We will now consider few graphene samples grown on SiC, in order to summarize the characterization techniques employed to identify and assess graphene quality. Our goal is not to show results but to describe each technique and how to analyze the observations.

2.3.1. Topographic characterization

After the growth of graphene, the sample is investigated with atomic force microscopy (AFM) in order to observe its morphology. The AFM system we use is a Veeco dimension III setup, employed in tapping mode, equipped with a silicon tip. The data are then processed with the analysis software WSxM [126]. The topographic image is very useful to observe the morphological aspects of the graphene, but also the phase image can be very helpful as well. The phase image represents the shift between the free oscillating cantilever and when it comes in contact with the sample's surface. The phase is sensitive to the elastic properties of the surface that emanate from the crystallinity and the stiffness. Hard and more crystalline regions will lead to elastic interactions between the tip and the sample, which is translated into a less negative or zero phase shift, and will appear as brighter regions in the corresponding phase image [127–129]. In contrast, amorphous or softer regions will lead to inelastic interactions between the tip and the sample due to energy dissipation, and thus a more negative phase shift, which then appears as darker regions in the phase image [127]. In the case of graphene, a difference in the number of graphene layers will also give rise to such phase shift [130].

We will distinguish in the following between two graphene morphologies corresponding to the two recipes we have mentioned in table 2.2. In Fig. 2. 3[1], we present a typical AFM view of graphene grown on SiC (0001) with 17% of H_2 in the gas mixture (recipe II from table 2.2 but at 1450°C). The morphology exhibits terraces with widths ranging between 150 and 250 nm. The height of each step is around 0.75 nm, which corresponds to three SiC bilayers. Since we know by other means that the surface is covered with graphene, this indicates that the number of graphene layers doesn't change from a step terrace to the next. However, we notice irregular shapes appearing between two adjacent steps in some areas, indicated by the red arrows in Fig. 2.3(a). The height of these steps is around 0.35 nm, equivalent to an extra graphene layer. We can also make this assumption by analyzing the phase image: as we can see in Fig. 2.3(b), we can notice in some areas a difference in contrast due to a phase shift that we attribute to an extra graphene layer. Other studies have reported the presence of extra graphene layers at step edges or between steps [80,115]. In our case, based on height measurements, we only detect one extra layer each time, and not more. In some cases, the phase image doesn't reveal any difference in contrast (Fig. 2.3(c)), probably an instrumental issue or a worn out tip.

[1] In Fig. 2.3, we have placed the full height scale of image Fig. 2.3(a), but in the rest of the manuscript we will only note the maximum value of the scale as the z-scale, even for the phase images.

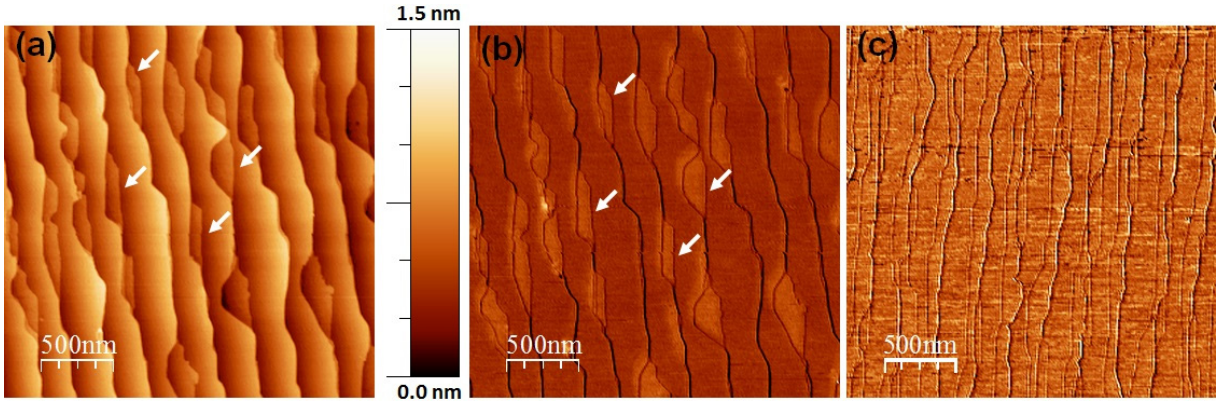

Figure 2.4: (a) *Typical AFM image of graphene grown on SiC (0001) at 1450°C, 800 mbars, 5 min and 17% of H_2.* ***(b)*** *The corresponding phase image (Maximum scale 15°).* ***(c)*** *Phase image (Max scale 5°) of another sample but same growth conditions.*

In Fig. 2.4, we present a typical AFM image of graphene grown on the SiC (0001) at 100% of H_2 (recipe I from table 2.2), for 5 minutes. The morphology seems different from that of Fig. 2.3(a), mainly due to the presence of wrinkle-like shapes, 1 nm-high, indicated by red arrows in Fig. 2.4(a). The origin of these wrinkles will be discussed in **Chapter 3**. We can also discern the SiC steps presenting widths ranging between 200 and 500 nm, and heights between 0.75 and 0.80 nm. In addition, we notice a lot of irregular shapes which can be attributed to multiple layers deposition. The extra layers deposition in this case seem a lot more important than what we observe in Fig. 2.3(a). The extra layers do not seem very evident in the phase image, but we were able to point out few of them after enhancing a bit the contrast. The extra layers are indicated with white arrows in Fig. 2.4(b).

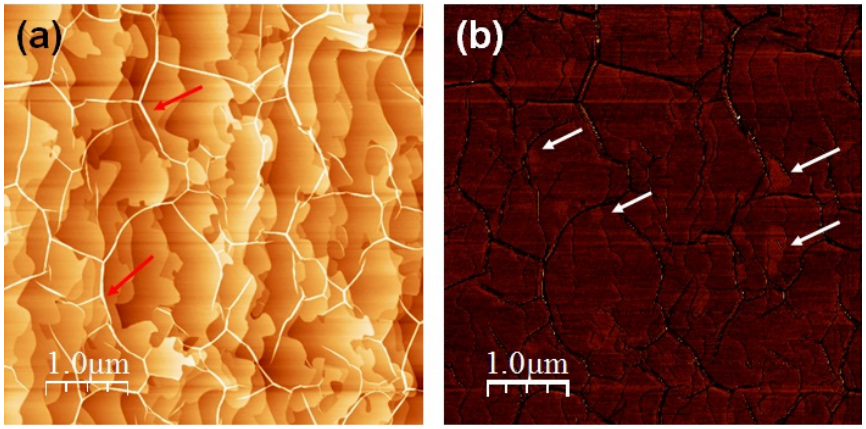

Figure 2.3: (a) *AFM image of graphene grown on SiC (0001) at 100% H_2, 1450°C and 800 mbars with the corresponding phase image in* ***(b)****. The z-scale is 3 nm and 15° in* ***(a)*** *and* ***(b)*** *respectively.*

2.3.2. Scanning electron microscopy (SEM)

For a larger scale of imaging we use a field effect scanning electron microscopy (SEM - Zeiss Supra 40), but it lacks the height information that the AFM offers. SEM can be helpful to image different areas of the sample and check the uniformity. It can be faster than AFM for large scale imaging. But interestingly it can have other uses such as exposing areas with extra layers. In fact, the mechanical properties of the different number of graphene layers seem to give a different contrast with SEM as we can see in Fig. 2.5(a). Therefore, it can complete the AFM whenever the phase image fails to uncover areas with different thicknesses. Fig. 2.5(a) resembles a lot to the LEEM image presented in reference [80] which evidences multilayers of graphene at step edges.

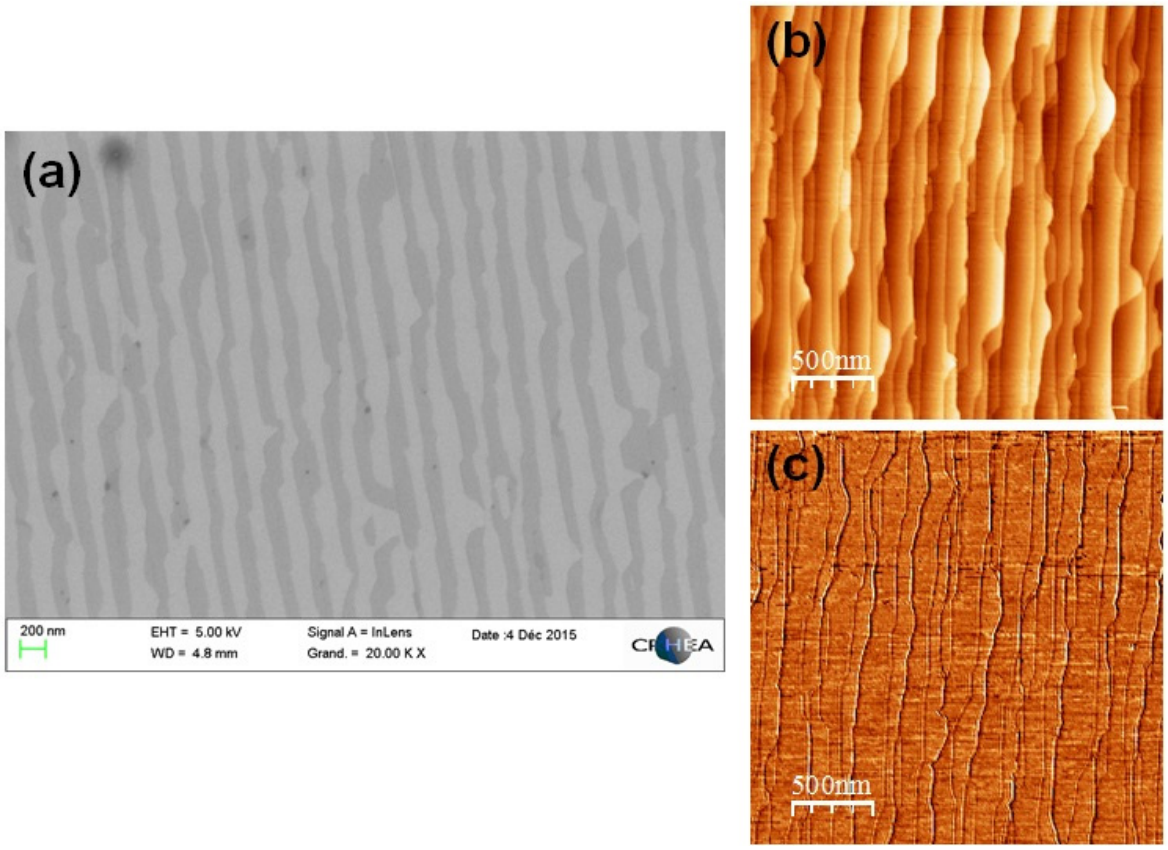

Figure 2.5: ***(a)*** *SEM image of graphene grown on SiC (0001) at 1450°C, 800 mbars, 5 min and 17% of* H_2. ***(b)*** *and* ***(c)*** *corresponding topographic and phase AFM images respectively. The z-scale is 2 nm in* ***(b)*** *and 5° for the phase image in* ***(c)***.

2.3.3. X-ray photoemission spectroscopy (XPS)

Topographic analysis is followed by chemical characterization such as X-ray photoemission spectroscopy (XPS) and Raman spectroscopy. X-ray photoemission spectroscopy is a surface analysis technique based on the photoelectric effect consisting of exciting electrons with a photon source. In order for the electrons to escape into vacuum, the energy needs to be larger than the binding energy of the electron (E_B), added to the work function of the sample (ϕ_S). In the case of XPS, the incident photons energy is sufficient to excite atomic core-level electrons. The photoemission process is illustrated in Fig. 2.6(a). Another mechanism occurs when the photoelectron is emitted: an electron from a higher state takes the place of the emitted photoelectron and the extra quantum of energy is acquired by a third electron which is called the Auger electron.

The excited photoelectrons are detected and analyzed as a function of their kinetic energy, calculated as follows:

$$E_{kin} = h\nu - E_B - \phi_A \qquad (2.1)$$

Where $\boldsymbol{E_B}$ is the binding energy of the electrons, $\boldsymbol{h\nu}$ the excitation energy and $\boldsymbol{\phi_A}$ the analyzer's work function. Note that this expression is independent of the sample's work function and that the binding energy in equation (2.1) is referenced to the Fermi level ($\boldsymbol{E_F}$). The Fermi level is common for the analyzer and the sample since they are both in electrical contact. A simplified energy diagram of the photoemission process is shown in Fig. 2.6(b), inspired from reference [131]. Since core-level electrons energies are well-known for a particular atom, the photoemission spectrum can be presented as a function of the binding energy to provide a first level of information concerning the chemical composition of the sample's surface. We present a spectrum of the whole energy range in Fig. 2.7 known as the survey. The low intensity background we see in this figure is due to secondary electrons generated when photoelectrons interact with other electrons on their way out of the sample. In addition, next to every intense line we see a less intense one, which is due to photoelectrons of the parent line interacting with other electrons in the surface region. They are known as the energy loss lines, because they have lost part of their kinetic energy and thus appear at a higher binding energy with respect to the parent line.

The binding energy of core-level electrons in an atom is also altered by its environment and the bonding configuration in which this atom exists. In other words, if an atom exists in different bonding configurations in a solid, different peaks with different binding energies will appear in the corresponding core-level spectrum. For example, if we take the C1s core-level of graphene on SiC, the carbon atom will give rise to two energy states, one corresponding to the sp^3-bond configuration with silicon in the SiC substrate and the other corresponding to the sp^2-bond configuration in graphene. This is what we call the core-level chemical shift. The chemical shift rises from the transfer of valence charges that occurs when one atom bonds with a more electronegative atom. The core-level electrons in the former atom will experience an increase in

the coulomb attraction due to the partial loss of valence charge and thus an increase in their binding energy compared to the elemental isolated atom

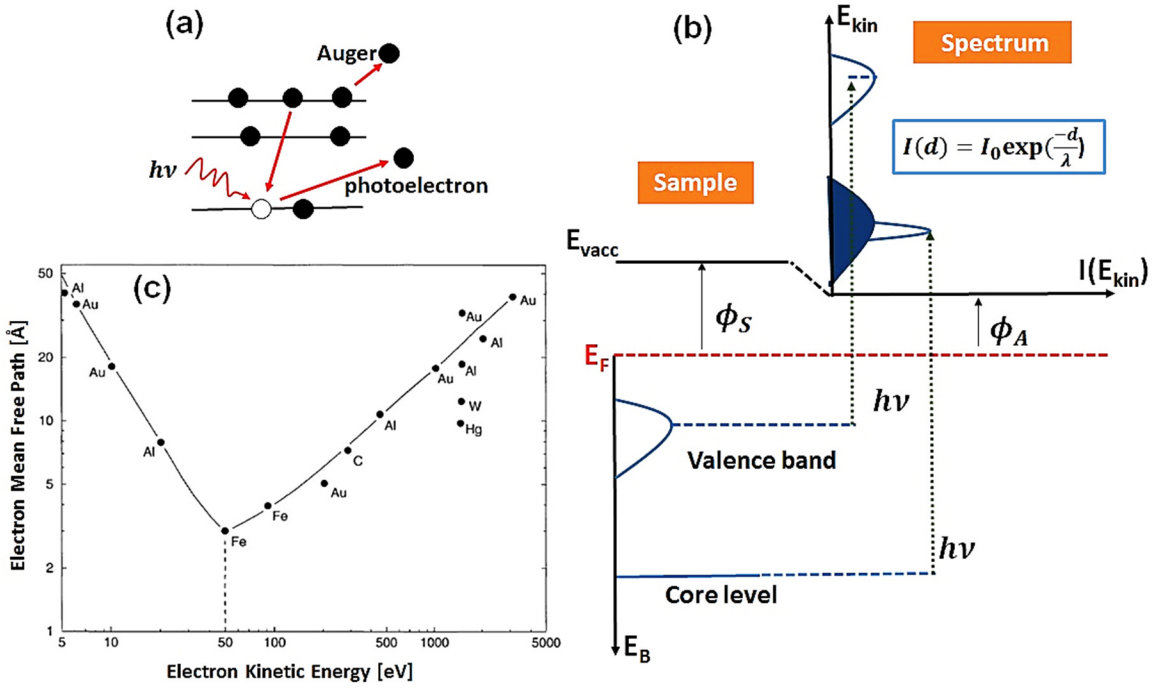

Figure 2.7: (a) *Photoemission process upon excitation with X-rays, with the energy diagram represented in* ***(b)****, inspired from [131].* ***(c)*** *Inelastic mean free path of electrons as a function of their kinetic energy for different materials, taken from [132].*

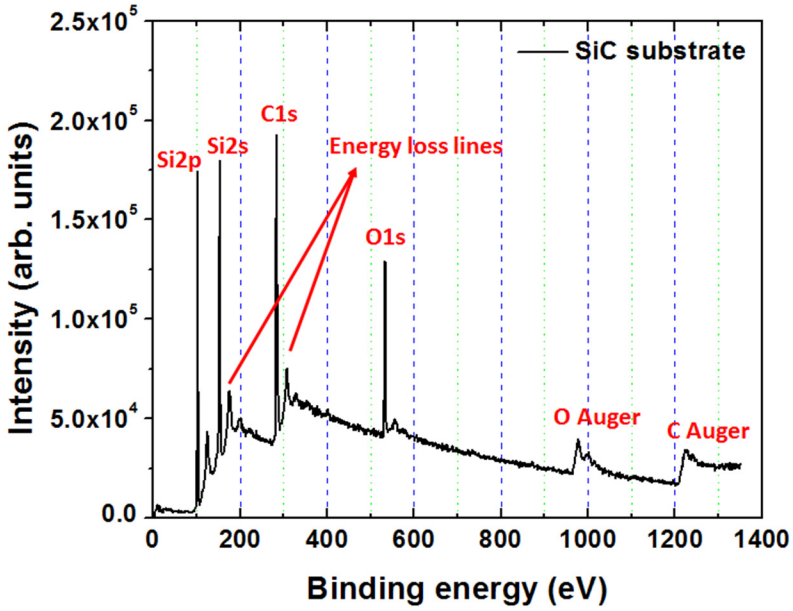

Figure 2. 6: *Survey of a SiC substrate recorded with an X-ray source Al Kα 1486.6 eV.*

Another shift can occur for non-conductive samples, due to insufficient charge-compensation. When photoelectrons leave the sample, this latter will become positively charged, but if the sample is conductive, the accumulated charges can be compensated with a charge transfer from the substrate or from the metallic substrate holder. On the other hand, when the sample is not conductive, we use a Flood Gun that fires electrons on the sample's surface, to partially compensate the charge accumulation. Thanks to this type of shift, it is possible with XPS to known when the sample's conductivity has changed or is effected in anyway. For example, Emtsev et al. [105] have demonstrated on the basis of XPS and ARPES that when the deposited graphene thickness increases, the graphene peak shifts towards higher binding energies. They attribute this upshift to a difference in carrier density between the bottom graphene layer and the topmost graphene layer. In fact, they argue that when graphene is grown on a buffer layer a negative charge transfer can occur from the substrate to the graphene layer. However, these charges remain close to the interface. Therefore, there will be less charges transferred to the topmost graphene layer when the thickness is increasing. In this case, the XPS will be probing a more neutral graphene layer.

The key characteristic of the photoemission techniques is their sensitivity to the surface. It emanates from the short inelastic mean free path (IMFP) $\boldsymbol{\lambda}$ of electrons in solids, due to the inelastic scattering between electrons. The values of $\boldsymbol{\lambda}$ as a function of the electrons kinetic energy is shown in Fig. 2.6(c), taken from reference [132]. This curve is known as the universal curve since it is weakly dependent on the material properties. Then, for a fixed excitation energy, the photoelectron signal rises from a depth of the order of $\boldsymbol{\lambda}$ i.e. few atomic layers. Hence, by changing the excitation energy, ergo the kinetic energy, the probing depth can be controlled. The intensity of the electron flux from a depth $\boldsymbol{d}$ is given by:

$$I = I_0 \exp(-\frac{d}{\lambda}) \qquad (2.2)$$

Where $\mathbf{exp}(-\frac{\boldsymbol{d}}{\boldsymbol{\lambda}})$ is the probability for an electron to travel a distance $\boldsymbol{d}$ without any inelastic scattering. If the photoelectrons are emitted with a certain angle $\boldsymbol{\theta}$ the depth of analysis will become $\boldsymbol{\lambda cos\theta}$ ($\boldsymbol{\theta}$=**0** means normal to the surface*)*. The IMFP in graphite or FLG ranges between 20 and 30 Å for electrons with a kinetic energy of 1200 eV, i.e. C1s core level electrons [133]. Additional calibrations pinpointed the IMFP in FLG to be 26 Å [131], i.e. 7 layers of graphene. Furthermore, a quantitative analysis of the XPS spectra permits to determine the surface composition and to calculate the deposited graphene thickness. Th. Seyller and K. Emtsev [79,131] proposed two models to calculate the graphene thickness. The first is based on the attenuation of the Si2p core-level peak intensity of SiC before and after the graphene growth $\boldsymbol{d = -\lambda \ln(\frac{I}{I_0})}$ derived from equation (2.2), but in this case I_0 and I represent the peak intensity before and after growth. The second model is described by the following equation:

$$D = \lambda \ln(\frac{I_G N_{SiC}}{I_{SiC} N_G} + 1) \qquad (2.3)$$

I_G/I_{SiC} represents the integrated intensity ratio of the graphene peak to that of the SiC peak in the C1s core-level spectrum; N_{SiC} and N_G are the densities of carbon atoms in SiC and graphite respectively. This formula explains why in previous discussions we mentioned that the intensity ratio represents the thickness. Compared to the method based on Si signal attenuation, this method appears more reliable since the graphene signal and the reference are contained in the same spectrum (the C1s spectrum). The estimated error is considered to be 0.1 ML by Th. Seyller and co-workers, obtained by comparing thickness results from different techniques such as LEEM, ARPES and Raman spectroscopy. Nevertheless, from our experience, by comparing our XPS results to Raman results, we suspect that the error is more important, around 0.5 ML and increasing with the number of layers.

For this current study we used an XPS Thermo Scientific Kα system equipped with an Al Kα monochromatized source. Hence, the samples are excited with a photon energy of 1486.6 eV, focalized in a spot size of 400 microns in diameter, under UHV conditions. Photoelectron are collected by a multi-channel detector placed after a hemispherical analyzer. We present in Fig. 2.8 a typical C1s core-level spectrum of graphene grown on SiC (0001), at 1600°C, 800 mbars, 25% H_2 and 15 minutes of 5 sccm C_3H_8. The carbon signal coming from the SiC substrate gives rise to the peak at the lowest energy (283.86 eV). It represents the carbon in the sp^3 configuration, bonding with silicon atoms in the SiC bulk. The graphene peak is represented by the asymmetric peak at 284.66 eV, consisting of carbon atoms in the hybridized sp^2 configuration. The **S1** and **S2** peaks at 285.05 eV and 285.60 eV respectively, represent the buffer layer. This latter exhibits two peaks since the carbon atoms forming the interface exist in two bonding configurations. Part of the carbon atoms in the buffer layer are bound together with sp^2 bonds, others share covalent bonds with the substrate. ARPES measurements done by Emtsev et al. [105] revealed that the valence σ-states of the buffer layer are down shifted with respect to graphite, hence the corresponding electrons

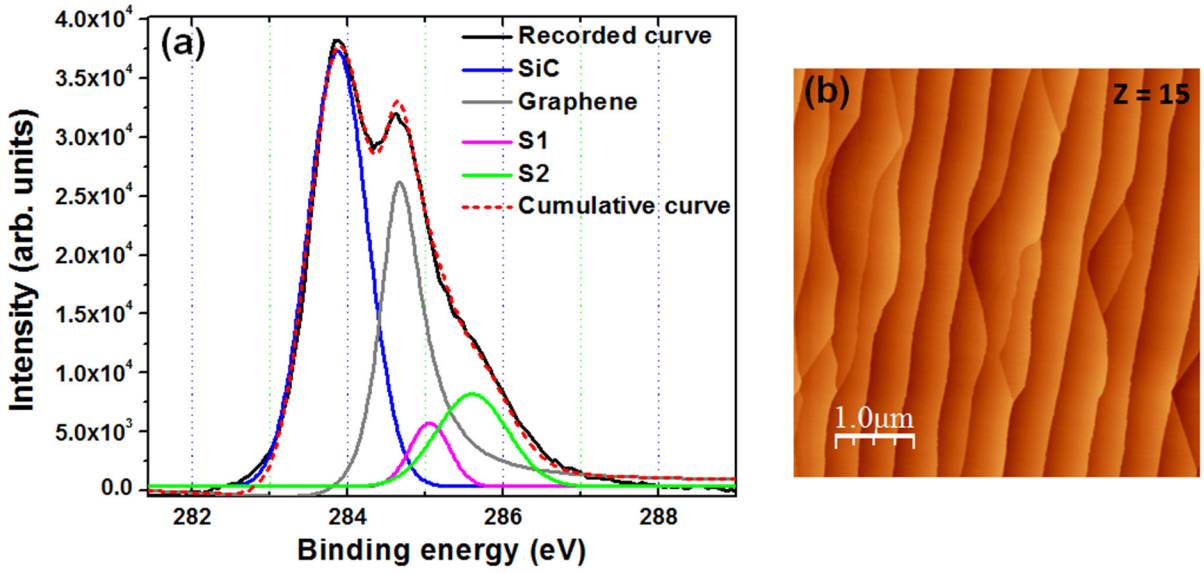

Figure 2.8: (a) *Typical C1 core-level spectrum of graphene grown on SiC (0001) in conditions promoting the formation of a buffer layer.* ***(b)*** *The corresponding AFM image.*

binding energy will be more important. Accordingly, we attribute the higher binding energy to the **S2** component emanating from sp^2-bonded carbon atoms in the buffer layer, and since other atoms share covalent bonds with the substrate, their corresponding peak (**S1**) should be somewhere between the **S2** peak and the SiC substrate.

We add that in this work, when comparing different spectra, we sometimes modify the binding energy to align the SiC peaks of the different samples together. The reason we do this is to avoid congestion and to see better the graphene peak. We also normalize in some cases the whole spectra to the SiC peak, which allows us to compare the graphene peak intensity of different spectra measured in different sessions. In fact, the XPS we use allows us to study up to twenty samples each time, hence it is possible that the vacuum conditions are not always the same for the different sessions. Also, another parameter which can change between sessions is the focus of the X-ray gun on the sample. For these reasons, the entire recorded spectra might be more or less intense, this is why we sometimes normalize the C1s spectra to the SiC peak. Another way to get around this issue is to calculate the ratio sp^2/sp^3 when studying the thickness. We will indicate whenever we do a treatment to the spectra we present.

To summarize, XPS can be an important tool to identify the deposition of sp^2-bound carbon, it can even reveal the presence of the $6\sqrt{3}$ buffer layer. It is a surface sensitive probing technique, perfect for FLG and thin layers, allowing to identify the number of deposited layers. It can even allow to detect any change in the sample's conductivity. Therefore, it is essential to complete our AFM observation with XPS. However, to further study graphene, other techniques can be applied such as Raman spectroscopy.

2.3.4. Raman spectroscopy

Raman spectroscopy is a characterization technique based on the excitation of the sample with monochromatic light and the detection of photons after their interaction with vibrational, rotational and other low-frequency modes in the studied material. The photon source is usually a laser in the visible, near infrared or near ultraviolet region. The laser radiation undergoes inelastic scattering by molecular vibrations, phonons or other types of excitations [134]. The wavenumber of the emitted photons is then analyzed and subtracted from that of the incident light to obtain what we call the Raman shift in cm^{-1}. The Raman shift corresponds to discrete energy levels particular to each molecule and crystal. It is therefore dependent on the chemical composition of the material, and brings a great deal of information concerning not only the nature of the material, but also concerning the material's electrical and mechanical properties, since they have a direct effect on its band structure. We present in Fig. 2.9, the different light scattering mechanisms which can occur upon exposing the sample to a laser radiation. The Rayleigh scattering represents the laser line and is usually filtered out. In addition, Anti-Stokes scattering lines are known to be less intense than Stokes lines.

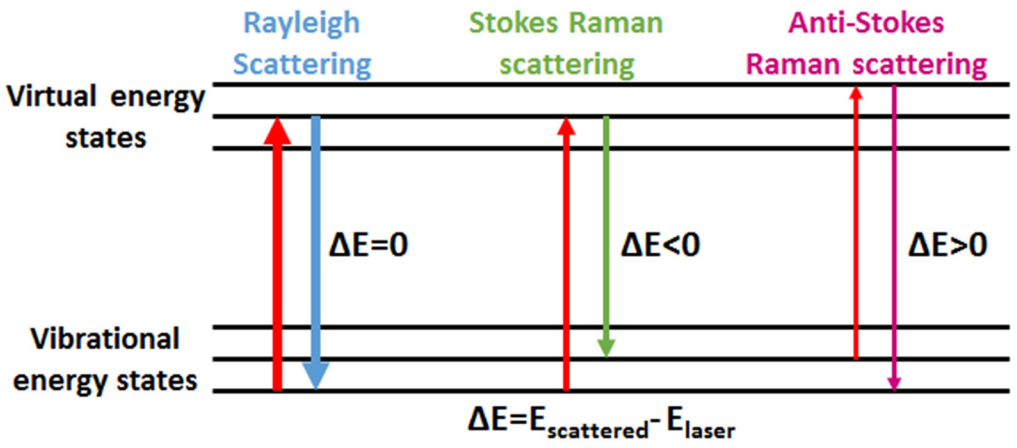

Figure 2.10: *Scattering mechanisms when exciting the sample with a laser source. In this case we considered the molecule in vibrational energy states.*

Many studies have adopted this technique for the identification and analysis of graphene. We present in Fig. 2.10(a) Raman spectra of graphite and graphene produced by mechanical exfoliation, taken from reference [119]. The two most intense features in Fig. 2.10 are the G peak at 1580 cm^{-1} and the 2D peak at 2700 cm^{-1}. These peaks can be also observed in graphite [135,136]. The G peak rises from the doubly degenerate E_{2g} mode, due to the bond stretching of all pairs of sp^2 atoms in the graphene honeycomb structure [135,137]. The six sp^2 atoms forming rings can also undergo what is called "breathing modes" and give rise to the D peak at 1350 cm^{-1}, which is only activated by defects [138,139], see Fig 2.10(b) for defected graphene, taken from reference [140]. It originates from zone boundary phonons, i.e. around the Brillouin zone corners K (or K'),

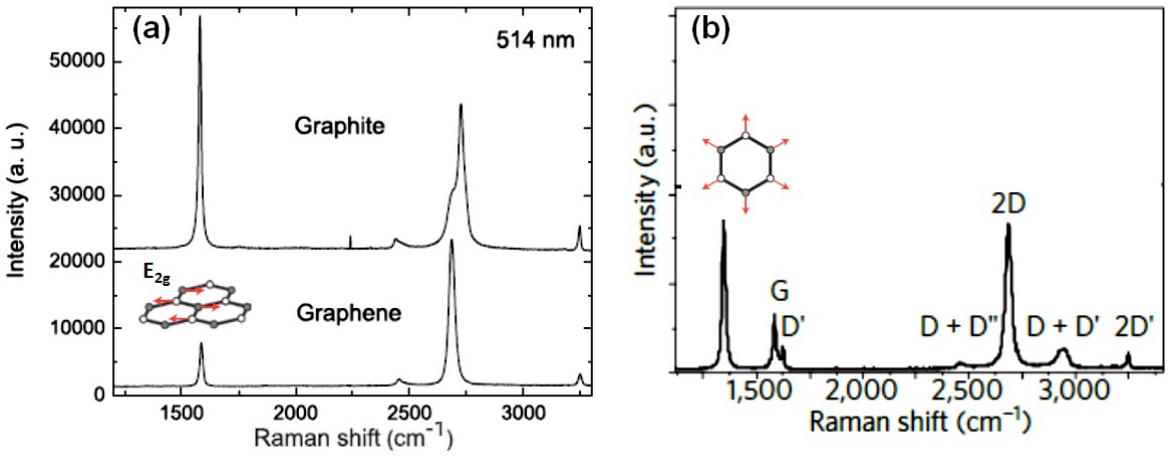

Figure 2.9: ***(a)*** *Graphite and graphene Raman spectra taken at a laser wavelength of 514 nm. They are both rescaled to have the same 2D peak intensity. Figure in inset shows the displacement of atoms giving rise to the in-plane doubly degenerate optical mode E_{2g} [119].* ***(b)*** *Raman spectrum of defected graphene [140]. Figure in inset showing the breathing modes of the six-atom ring.*

activated by double resonance [139,141] and is strongly influenced by the excitation energy [141,142], as it is also the case for the 2D peak. The same process can occur intra-valley i.e. double resonance within the same cone K (or K'), resulting in a peak at ~1620 cm^{-1}, noted as the D' peak, appearing for defected graphite/graphene [143,144]. We present the double resonance mechanism in more details in **Appendix A**.

Raman spectroscopy can be useful to calculate the number of graphene layers deposited on SiC by examining the G-peak and using a highly oriented pyrolytic graphite (HOPG) as a reference as follows [90,145]:

$$N = \frac{A_G}{A_{HOPG}} \times \varphi \qquad (2.4)$$

This is an empirical relationship corresponding to the experimental configuration of the Raman measurements. Where N is the number of layers, A_G the integrated intensity of the sample's G-peak and A_{HOPG} the integrated intensity of the HOPG's G-peak. φ is a constant that depends on the experimental configuration of the Raman measurements, in our case it is 1/0.03 [146]. We mainly use this equation in our study, but there are other means to confirm this calculation e.g. by examining the 2D-peak. In fact, the 2D-peak broadens and shifts towards higher wavenumbers when the number of graphene layers is increasing [119,141] (More details in **Appendix A**).

The interest in Raman spectroscopy does not stop here, some studies claim that the $6\sqrt{3}$ buffer layer for graphene grown on SiC (0001) can be detected with Raman spectroscopy [147–149]. It presents two broad bands around 1200 and 1660 cm^{-1}, i.e. just beneath the D and G bands as we show in Fig. 2.11(a), taken from reference [149].

Further studies have shown that the G and 2D modes are also sensitive to charge doping in graphene [150–153]. This feature can be anticipated since doping will change the Fermi surface and will affect phonons probed by the Raman mechanism, in particular phonons responsible for the D, G and 2D bands. The G peak was found to blue shift for both electron and hole doping, accompanied with a decrease in the peak's width. The 2D peak broadens for important doping, especially for hole doping, added to an upshift in frequency, but for electron doping it is more or less stable for small charge density, however it downshifts for electron density larger than 3.2×10^{13} cm^{-2}. We show this behavior in Fig. 2.11(b, c), taken from reference [150]. Another important parameter is the I(2D)/I(G) intensity ratio, it is also affected by doping, for example a sample slightly doped will have a 2D peak three times more intense than the G peak.

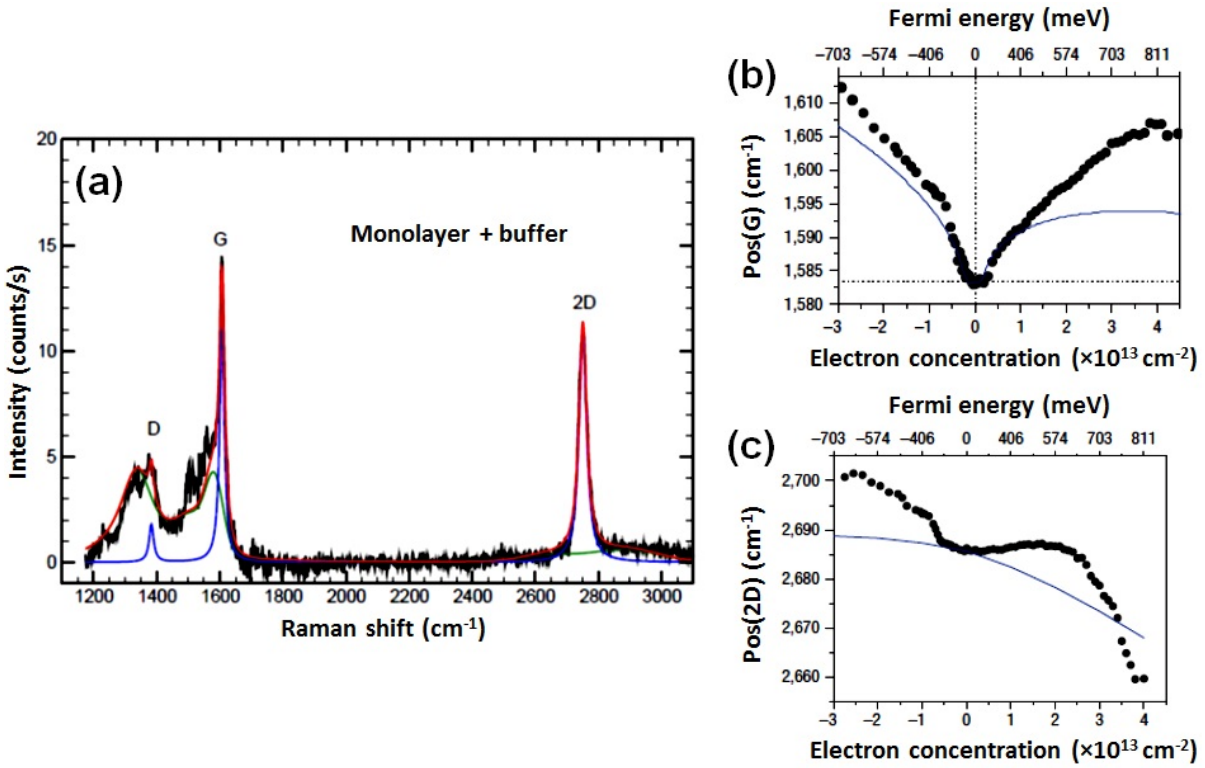

Figure 2.11: (a) *Raman spectrum recorded for a monolayer and a buffer layer grown on SiC (0001). The buffer layer contribution is presented by the green line and the monolayer contribution by the blue line [149].* ***(b)*** *and* ***(c)*** *represent the G and 2D peak frequencies as a function of the electrically-induced charge carrier concentration. The negative electron concentration is the hole concentration [150].*

Moreover, the G and 2D modes are affected by strain and stress, since these latter are known to influence the band structure [154–157]. Strain modifies the crystal's lattice, which will influence its vibrational properties, or in other words the crystal's phonons. The shift in phonon frequencies with strain is proportional to what is called the Gruneïsen parameters, which were initially developed to describe the thermo-mechanical properties of crystals [158]. For example the Gruneïsen parameter for the doubly degenerated E_{2g} phonon is defined as [155,158]:

$$\gamma_{E_{2g}} = -\frac{1}{\omega^0_{E_{2g}}} \times \frac{\partial \omega^h_{E_{2g}}}{\partial \varepsilon_h} \qquad (2.5)$$

$\boldsymbol{\varepsilon_h = \varepsilon_{ll} + \varepsilon_{tt}}$ is the hydrostatic component of the applied uniaxial strain, $\boldsymbol{l}$ is the longitudinal component, parallel to the strain, and $\boldsymbol{t}$ is the transverse component. For biaxial strain $\boldsymbol{\varepsilon_{ll} = \varepsilon_{tt} = \varepsilon}$; $\boldsymbol{\omega^0_{E_{2g}}}$ is the G-peak frequency at zero strain while $\boldsymbol{\omega^h_{E_{2g}}}$ is the position at strain $\boldsymbol{\varepsilon_h}$. The Gruneïsen parameters can differ for uniaxial and biaxial strain, but even for uniaxial strain there is a large discrepancy in the reported values in the literature, especially between simulations and experiments [156,159]. The main reason could be the difficulty in calculating these parameters in

the case of uniaxial strain which depends on Poisson's ratio and on the degree of adhesion between the graphene and the substrate [155]. Regarding the G and the 2D peaks, they are known to downshift for tensile strain and upshift for compressive strain. It was also found that the 2D peak shifts twice the shift of the G peak. This can allow to distinguish between the effects of the strain and the doping on the Raman spectrum [90,154]. We add that usually studies consider the case of biaxial strain since it cannot be excluded, therefore the strain is calculated with the following equation deduced from equation (2.5):

$$-2\gamma_i \varepsilon = \frac{\Delta\omega_i}{\omega_{0i}} \qquad i = G, 2D \tag{2.6}$$

To conclude, Raman spectroscopy, a technique based on electron scattering by molecular vibration and phonons, brings a wealth of information concerning the graphene properties. The unique phonon dispersion diagram of graphene gives rise to different peaks, mainly around 1350, 1580 and 2700 cm^{-1}, known as the D, G and 2D modes. Other peaks may also appear due to defects, but they are less intense. The intensity, FWHM and frequency of the three main bands reveal a lot of information, related to doping, strain, the presence of a buffer layer or not and the number of graphene layers, which is completely expected since these parameters will influence the phonon dispersion in graphene. Pristine single-layer graphene, defect-free is expected to have a 2D-peak with a Lorentzian shape and a FWHM of 25 cm^{-1}, and a symmetric G peak with a FWHM around 20 cm^{-1}. However, it is rarely the case: the number of layers upshifts the 2D peak and soften it. Doping upshifts both the G and 2D peaks, but especially the G-peak, and influences their width and their intensity. Defects will also influence the peaks frequency and width. And finally, strain impacts both G and 2D peaks, but has a larger effect on the 2D peak.

Since our lab is not equipped with this technique, Raman spectra presented in this manuscript were recorded in two different labs: mostly in L2C in Montpellier with the help of Matthieu Paillet and Benoit Jouault; and LMP Leti with the help of Timotée Journot. The Raman setup in the lab L2C is a home-made setup in which an Acton spectrometer was fitted with a Pylon CCD detector and a 600 grooves/mm grating, whereas in LMP Leti the Raman setup is a commercial setup: Raman Renishaw Invia. All the samples were excited with a 532 nm (2.33 eV) continuous wave frequency doubled Nd:Yag laser through a ×100 objective (numerical aperture 0.9). The width of the focused laser spot was ~ 400 nm. The spectra were corrected by subtraction of the SiC substrate Raman fingerprint. Acquisition time was 60 s and the power impinging on the samples was ~1mW. We show in Fig. 2.12 a Raman spectrum of graphene grown on SiC (0001). The G-peak appears at 1589 cm^{-1} and the 2D-peak at 2708 cm^{-1}, slightly upshifted compared to exfoliated graphene (1582 and 2700 cm^{-1}) [90,155,160]. They seem quite symmetric with FWHM equal to 3.5 cm^{-1} and 31 cm^{-1} for the G and 2D peaks respectively. We use exfoliated graphene as a reference since it is usually considered strain free and slightly doped. It is worth noting that one can find different 2D frequencies in the literature for exfoliated graphene, since the 2D-band depends on the excitation energy [119,141]. However, we will settle for the values considered in reference [90] i.e. 1582 and 2670 cm^{-1} for exfoliated graphene, since the Raman setup we used is

similar to the one presented in this paper. The number of layers is calculated with equation (2.4) to be 1.2 MLs, which could mean one monolayer with patches of bilayers at step edges. Defect-activated peaks also appear but they are not so intense. The reason behind the blue shift could be compressive strain, doping or both as we will discuss in **chapter 3**.

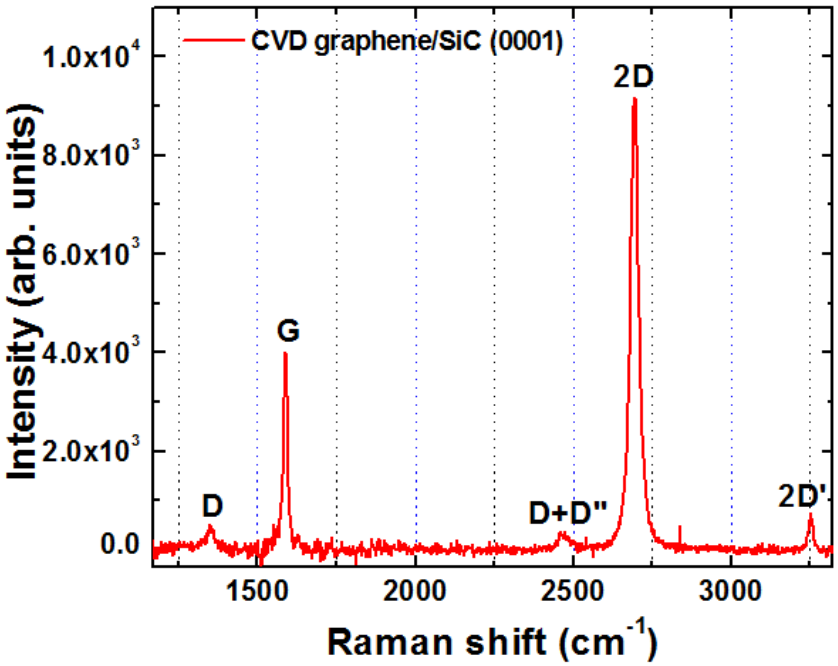

Figure 2.12: *Raman spectrum taken at 532 nm for graphene grown on SiC (0001) at 1550°C, 800 mbars, 17% H_2.*

2.3.5. Low-energy electron diffraction (LEED)

In **chapter 1**, we have mentioned many works based on low-energy electron diffraction (LEED), in particular to detect graphene, the 6√3 buffer layer and disorder. This technique is based on bombarding the sample with electrons, which will interact with the crystal by backscattering and diffraction, giving us a direct idea on the symmetry of the surface structure and the orientation of the deposited layer compared to the substrate. Therefore, it is a perfect method to monitor all the surface or interface reconstructions present after the growth process. We will start by explaining briefly the theoretical aspects behind the technique. Then we will apply it to graphene and show how to properly analyze diffraction patterns.

LEED is a surface probing technique since it relies on low-energy electrons, in the range of 20 to 500 eV, which only interact with surface atoms (about one or two nanometers for carbon/silicon materials). In the range of low-energy electrons (20-500 eV) the IMFP is between 4 and 10 Å in graphite [133], but we rarely use energies higher than 200 eV, which limits the IMFP to 6 Å for 200 eV. Considering our thin deposition of graphene, we can already see the structure of the overlayer and that of the substrate with an electron energy of 120 eV, this is why there is no need to go higher than 200 eV. The idea behind the experimental set is simple: the crystal is

maintained at UHV and subjected to collimated mono-energetic electrons, as we show in Fig. 2.13(a), which will interact with surface atoms and diffract, to be later detected if they follow the constructive interference rule:

$$dsin\theta = n\lambda \qquad (2.7)$$

This equation is similar to Bragg's law for X-ray diffraction: ***d*** being the spacing between atoms, ***n*** is the order of the diffraction beam, ***λ*** is the incident electrons wavelength and ***θ*** is the angle of the diffracted beam with respect to the surface. Hence, ***dsinθ*** is the path difference between two neighboring scattered waves, see Fig. 2.13(b).

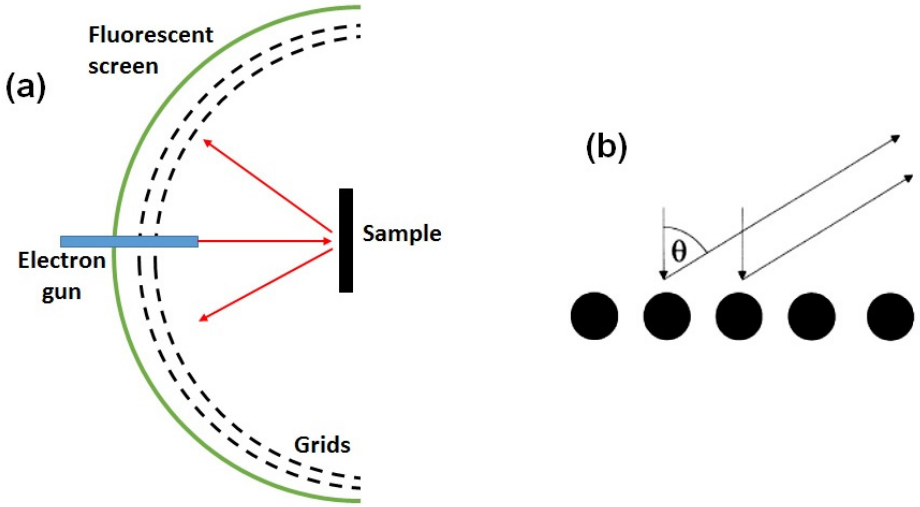

Figure 2.13: (a) *Conventional (normal incidence) LEED setup.* ***(b)*** *Diffraction of an electron beam with a normal incidence by a periodic set of atoms.*

Electrons will undergo multiple, elastic and inelastic scattering, but we are only interested in elastically scattered electrons. Therefore, the diffracted electrons will pass through two grids, the first at the same potential as the sample, the second at a potential necessary to reject all scattered electrons with energies different from the incident beam. After the two grids, there is a collector coated with phosphorus and biased with a positive potential in the order of several kV. The elastically scattered electrons are accelerated after passing through the repellent grids and hit the fluorescent screen with several keV energies, giving a visual display of the diffraction pattern [161,162]. The projection of the diffraction spots on the hemispherical screen gives a direct image of the reciprocal surface lattice. This allows a semi-quantitative analysis of the diffraction pattern where the ratio of lattice parameters can be estimated. It is also possible to do a more quantitative analysis by recording the intensity of the spots as a function of the electron beam energy to generate I-V curves, which will provide accurate information concerning the position of the atoms in the surface unit cell. However, our experimental set used in this work doesn't have this option.

Since we are using low-energy electrons, they will be scattered by surface atoms i.e. the first layers of the surface. Hence, the diffraction patterns will be two-dimensional. The so-called

Ewald construction allows to illustrate the diffraction process. The Ewald sphere has a radius equal to the length of the incident wavevector *k*, and its circumference is touching the 00 spot. Contrary to X-ray diffraction, LEED diffraction is limited to few atomic planes and almost two-dimensional, therefore the reciprocal lattice points are replaced with rods. The intersection of the sphere with the reciprocal lattice rods will give a diffracted beam in the direction indicated by a wavevector *k'* drawn from the center of the sphere to the intersection point, see Fig. 2.14. For example the 10 rod is intersected if $\lambda < d_{10}$. It is worth noting that the diffraction is not strictly limited to the first atomic layer, but can also arise from other slightly deeper surface layers, particularly when increasing the energy of the incident electrons. The intensity ratio of the diffraction spots of surface and subsurface materials can therefore change when increasing the electrons energy, but also the diffraction spots will move closer to each other when increasing the electrons energy, in a way to keep the equality of equation (2.7) [161,163].

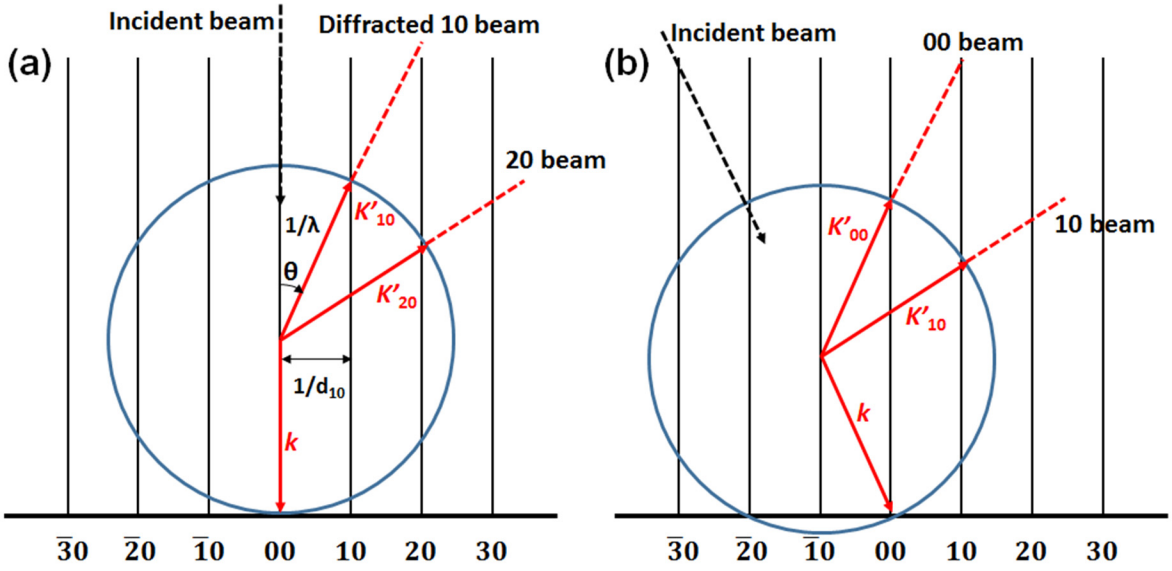

Figure 2.14: *Ewald construction for the case of normal incidence* ***(a)*** *and non-normal incidence* ***(b).***

In the present work, we use a LEED setup with a 45° electron beam incidence and a spot size about 1 mm^2, with electron energies between 60 and 200 eV. Two differences arise compared to conventional LEED patterns (obtained with normal incidence): first the position of the electron gun and the (0,0) spot will not be in the center of the diffraction pattern, as it is the case for normal-incidence LEED. Second, the probing depth will be multiplied by *sin45°* and the path of the electrons will be multiplied by *2×sin45°*, therefore it will be more surface sensitive. For example for 200 eV, the penetration depth will be 4.2 Å. The fluorescent screen is still placed facing the sample as in Fig. 2.13(a) and behind it we place a camera to record the diffraction patterns.

We present in Fig. 2.15(a) a LEED image of graphene grown on SiC (0001) with conditions promoting the development of a buffer layer (1600°C, 800 mbars, 15 min, 17% H_2); we show in

the inset a LEED image of SiC showing the (1×1) SiC symmetry. At the bottom of the image in Fig. 2.15(a), we can see the electron gun and usually we consider the highest spot as the zero spot by default, but for now for the sake of clarity we will pick a random spot and consider it the (0,0) diffraction spot. The SiC substrate's reciprocal lattice vectors are $\boldsymbol{S_1}$ $(12,\bar{6})$ and $\boldsymbol{S_2}$ (6,6), which correspond to SiC (1,0) and (0,1) respectively. The graphene's reciprocal lattice vectors are $\boldsymbol{C_1}$ (13,0) and $\boldsymbol{C_2}$ (0,13), which correspond to graphite (1,0) and (0,1) respectively [2,76]. We notice that the graphene spots are at a 30° angle with respect to the SiC spots. The other spots correspond to different order of diffraction or in some cases they correspond to a double or multiple diffraction. In fact, as the incident beam is backscattered from the substrate, it can meet other atoms of the overlayer on the way out and get diffracted another time, or multiple times [164]. These diffractions can sometimes be detected, but they are less intense than other spots. It is possible to determine their coordinates by adding the unit vectors $\boldsymbol{S_1}$, $\boldsymbol{S_2}$, $\boldsymbol{C_1}$ and $\boldsymbol{C_2}$ [76]**.** It is worth noting that the SiC spots are sometimes considered part of a (√3×√3)-R30° surface reconstruction, since this surface reconstruction appears just before the (6√3×6√3) reconstruction [76,106].

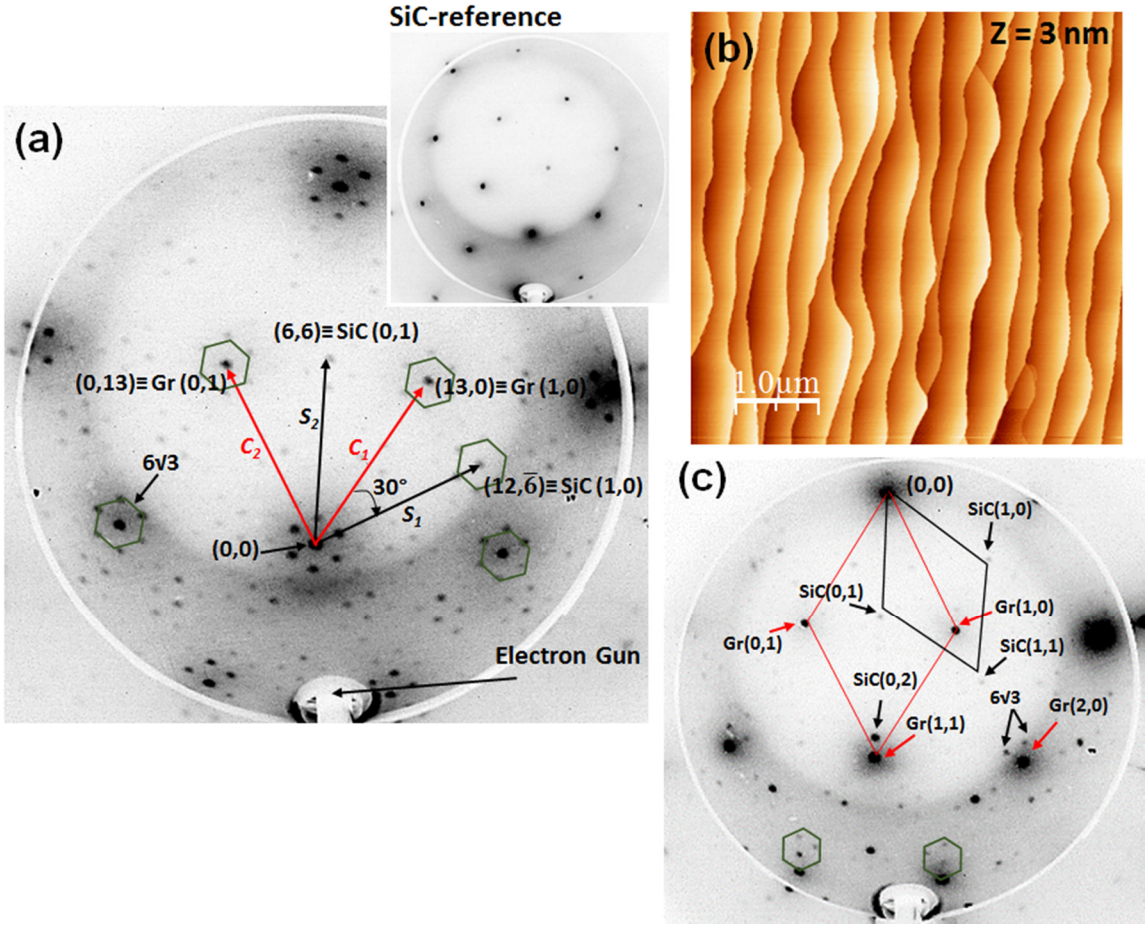

Figure 2.15: ***(a)*** *LEED pattern of graphene grown on SiC (0001) with the corresponding AFM image in* ***(b)****. Inset of* ***(a)*** *SiC reference without any graphene deposition.* ***(c)*** *LEED pattern of another sample grown under different growth conditions and different substrate. Electron energy: 140 eV.*

In addition, in Fig. 2.15(a) we also see around each spot six more spots forming a hexagon. These spots can be attributed to the (6√3×6√3) surface reconstruction [106]. The interesting part is that we also see this reconstruction around the graphene spots, which proves what different studies suggested that the (6√3×6√3) SiC reconstruction coincides with the (13×13) graphene super lattice [2,105,165]. Therefore, if we try to calculate the lattice constant using the (13,0) spot as follows: (6/13)√3×3.08 Å i.e. 3.081 being the SiC lattice constant [166], we will obtain 2.46 Å, which is in the vicinity of the graphite's lattice constant [25,26,167].

Another way to prove that it is really graphene is by calculating the ratio of the distance between the (0,0) spot and that of the graphene to the distance between the (0,0) spot and that of the SiC; we will obtain the ratio of the lattice constant of SiC to that of graphene. Finally, it is important to add that sometimes we do not detect all these diffraction spots, and especially the hexagon-forming spots, we only detect part of this hexagon as we can see in Fig. 2.15(c). We can only see two spots of the hexagon and the center point. Note that we have considered another spot as the (0,0) point. Different reasons can be behind the faint diffraction spots and the fluctuation in intensity such as multiple diffraction or the experimental setup, since we are recording these images with a camera, but mainly the fluorescent screen which is old and stained in some areas. Also, the growth conditions could be affecting the diffraction pattern since this latter sample was grown with different growth conditions and on a different SiC substrate. However, we can still identify the diffraction spots.

In another set of growth conditions, this time rich in hydrogen, the diffraction pattern can be completely different. We present in Fig. 2.16 graphene grown on SiC (0001) under 100% H_2 at 1450°C. As we can see no surface reconstructions associated to (6√3×6√3) or (√3×√3) can be

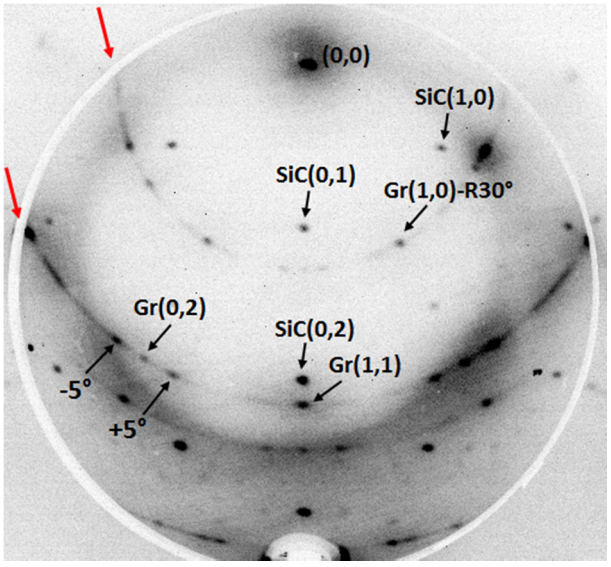

Figure 2.16: ***(a)*** *AFM image and LEED pattern* ***(b)*** *of graphene grown with 100% H_2 on SiC (0001). Electron energy: 140 eV.*

detected, but instead diffraction rings are observed, indicated by red arrows. This behavior is comparable to the growth on the C-face of SiC [78,105] and ascribed to in-plane rotational disorder. The graphene layer grows in domains with different orientations which are detectable with LEED leading to a ring-like diffraction pattern. We can still detect the 30°-angle spot of the overlayer along with other orientations.

In summary, LEED is a surface sensitive technique based on electron diffraction, allowing the detection of the surface symmetry and the alignment of the overlayer with respect to the substrate. It is also sensitive to surface reconstruction and disorder making it a useful tool to identify the presence of a buffer layer or disorder within the graphene sheet.

2.3.6. Device processing and electrical measurements

To assess the electrical properties of the graphene sheets we considered the Van der Pauw method [168,169] at 300 K. Not all samples were studied electrically, mainly because the substrate needs to be semi-insulating for explicit electrical measurements. Therefore, we chose to work with n-doped SiC, which is cheaper, to optimize the growth and the structural aspects of the graphene. Besides, processing every sample we grow can be time consuming and not necessary. For this reason, we only considered optimized growth recipes to grow graphene on semi-insulating SiC substrates for the electrical measurements.

To estimate the graphene's sheet resistance, charge carrier type and density, and carrier mobility we employed the four-probe Van der Pauw technique on two configurations suggested by L.J. Van der Pauw: clover-shaped patterns and Hall bars, as presented in Fig. 2.17. The Hall bars are 700 µm-long and 70 µm-wide. These patterns are defined with photolithography and plasma etching. First, before the processing, the sample is annealed under UHV at 300°C for 1 hour to desorb any contamination and moisture. Second, the technological steps start by cleaning the sample with three different solvents: Biosane, Acetone and Isopropanol. The sample is placed 15 minutes in each solvent under ultra-sounds. Then a 1 µm-thick film of reversible photoresist AZ 5214E is spin coated on the sample. After that, the sample is exposed to ultra-violet (UV) light for few seconds with the right mask for the contacts. Then, the sample is placed in a solvent to remove the un-polymerized patterns in the photoresist. The openings in the photoresist are checked with a profilometer, just before placing the sample in the reactive ion etching reactor. In fact, we do a short H_2 etching (20 seconds) of the sample just before the metal deposition to increase the adherence of the metal to the graphene layer. This step will create defects within the graphene in the mask opening, but it will not completely remove the graphene layer as evidenced with XPS. On a side note, few samples were processed without this step, but did not show any difference in the electrical properties of the graphene layer. After the H_2 etching, 300 Å and 2000 Å of titanium and gold are deposited respectively, by electron beam physical vapor deposition. Then, the photoresist is removed with lift-off technique. The second stage of the processing is similar, but now the mask allows to define the Hall bars and the clover-shaped patterns and electrically isolate

the different devices. After the successive steps of spin coating, exposing to UV and removing the un-polymerized photoresist, the patterns are defined with O_2 plasma etching followed by the removal of the photoresist with Acetone. The sample is now ready for electrical measurements.

For the clover-shaped pattern the method consists on making four ohmic contacts on the four extremities of the pattern, then we measure the potential difference between points 2 and 3 when a current is injected between 1 and 4 to obtain the resistance R_{23} (Ω). The measurement is repeated for two other points e.g. between 3 and 4, we inject a current between 1 and 2, to obtain R_{34}. We repeat the same process four times to find R_{23}, R_{34}, R_{41} and R_{12}.

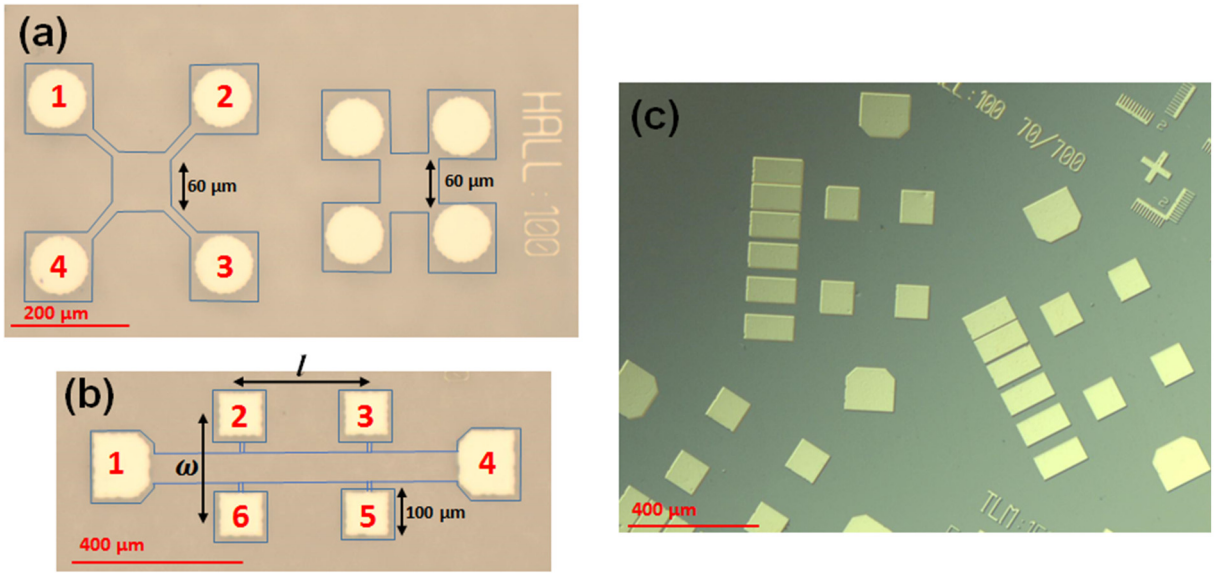

Figure 2.17: *Optical images of* ***(a)*** *clover-shaped Van der Pauw pattern;* ***(b)*** *and* ***(c)*** *Hall bars, with the four-probe configuration. The blue lines were manually added to show the etched mesas of graphene.*

The resistivity is then calculated in Ω.cm as follows:

$$\rho = \frac{\pi e}{ln2} \times \frac{R_{23} + R_{34} + R_{41} + R_{12}}{4} f \qquad (2.9)$$

Where ***e*** is the film thickness, and *f* a correction factor [168,169]. We will also obtain the sheet resistance **R□** in Ω/sq (or Ω/□) by ignoring the thickness *e*. For the measurements of the charge carrier concentration and mobility we need to apply a magnetic field (in our case B = 0.35 T) to induce a Hall Effect. Applying a magnetic field normal to the plane will generate a Lorentz force perpendicular to the lines of the magnetic field and carrier current and deviates the carrier charges, hence giving rise to a potential difference known as the Hall voltage with a sign depending on the carrier type (electrons or holes). For example, if we apply a current between points 1 and 3 (Fig. 2.17(a)) without a magnetic field we will measure zero voltage between points 2 and 4. In

contrast, when we apply a magnetic field normal to the plane, we can measure between points 2 and 4 the Hall voltage. After measuring the Hall voltage V_H we are able to calculate the Hall resistance R_H (Ω/T) with the following equation:

$$R_H = \frac{V_H}{I \times B} \qquad (2.10)$$

This will allow us to deduce the sheet carrier concentration and the carrier mobility with the following equations:

$$n_S = \frac{1}{q \times R_H} \quad ; \quad \mu_S = \frac{1}{q \times n_S \times R_\square} \qquad (2.11)$$

Where n_s is the sheet carrier density, generally given in cm^{-2}; q is the elementary charge; μ_S is the sheet carrier mobility generally expressed in $cm^2/V.s$.

A similar study can be done with the Hall bars presented in Fig. 2.17(b) by considering another four-probe approach. This time we will inject the current along the Hall bar between point 1 and 4 (see Fig. 2.17(b)) and measure at first the voltage between 2 and 3 or between 5 and 6. This will give us the resistance in Ω, then by multiplying by ω and dividing by l we obtain the sheet resistance in Ω/sq. The Hall voltage is measured between contacts 2 and 6 or contacts 3 and 5 while injecting a current between contacts 1 and 4 and applying a magnetic field. In addition, the mask we use for the lithography allows us to define Hall bars with different in-plane orientations with respect to the substrate's offcut direction (see Fig. 2.17(c)). This way we can check the symmetry of the sample and measure the mobility in different directions to see if it is influenced by the substrate's steps. To summarize, this techniques is simple and basic, allowing us to gain insights into the electrical quality of our graphene sheets and calculate the charge density and carrier mobility.

2.4. General conclusion

We have reported in this chapter the experimental methods behind this work. In a first part, we presented the experimental setup we used for the growth of graphene and sample preparation. The system we used is a horizontal hot-wall CVD reactor, initially built for 3C-SiC, silicon and other SiC polytypes growth. The inner part of the reactor is entirely made of graphite which allows the growth of graphene on SiC at high temperatures. We also presented the different experimental details for the growth of graphene on SiC.

In a second part, we described all the characterization techniques employed for the identification and analysis of the as-grown graphene. AFM is very useful when it comes to information concerning the topography, while SEM can bring additional images of the surface, with the ability to explore uniformity at a large scale. The AFM phase image and SEM can also give us a qualitative idea on the number of layers, due to their sensitivity to the mechanical properties of the surface. XPS can be a great analysis technique to identify graphene and the presence of the $6\sqrt{3}$ buffer layer. It is based on exciting core-level electrons with X-rays, which gives an idea on the surface energy states, once detected and analyzed. It is sensitive to the IMFP of electrons within graphene making it a surface analysis technique. Raman spectroscopy is also a very appealing technique for graphene, based on the phonon dispersion within graphene. It aims to excite vibrational states and other types of low-frequency modes with a laser beam. Analyzing the energy shift between the incident and emitted electrons can bring a lot of information concerning the phonon modes in play which is influenced by the graphene quality, crystallinity, doping level, strain and number of layers. We also considered LEED for analyzing the structure of the graphene layers. It is also a surface sensitive technique, based on the diffraction of low-energy electrons by surface atoms. This technique allows to detect the $6\sqrt{3}$ buffer layer or disorder within the graphene sheets. And finally, we used the four-probe Van der Pauw method to assess the electrical properties of graphene at 300 K.

In conclusion, the different characterization techniques complete each other. We systematically do AFM on all samples then XPS. These two techniques, combined together, already bring a lot of information: first concerning whether we have deposited graphene or not and second concerning the structure of graphene, whether it is associated with a buffer layer or not. LEED is used to confirm this last observation, but it is not systematically done on all samples, since it takes more time considering that we can only put three samples at a time and wait to reach vacuum conditions. SEM is used occasionally to check the uniformity of the growth whenever the sample is large i.e. around 2×2 cm^2. For further and advanced investigations, the best samples are studied with Raman spectroscopy with an external collaboration. This takes more time depending on the availability of the Raman setup, but allows a deeper understanding of the graphene properties. In addition, it allows to uncover anomalies on a small scale since the spot size is 400 nm, which is relatively small compared to XPS where the spot size is 400 microns. Finally, to complete the work, few samples are processed for the evaluation of the electrical properties of the epitaxial graphene.

Chapter 3

Graphene CVD on silicon carbide

In this chapter we will discuss the growth on silicon carbide of graphene by CVD from an external carbon source. First, we will present a thermodynamic study which will give us insights into the growth process, while comparing our approach to the Si sublimation technique. In a second part, we will reveal the influence of each of the growth parameters on the graphene epitaxy, to finish by focusing on the graphene's quality and electrical performance. It is important to keep in mind that we only study the Si-face of SiC substrates.

3.1. Direct growth under H_2: A Thermodynamic approach

In **chapter 1** we have presented two approaches to grow graphene on SiC: the thermal decomposition of SiC, also known as the Si sublimation technique, and the growth from an external carbon source denoted as direct growth. The Si sublimation technique is known to be carried out either under UHV [2,4,76] with temperatures between 1200 and 1400°C or under argon [80] at higher temperatures, generally between 1650 and 2000°C, depending on the pressure. In addition, some studies have investigated graphene grown from an external carbon source [11,13,16]. Since the Si sublimation requires specific conditions of low pressure and high temperature, it can be inhibited or minimized by reducing the growth temperature, as these previous studies did [11,16], or it can be minimized due to well controlled gas flow mixtures [13]. In our research group three approaches were developed to grow graphene: the first was developed under a pure argon atmosphere [101] where long growth times were required (starting from 15 minutes) and the temperature was kept around 1300°C to avoid Si sublimation, but its contribution to the growth was not completely ruled out. The second approach was carried out in a pure hydrogen atmosphere [17,18], which has allowed a wider range of growth conditions with temperatures varying between 1100 and 1650°C and pressures between 100 and 800 mbars. Finally, the third approach considers a mixture of argon and hydrogen and is the main focus of this chapter.

The question that we will try to answer here is: should we expect a contribution to the growth from the substrate itself by Si sublimation in a hydrogen atmosphere? Or only in a pure argon atmosphere? To address this problem we have conducted a set of experiments under our standard growth conditions with hydrogen and argon. We even attempted deliberately to grow graphene by Si sublimation in our CVD reactor.

In order to really understand what happens in our H_2-Ar-C_3H_8-SiC system we had to do some thermodynamic calculations, performed in the frame of a collaboration with Christian Chatillon and Elisabeth Blanquet from the laboratory SIMaP in Grenoble. Therefore, this part will be a combination of experimental results and thermodynamic calculations. First, we will start with some Si sublimation experimental attempts, then we will present the software FactSage™ and the model used for the calculations. Finally, we will discuss the calculation results and compare our growth technique to the Si sublimation technique.

3.1.1. Si sublimation attempts under H_2 or argon

Most of our graphene growths are carried out with 17% of H_2 and 83% of argon in the total gas mixture flow rate of 12 slm, at temperatures around 1450 or 1550°C; at a pressure of 800 mbars and for a growth time of 5 minutes. We will apply these conditions without any propane to evaluate the contribution of the substrate to the growth of graphene. Please note that in this entire chapter whenever we write x% of H_2 the remaining percentage is argon. We present in Fig. 3.1 SiC annealing experiments under a H_2-Ar mixture. Fig. 3.1(a, b) shows AFM images after SiC annealing for 5 minutes without any propane, under 800 mbars of a 17% H_2 (2 slm) + 83% argon

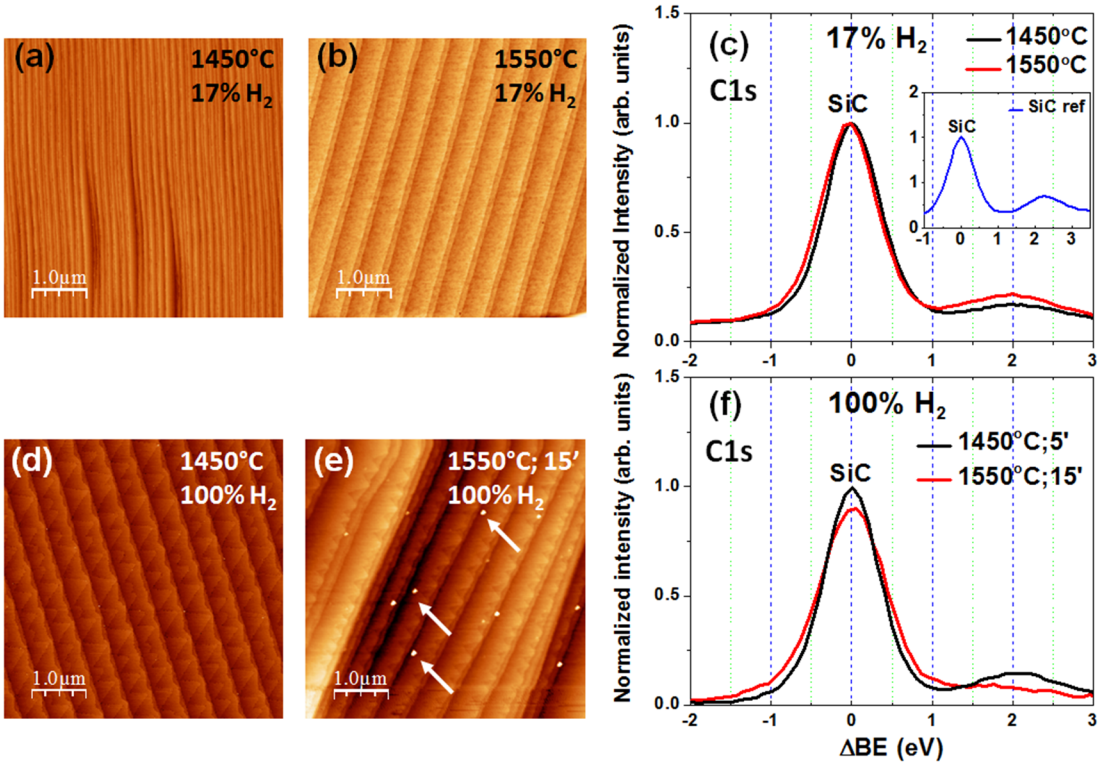

***Figure 3. 1: (a)** and **(b)** 5×5 µm² AFM images of SiC annealing for 5 minutes under 17% of H_2 at 1450°C and 1550°C respectively, with the corresponding C1s core-level spectra in **(c)**. Figure in inset: SiC reference before any annealing. **(d)** and **(e)** AFM images of SiC annealing under 100% of H_2 at 1450°C for 5 minutes and 1550°C for 15 minutes respectively. **(c)** The corresponding C1s core-level spectra. (AFM z-scale is 5 nm).*

(10 slm) carrier gas mixture at 1450°C (Fig. 3.1(a)) and 1550°C (Fig. 3.1(b)). Note that the two substrates do not have the same miscut angle, but this parameter is not so important for this particular study. As we can see, the annealing results in straight steps, 1.5 nm-high, separated by small terraces with lower steps (0.75 nm-high). The height and shape of the steps suggest a bare SiC surface with a step-height corresponding to ***½c*** (out-of-plane lattice constant of 6H-SiC). The C1s core-level peaks in Fig. 3.1(c) only show the carbon peak corresponding to SiC with a small bump at higher binding energy which corresponds probably to carbon contamination from our graphitic reactor. We show for comparison in the inset of Fig. 3.1(c) the C1s core-level spectrum of bare SiC as a reference. In this spectrum, we can detect the SiC peak at 283.8 eV and a small bump at 286 eV attributed to contamination from the atmosphere or from the plastic container.

In the XPS spectra presented here, the SiC peaks were taken as energy references and normalized, since for this analysis the binding energy and intensity do not interest us as we are only looking for the manifestation of the graphene peak; but we will mention the binding energy when necessary. We can deduce that for this particular annealing condition that no graphene was formed. We have then increased the amount of H_2 to 100% (12 slm) at 1450°C for 5 minutes, without any propane. The corresponding AFM image in Fig. 3.1(d) presents 1.5 nm-high steps, consistent with 6H-SiC steps, with some triangular shapes frequently observed after hydrogen etching. Increasing the temperature to 1550°C and the annealing time to 15 minutes results in a

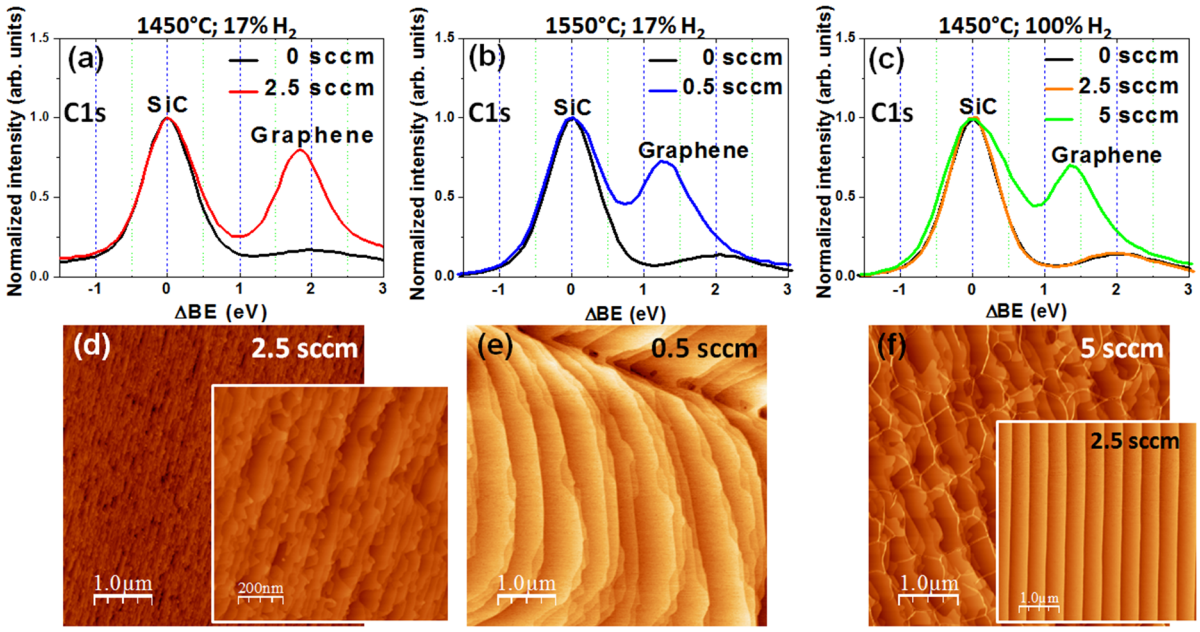

Figure 3. 2: ***(a)*** *to* ***(c)*** *C1s core-level spectra of graphene growths at* ***(a)*** *1450°C, 17% H_2 and 2.5 sccm C_3H_8;* ***(b)*** *1550°C, 17% H_2 and 0.5 sccm C_3H_8;* ***(c)*** *1450°C, 100% H_2 and 2.5-5 sccm C_3H_8.* ***(d)*** *to* ***(f)*** *The corresponding 5×5 µm² AFM images with a 5 nm-z scale. Inset in* ***(d)*** *is a 1×1 µm² image. Inset in* ***(f)*** *is a 5×5 µm² AFM image of the growth under 2.5 sccm of C_3H_8.*

similar morphology with the addition of some droplets indicated by the white arrows, which we will later ascribe to silicon droplets. The corresponding C1s core-level spectra again shows no sign of graphene since we only see the SiC peak. To summarize, annealing SiC with H_2 whether at 1450°C or at 1550°C, for 5 minutes or 15 minutes, for a small or an important amount of H_2, the SiC substrate does not form any graphene.

To complete our investigations, we added a small amount of propane to see what happens. For the first growth condition (17% H_2 at 1450°C), adding 2.5 sccm of propane leads to the manifestation of a carbon peak in Fig. 3.2(a) at 284.4 eV, in the vicinity of sp^2 carbon, which suggests the presence of graphene. The corresponding AFM image in Fig. 3.2(d) shows a different morphology from Fig. 3.1(a). We can see in the inset of Fig. 3.2(d) (compared to Fig. 3.1(a)) that the steps are no longer straight, the terraces seem rougher, and crooked patterns appear between steps. All these observations suggest that graphene growth has taken place. Fig. 3.2(b) also presents a graphene peak at 284.8 eV, with an obvious change in morphology in the corresponding AFM image in Fig. 3.2(e) compared to Fig. 3.1(b) for 17% H_2 at 1550°C. Under these conditions, only 0.5 sccm of propane were enough to form graphene. On a side note, we still notice etching effects on the surface, either in the pre-growth high temperature plateau or during the growth, as a hollow line appears in the AFM image, which could be a polishing scratch etched by H_2. Finally, for an excess of H_2 (12 slm of H_2) at 1450°C without any argon in the gas mixture, the graphene peak (at 284.6 eV) in Fig. 3.2(c) appears only when adding 5 sccm of propane. The corresponding AFM image in Fig. 3.2(f) exhibits wrinkles associated with a graphitic deposition [17,18]. Note that the graphene peak is not always at the same position for the different samples (284.4 eV, 284.8 and 284.6 eV), which could rise from the different thicknesses of the deposited graphene [105]. For 2.5 sccm of propane no graphene peak appears, and if we compare the corresponding AFM image (inset of Fig. 3.2(f)) to Fig. 3.1(d), we only see straight steps without any triangular shapes associated with etching. We believe that etching is still present but not as aggressive as in Fig. 3.1(d), since adding a small amount of propane can slightly reduce the etching of SiC by H_2, as already demonstrated by other studies [170,171].

So far we have conducted SiC annealing with H_2 in the range of our graphene growth conditions. Without adding propane to the gas mixture, there is no chance to form graphene on the surface. In contrast, in some conditions a very small amount of propane (0.5 sccm) is enough to deposit graphene (Fig. 3.2(b)). Therefore, a first conclusion can be that the main source of carbon for the graphene growth in our H_2/Ar system is propane, without any contribution from Si sublimation, but at this point we cannot rule out other contributions from the substrate due to H_2 etching. However, if we compare our work to the literature, the Si sublimation process is carried out under UHV or argon. Since we cannot achieve UHV conditions, we have tested SiC annealing under only argon without any hydrogen, in the range of our graphene growth conditions i.e. 1550°C, 800 mbars, 5 minutes. The first attempt was done without any propane for 5 minutes with 10 slm of argon, presented in Fig. 3.3(a). The SiC steps are straight and 0.75 nm-high, corresponding to 6H-SiC. Even when adding 5 sccm of propane (Fig. 3.3(b)) the morphology does

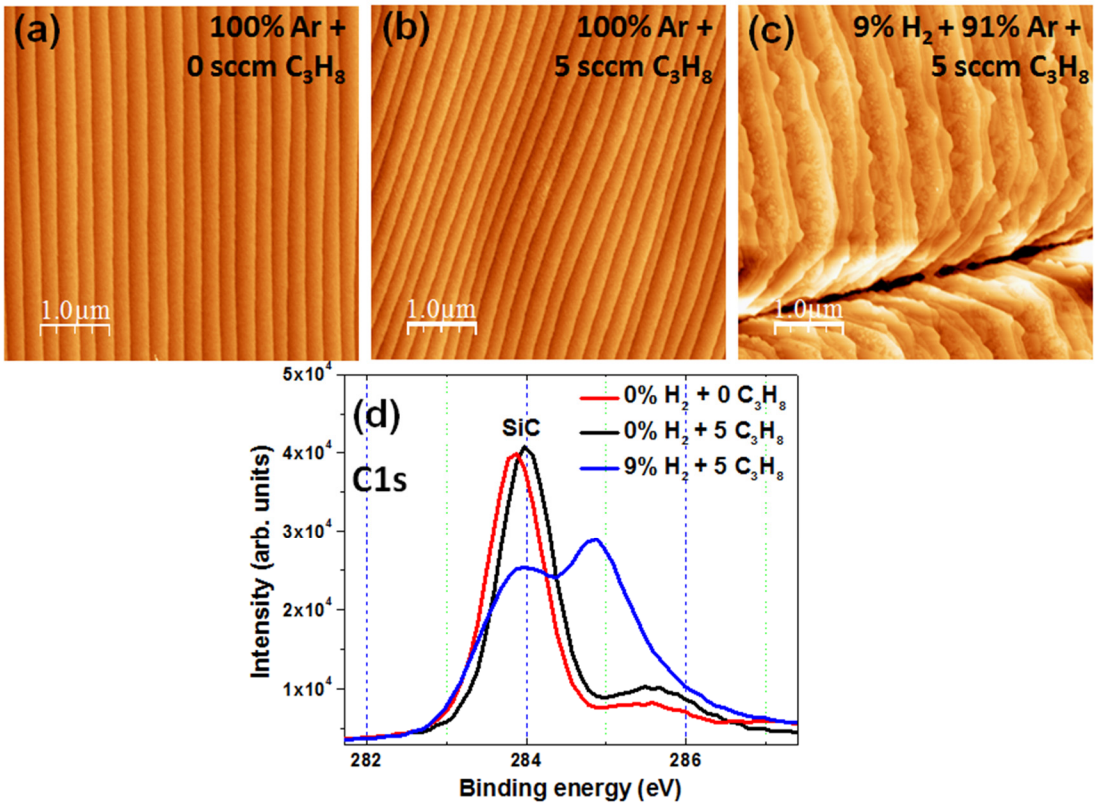

Figure 3. 3: ***(a)*** *and* ***(b)*** *5×5 µm² AFM images of Growth attempts under argon without any H_2:* ***(a)*** *without C_3H_8 and* ***(b)*** *with 5 sccm of C_3H_8.* ***(c)*** *AFM image of graphene growth under 9% of H_2 and 5 sccm of C_3H_8. All the growths are carried out at 1550°C, 800 mbars and for 5 minutes.* ***(d)*** *The corresponding C1s core-level spectra. (AFM z-scale is 3 nm).*

not change. The corresponding C1s core-level spectra show no sign of a graphene deposition for the growth under argon, with or without propane, see Fig. 3.3(d). Adding just 1 slm of H_2 (Fig. 3.3(c)) to the gas mixture led to the formation of graphene confirmed by the manifestation of a graphene peak at 284.8 eV and the attenuation of the SiC peak in Fig. 3.3(d), associated with an important change in the morphology. A previous study [101] has demonstrated that the growth of graphene under argon on SiC requires specific conditions, mainly longer growth time. Hence, it is not surprising that no graphene is detected with only 5 minutes. However, adding just a small amount of H_2 (9% in the gas mixture) allows to grow graphene within 5 minutes. This confirms that the growths under H_2 or argon are two different approaches, mainly related to the different thermodynamics of the two systems. In addition, the study [101] did not rule out the possibility of Si sublimation under Ar + C_3H_8. Therefore, there is no reason for the growth not to take place without any propane under argon.

For this reason, we tried to grow graphene by Si sublimation under argon without any propane, but to achieve this objective we had to change completely our growth conditions. We present in Fig. 3.4 our graphene growth with Si sublimation confirmed with AFM and XPS. The growth was done during 10 minutes, but we had to reduce the pressure to 100 mbars of argon and

increase the temperature to 1600°C while no propane was added. The C1s core-level in Fig. 3.4(a) presents a graphene peak at 284.9 and 285 eV for the 1600°C-growth and the 1650°C-growth respectively. The SiC peaks were already aligned, so we did not have to shift them for further analysis. The 1650°C-graphene peak seems slightly more intense than the other peak, suggesting a more important growth rate at the higher temperature, which is reasonable considering that increasing the temperature will increase the Si sublimation. In the corresponding AFM image in Fig. 3.4(b) of the 1650°C-growth, we notice irregular shapes, step-bunching, different contrasts and also wrinkles indicated by white arrows. All these features suggest an epitaxy on the SiC substrate. We also detect different contrasts in the phase image (Fig. 3.4(c)), which also suggest an epitaxy of incomplete layers. Our aim was not to optimize this growth, but only to show that Si sublimation is possible for the right growth conditions under argon.

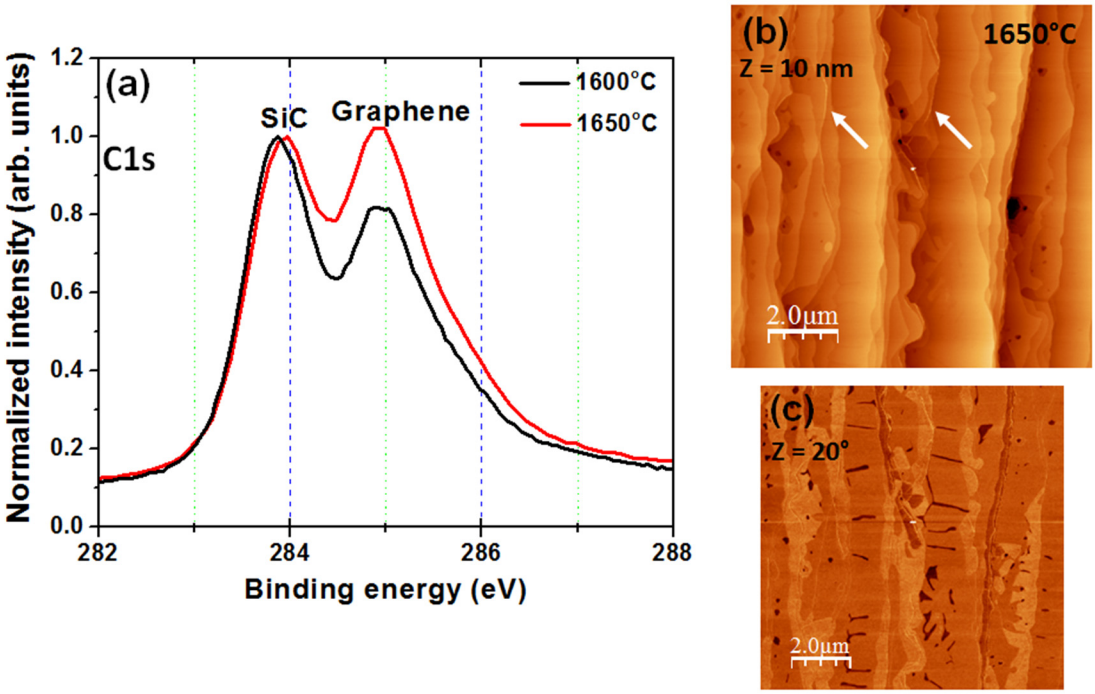

Figure 3. 4: *Si sublimation attempt under 100 mbars of argon, for 10 minutes, without any C_3H_8.* ***(a)*** *C1s core-level spectra of the growth attempts at 1600 and 1650°C.* ***(b)*** *and* ***(c)*** *the corresponding 10×10 µm² AFM topographic and phase images of the 1650°C-growth.*

To summarize this part, we have demonstrated on the basis of AFM and XPS that annealing SiC with H_2 or H_2+Ar is not likely to result in graphene formation, regardless of the amount of H_2 we add, or the temperature, or the annealing time. To achieve graphene growth, it is necessary to add propane to the H_2-Ar mixture; even a small amount of propane is sufficient to grow graphene in some cases. This leads us to the impression that under H_2, propane is the main source of carbon in the graphene growth on SiC and not the substrate, compared to the Si sublimation technique. We also demonstrated that growth attempts with argon only, with or without propane, cannot be achieved within 5 minutes in contrast to the growth with H_2-Ar, even if the H_2 amount is not

important in the gas mixture. We believe that the reason behind this behavior is related to the different thermodynamics in the two systems. For these reasons thermodynamic calculations seem necessary. Finally, we have observed that Si sublimation is only possible under argon, but we had to change drastically the growth conditions, by reducing the pressure to 100 mbars and increasing the temperature and the growth time to 1600°C and 10 minutes respectively. By doing so, we have proven that we cannot rule out the Si sublimation in a growth under argon, but we can do that without any doubt in a hydrogen atmosphere, even if the hydrogen is mixed with argon. To confirm these deductions, we carried out thermodynamic simulations, which will reveal to us the physics behind the growth under H_2 (or H_2 + Ar). But first, before we present the thermodynamic calculations, we will describe in the following paragraph the software we used for this study.

3.1.2. Thermodynamics and FactSage

The thermodynamic approach allows to study a chemical system at equilibrium and to determine its composition at a given temperature and pressure. In other words, it allows to calculate the concentration of species after having reacted together and reached equilibrium. Thermodynamic equilibrium is defined when the Gibbs free energy $\boldsymbol{G}$ of the system is minimal i.e. when $\boldsymbol{dG = 0}$ and $\boldsymbol{d^2G > 0}$. Consequently, when introducing different constituents into a reactor under a fixed temperature and pressure, some transformations will occur such as chemical reactions and heat transfer in a way that the Gibbs free energy of each constituent decreases until reaching a minimum. $\boldsymbol{G}$ is correlated to the system's parameters with the following equation:

$$dG = VdP - SdT + \sum_i \mu_i dn_i \qquad (3.1)$$

Where $\boldsymbol{V}$ is the volume, $\boldsymbol{P}$ the pressure, $\boldsymbol{T}$ the temperature, $\boldsymbol{S}$ the entropy, $\boldsymbol{\mu_i}$ and $\boldsymbol{n_i}$ the chemical potential and the number of moles of the specie $\boldsymbol{i}$. For a constant pressure and temperature, $\boldsymbol{G\,(P,T)}$ will be equal to $\sum_i \mu_i dn_i$.

Accordingly, to be able to define a thermodynamic equilibrium, one needs to know the variation of $\boldsymbol{G}$ of the species reacting together and that of the species created. To this end, an international work allowed to create different databases for such calculations. For example, we mention the **Scientific Group Thermodata Europe (SGTE)** [172], which considers that the reference of $\boldsymbol{G}$ is the one at 298 K and 1 bar. Additional studies were done to complete these databases, such as the work of Allendorf on Si-C-H-Cl systems [173,174] and the work of Rocabois [175] which was compiled to form the SIMaP private database **ROCA** for thermodynamic simulations. In this particular study we use the software FactSage™ [176] which is a fusion of FACT-Win of the research center in computational thermochemistry of the polytechnic school of Montréal and ChemSage of GTT-technologies. It has different calculation modules, but the one we use allows to calculate the activities and the concentrations of species created upon chemical reactions in a closed system, while achieving the minimal Gibbs free energy. Therefore, we can introduce the species we want to react together and set the temperature and the pressure. In our case, since we are working in a H_2-Ar-SiC system, we add H_2, argon and C_3H_8 (when necessary) as gases, and SiC as a solid, all quantified in moles. Then FactSage will

generate all the possible species which can be created at equilibrium, with their activities and concentrations. Note that the activity for gases represents their partial pressure. Also, note that we cannot add the introduced gases in laminar flow i.e. in liters/min (slm), but to stay consistent with our experimental conditions we will keep the gases in the same composition, for example for the growth under 2 slm H2, 10 slm Ar and 5 sccm C_3H_8, we will consider 2000 moles of H_2, 10 000 moles of Ar and 5 mole of C_3H_8.

It is important to keep in mind that we cannot simulate with these thermodynamic calculations the exact deposition of graphene since there are a lot of parameters that we cannot consider, such as the size of the reactor, the deposition kinetics, the substrate's miscut angle, the speed of the gases which are in a continuous flow etc… Nevertheless, this approach is still very helpful to understand the evolution of our chemical system H_2-Ar-C_3H_8-SiC, and will allow us to compare our growth technique to the Si sublimation technique.

3.1.3. Graphene on SiC through Thermodynamic calculations

3.1.3.1. Hydrogen-argon atmosphere

After presenting the calculation method, we show the results starting with what happens when we anneal SiC under H_2 and argon since most of our growths were carried out in a H_2-Ar mixture. In the first simulation we added 2×10^3 moles of H_2 and 10×10^3 moles of argon, i.e. 17% of H_2 + 83% of Ar, to 100 moles of solid SiC. Hydrogen reacts strongly with SiC and creates over 60 different molecules, including isomers, containing C-H and Si-H bonds. The calculation involves 51 carbon-based species (either C(g) or with C-H, C-Si and C-Si-H bonds) and 43 silicon-based molecules, consisting of Si-H, C-Si and C-Si-H bonds, for example such as CSi(g), CHSi(g), C_2H_2Si(g) etc…. The isomers are referred to as (g), (g2) and (g3) and so on for the first, the second and the third isomer.

We present in Fig. 3.5 the partial pressure of all the created species as a function of the temperature ranged between 1000 K and 2200 K at 800 mbars, with the exception of few weak partial pressures who do not reach 10^{-7} bars for better clarity, such as: C_2(g), C_3(g), C_4(g), C_2H_5(g), C_2H_6(g), C_3H_8(g), C_2Si_2(g),CH_3Si(g), C_2H_5Si(g), H_6Si_2(g), etc… in total 35 species were omitted. We also removed the H_2 and argon partial pressures, which appear at higher pressure values. We will abstain in the following from adding the notation (g) since all of the species presented here are in the gas phase.

We first notice in the graph in Fig. 3.5 the increasing pressure of H with the temperature due to H_2 decomposition. Second, for temperatures lower than 1800 K the dominant gas is CH_4, but actually the CH_4 partial pressure is decreasing between 1000 and 1600 K, then slightly increasing. After 1800 K, CH_4 is stable but other gases start to increase in pressure such as Si, CH_3, C_2H_2, HSi, CSi_2, etc… mostly species containing Si and H. For a clearer discernment we illustrate in Fig. 3.6 the sum of all the partial pressures of gases containing carbon and all the gases containing silicon, by taking into consideration the atomic concentration as well. These parameters will be referred to as **FluxC** and **FluxSi** for the gases containing carbon and silicon respectively.

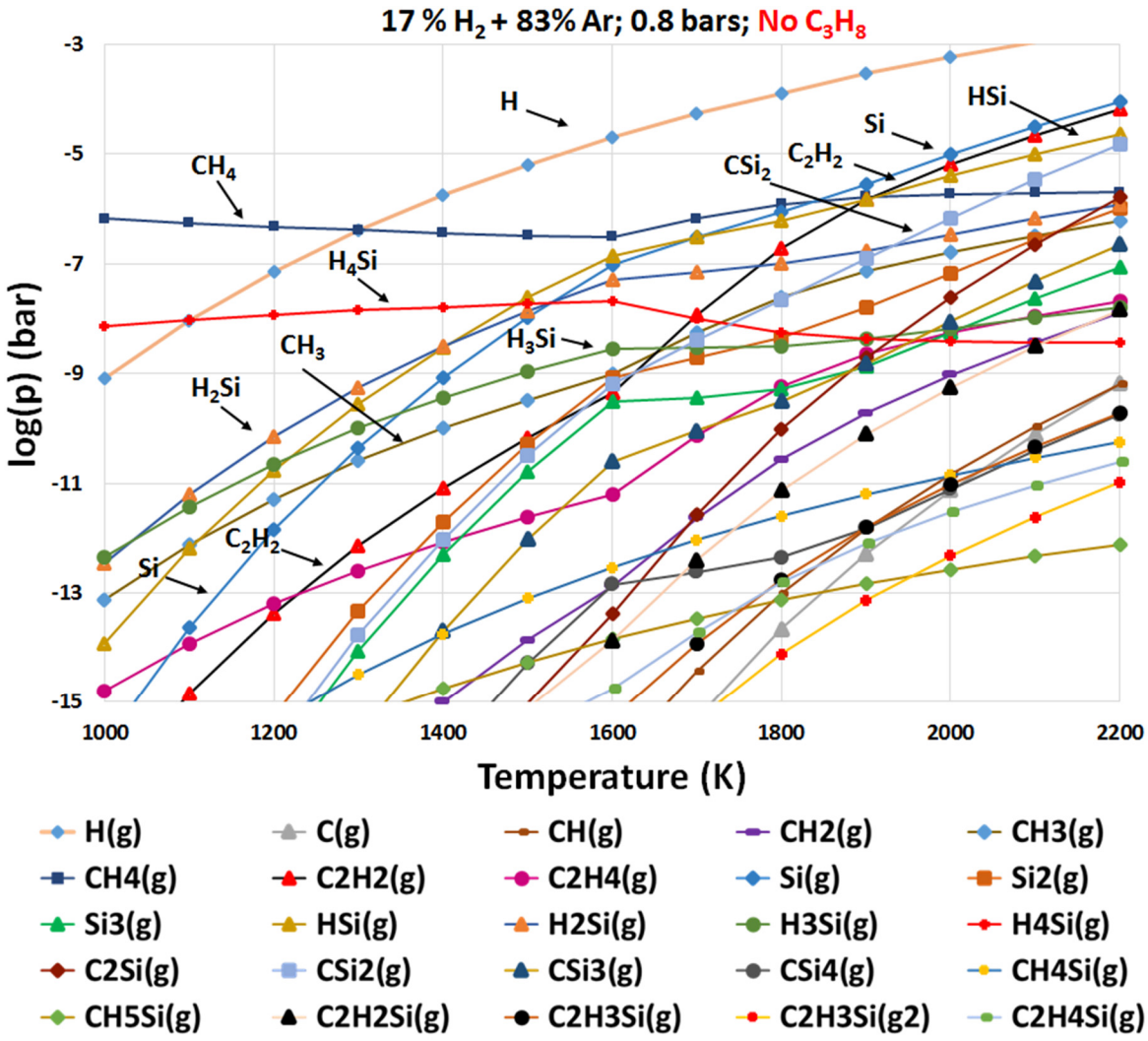

Figure 3. 5: *Partial pressure of the C- and Si-gaseous species as a function of the temperature produced by the reactions of H_2+SiC+Ar.*

As we can see in Fig. 3.6(a), **FluxC** is much more important than **FluxSi** at 1000 K. This latter increases with the temperature while the former slightly decreases, until the two curves cross at 1600 K. This means that H_2 is etching the SiC substrate and creating in the gas phase a lot more carbon species than silicon species between 1000 and 1600 K. Then, when increasing the temperature, the etching continues to increase but this time both gaseous species containing Si and C atoms are being created with an equal amount.

This behavior is mainly due to the CH_4 gas, as we can see in Fig. 3.6(b). The vapor pressure of CH_4 alone is higher than all the partial pressures of the silicon species combined together for temperatures lower than 1600 K. After that, the CH_4 pressure becomes stable while other vapor pressures continue to increase. This phenomenon is very likely to lead to a silicon residue at the surface of SiC in the temperature range 1000 - 1600 K. Indeed, this was observed in a study in the

year 2000 by Neyret et al. [171] who conducted similar calculations and demonstrated experimentally the formation of silicon droplets when annealing SiC under only H_2 at 1700 K and 1 bar. For this reason, we believe that the droplets observed in Fig. 3.1(e) are silicon droplets. Increasing the H_2 amount in the gas mixture will displace the intersection of the two curves **FluxC** and **FluxSi.** As we can see in Fig. 3.6(c), we have increased the H_2 amount to 100%, which shifted the intersection to 1800 K instead of 1600 K. Also, notice that the whole graph shifted up to higher vapor pressures, due to the increase of etching when increasing H_2. These last two observations suggest that increasing H_2 increases the etching of SiC, mainly into C-H species. Therefore, a higher temperature (1800 K) is required to increase the formation of Si-H species.

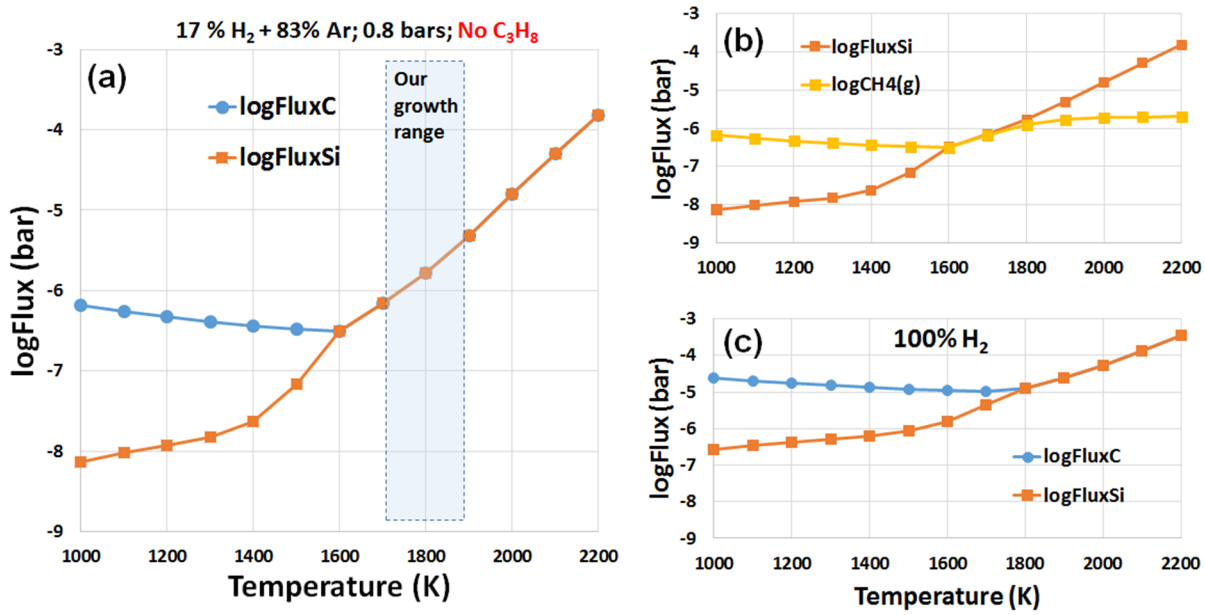

Figure 3. 6: (a) *FluxC and FuxSi as a function of the temperature.* ***(b)*** *FluxSi vs. the partial pressure of CH_4.* ***(c)*** *FluxC and FluxSi as a function of the temperature for 100% of H_2.*

To limit the formation of silicon residues at the surface, propane can be added to the gas mixture [171], as we present in Fig. 3.7. This time we are doing the same calculations but with 0.04% of propane, consistent with our experimental conditions. Similar effects will occur: H_2 will etch the substrate, which will release carbon- and silicon-based gases into the atmosphere. However, this time we also have the decomposition of propane. We show in Fig. 3.7 the most dominant species in the gas phase. Compared to the previous calculations (Fig. 3.5), we notice that the vapor pressure of CH_4 is more important than before, but it drops rapidly with the temperature while the C_2H_2, CH_3 and the other gases vapor pressures are increasing while that of the silicon-based gases remain under the level of C_2H_2. We also notice a lower vapor pressure of the Si-H species, such as H_4Si, H_3Si and other silicon-based gases, compared to the previous case (Fig. 3.5). In general, the C-H species have higher vapor pressures than the previous case, whereas the Si-H species have lower vapor pressures. All vapor pressures are increasing with the temperature

(except for that of CH_4) in a way that the Si-H species vapor pressures remain below those of the C-H species. These major changes are due to the decomposition of propane, which is presented in Fig. 3.8(a).

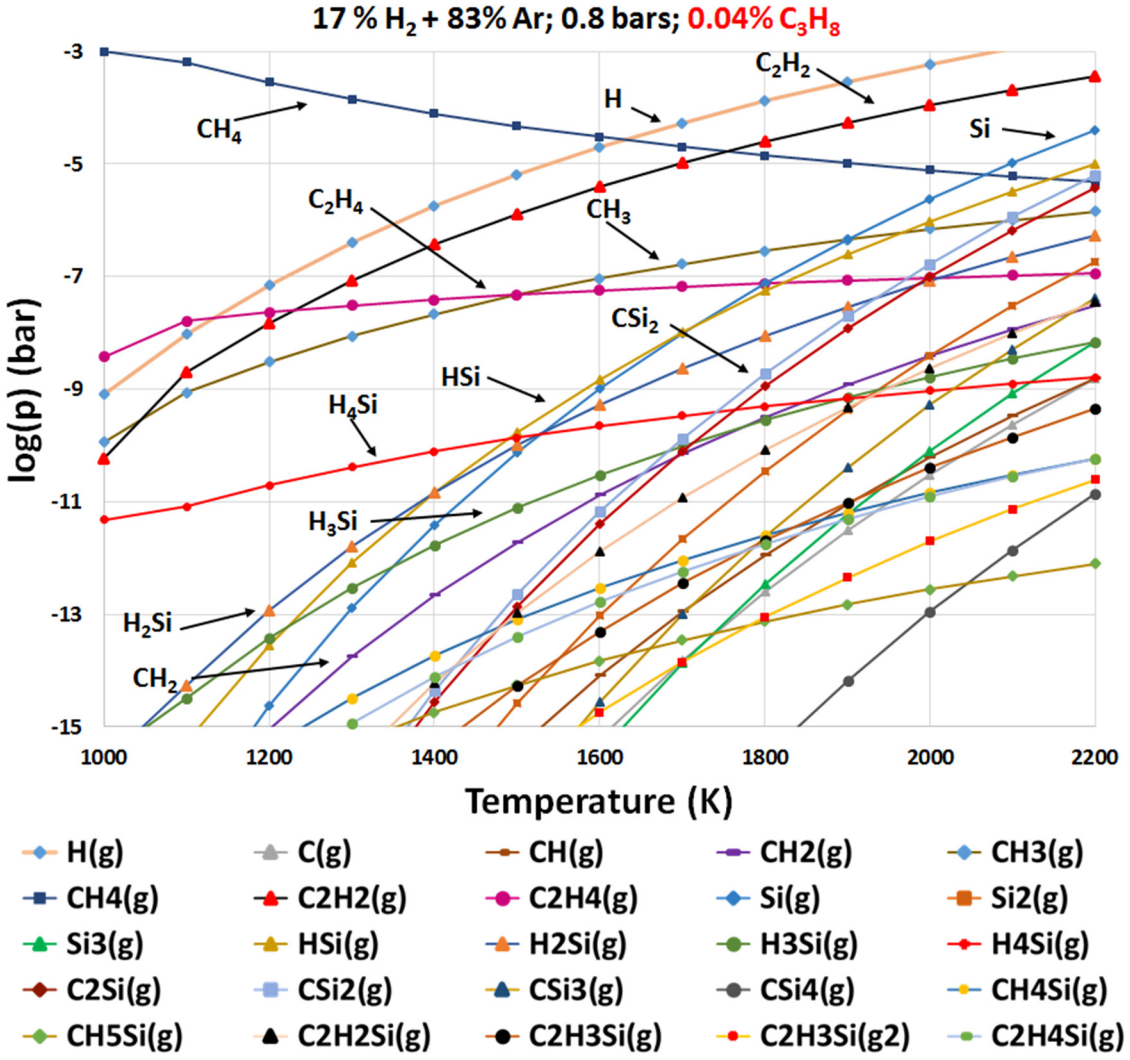

Figure 3. 7: *Partial pressure of the C- and Si-gaseous species as a function of the temperature in the H_2-Ar-SiC-C_3H_8 system.*

The decomposition of propane can be estimated by doing simulations with H_2+Ar+C_3H_8 without any solid SiC, while keeping the same gas ratios, i.e. 17% H_2 + 83% Ar + 0.04% C_3H_8. The decomposition of C_3H_8 is shown in Fig. 3.8(a). This figure reveals the decrease of the C_3H_8 pressure while it is being decomposed into other gases, mostly CH_4 and C_2H_2. However, the CH_4 vapor pressure is decreasing with the temperature increase, which means that for higher temperatures the propane decomposes less into CH_4 and more into other gases. Note that we omitted gases with vapor pressures lower than that of C(g) to avoid congestion such as C_i gases (i = 2 to 5). As we can see, the decrease of CH_4 in Fig. 3.8(a) is exactly the same as in Fig. 3.7,

with matching values of vapor pressure. Likewise, for the gases C_2H_2, C_2H_4, CH_3 and all the C-H gases, the curve evolution appearing in Fig. 3.8(a) is similar to Fig. 3.7 (even for the C_i gases (i = 1 to 5) and the C-H gases that we omitted in Fig. 3.7 to avoid congestion such as C_2H_3, C_2H_5 and C_2H_6). In view of these results, we can conclude that the C-H-species vapor pressures that we observe in Fig. 3.7 emanate from the decomposition of propane and not from the etching of the substrate, as if the etching is reduced. In fact, different studies have attested that adding propane to an H_2-annealing of SiC reduces the etching of the SiC [170,171]; in particular, it reduces the etching into C-H species by adding C-H gases from the decomposition of propane. We assume that this is what is happening in our case, because we still see Si-based species in Fig. 3.7, which means that the etching is occurring by forming Si-H, Si-C and Si-C-H gases, while the C_i (i = 1 to 5) and C-H gases formation (from the substrate) is inhibited. With this in mind, if we only consider the gases coming from the substrate, the vapor pressures of the gases Si and Si-H are dominant in Fig. 4.7 compared to the Si-C and Si-C-H gases.

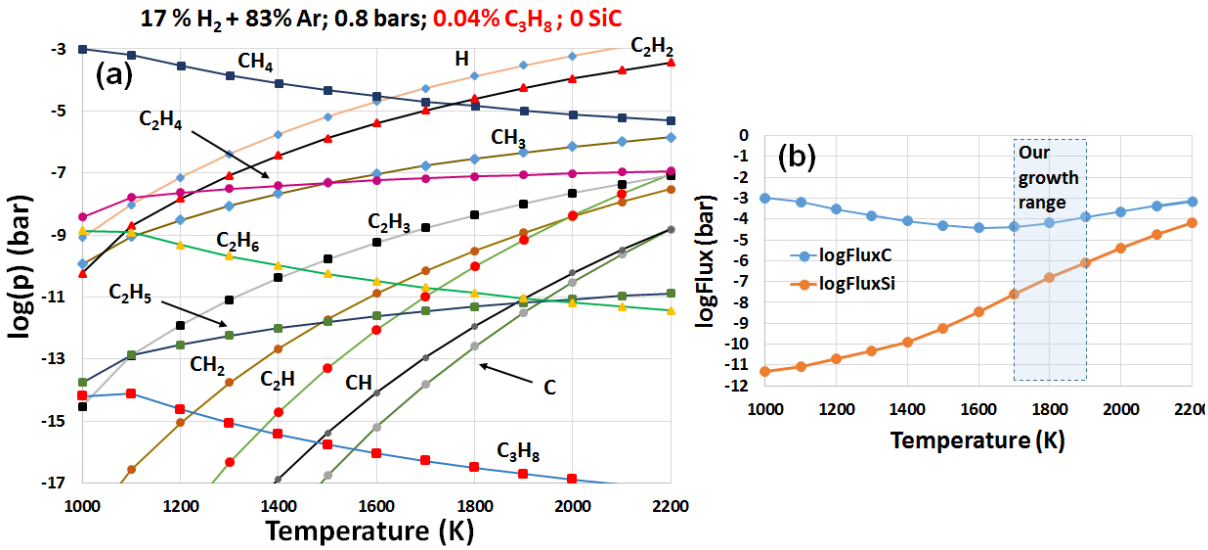

Figure 3. 8: (a) *Partial pressure of C-gases from the decomposition of C_3H_8 in a H_2-Ar-C_3H_8 system (without SiC(s)).* ***(b)*** *FluxC and FluxSi as a function of the temperature in the H_2-Ar-SiC-C_3H_8 system under 17% H_2.*

We also show in Fig. 3.8(b) the **FluxC** and **FluxSi** parameters, which reveal a higher vapor pressure for the carbon-curve compared to the Si-curve in the whole temperature range. The two curves never cross, yet this does not mean that we will have a silicon residue, because as we have proven previously that when adding propane to the gas mixture the formation of C-H species by etching decreases. Therefore, the substrate is releasing less CH_4 to create the material loss required to form a silicon-rich surface. We can also notice the decrease in substrate etching in this same graph (Fig. 3.8(b)) since the **FluxSi** curve is at lower pressures compared to the previous case. At some point, the atmosphere can be saturated with carbon from the propane leading to a carbon deposition, which will result in graphene formation. To conclude, it is possible to say that when

adding propane to the gas mixture, we are able to reduce and inhibit completely the formation of C-H species generated by SiC etching, but at the same time the SiC etching is still present, resulting in Si-H, Si-C and Si-C-H gases with lower vapor pressures than in the case of H_2-Ar annealing without propane.

As a conclusion for this part, we can deduce from the thermodynamic analysis that annealing SiC under H_2 or H_2 + Ar will etch the SiC substrate, which will release carbon- and silicon-based molecules consisting of C-H and Si-H bonds. Over 60 species can be created, mostly carbon-based molecules with vapor pressures much more important than those for silicon-gases at low temperatures, depending on the amount of H_2. This difference rises from the significant formation of CH_4, leading to silicon condensation at the right conditions. However, increasing the temperature will reduce this vapor pressure difference, and prevent any silicon residue from forming. Adding propane to the calculations increases the carbon-gases vapor pressures due to the propane's thermal decomposition and at the same time decreases the etching of the substrate into Si-based species while inhibiting completely the formation of C_i (i = 1 to 5) and C-H species by SiC etching. This will reduce the risk of having condensed silicon droplets. The extra carbon in the gas phase may condensate at some point to form graphene.

3.1.3.2. Argon atmosphere

We have studied so far the annealing of SiC under an H_2-Ar atmosphere with and without propane. The case with propane corresponds to the CVD growth of graphene on SiC. We show now another simulation with FactSage of the annealing of SiC under a pure argon atmosphere, which is also employed to grow graphene by thermally decomposing the SiC substrate, known as the Si sublimation technique. For these thermodynamic calculations, no propane was added nor hydrogen, but only 10 000 moles of argon with 100 moles of solid SiC. The temperature was varied between 1000 and 2500 K, and the total pressure set at 0.8 bars.

We present in Fig. 3.9, the vapor pressures of the created gases from the thermal decomposition of SiC under argon. 19 species are created, either Si-gases, C-gases or Si-C gases. The vapor pressures of all the gases are increasing with the temperature, confirming the increase of the thermal decomposition of SiC for higher temperatures. As we notice, the Si-gases have vapor pressures higher than the C-gases for the whole temperature range. The Si(g) remains dominant with a vapor pressure at least 10 000 times more important than any of the C_i-gases (i = 1 to 5). Other species appear at high vapor pressures with Si-C bonds such as Si_2C, SiC_2, Si_2C_2 etc… but they have vapor pressures below that of Si(g) and higher than the Ci-gases. These important differences in vapor pressure are what makes the growth of graphene by Si sublimation possible: by thermally decomposing SiC, we are evaporating more Si-species than C-species, which will lead to an excess of carbon at the surface of the substrate and form graphene under the right conditions.

We also show in Fig. 3.10, **FluxC**, **FluxSi** and the partial pressure of Si(g) as a function of the temperature. **FluxC** is the sum of all the partial pressures of the gases containing carbon such as the C_i-gases (i = 1 to 5), SiC(g), SiC_2, Si_2C_2 etc… Whereas **FluxSi** is the sum of all the partial

pressures of the gases containing silicon such as the Si_j-gases (j = 1 to 6), SiC_2, Si_2C_2, Si_3C_2 etc… As we can see in Fig. 3.10, **FluxSi** remains dominant throughout the whole temperature range. In fact, it depends on the partial pressure of Si(g), which is aligned with FluxSi between 1000 K and 2300 K where the partial pressures of other gases becomes important. This figure confirms our previous deduction that the SiC is decomposing into Si-species more than C-species.

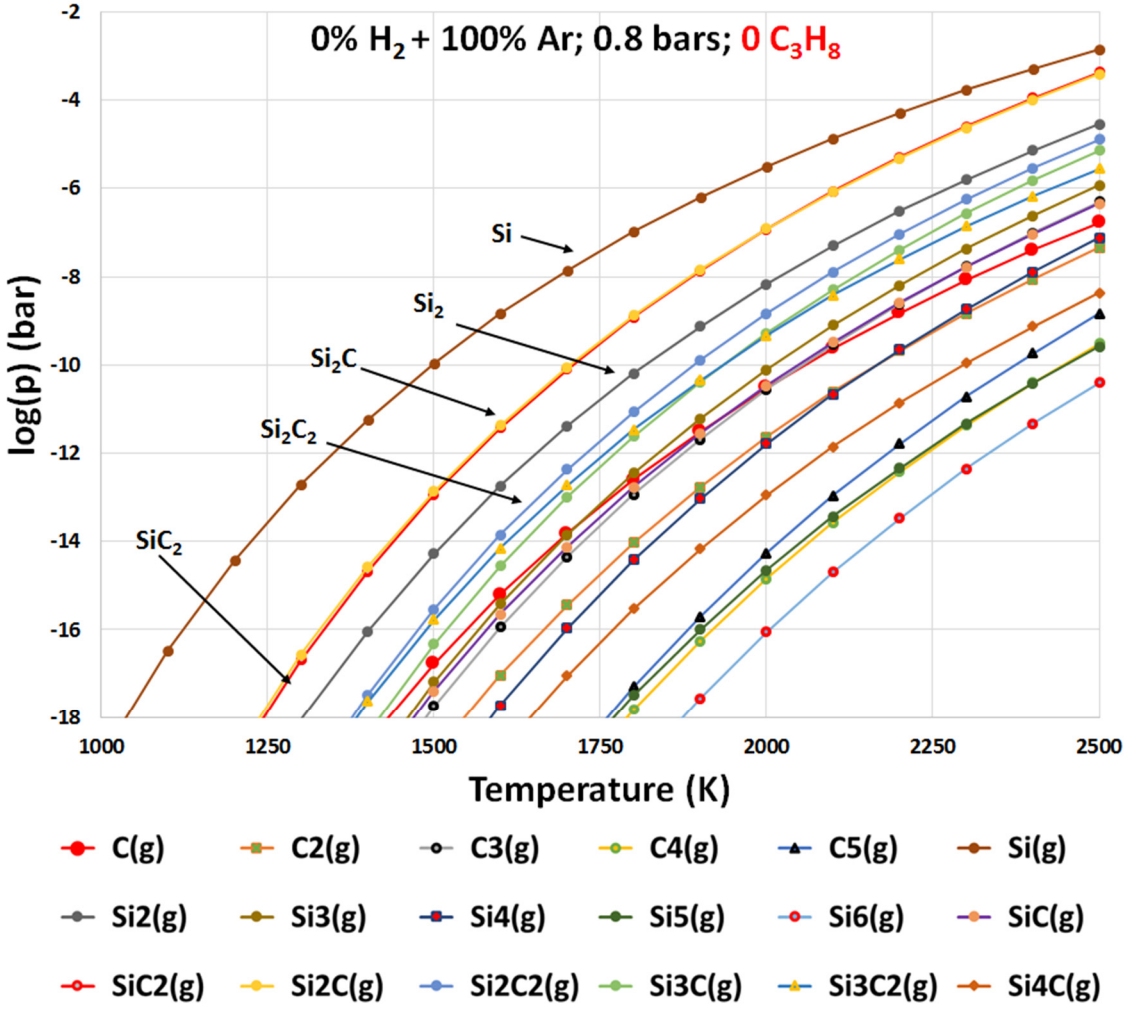

Figure 3. 9: *Partial pressure of the C- and Si-gaseous species as a function of the temperature produced by the thermal decomposition of SiC(s) under argon atmosphere.*

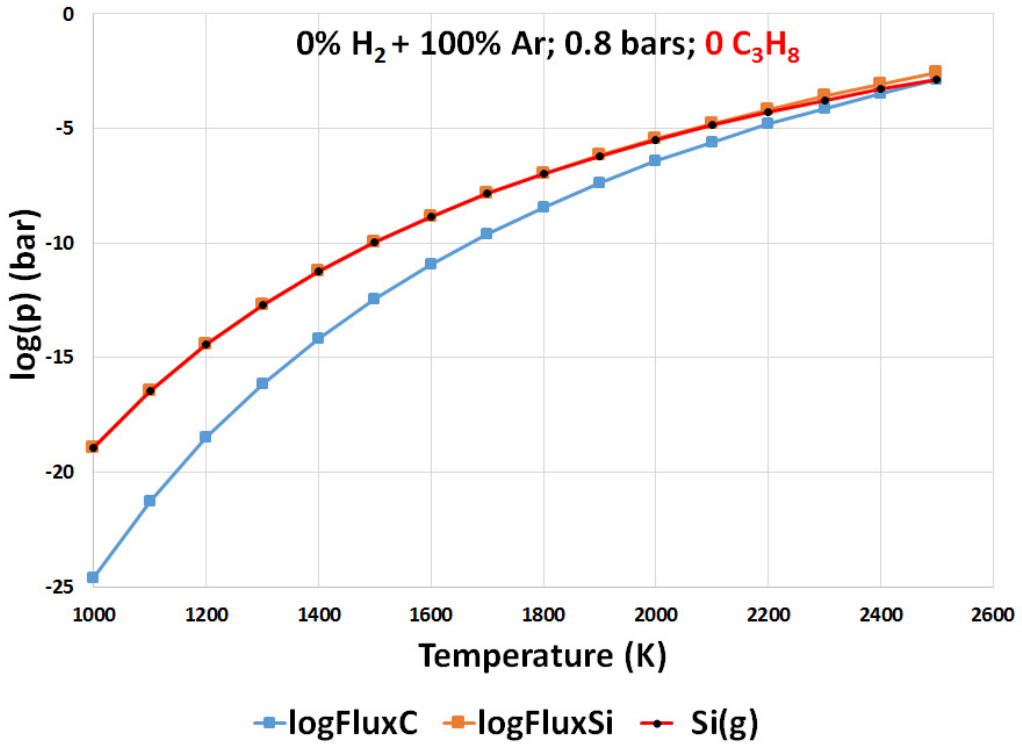

***Figure 3. 10: FluxC** and **FluxSi** and the partial pressure of Si(g) and as a function of the temperature in the Ar-SiC system.*

3.1.4. Discussion and conclusion

In a first part, we have demonstrated experimentally on the basis of XPS and AFM that graphene cannot grow from the SiC substrate when this latter is being annealed under hydrogen or hydrogen-argon. We attempted to grow graphene with different amounts of hydrogen in the gas mixture, two temperatures of 1450 and 1550°C and annealing times between 5 and 15 minutes, but the corresponding XPS C1s core-level showed no signs of a graphitic deposition. The absence of the graphene formation is not related to the growth time nor the temperature, but it is due to the presence of hydrogen, which changes the thermodynamics of the growth, preventing the graphitization of SiC. Unless we add propane to the H_2, no graphene will be deposited, in contrast to the Si sublimation technique that does not require propane.

The Si sublimation from SiC under argon (or UHV) is a completely different thermodynamic system. Under the effect of the temperature, SiC will decompose into silicon-containing gases and carbon-containing gases. However, the silicon gases have a higher vapor pressure than carbon gases, especially Si(g) which is dominant in the gas phase, having a vapor pressure 10 000 times more important than C-gases (without C-Si bonds). Even when increasing the sublimation temperature, all the vapor pressures increase but the Si(g) remains dominant. This

means that the sublimation of silicon from SiC is much more important than the sublimation of carbon, leading to an excess of carbon at the surface of SiC, which under the right conditions will form graphene. In this work, we were able to sublimate silicon and graphitize the SiC substrate by modifying our usual growth conditions, i.e. by decreasing the pressure to 100 mbars and increasing the temperature and the annealing time to 1600°C and 10 minutes respectively.

Adding hydrogen to the gas mixture changes the thermodynamic system, since H_2 etches the SiC and creates new species with C-H and Si-H bonds, species that did not exist in the previous system under argon only. With the help of FactSage, we were able to find all the released gaseous species at equilibrium and calculate their vapor pressures. First calculations without any propane have shown that indeed the carbon-based gases have higher vapor pressures than the silicon-based gases, especially CH_4, which is dominating almost through all the temperature range reaching 2200 K. The difference in vapor pressures induces a contrary effect than in the previous system by creating an excess of silicon at the surface of the substrate rather than an excess of carbon. Indeed, a study has shown that silicon droplets will form under the right conditions when exposing SiC to H_2 at high temperatures [171]. To avoid the formation of silicon droplets, Neyret et al. [171] suggested to add propane to the gas mixture, which will saturate the atmosphere with carbon and reduce the formation of CH_4 from SiC etching, therefore reducing the large difference in vapor pressure between the C-species and the Si-species.

We were able to confirm this behavior by doing calculations with propane in the gas phase. Adding propane to the H_2-Ar mixture raises the total vapor pressure of the carbon-species since propane also decomposes into carbon-gases, mostly into CH_4 and C_2H_2. For clarity we will note these gases as C-H(propane), i.e. coming from the decomposition of propane. At the same time, adding propane reduces the SiC etching: by reducing the formation of the Si-species and by completely inhibiting the formation of C_i (i = 1 to 5) and C-H species coming from the substrate, which we will refer to as C-H(substrate). Therefore, the C_i and C-H species in the gas phase are only emanating from the decomposition of propane and not from the substrate. We can then deduce that in the H_2-Ar-C_3H_8-SiC system the main source for the graphene growth is the propane. The SiC etching into Si-H species can also be a contributor to the growth, only in the case with propane. In fact, propane will inhibit the formation of the C-H(substrate) species, but the Si-based species will continue to form, which can lead to some kind of carbon residue at the surface, since the Si and Si-H gases have vapor pressures higher than the other species emanating from the substrate. Hence, we deduce that in the presence of propane two factors contribute to the growth, the thermal decomposition of propane and the SiC etching into Si-based species. However, it is difficult to quantify the Si-H contribution, since the propane is the major source of carbon. In the absence of propane, the SiC etching will produce C-H(substrate) species a lot more than the Si-species, preventing any carbon excess from occurring at the surface. We summarize the different thermodynamic systems in table 3.1.

Finally, it is important to go beyond pure thermodynamic calculations: even though propane decomposes mostly into CH_4, yet this gas is less likely to be the main source of carbon

for graphene. In fact, the surface reactivity of CH_4 is very low compared to the other gases, with a reactive sticking coefficient (or sticking probability) in the order of 10^{-5} while C_2H_4 and C_2H_2 have sticking probabilities 100 times more important [177,178]. Other gases such as CH_2 and CH_3 are even more reactive with sticking coefficients higher than 0.1 [177,178]. As a consequence, even though some gases such as CH_3 are not dominant in the gas phase, they still participate in the deposition due to their high sticking coefficient. It is also important to be aware of the limitations of our calculation model since there are different parameters that we cannot take into consideration, such as the growth kinetics, the continuous flow of gases (H_2, Ar and C_3H_8) and the contamination from the reactor's walls, which may introduce other species.

To summarize, annealing SiC under H_2 is not likely to produce graphene in contrast to the annealing under argon. We were able to demonstrate this experimentally and prove theoretically with thermodynamic calculations that talking about Si sublimation under hydrogen is irrelevant. The main reason behind this is the high vapor pressure of the carbon-gases created upon etching of SiC by H_2. Therefore, propane is essential to grow graphene on SiC in a hydrogen atmosphere. The etching of the substrate can also be a source of carbon in the presence of propane, but since propane reduces the etching it is difficult to evaluate the magnitude of this effect.

Table 3. 1: *Summary of the outcomes of the different thermodynamic systems with solid SiC.*

Gas mixture	Partial pressures	Outcome	Graphene?
17% H_2 + 83% Ar + 0% C_3H_8	FluxC > FluxSi	Possibly silicon residue from SiC substrate etching	Not likely
17% H_2 + 83% Ar + 0.04% C_3H_8	FluxC > FluxSi	Carbon deposition from propane decomposition	Probably
0% H_2 + 100% Ar + 0% C_3H_8	FluxSi > FluxC	Carbon residue from SiC substrate decomposition	Probably

3.2. Influence of the growth parameters

In this part, we have studied the effects of the different growth parameters in order to understand the growth mechanisms to be able to prepare state-of-the-art graphene on SiC. Therefore, it is preferable to go through the different growth parameters to evaluate their influence on the growth and on the graphene characteristics. In this part we explore different growth parameters, such as the growth time, the propane flow, the hydrogen percentage in the gas mixture, the growth temperature and other parameters which could influence the graphene properties such as the substrate's miscut angle (or offcut).

3.2.1. Growth time and propane flow rate

Growth time variation:

We now discuss the effects of the growth time and the propane flow rate on the growth. For the growth time study, the SiC substrates were from Xiamen and usually have miscut angles around 0.4°. Fig. 3.11 displays AFM images for different growth times carried out at 1550°C and 17% of H_2. We can see in Fig. 3.11(a, b) and in the inset of Fig. 3.11(a) for 1.25, 2.5 and 5 minutes of growth that the morphology is very similar, presenting straight steps with rough edges. In Fig. 3.11(c) for 10 minutes of growth, the terraces become a bit wider as some irregular step-bunching occurs. And finally Fig. 3.11(d) for 20 minutes of growth, we can still see that the SiC steps and the terraces seem smaller and increased in number along with rough edges indicated by

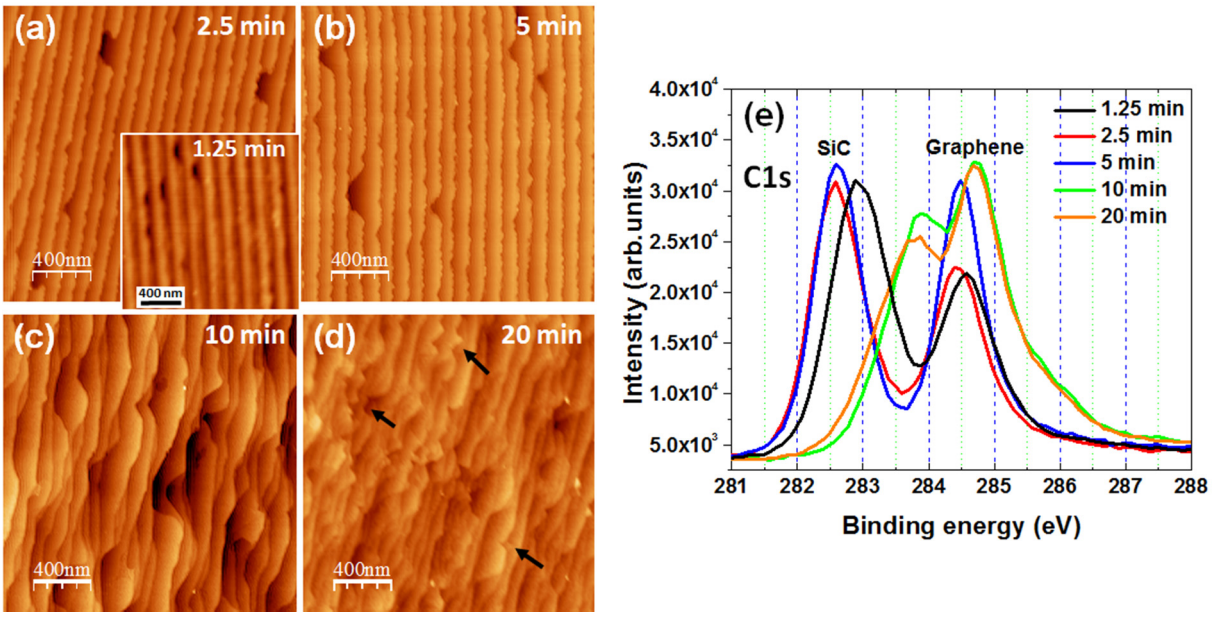

Figure 3. 11: *2×2 µm² AFM images of graphene grown with 17% of H_2 at 1550°C for different growth times:* ***(a)*** *2.5 min,* ***(b)*** *5 min,* ***(c)*** *10 min,* ***(d)*** *20 min. AFM z-scale is 5 nm. Inset of* ***(a)*** *is the 1.25 min-growth (z-scale: 2 nm)* ***(e)*** *Corresponding C1s core-level spectra for the different samples.*

arrows. Surprisingly, the roughness is more or less the same for the different growths (RMS around 0.4 nm), while steps remain around 1.5 nm-high, except for the 10 minutes growth were some steps are 2 nm-high.

All samples present a graphene peak in the corresponding C1s core-level spectrum in Fig. 3.11(e) around 284.5 eV, even for 1.25 minutes of growth i.e. 75 seconds. We did not shift the peaks nor normalize the spectra, since interesting observations can be made in the untreated spectra. Analyzing the integrated peak's intensities allows us to calculate the number of graphene layers [79]. To estimate the number of graphene monolayers (MLs) we have fitted the SiC and graphene peaks of the set presented in Fig. 3.11, then using equation (2.3) from **part 2.3.3 XPS** we calculated the number of deposited layers, presented in table 3.2. For reasons of simplicity we have considered the buffer layer peaks within the graphene peak, but it can be corrected by subtracting the thickness of the buffer layer from the calculated thickness. We estimated an error value around 0.2 MLs from the choice of the graphene lattice parameter and the buffer layer thickness (2 Å as measured with TEM [110] or equal to the distance between two graphene layers i.e. 3.3 Å). However, from our experience by comparing thickness values with Raman data we suspect a larger error of 0.4 MLs and more for thicker depositions.

Table 3. 2: Calculated number of layers as a function of the growth time

Growth time (min)	Number of layers (MLs)
1.25	1.6
2.5	1.9
5	2.4
10	4.8
20	5.3

The number of layers is between 1 and 2 for the growth times 1.25 and 2.5 minutes. We attribute the extra layers to patches of bilayers at step edges or between two steps. The number of layers increases to 4.8 for 10 minutes and 5.3 for 20 minutes of growth. What is interesting is that for 1.25 minutes we already have a monolayer of graphene. These calculations are in agreement with Fig. 3.11(e), where we notice an increase in the intensity of the graphene peak when increasing the growth time: a noticeable increase is detected between the growth of 2.5 and 5 minutes, then a small increase is added for the 10 and 20 min-growth. However, it is strange that the graphene peak of the 20 min-growth is not more intense than that of the 10 min-growth, especially since the SiC peak of the 20-min growth is more attenuated than that of the 10 min-growth. In addition, in the AFM image of the 20 min-growth in Fig. 3.11(d), the steps seem narrower and more compact compared to Fig. 3.11(c) for 10 minutes, possibly due to overgrowth

taking place between steps. Therefore, we cannot rule out that there is more graphene for the 20 min-growth, but regarding the graphene peak intensity, it remains unclear why it is as intense as the 10 min-growth graphene peak.

Now concerning the peak's positions, the SiC peak of the 2.5- and 5-min growth are aligned at 282.6 eV, but the peak of the 1.25 min-growth is slightly upshifted towards higher binding energy. For the 10 and 20 min-growth, the SiC peak is shifted to 283.9 eV, i.e. 1.3 eV more compared to the 2.5 and 5 min-growth. The corresponding graphene peak is also shifted to 284.7 eV, i.e. a shift of 0.2 eV compared to the 2.5- and 5-min growth. We suspect that this shift is related to the thickness of the deposited graphene as Emtsev et al. have suggested in their work in reference [105]. Emtsev et al. have demonstrated on the basis of XPS and ARPES that when the deposited graphene thickness increases the graphene peak shifts towards higher binding energies. The reason rises from charge transfer from the substrate to the graphene layer when a buffer layer is present. However, they argue that these charges remain close to the interface, resulting in less charge transfer to the topmost graphene layer when the thickness is increasing. Therefore, the XPS will be probing a more neutral graphene layer. This explains the upshift of the green and orange peaks in Fig. 3.11(e), which correspond to the 10 and 20 minutes of growth respectively. Regarding the upshift of the 1.25 min-sample, it can be due to the presence of incomplete graphene layers for such a short growth time, even if the surface resembles a lot that of the 2.5 min-growth, see Fig. 3.11(a) and its inset. Although we calculate 1.6 MLs for 1.25 minutes, the XPS spot diameter is 400 microns, which means that we cannot rule out the presence of incomplete layers, hence a less conductive sample leading to the upshift in binding energy.

To better visualize the evolution of the deposited thickness as a function of the growth time, we show in Fig. 3.12 the sp^2/sp^3 intensity ratios of the different growths i.e. the maximum intensity ratio of the graphene peak to that of the SiC peak. We also illustrate the estimated number of layers as a function of the growth time, previously presented in table 3.2. We can see in Fig. 3.12(a) three sets grown at 1550°C, 800 mbars, 17% of H_2 and 5 sccm of propane, on three different substrates. The red curves correspond to the set of samples we have discussed so far. The three sets show similar trends, the increase in the growth duration induces an increase in the deposited thickness, except between the 10- and the 20-min growth were the thickness seems stable. We show in Fig. 3.12(b) two other time sets, grown in the same growth conditions as before but at 1450°C and 100% H_2 for the orange curve. In this case, the intensity ratio reaches higher values compared to the previous sets. On the other hand, we notice that all the 17% H_2 curves increase with a small slope, whereas the 100% H_2 curve is straighter, reflecting a more dependent relation between the growth time and the thickness. Hence, we can deduce that the 100% H_2 conditions allow to achieve a thicker deposition and a better control of the thickness with the growth time. One possible explanation for this behavior can be related to the etching contribution to the growth, which is more important in the case of the 100% of H_2. In this latter case, increasing the growth duration is associated with an increase in the etching contribution, not to mention the contribution of the decomposition of propane, leading to a linear evolution between the deposited

thickness and the growth time. On the other hand, in the case of the 17% H_2-growth, the H_2 etching contribution to the growth is less important and probably minimal. In addition, the presence of propane in the gas mixture reduces the etching contribution, based on our previous thermodynamic calculations. To this end, we can consider a certain equilibrium between the propane contribution

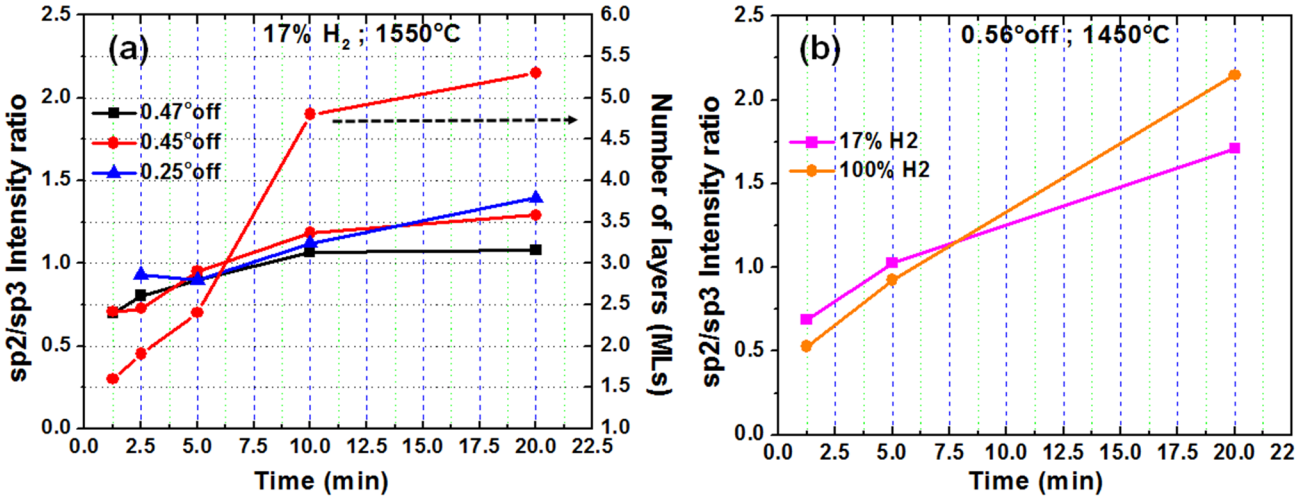

Figure 3. 12: *sp^2/sp^3 intensity ratio for different sets and different conditions of hydrogen and temperature:* ***(a)*** *17% H_2 at 1550°C.* ***(b)*** *Same substrate at 1450°C but two growths under 17 and 100% of H_2.*

and the etching contribution, which can explain the less linear evolution in the case of the 17% H_2 growth.

To conclude, we can say on the basis of XPS data that the number of layers increases with the growth time, without affecting substantially the morphology of the surface, as we have seen with AFM. This increase in thickness is accompanied with a change in the sample's conductivity, due to less charge transfer from the substrate to the topmost graphene layer. In addition, we noticed that the growth at 1450°C possibly leads to thicker depositions. Also, the growth with 100% of H_2 seems to allow a better control of the deposited thickness compared to the growth under 17% of H_2, where the number of layers seems more stable or slowly varying with the time. We attributed these differences to the role of the SiC etching and its contribution to the growth, which is more important in the case of the 100% H_2-growth.

Propane flow rate variation:

We will now discuss the effects of the propane flow rate on the growth by considering different growth sets at 1450 and 1550°C. The first set was prepared on 0.15°-off SiC substrates, under 17% H_2 and 5 sccm of propane at 1550°C and 800 mbars, for 5 minutes. The corresponding AFM images are displayed in Fig. 3.13(a-d) for propane flows of 0.5, 2.5, 10 and 40 sccm. Apart the remnants of polishing scratch in Fig. 3.13(a) and (d), no particular changes in the morphology are detected; we only notice that the step terraces for 0.5 sccm (Fig. 3.13(a)) seem to be the largest

among the other samples. The corresponding C1s core-level spectra are presented in Fig. 3.13(e) for the growths between 0 sccm and 40 sccm of propane. All spectra reveal a graphene peak with a changing intensity, except for the 0 sccm-spectrum where we only detect the SiC peak at 283.9 eV and a small bump at 286 eV, attributed to carbon contamination. Adding 0.5 sccm of propane to the growth results in the manifestation of a graphene peak at 284.9 eV and a shift of the whole spectrum to lower binding energies compared to the 0 sccm-spectrum. Increasing the propane flow rate led to an increase in the graphene peak intensity and a down shift of the spectra to lower binding energies. We attribute the downshift to an increase in the sample's conductivity associated with the deposition of graphene. However, adding 20 and 40 sccm of propane induces an important upshift associated with the increase in the number of layers. We also notice for these last two curves that the SiC peak intensity decreases a bit while the graphene peak intensity increases even more, which confirms the more important deposition.

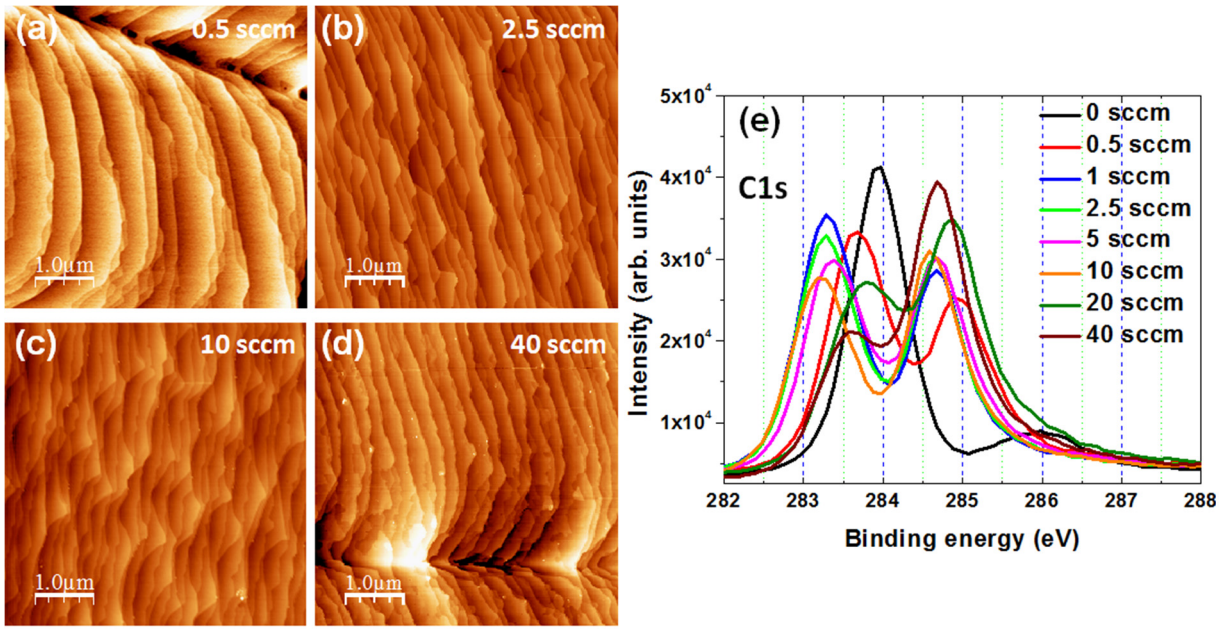

Figure 3. 13: *5×5 µm² AFM images of graphene grown with 17% of H_2 at 1550°C for different propane flows:* ***(a)*** *0.5 sccm,* ***(b)*** *2.5 sccm,* ***(c)*** *10 sccm,* ***(d)*** *40 sccm. AFM z-scale is 3 nm.* ***(e)*** *Corresponding C1s core-level spectra for the different samples.*

The second set is prepared with 100% of H_2 at 1450°C while the other growth parameters are kept the same. Similarly to before, we present AFM images and XPS measurements in Fig. 3.14. The AFM images reveal a change in morphology when increasing the propane flow. In Fig. 3.14(a) for 5 sccm of propane we can see clearly the steps covered with wrinkles in contrast to the growth with 2.5 sccm of propane (figure in inset of Fig. 3.14(a)), where only straight steps appear. When increasing the propane flow rate to 10 sccm (Fig. 3.14(b)), irregular shapes start to appear across the steps. The same observation can be made for 20 sccm (Fig. 3.14(c)) and 40 sccm (Fig. 3.14(d)): irregular patterns appear with brighter areas indicated by black arrows, along with smaller wrinkles. All these observations suggest a more important deposition for higher propane

flow rates. Indeed, XPS measurements (Fig. 3.14(e)) reveal an increase in the graphene peak intensity with the propane flow rate. Interestingly, the spectra which exhibit a graphene peak are aligned together at lower binding energies compared to the spectra without any signs of graphene (for 0 and 2.5 sccm). In this case, even though the increase in the deposited thickness with the propane is clear, the spectra remain aligned together which is the opposite of the previous observations. However, for this propane set the growth was carried out under 100% H_2, which usually leads to a hydrogenated interface and no shared bonds with the first graphene layer and the substrate. For this reason, we presume that no or little charge transfer occur from the substrate to the graphene layers, hence little charge difference will occur between the bottom and top graphene layer for important depositions. Therefore, the different samples with different graphene thicknesses are most likely to be similar in terms of conductivity and thus present aligned spectra in XPS.

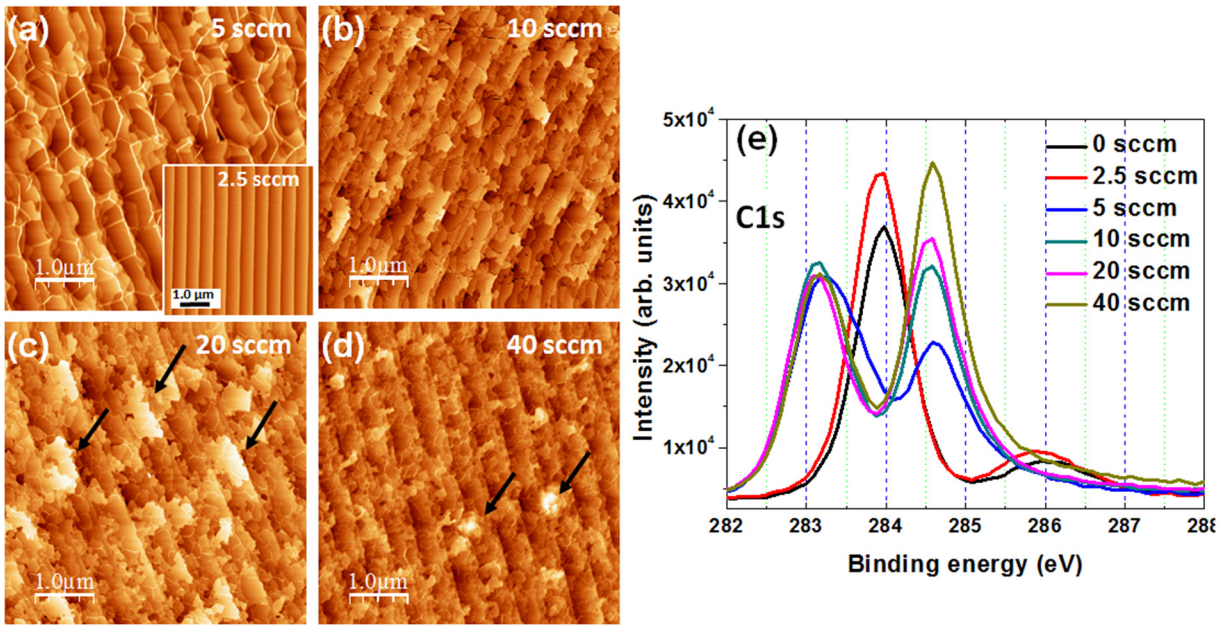

Figure 3. 14: *5×5 µm² AFM images of graphene grown with 100% of H_2 at 1450°C for different propane flow rates:* ***(a)*** *5 sccm,* ***(b)*** *10 sccm,* ***(c)*** *20 sccm,* ***(d)*** *40 sccm. AFM z-scale: 5 nm. Inset of* ***(a)*** *5 sccm of propane.* ***(e)*** *Corresponding C1s core-level spectra for the different samples.*

To evaluate the deposited thickness we show in Fig. 3.15(a) the sp^2/sp^3 intensity ratio as a function of the propane flow rate for the two sets and a third set carried out at 17% of H_2 at 1450°C. We can deduce from these curves and the previous observations that indeed increasing the propane flow rate increases the deposited thickness. For the growth under 17% of H_2 at 1550°C only 0.5 sccm of propane is enough to instigate a graphene deposition. In contrast, under 100% of H_2 at 1450°C, 5 sccm of propane is required to achieve graphene deposition. In fact, as we have demonstrated in the previous part with thermodynamic calculations, in the case of high hydrogen amount, the SiC etching by H_2 is prevailing, releasing mainly carbon-based species in the gas phase, but adding propane will reduce the etching. Therefore, a sufficient amount of propane is

required to decrease the etching and promote graphene growth. In this present case 5 sccm of propane is needed for the growth to take place. In addition, the set grown with 17% of H_2 at 1450°C shows a similar behavior as in Fig. 3.13(a-d). However, AFM images presented in Fig. 3.15(b, c) show areas of over deposition for the 40 sccm-growth (Fig. 3.15(c) compared to the 20 sccm-growth in Fig. 3.15(b)).

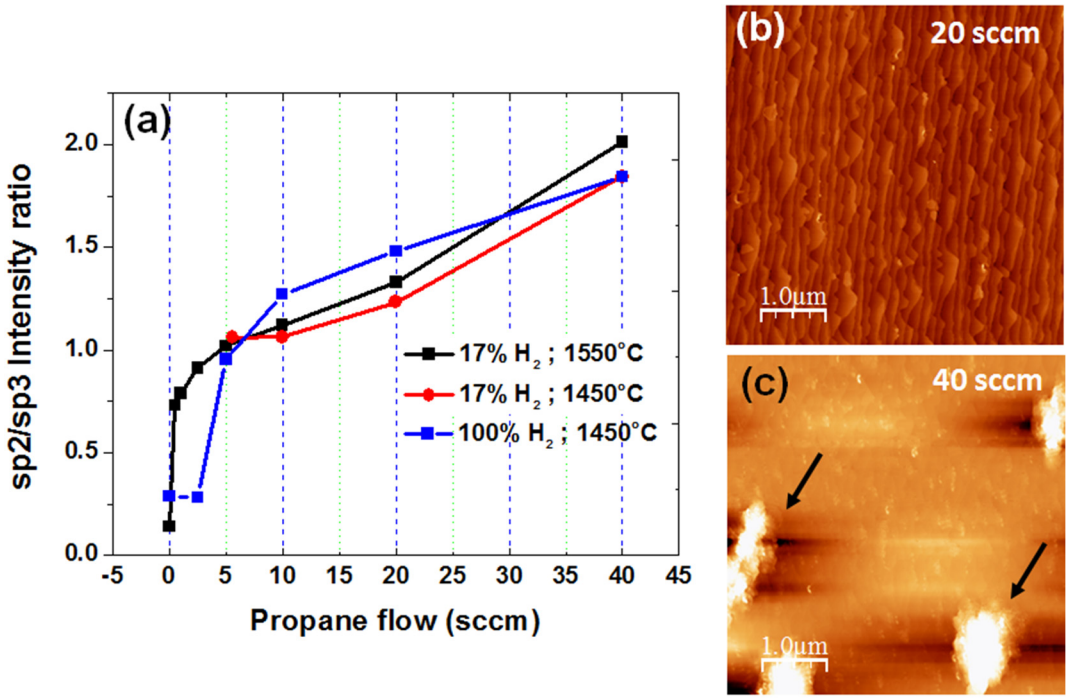

Figure 3. 15: (a) *sp^2/sp^3 intensity ratio for different sets and different conditions of H_2 and temperature.* ***(b)*** *and* ***(c)*** *5×5 µm² AFM images of the growth under 17% of H_2 at 1450°C.* ***(b)*** *20 sccm of propane, AFM z-scale: 3 nm.* ***(c)*** *40 sccm of propane, AFM z-scale: 20 nm.*

As a summary, we have demonstrated that the graphene thickness can be controlled with the growth time and the propane flow rate, based on AFM and XPS measurements. The ideal growth conditions, regarding the morphology, seem to be around 2.5 sccm of propane and 5 to 10 minutes for 17% of H_2 at 1550°C, whereas for 100% of H_2 5 sccm of propane is required with a growth time around 5 minutes at 1450°C. The growth under 17% of H_2 at 1450°C presents areas of over deposition for 40 sccm of propane, therefore a higher temperature seems to be necessary for a uniform growth when using important amounts of propane. In addition, we believe that the 100% H_2-growth allows a better control of the thickness when changing the growth time. In fact, we notice that in this latter case, the thickness seems more dependent on the growth time compared to the growth under 17% of H_2, where the deposition rate appears to be more or less stable or slightly increasing with the growth time. We also noticed an energy shift in XPS with the growth time and the propane flow rate for the growth under 17% of H_2. The samples grown with 20 and 40 sccm, or for 10 and 20 minutes seem to have the most upshifted peaks probably due the increase in the number of layers, which will result in a topmost graphene layer with less charge transfer

compared to the graphene layer close to the interface. On the other hand, the samples grown with 100% H_2 for different propane amounts present aligned peaks without any shift in the binding energy, which we attributed to comparable charge density in the different samples regardless of the graphene thickness. This is due to a minimum charge transfer from the substrate to the graphene layer because of the absence of bonds with the substrate and the presence of a hydrogenated interface under these hydrogen-rich conditions.

3.2.2. Growth temperature

It is important and necessary to understand the influence of the temperature on the graphene growth on SiC. In graphene growth by Si sublimation, the temperature plays a crucial role in controlling the uniformity of the growth and the thickness of the graphene layer [76,90,105]. It is thought that the growth is more uniform when the temperature is sufficiently high: around 1650°C in an argon atmosphere. In addition, some studies aim for higher temperatures reaching 2000°C, to obtain thicker graphene layers [90], but of course this depends on the experimental setup and its ability to support high temperatures. In CVD of graphene on SiC, it was also demonstrated that the growth temperature has a direct influence on the quality and morphology of the graphene layer [12,18,103]. In this part, we will discuss the influence of the growth temperature on the morphology, the number of layers and the structure of graphene grown on SiC by CVD.

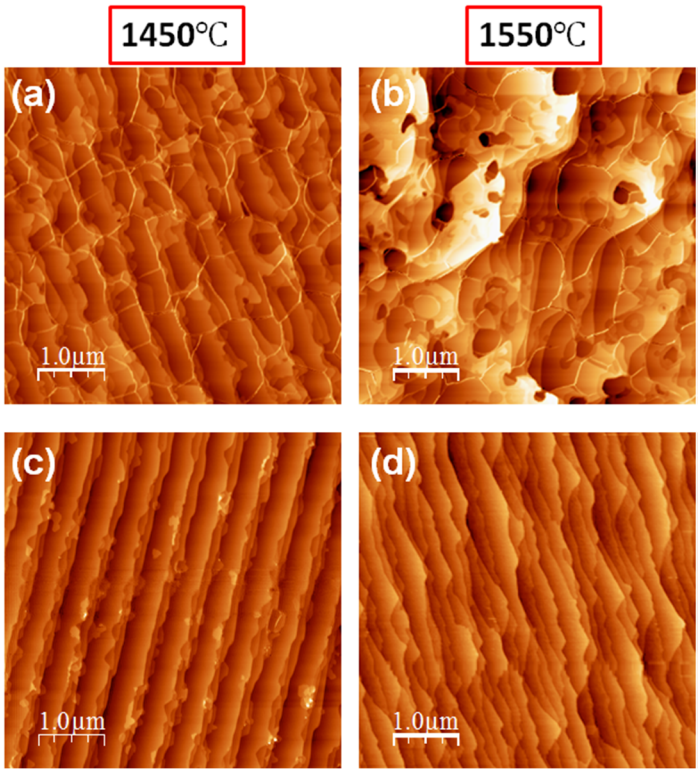

Figure 3. 16: *5×5 µm² AFM images of graphene grown with 100% of H_2 at* ***(a)*** *1450°C and* ***(b)*** *1550°C. AFM z-scale: 5 nm. 5×5 µm² AFM images of graphene grown with 17% of H_2 at* ***(c)*** *1450°C and* ***(d)*** *1550°C. AFM z-scale: 3 nm.*

In Fig. 3.16(a, b), we compare the growths at 1450 and 1550°C under 12 slm of H_2 (100% of H_2) at 800 mbars and 5 sccm of propane for 5 minutes. In Fig. 3.16(a) for the growth at 1450°C we can discern the SiC steps covered with wrinkled graphene. In contrast, in Fig. 3.16(b) for the growth at 1550°C, we still see the wrinkles and few steps, but we also see irregular shapes and etching pits. We attribute these etching pits to the high reactivity of H_2 with the substrate at this temperature. For this reason, it seems that the growth under 100% of H_2 should be carried out at 1450°C and not 1550°C to avoid any excessive etching of the SiC substrate or the graphene layer.

In Fig. 3.16(c, d), we show the growth under the same conditions but with less hydrogen in the gas mixture, i.e. 2 slm of H_2 + 10 slm of argon (17% of H_2). In Fig. 3.16(c), we can see straight steps of SiC with few crooked edges, along with narrower terraces growing between two adjacent larger ones. We can also see patches of brighter contrasts on terraces and step edges, with heights between 0.35 and 0.45 nm. These two observations can rise from the growth mechanism of graphene which can occur at step edges or/and between two adjacent terraces, and also possibly on the terrace. Therefore, we attribute the brighter patches to extra graphene layers or graphene islands. On the other hand, the surface looks more uniform in Fig. 3.16(d) since first we do not see any extra patches and second the terraces appear to be of the same width, with the exception of few larger terraces probably due to step-bunching under the effect of the higher temperature. Therefore, the higher growth temperature seems to accelerate the growth and promote a more uniform deposition in this case. The reason behind this can be due to the influence of the temperature on the diffusion of carbon atoms on the surface. Hence, the higher is the temperature, the higher is the chance of having uniform growth with identical terrace-width instead of graphene patches. To this end, we rarely grow graphene with 17% of H_2 at temperatures lower than 1450°C.

In a second part, we present the influence of the temperature on the deposited thickness in Fig. 3.17(a, b), estimated with Raman spectroscopy, for two H_2 amounts (17% and 100%). For each graph we present two substrates with different miscut angles. The growths are done at 800 mbars, 5 minutes of 5 sccm of propane. In Fig. 3.17(a) (for 17% of H_2) the number of layers is between 3 and 4 MLs at 1350°C, then it decreases when increasing the temperature to 1450°C and it remains stable between 1450 and 1550°C. On the contrary, in Fig. 3.17(b) we notice an opposite behavior since the number of layers is increasing with the temperature. However, this effect seems more evident on the 1°off substrate (black curve), whereas the other curve (red curve) is less dependent on the temperature. We will come back later to the effect of the substrate's miscut angle on the growth. For now, for a given offcut, we correlate the variation in the number of layers with the temperature to the H_2 etching of the substrate. As we previously discussed, the H_2 etching of the substrate can be a source of carbon which can contribute to the growth of graphene. In Fig. 3.17(a) the etching contribution is minimal since the amount of H_2 is only at 17%, and the main contributor to the growth in this case is propane. When increasing the temperature the propane will decompose even more (see Fig. 3.8(a)), which will reduce the substrate etching contribution to the growth (based on our previous thermodynamic calculations). This phenomenon also occurs for the 100% H_2-growth in Fig. 3.17(b), but the etching in this case is significant

enough to compensate the effects of the propane. In this case, when increasing the temperature under 100% of H_2, the etching will rise and therefore will increase its contribution to the growth along with the number of deposited layers.

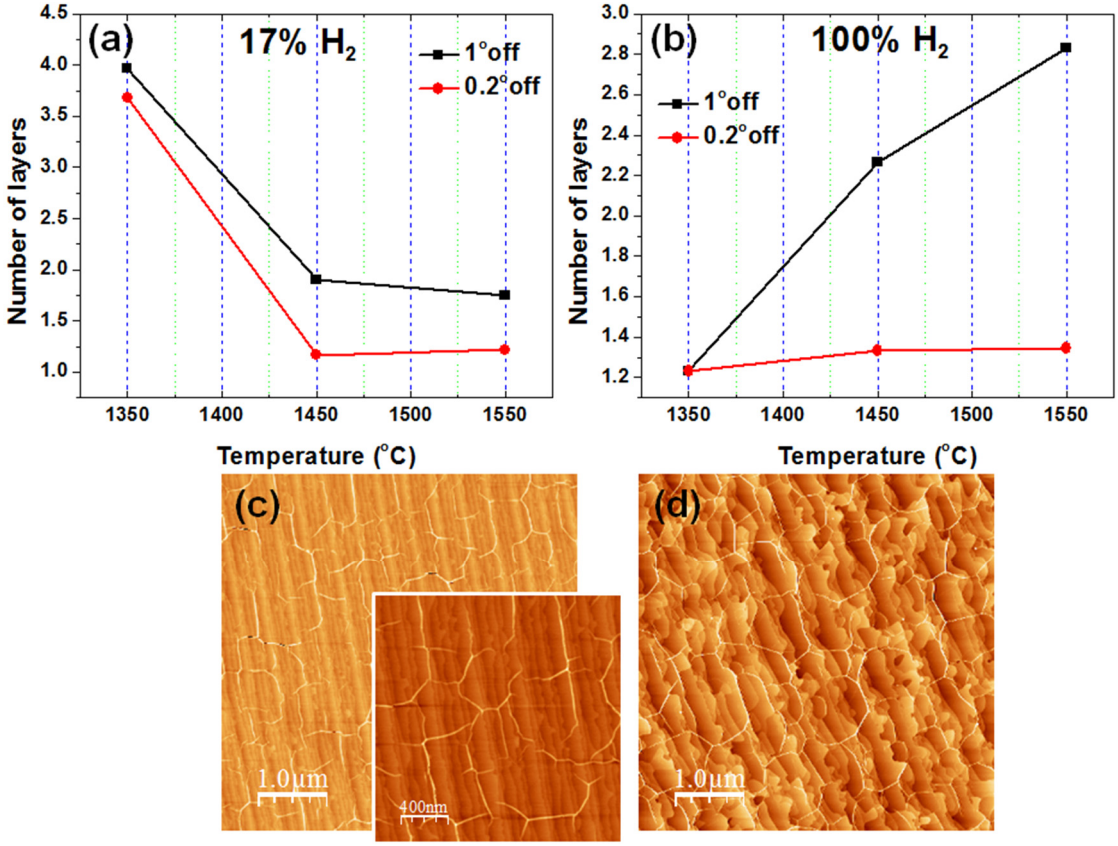

***Figure 3. 17: (a)** and **(b)** Estimated number of layers, calculated with Raman spectroscopy, as a function of the temperature for two different H_2 amounts: **(a)** 17% of H_2 and **(d)** 100% of H_2. **(c)** and **(d)** 5×5 µm² AFM images of graphene grown with 100% of H_2 at **(c)** 1350°C and **(d)** 1450°C. AFM z-scale: 3 nm. Figure in the inset of **(c)** is a 2×2 µm² AFM image.*

We show for comparison in Fig. 3.17(c, d), the growth under 100% of H_2 at 1350°C (Fig. 3.17(c)) and at 1450°C (Fig. 3.17(d)). The two morphologies are alike, with the exception of larger terraces at 1450°C, probably due to the higher growth temperature, which promotes step-bunching. We did not present the 1350°C-growth in Fig. 3.16 because it is a different substrate.

To conclude this part, we have shown that with 100% of H_2 it is better to grow graphene at 1450°C rather than 1550°C to avoid any etching effects on the morphology. In contrast, with 17% of H_2, a higher growth temperature is required to obtain a uniform graphene deposition with complete layers and no small graphene patches or islands. We correlate this behavior to the influence of the temperature on the growth mechanism of graphene and on the diffusion of carbon atoms at the surface. We also discussed the influence of the temperature on the number of graphene layers. The latter decreases when the temperature is increased under 17% of H_2 due to the decrease

of the etching contribution upon propane decomposition. In contrast, the etching contribution remains dominant while the temperature is increased under 100% of H_2, leading to an increase in the deposited number of graphene layers.

In a third part, we will show the influence of the growth temperature on the graphene morphology and structure. We present in Fig. 3.18 three growths under 33% of H_2, 800 mbars, and 5 minutes of 5 sccm of propane. In Fig. 3.18(a), for graphene grown at 1350°C, we can detect some wrinkles all over the surface with the manifestation of few irregular shapes which we attribute to incomplete graphene layers. The corresponding LEED pattern in Fig. 3.18(d) exhibits elongated rings, indicated by red arrows, suggesting the presence of IRD. The growth at 1450°C Fig. 3.18(b) seems more uniform with a complete coverage of wrinkles all over the surface. The corresponding LEED pattern in Fig. 3.18(e) also shows the manifestation of elongated rings and therefore IRD. On the other hand, the growth at 1550°C in Fig. 3.18(c) shows no signs of wrinkles at the surface and no signs of IRD in the corresponding LEED pattern in Fig. 3.18(f), but instead we can detect some diffraction spots of the $(6\sqrt{3}\times6\sqrt{3})$ surface reconstruction indicated by blue circles. We presume that these observations are related to the presence of hydrogen at the interface and the influence of the temperature on the hydrogen intercalation. In fact, some studies have shown that annealing a graphene sample under H_2 will lead to the intercalation of hydrogen at the interface [84,86]. However, few studies [86,111] have demonstrated that this effect is reversible under a sufficiently high temperature annealing. We think that a similar effect can happen when

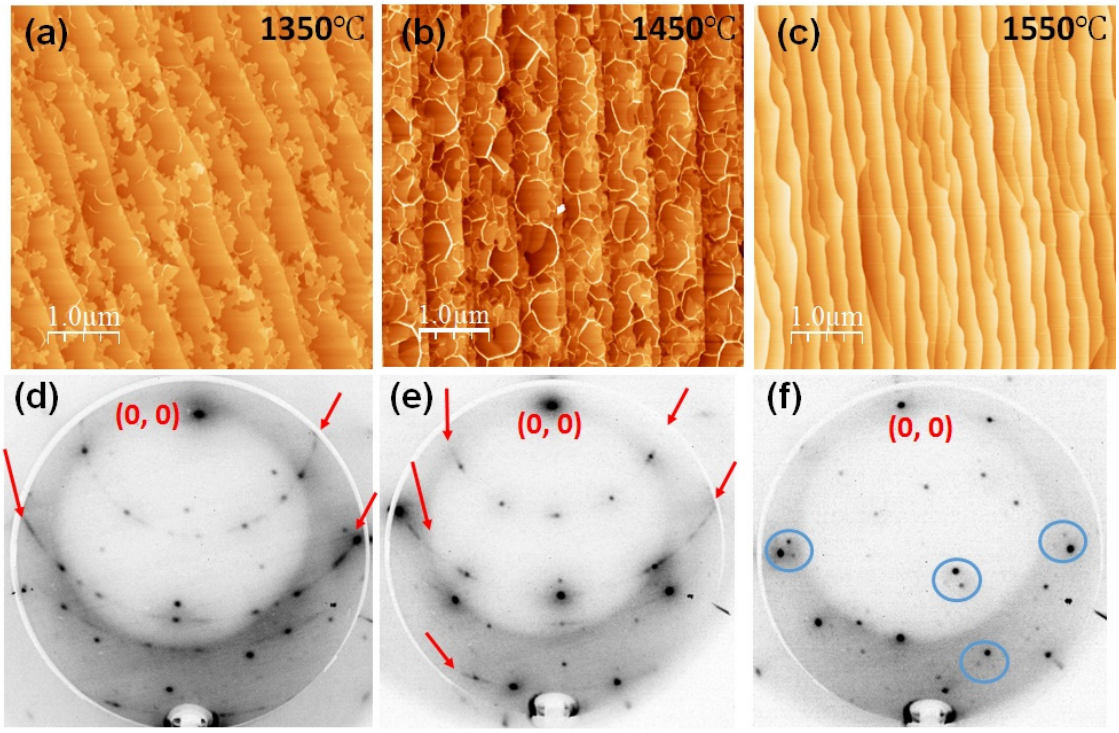

Figure 3. 18: *5×5 µm² AFM images of graphene grown with 33% of H_2 at* ***(a)*** *1350°C,* ***(b)*** *1450°C and* ***(c)*** *1550°C. AFM z-scale is 3 nm.* ***(d)*** *to* ***(f)*** *The corresponding LEED images taken at an electron energy of 140 eV.*

changing the growth temperature in our growth conditions. At 1350 and 1450°C, hydrogen is expected to be bonding with silicon atoms of the substrate, whereas at 1550°C, even if hydrogen can bond with the silicon atoms during the temperature ramp, it is very likely that these bonds will break and release hydrogen at 1550°C. Therefore, to achieve an important hydrogenation of the interface at this temperature more hydrogen is required, at least more than 33%. Regarding the structure observed with LEED and the differences in AFM, graphene appears to be disordered and wrinkled when the H-Si bonds are supposed to exist. In contrast, graphene seems to be associated with a ($6\sqrt{3}\times6\sqrt{3}$) surface reconstruction when the substrate is expected to be sharing bonds with the first carbon layer. These observations are related to the hydrogenation of the interface but will not be discussed here as they are the main subject of the next paragraph where we will discuss in details this matter based on AFM, LEED, Raman spectroscopy and XPS measurements.

For now, we conclude that 33% of H_2 are enough to hydrogenate the interface at 1350 and 1450°C, manifested by wrinkles and IRD detected with AFM and LEED respectively. In contrast, the same amount of H_2 is not enough to hydrogenate the interface at 1550°C since no wrinkles nor IRD were detected in AFM and LEED, but instead we detected the $6\sqrt{3}$ structure. We cannot rule out the possibility of hydrogen bonding with silicon under the temperature ramp, but at 1550°C there is a big chance that these bonds will break and release the hydrogen. We believe that to achieve a significant hydrogenation at this temperature more hydrogen is required.

3.2.3. Hydrogen amount in the gas mixture

3.2.3.1. First observations

In **chapter 2** we have presented two different growth conditions for graphene on SiC (0001) (see table 2.2): high amount of H_2 (100%) in the gas mixture and low amounts of H_2 (17-25%). In this part, we will discuss in details the influence of H_2 on the growth of graphene by changing the H_2 % in the gas mixture. In a first part, we will conduct a study based on AFM, Raman spectroscopy and LEED. In a second part, a similar study will be carried out based on XPS measurements. The growth conditions for the first set of samples is presented in table 3.3.

Table 3. 3: *Growth conditions for the different samples*

Samples	Hydrogen-argon	Referred to as
Sample 1	1 slm H_2 + 10 slm argon	9% H_2
Sample 2	2 slm H_2 + 10 slm argon	17% H_2
Sample 3	3 slm H_2 + 9 slm argon	25% H_2
Sample 4	4 slm H_2 + 8 slm argon	33% H_2
Sample 5	6 slm H_2 + 6 slm argon	50% H_2
Sample 6	9 slm H_2 + 3 slm argon	75% H_2

All the samples were grown at 1550°C, 800 mbars and 5 minutes of 5 sccm of propane. The substrate's miscut angle for this study was 0.09°. Also note that the total gas mixture is 12 slm of hydrogen and argon, but since the argon controller is limited to 10 slm, the total gas mixture is 11 slm for the first sample in table 3.3.

AFM observations:

We first present the AFM observations in Fig. 3.19 of the full set. For the first sample grown with 9% of H_2 (Fig. 3.19(a)), the surface presents terraces with widths between 200 and 300 nm and step heights between 0.35 and 0.50 nm. Most of the terraces defined by steps are atomically flat, but few terraces edges are decorated by rougher ribbons indicated by white arrows in Fig. 3.19(a) (height around 0.22 nm). This is no longer observed in Fig. 3.19(b), grown with a higher H_2 percentage (17%). However, when investigating the phase image, we notice a difference in contrast (image in inset of Fig. 3.19(b)), which suggests a non-uniform deposition. The terraces are now a bit larger, reaching a width of 380 nm. Steps with the same phase contrast present heights around 0.8 nm, whereas steps with different phase contrast have heights around 0.35 nm. Note that the two regions with different contrasts seem equal in terms of surface coverage. Fig. 3.19(c) with 25% of H_2 presents terraces with widths between 300 and 350 nm and open pits with widths

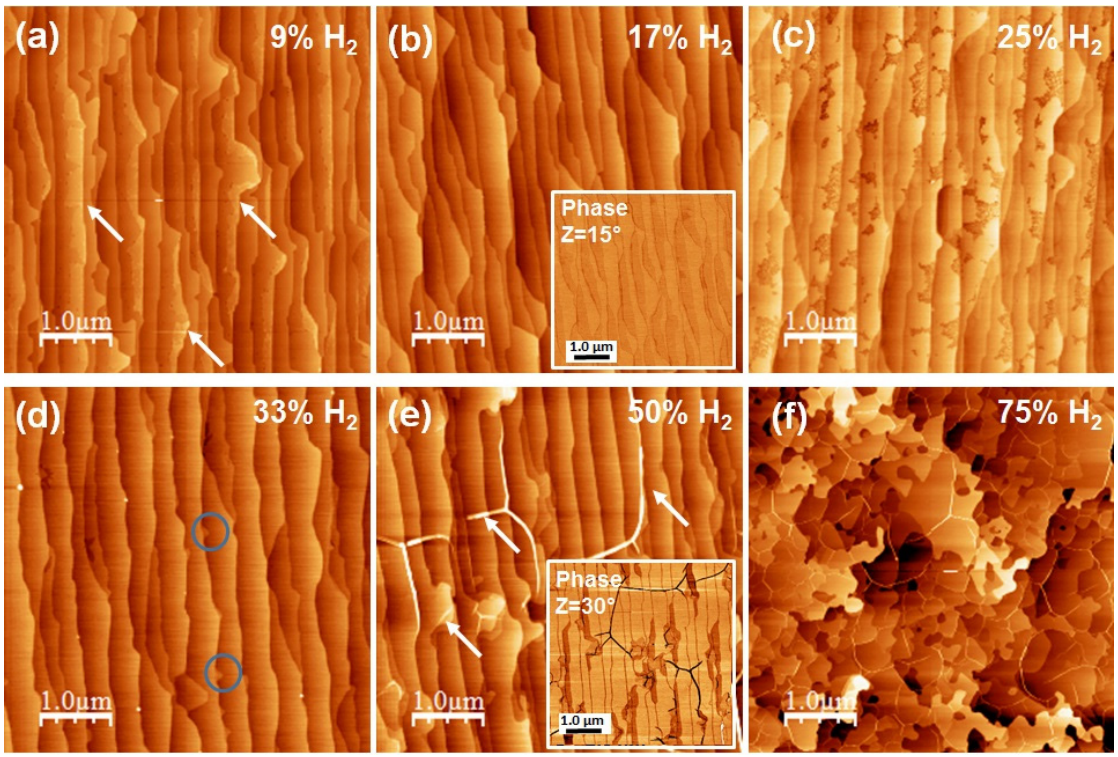

Figure 3. 19: *5×5 µm² AFM images of the grown graphene samples at 1550°C, 800 mbars, 5 sccm of propane for 5 minutes, with different H_2 percentage in the gas mixture. The figures in the inset of* ***(b)*** *and* ***(e)*** *are the corresponding phase images. The AFM topographic z-scale is 2.5 nm.*

reaching 120 nm. Again the heights range between 0.3 and 0.8 nm similar to the previous samples. Increasing the H_2 to 33% (Fig. 3.19(d)) leads to a more uniform surface, both in topography and phase contrast, with terraces between 300 and 450 nm-wide and a uniform step-height around 0.8 nm, with the exception of few very small features with heights around 0.4 nm and widths of 60 nm, indicated by blue circles. When the H_2 reaches 50% (Fig. 3.19(e)) wrinkles start to appear, with heights of ~1.5 nm and widths of ~50 nm. A phase contrast is observed in some regions (inset of Fig. 3.19(e)), attesting for non-uniform thicknesses. Same phase contrast steps are ~0.8 nm-high and different phase contrast steps are ~0.4 nm-high. Note that the difference in phase contrast is only important for the sample of 17% H_2. For the rest of the samples the brighter regions are dominant (see inset of Fig. 3.19(e)). The more we add hydrogen, the more wrinkles will appear (Fig. 3.19(f)), with sizes similar to the previous sample, but the growth seems to be no longer homogenous since we notice different contrasts and irregular shapes on the steps. The deposition seems to be more important in this last case.

The step-height measurements and the differences in phase contrast suggest a graphitic deposition, but to understand these observations we have to mention that graphene deposition will be later confirmed with Raman spectroscopy. Therefore, knowing that we have graphene, AFM observations reveal a non-uniform deposition in some cases. In fact, if we only consider the SiC steps, their height should be equal to half a lattice or a complete lattice (½ ***c*** or ***c***; ***c*** being the out-of-plane lattice parameter of SiC), i.e. around 0.75 or 1.5 nm for 6H-SiC. Then if we consider that graphene grows in a step-flow manner, as many studies suggested, one would expect to maintain the SiC step-height. However, the heights we measure in Fig. 3.19(a) for 9% of H_2, around 0.35 and 0.5, suggest that an extra graphene layer has been deposited between two neighboring SiC steps. In addition, extra ribbons 0.2 nm-high appear at step edges, which we also attribute to extra graphene layers. In the case of 17% of H_2, the phase image (inset of Fig. 3.19(b)) presents areas with different contrasts: steps with the same phase contrast are 0.8 nm-high, which can be ascribed to SiC covered with graphene. In contrast, steps with different phase contrast have heights around 0.35 nm, which can be attributed to an extra graphene layer. Similar observations can be made for the 25% H_2-growth in Fig. 3.19(c), along with open pits suggesting incomplete graphene layers. The most uniform sample seems to be the one grown at 33% of H_2, presented in Fig. 3.19(d), where the surface is dominated by 0.8 nm-high steps, attributed to SiC covered with graphene and confirming the step-flow growth of graphene for the right conditions. Finally, for the 50% H_2-growth (Fig. 3.19(c)), the phase image uncovers different phase contrasts attesting for the growth of extra graphene layers in some areas, mostly between two adjacent steps.

Raman spectroscopy measurements:

Raman spectroscopy confirms the presence of graphene as we present in Fig. 3.20(a). All samples present the graphene fingerprint i.e. the D, G and 2D modes around 1350-1370 cm^{-1}, 1590-1615 cm^{-1} and 2700-2730 cm^{-1}, respectively. The defect-induced D-peak appears in some samples around 1350 cm^{-1}, but we do not notice any particular evolution from one sample to another. The D-peak appears clearly on the 9% and 75% H_2 samples, but more intensely on the

25% H_2 sample, which seems in good agreement with the poor morphology. We suppose that the D-peak is induced by the rough ribbons at the step edges in Fig. 3.19(a), by the open pits and incomplete layers in Fig. 3.19(c) and by the irregular shapes in Fig. 3.19(f). In this latter case another factor contributes to the rise of the D-peak as we will add next in the LEED investigation. We also show in Fig. 3.20(c-h) the estimated number of layers for each sample calculated by normalizing the G-peak integrated intensity to that of a HOPG reference (please refer to equation (2.4) in **chapter2, part 2.3.4** for more details). To be able to do this type of statistics, Raman maps were recorded with different sizes for the different samples: for samples 9% H_2, 17% H_2, 25% H_2 and 75% H_2 the map size is 10×10 μm^2 with a step of 1 µm. For the sample 33% of H_2, the map size is 7×15 μm^2 with a step of 0.25 µm. And finally for the sample 50% H_2, the map size is 15×15 μm^2 with a step of 0.3 µm.

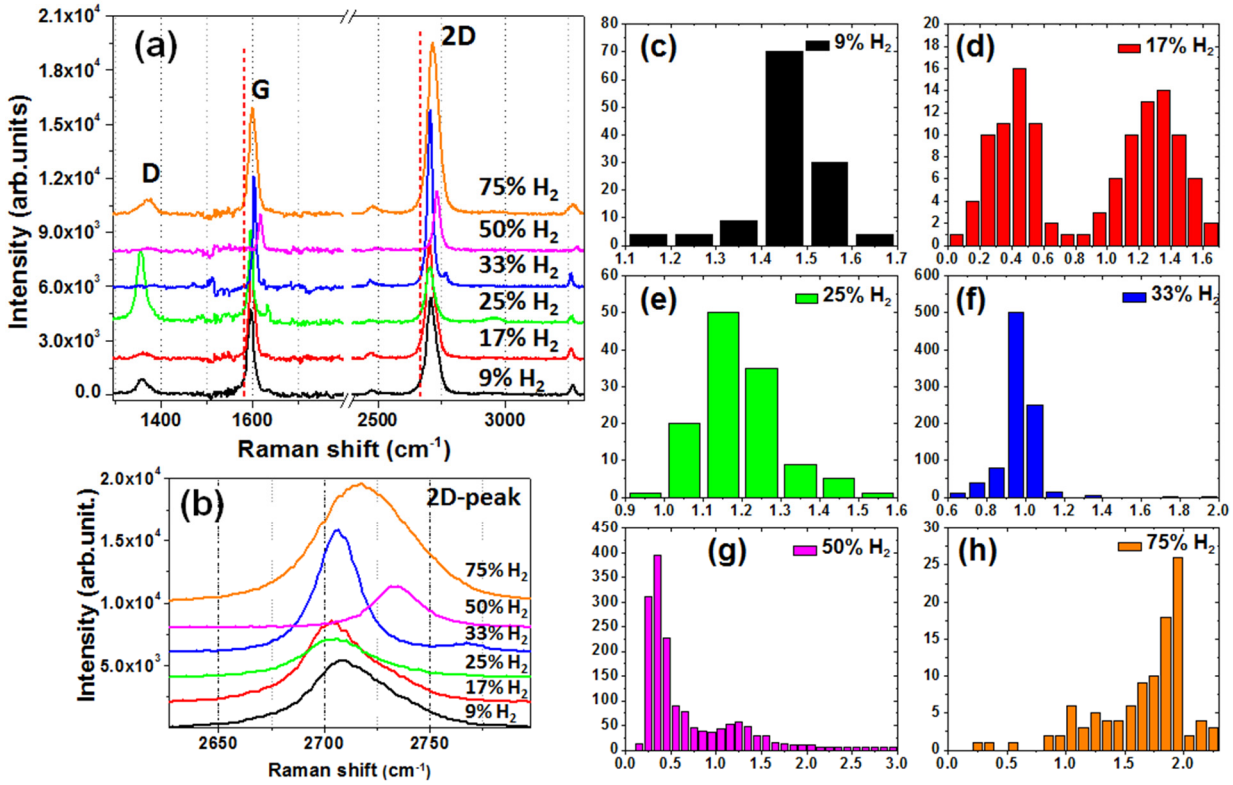

Figure 3. 20: (a) *Raman spectra of the different samples. The red lines show the reference peaks of exfoliated graphene at 1582 and 2670 cm^{-1}.* ***(b)*** *A closer look on the 2D-peak.* ***(c)*** *to* ***(h)*** *Statistical charts of each sample showing the estimated number of layers on the X-axis.*

It seems that the estimated number of layers is consistent with the AFM observations in Fig. 3.19. In fact, all the calculated number of layers present a decimal number which is due to the extra layer we have previously detected either with the topographic AFM image or with the phase image. The Raman laser spot diameter being 400 nm, each Raman spectrum rises from areas with different thicknesses, which explains the asymmetric shape of the 2D-peak presented in Fig. 3.20(b). The most uniform sample seems to be the one grown with 33% of H_2 (Fig. 3.20(f)),

since the number of layers is around one single graphene layer, which confirms our AFM observations. In addition, Fig. 3.20(c, e) presents 1 to 1.7 layers of graphene for the different samples, which means a single-layer deposition with patches of multilayers. However, we measured with AFM step-heights of 0.8 nm along with areas 0.35 nm-high, we deduce that the difference between different areas does not exceed one monolayer. Therefore, the values we extract from Raman spectroscopy attest for a single graphene layer with areas or patches of bilayers. For the 17% H_2-growth, the statistical chart in Fig. 3.20(d) reveal a bimodal distribution, one showing a number of layers less than one and the other showing a number of layers more than one. The laser spot must be detecting at the same time areas without any graphene and areas with graphene, which explains the detection of 0.5 layers. We also suspect areas without any graphene for the sample grown with 50% since the statistical chart in Fig. 3.20(g) shows important data around 0.5 layers. Finally, the sample grown with 75% of H_2 presents a number of layers reaching 2 (Fig. 3.20(h)), which explains the large 2D-peak in Fig. 3.20(b), since this latter's FWHM is sensitive to the number of graphene layers as well [141]. This last observation confirms our previous assumption that the deposition is more important for the 75% H_2 sample. Finally, we add that the 2D peaks in Fig. 3.20(b) seem shifted from one another, especially the 50% H_2 sample, which is shifted towards higher wavenumbers. Different parameters can lead to a shift in Raman peaks, but we will discuss this later on in **part 3.3**.

We also attempted to estimate the number of graphene layers with XPS, by calculating the ratio of the integrated intensity of the graphene peak to that of the SiC peak. However, the values seem to be overestimated with XPS compared to Raman spectroscopy by at least 0.6 MLs. This inconsistency could be due to the two different approaches for the estimation of the number of graphene layers and/or related to the spot width of each technique, which is 400 microns for the XPS gun but 400 nm for Raman spectroscopy.

LEED investigations:

In order to have better insights into the influence of the hydrogen on the structure of graphene we have conducted LEED measurements, as we show in Fig. 3.21. We show only four LEED patterns with their corresponding AFM images. Fig. 3.21(b) corresponds to the growth with the lowest H_2 amount. It is possible to detect graphene and SiC diffraction spots, but also we notice the manifestation of an interface reconstruction, indicated by white circles and arrows in Fig. 3.21(b). To be specific, a $(6\sqrt{3}\times6\sqrt{3})$ SiC interface reconstruction, rotated 30° with respect to the substrate. This interface reconstruction appears in Fig. 3.21(b, d) and less intensely in Fig. 3.21(f). In this latter case we had to zoom in and change the contrast to be able to see the $6\sqrt{3}$ structure. Also, we detect in this same figure some elongated shapes and satellites next to the diffraction spots of graphene, indicated with yellow arrows. These shapes are identified as a graphitic phase with in-plane rotational disorder (or IRD). Therefore, for this sample grown with 50% H_2 (Fig. 3.21(f)) it is possible to see the $6\sqrt{3}$ interface reconstruction and IRD. Finally, in the Fig. 3.21(h) for 75% H_2, no signs of the $6\sqrt{3}$ are present, we only see elongated shapes revealing IRD. Combining LEED with AFM observations, the IRD phase exposed by LEED is correlated to

the presence of wrinkles in AFM images. We believe that the IRD also contributes to the D-peak observed in the corresponding Raman spectrum in Fig. 3.20(a), but somehow this peak is not detected for the 50% H_2 sample even though we do observe IRD in the corresponding LEED image (Fig. 3.21(f)). We do not present the LEED patterns of the samples grown with 25 and 33% of H_2, because they show similar features to the 9% and 17% H_2 samples.

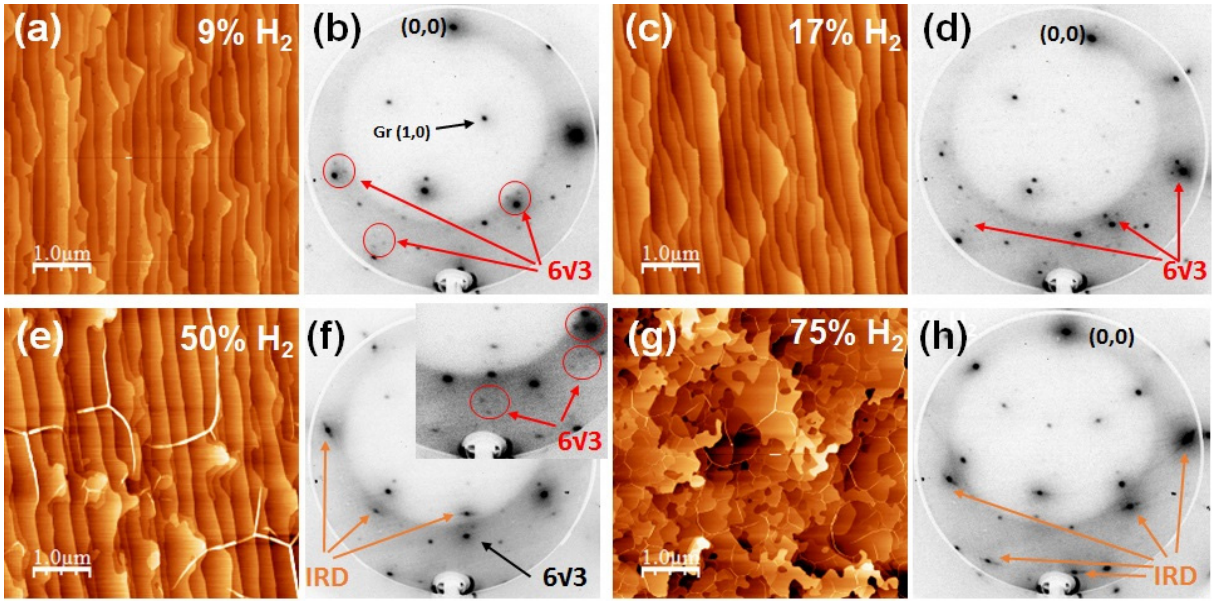

Figure 3. 21: *5×5 µm² AFM topographic views of the different grown samples:* ***(a)*** *under 9% H_2,* ***(c)*** *under 17% H_2,* ***(e)*** *under 50% H_2 and* ***(g)*** *under 75% H_2. Images in* ***(b)***, ***(d)***, ***(e)*** *and* ***(h)*** *represent the corresponding LEED images taken at an electron energy of 140 eV.*

3.2.3.2. Interface control: discussion and conclusion

Combining AFM and Raman observations, we can deduce that the hydrogen amount in the gas mixture has a direct influence on the deposited thickness. Based on the Raman histograms for the number of layers in Fig. 3.20(c-h), the graphene thickness seems more or less stable but slightly decreasing when increasing the H_2 amount from 9% to 33%, regardless of the areas with 0.5 MLs for 17% of H_2. The number of layers then reaches a minimum for 50% of H_2 (Fig. 3.20(g)), but increases when increasing the H_2 amount to 75% (Fig. 3.20(h)). These observations are in good agreement with AFM topographic changes, where we first see extra layers at step edges for the 9% H_2-sample in Fig. 3.19(a). These aspects are no longer observed in Fig. 3.19(b) for 17% H_2, but we do detect a difference in phase contrast suggesting a difference in the deposited thickness. Fig. 3.19(c) presents incomplete layers, but Raman is not very sensitive to the small open pits, since we estimate a number of layers mostly around 1.15 and 1.25 graphene layers. Increasing the H_2 amount to 33% limits the number of layers to one single graphene layer, with few discrepancies. Finally, with H_2 amount equal and greater than 50%, other features such as wrinkles start to appear as we can see in Fig. 3.19(e, f), along with irregular patterns for 75% of H_2, suggesting a thicker deposition. These observations seem difficult to interpret, since each sample appears to be

particular with its own anomalies, but we believe that the influence of H_2 on the thickness of graphene is related to the etching of SiC, since we consider that the latter is also a source of carbon in the presence of propane as we previously discussed. The variation of H_2 should change the etching contribution to the growth, but quantifying these effects seems complicated. In spite of that, the growth with 33% of H_2 appears to be the most homogeneous and uniform for these growth conditions.

According to AFM and LEED observations, graphene grown with low hydrogen percentage in the gas mixture seems associated with a ($6\sqrt{3}\times6\sqrt{3}$) surface reconstruction as evidenced by LEED patterns. We have previously correlated this interface reconstruction in **chapter 1** to a buffer layer, or a zeroth graphene layer, which shares covalent bonds with the substrate. Increasing the H_2 amount to 50% (Fig. 3.19(e)) has initiated the emergence of few wrinkles at the surface and in-plane rotational disorder (IRD) in the corresponding LEED image (Fig. 3.21(f)). We also see in Fig. 3.21(f) diffraction spots corresponding to the $6\sqrt{3}$ structure, which means that both structures, the IRD and the $6\sqrt{3}$ structure, coexist. In Fig. 3.21(h), corresponding to the highest percentage of H_2, we only see IRD without any signs of a buffer layer in the LEED pattern along with a surface covered by wrinkles in Fig. 3.19(f) and Fig. 3.21(g). These observations are related to what is happening at the interface between the graphene layer and the substrate. Without the presence of hydrogen such as in the case of Si sublimation under UHV or argon, the first carbon layer can bond with the substrate and form the buffer layer. However, few studies have shown that a post-growth annealing under H_2 can introduce hydrogen at the interface, which will bond with the silicon of the substrate, replacing the bonds with the buffer layer [84,86]. In other words, the hydrogen can passivate the Si dangling bonds, preventing them from bonding with the first carbon layer to create a buffer layer.

In our case, for small amounts of H_2 (9%-33%) during the growth, we still observe the buffer layer's features. This could be due to the insufficient amount of hydrogen to passivate all of the silicon dangling bonds, allowing them to bond with the first carbon layer and form a buffer layer. An important amount of hydrogen is required to passivate the silicon dangling bonds (more than 50% of H_2), inhibiting the formation of the buffer layer. In the absence of the buffer layer, i.e. when the interface is hydrogenated, graphene seems to grow in domains with different orientations, see the LEED pattern in Fig. 3.21(h) where we detect elongated shapes attributed to IRD. We also detect wrinkles on the surface for the cases with 50 and 75% of H_2 in Fig. 3.19(e, f). We suspect that because of the absence of the buffer layer, the graphene sheet will be freestanding. As a response to important amount of thermal strain when cooling down, wrinkles will appear at the surface to relieve the strain. We will talk more about this later on when we discuss strain in the epitaxial graphene layer (**part 3.3**). We usually associate wrinkles to the presence of IRD, but it is important to note that the observation of wrinkles does not always mean that we have IRD without the confirmation of LEED. Some studies were able to detect wrinkles on graphene grown under UHV on SiC (0001) [113]. Therefore, wrinkles are mainly a strain-relief process, but it is necessary to complete their detection with LEED measurements to associate them with IRD.

We add that, IRD or disorder can also be translated into the emergence of the D-peak in the corresponding Raman spectrum. In the presence of the buffer layer, for low amount of H_2, the graphene sheets seem well ordered with LEED, all oriented with a 30° angle with respect to the substrate, but we detect a D-peak for 9% and 25% H_2 for reasons related to the morphology and not to the presence of disorder. We also do not detect any wrinkles with AFM for this case, either because graphene on a buffer layer does not present significant strain, or because the buffer layer prohibits strain relaxation. At this point we cannot add more before discussing the strain. On the other hand, in the intermediate case, with 50% of H_2, we can see in the LEED measurements (Fig. 3.21(f)) that IRD coexist with the $6\sqrt{3}$ structure. In this case, the hydrogen is enough to create some bonds with silicon, and thus a bit of disorder, yet it does not seem enough to avoid completely the presence of the buffer layer. Hence, no D-peak is observed in the corresponding Raman spectrum and only few wrinkles appear at the surface, probably because the buffer layer is prohibiting enough strain relief and the manifestation of significant disorder.

As a conclusion, we can deduce from the AFM and LEED observations that a transition occurs when increasing the H_2 amount in the gas mixture for the growth of graphene, similarly to what has been observed in a previous study when varying pressure and temperature under pure hydrogen [18]. In our work, we can distinguish among three different cases: at low H_2 percentages (9%-33%), the $6\sqrt{3}$ structure is dominant; with a high H_2 percentage (75%) the IRD structure is dominant; for intermediate amount of H_2 (in this case at 50% H_2) it is possible to have both structures coexisting together. This can also explain the reason why we have more than two layers for 75% of H_2 even though the propane flow rate and the growth time are the same: in fact, for low H_2 amount the first carbon layer is a buffer layer, whereas for 75% of H_2 the first carbon layer is a graphene layer due to the sufficient passivation of the Si dangling bonds. Therefore, for the same propane flow rate and growth time we will obtain a buffer layer and a graphene layer for the low H_2 amount case, but instead two graphene layers for 75% of H_2. This means that the number of layers is also related to the hydrogenation of the interface and not only to the etching contribution to the growth as we previously suggested. Finally, the best choice of hydrogen amount seems to be around 33%, resulting in a uniform deposition and morphology.

3.2.3.3. XPS study: sample-set 2

To check the credibility of our observations, the same growth conditions were applied to another set of samples of a different substrate with a slightly larger offcut. The growth conditions are the same, similar to what is presented in table 3.3, with the exception of few changes in the hydrogen percentage. For example we added two samples grown with 67 and 100% of H_2. We present in Fig. 3.22(a-c) three AFM images and not for all the samples, because the topographic observations have not changed. Similarly to before, we start detecting wrinkles at the surface for a growth under 50% of H_2, indicated by white arrows in Fig. 3.22(b). Fig. 3.22(c) for 100% of H_2 displays a lot of wrinkles and open pits, possibly due to important hydrogen etching at 1550°C, which can probably be reduced by adding more propane to the growth. To evaluate the hydrogen effect in this study we performed XPS measurements. We present the C1s core-level for the

different samples in Fig. 3.22(d). All the samples present the graphene sp^2-peak except for the growth attempt conducted with 100% of argon (the black curve in Fig. 3.22(d)). Note that the 100% H_2-sample presents a graphene peak with reduced intensity and a very asymmetric shape (purple curve). We attribute these features to the important etching we see in Fig. 3.22(c). All the spectra were normalized to the SiC peak and aligned to the 100% H_2-SiC peak for clarity purposes. It is worth noting that the spectra corresponding to 0% H_2 and 9% H_2 had the highest binding energy and had to be shifted by -0.8 and -0.9 eV respectively, to be aligned with the 100% H_2-SiC peak. As to the other spectra, the shift is reduced for samples with higher H_2 amounts, for example the spectra corresponding to 17%, 33% and 50% of H_2 had to be shifted by -0.4, -0.2 and -0.1 eV, respectively. Two reasons can explain this shift: the sample's conductivity and the changing number of layers. First, the sample grown with 0% of H_2 presents no graphene peak, which makes it a bare SiC substrate and hence less conductive than graphene. Since XPS is sensitive to the conductivity of the sample, a less conductive sample will exhibit peaks at higher binding energies, see **part 2.3.3. XPS**. Note that the flood gun was not used while recording these spectra. Secondly, Emtsev et al. [105] have attributed the XPS shift to a change in graphene thickness and charge transfer. In fact, they believe that a charge transfer always takes place from the substrate to the

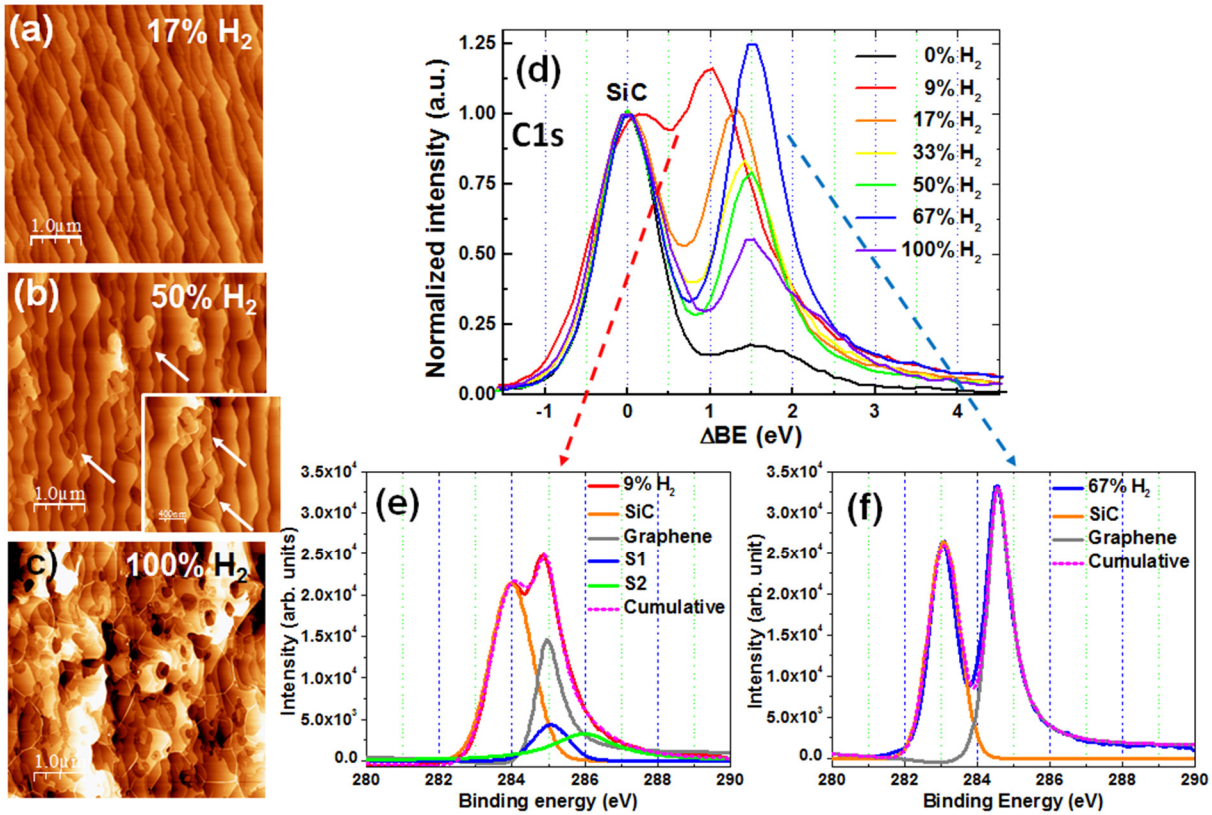

Figure 3. 22: ***(a)*** *to* ***(c)*** *5×5 µm² AFM topographic views of the different grown samples:* ***(a)*** *with 17% H_2,* ***(b)*** *with 50% H_2 and* ***(c)*** *with 100% H_2. AFM z-scale: 3 nm. In* ***(d)*** *the corresponding C1s core-level spectra of all the grown samples under different H_2 amount.* ***(e)*** *and* ***(f)*** *Fitting of the 9% H_2-sample in* ***(e)*** *and of the 67% H_2-sample in* ***(f)****.*

graphene layer, but resides mainly close to the interface [37,41,179]. Therefore when the thickness is increasing, the XPS will be probing more neutral graphene with a C1s peak shifted towards higher binding energies. We assume that a similar phenomenon is occurring in our case, especially since we have previously seen that H_2 influences also the thickness of the graphene, but also since the buffer layer is getting more hydrogenated with the increasing amount of H_2, the charge transfer is reduced as well for higher H_2 amounts.

Finally, since we know that the buffer layer is detectable with XPS, we considered two extreme samples: the 9% H_2 and the 67% H_2 samples, see Fig. 3.22(e, f). In Fig. 3.22(e), for the 9% H_2 sample, it was necessary to use four peaks to fit correctly the recorded spectrum: the SiC peak appears at 284 eV and is fitted with a Gaussian function; the asymmetric graphene peak appears at 284.9 eV, fitted with the Doniach-Sunjic function for asymmetric peaks [180]; and two peaks (**S1** and **S2**) fitted with a Gaussian function (for **S1**) and a Lorentzian (for **S2**). The **S1** and **S2** peaks correspond to the buffer layer, appearing at 285.1 and 286 eV respectively, with an area ratio **S1**/**S2** of 0.5, as expected for the buffer layer peaks [105]. Note that the **S1** peak corresponds to carbon atoms within the buffer layer sharing covalent bonds with the substrate, whereas the **S2** peak represents sp^2-carbon atoms within the buffer layer. In Fig. 3.22(f), for the 67% H_2, there was no need for four peaks to fit the spectrum correctly. Only two peaks were used: the SiC peak appears at 283.1 eV (fitted with a Gaussian) and the asymmetric graphene peak at 284.5 eV (fitted with the Doniach-Sunjic function). These observations confirm our previous conclusion that the buffer layer only appears for samples grown with low hydrogen amount, whereas for samples grown with a high hydrogen percentage in the gas mixture, no buffer layer is detected. The reason behind this behavior, as we explained before, ensues from the intercalation of hydrogen at the interface.

In summary, we have demonstrated the effects of the hydrogen amount in the gas mixture on the growth of graphene. The H_2 % has a direct influence on the morphology and on the deposited graphene thickness as evidenced by AFM and Raman spectroscopy. In addition, based on LEED investigations, the hydrogen appears to have an influence on the graphene structure as well. Low hydrogen-ratio growths are associated with a $(6\sqrt{3}\times6\sqrt{3})$-R30° interface reconstruction, while high hydrogen-ratio growths (equal and more than 50%) are associated with in-plane rotational disorder and wrinkles at the surface detected with AFM. We believe that it is all connected to the amount of hydrogen at the interface, since hydrogen is able to bond with the silicon from the substrate and prohibit the formation of the buffer layer. On the contrary, insufficient amounts of hydrogen at the interface will leave free dangling bonds able to bond with the first deposited carbon layer to form the buffer layer. Finally, we were able to confirm these deductions with XPS measurements, by looking in details into the C1s core-level spectra of the different samples. Low hydrogen samples exhibit extra peaks attributed to the buffer, whereas high hydrogen samples do not. We also suspect a reduced charge transfer from the substrate to the graphene layer when the interface is hydrogenated. In general, we find that it would be preferable to do growth with H_2 less than 50%, to avoid any disorder. Therefore, the growths with 17% to 33% seem to be the most promising,

but the most uniform sample in this study is the one grown with 33% of H_2. However, the growth with 9% or 25% of H_2 can be optimized by changing other growth parameters, such as the growth time or the propane flow rate to make the surface more uniform.

3.2.4. Substrate's miscut angle

In the previous paragraphs, while studying the effects of the growth conditions, we mentioned in some cases the substrate's miscut angle. This parameter is rarely mentioned in the literature and neglected in some studies where "on-axis" substrates with very small residual offcut (<0.1°) are mainly used[12,13,86][12,13,87][12,14,87]. However, when we order on-axis SiC substrates, the residual offcut is not always the same, ranging from 0.05° to 0.8°. This parameter can have a direct influence on the growth of graphene and is as important as any of the other growth parameters. For this reason, we will discuss in this part the effects of the substrate's miscut angle on the graphene growth by considering four substrates with different miscut angles: 0.05°, 0.2° and 1°-off 6H-SiC substrates and 4°-off 4H-SiC substrate, prepared with two different growth conditions: 17% of H_2 and 100% of H_2. This study was conducted on what was available as substrates, this is why we used a 4H-SiC polytype for the 4°-off. The 4H polytype will have smaller step-heights than the 6H polytype: 1 nm or 0.5 nm for 4H and 1.5 or 0.75 nm for 6H. Therefore, for a given offcut the 4H-SiC will have more steps than the 6H polytype, but as we will reveal in our discussion, the effects of the substrate's miscut are not related to the step-height, therefore it is not very problematic if we use 4H as the last substrate.

3.2.4.1. 17% H_2 at 1550°C

First, we will start with the growth with 17% of H_2, 1550°C, 800 mbars, 5 sccm of propane and a growth time of 5 minutes. Fig. 3.23 presents the AFM images of the four substrates with their respective LEED images. The first substrate (0.05°-off) in Fig. 3.23(a) stands out from the other three: it presents triangular clusters, up to 16 nm-high, along with important step-bunching of over 7 microns in width and 1.6 nm in height. At this stage, further investigations are required to identify the nature of the triangles whether they are graphene or SiC. The second substrate (0.2°-off) in Fig. 3.23(b) seems more uniform, no triangular shapes are observed, and the steps are smaller with widths varying between 150 and 350 nm and typical heights of 0.35 or 0.8 nm. The steps even get smaller and smaller as the offcut increases from 0.2° to 4° in Fig. 3.23(b-d), but the overall morphology remains unchanged, see inset in Fig. 3.23(b, c). The step-height is 1.5 nm for the 1°-off substrate and around 3 nm for the 4°-off substrate. If we analyze now the corresponding LEED images (Fig. 3.23(e-h)), it is possible to see the graphene and SiC diffraction spots, indicated by black and blue arrows respectively, but also the $(6\sqrt{3}\times6\sqrt{3})$ reconstruction coming from the buffer layer, indicated by the red arrows. The spots representing the buffer layer and SiC appear clearly in Fig. 3.23(e, f), but we can barely detect them in Fig. 3.23(g) and even not at all in Fig. 3.23(h), where only diffraction spots of graphene appear. The fact that we only see graphene diffraction spots in this latter image and no SiC spots, suggests that the deposited thickness is more important than the inelastic mean free path of electrons, i.e. more than 3 or 4 graphene layers.

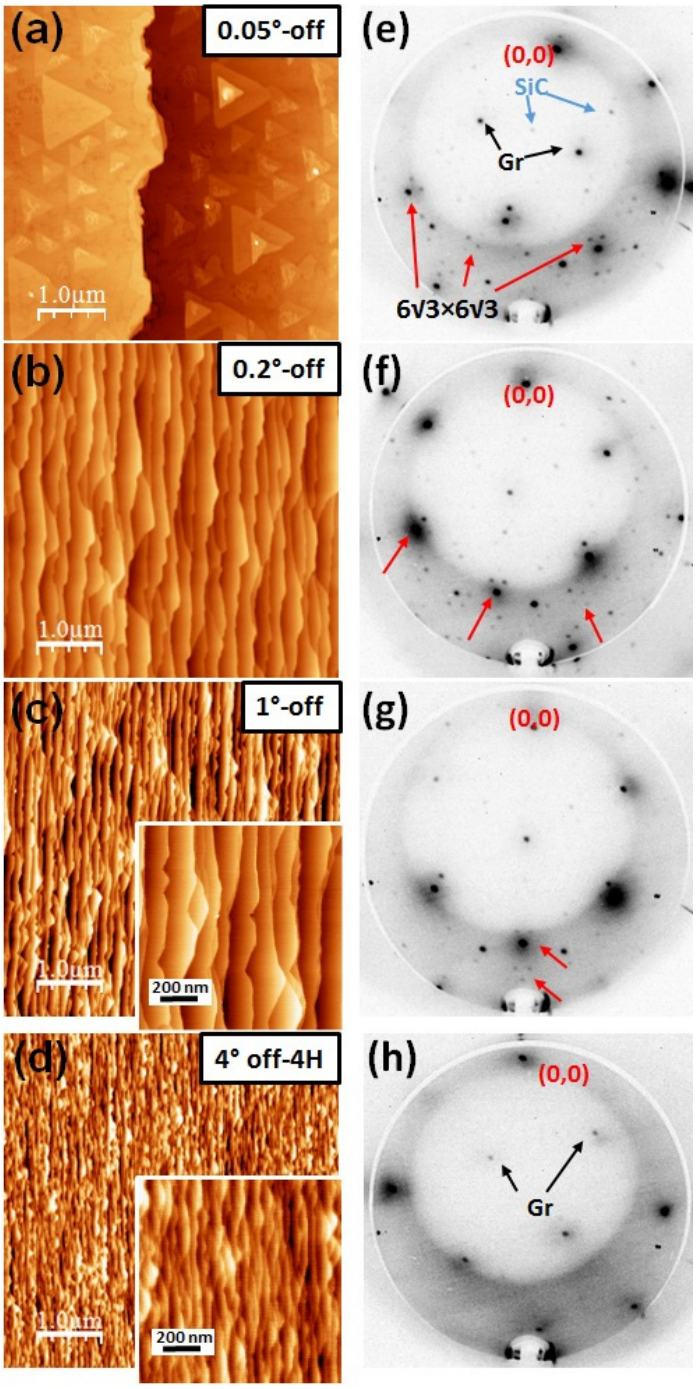

Figure 3. 23: *5×5 µm² AFM images of graphene grown with 17% of H_2 at 1550°C on different substrates with different offcuts:* ***(a)*** *0.05°,* ***(b)*** *0.2°,* ***(c)*** *1° and* ***(d)*** *4°. Inset of* ***(c)*** *and* ***(d)*** *are 1×1 µm² images. AFM z-scale is 5 nm.* ***(e)*** *to* ***(h)*** *Corresponding LEED images taken at an electron energy of 140 eV.*

The corresponding Raman spectra are presented in Fig. 3.24(a). All Raman spectra for the different samples present G peaks ranging between 1588 and 1598 cm^{-1} and 2D peaks ranging between 2690 and 2733 cm^{-1}, hence confirming the presence of graphene, even for the 0.05° off

substrate. We also detect D peaks around 1360 cm^{-1} for the 0.05 and 4°-off samples attesting for the presence of defects and/or disorder, but no specific evolution appears from one sample to another. Raman measurements reveal an increase in the deposited number of layers: 1.4, 1.2, 1.8 and 3 MLs for the 0.05, 0.2, 1 and 4°-off substrates respectively. The increase in thickness can also be investigated by examining the 2D-peak width: a single-layer graphene should have a narrow 2D-peak, which can be fitted with a single Lorentzian, whereas bilayer- and multilayer-graphene presents a wide 2D-peak, which can be fitted into four components [141]. Indeed, a closer look at the 2D-band (Fig. 3.24(c)) confirms the increase in the number of layers, since we notice that the FWHM is increasing with the offcut. In addition, we notice first in Fig. 3.24(b, c) that both the G and 2D peaks are upshifted compared to exfoliated graphene (dashed red lines), and second the bigger is the offcut the more they are upshifted, especially the 2D-peak. The blue shift is induced by different parameters, such as the number of layers, the doping and the strain (compressive strain for an upshift) [140,141]. We also notice in Fig. 3.24(b, c) that the peaks are becoming broader when the offcut is larger. This broadening is affecting both the G and 2D peaks, which means that it is emanating from a certain non-uniformity in the parameter that is influencing the G- and 2D-peak upshift. We will discuss these Raman observations in details in **part 3.3**.

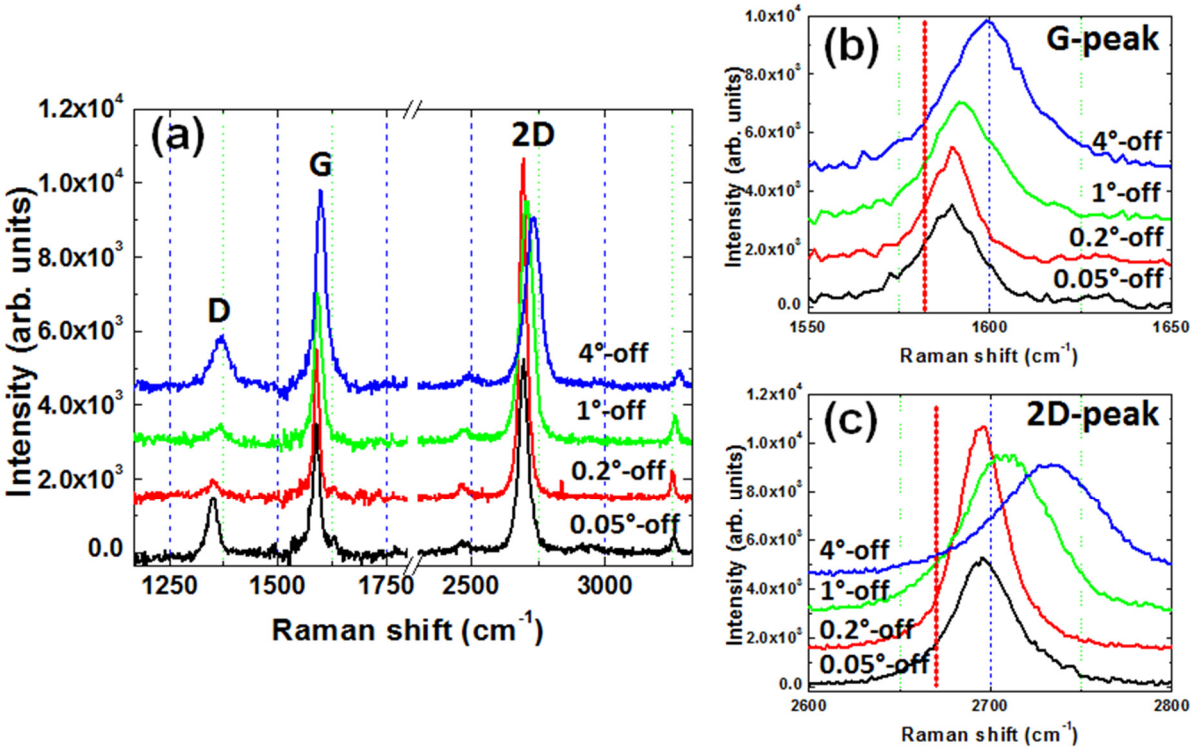

Figure 3. 24: *Raman spectra of the different growth samples, prepared with 17% of H_2 at 1550°C, presented in* ***(a)****, with a zoom-in on the G and the 2D peaks in* ***(b)*** *and* ***(c)*** *respectively. The red line in* ***(b)*** *and* ***(c)*** *represents the reference for exfoliated graphene around 1582 cm^{-1} and 2670 cm^{-1} for the G- and 2D-peak respectively.*

3.2.4.2. 100% H_2 at 1450°C

We have considered previously the case of graphene growth under conditions promoting the formation of a buffer layer. Now we will consider the case of growths promoting the hydrogenation of the interface between graphene and SiC. To do so, we kept the previous growth conditions while increasing the hydrogen amount to 100% in the gas mixture and decreasing the temperature to 1450°C. The rest of the parameters are the same as before: 800 mbars and 5 minutes of 5 sccm of propane. AFM images presented in Fig. 3.25(a-d) show the morphology of the as-grown graphene. As expected, the terrace's size is shrinking with the increase of the offcut and becoming almost indiscernible for the 4°-off substrate (Fig. 3.25(d)), even after zooming-in. Note the smaller scale for the 4°-off substrate (Fig. 3.25(d)). We do not perceive any triangular shapes on the 0.05°-off sample (Fig. 3.25(a)) as we did in the previous case, but instead we can detect wrinkles in the first two images (Fig. 3.25(a, b)) and in the third image after zooming-in (Fig. 3.25(c)), indicated by red arrows, for the 0.05, 0.2 and 1°-off substrates respectively. However, in Fig. 3.25(d) it is difficult to discern any wrinkles, probably because of the very small terraces and not because of their absence. LEED patterns for all the samples in Fig. 3.25(e-f) reveal graphitic rings, indicated by red arrows, suggesting in-plane rotational disorder (IRD) associated with graphene growth on hydrogenated interfaces. Therefore, even if we cannot see any wrinkles for the 4°-off substrate, we know that the interface is hydrogenated from the LEED pattern.

As we can see in the LEED patterns, the diffraction rings appear around the graphene spots whereas the SiC spots are well defined. In addition, we can detect hexagonal features indicated by green arrows in the LEED patterns. One can attribute them to the $(6\sqrt{3}\times6\sqrt{3})$ buffer layer, but if we compare them to the diffraction spots of the buffer layer in Fig. 3.23(e-g) we notice that the distance to the central point is not the same. In the previous case, the diffraction spots of the buffer layer are closer to the central point compared to the hydrogenated case. Hence, even though we cannot rule out the existence of a buffer layer in this case or at least the presence of some covalent bonds between the graphene layer and the substrate, we can presume that the buffer layer configuration is not the same. The buffer layer diffraction spots should be well defined and not elongated and faint as we see in Fig. 3.25(f, g). For this reason, we believe that these diffraction patterns might be emanating from a $(6\sqrt{3}\times6\sqrt{3})$ surface reconstruction accompanied with hydrogenated areas resulting in adjacent graphene domains with different orientations, and therefore in elongated shapes appearing as hexagons around few diffraction spots. More investigations such as TEM are required for confirmation.

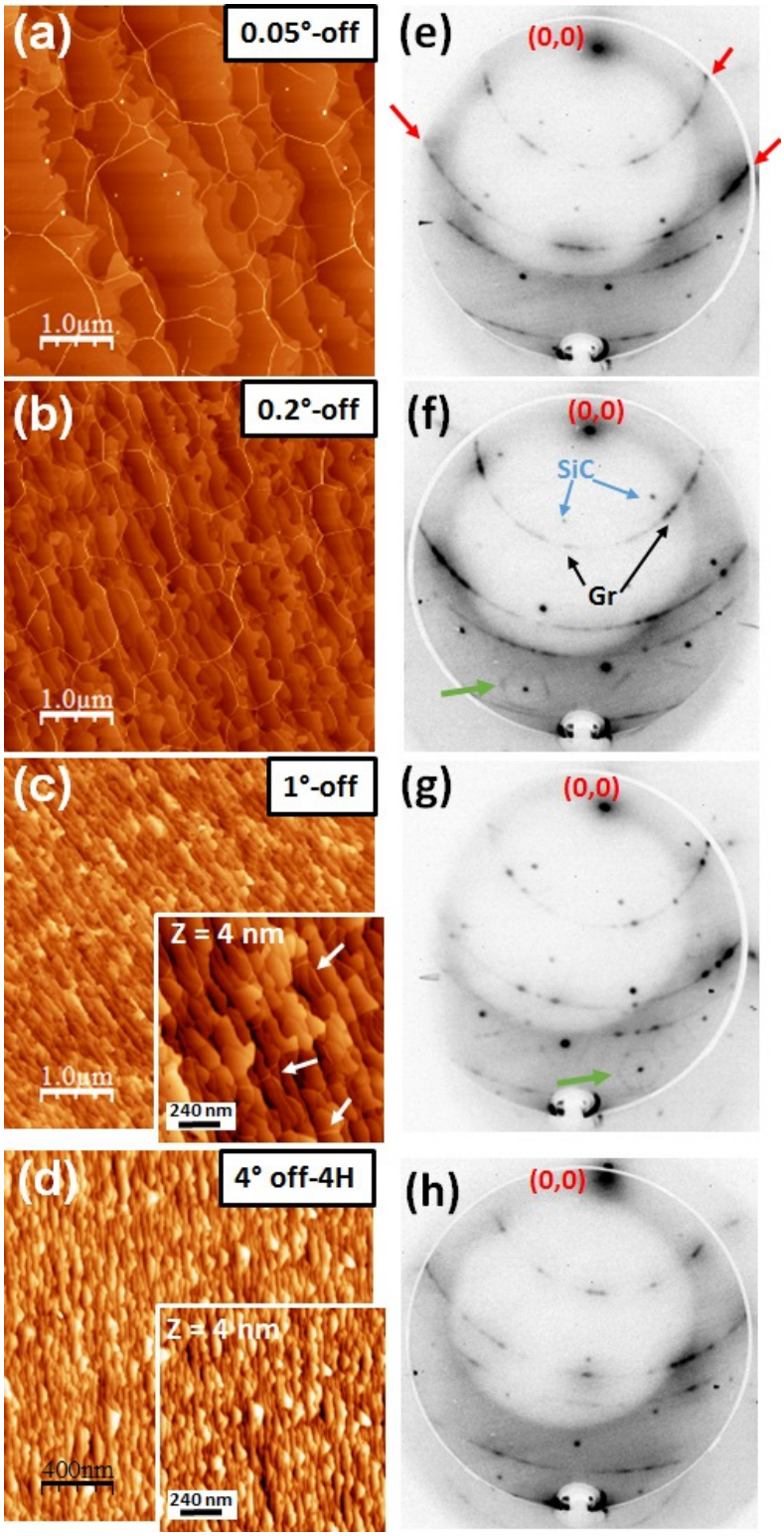

Figure 3. 25: *5×5 µm² AFM images of graphene grown with 100% of H_2 at 1450°C on different substrates with different offcuts:* ***(a)*** *0.05°,* ***(b)*** *0.2°,* ***(c)*** *1° and* ***(d)*** *4° (2×2 µm²). Inset of* ***(c)*** *and* ***(d)*** *are 1.5×1.5 µm² images. AFM z-scale is 5 nm.* ***(e)*** *to* ***(h)*** *Corresponding LEED images taken at an electron energy of 140 eV.*

Raman measurements in Fig. 3.26 show that all samples present the G, 2D and D peaks, confirming the growth of graphene. The D-peak appears around 1340 and reaches 1370 cm^{-1} for the different samples; the G-peak ranges between 1580 and 1613 cm^{-1}; and the 2D-peak ranges between 2690 and 2740 cm^{-1}. However, different measurements with Raman spectroscopy on the 0.05°-off substrate reveal areas without any graphene. Therefore, even though we do not see any triangular clusters in this case, achieving a uniform graphene growth on the 0.05°-off sample seems challenging for the different growth conditions. The estimated number of layers for the different samples ranges between 0.8, 1.4, 2.2 and 2.6 monolayers for the 0.05, 0.2, 1 and 4°-off samples, respectively. In Fig. 3.26(a), we notice that the D-peak is rising in size and intensity for larger offcuts, suggesting an increase in the disorder for substrates that are more off-axis. Zooming-in on the G-peak in Fig. 3.26(b) and the 2D-peak in Fig. 3.26(c), we reveal an important upshift towards higher wavenumbers as a function of the increase in the offcut. We also identify the broadening of the two peaks when the offcut is increasing.

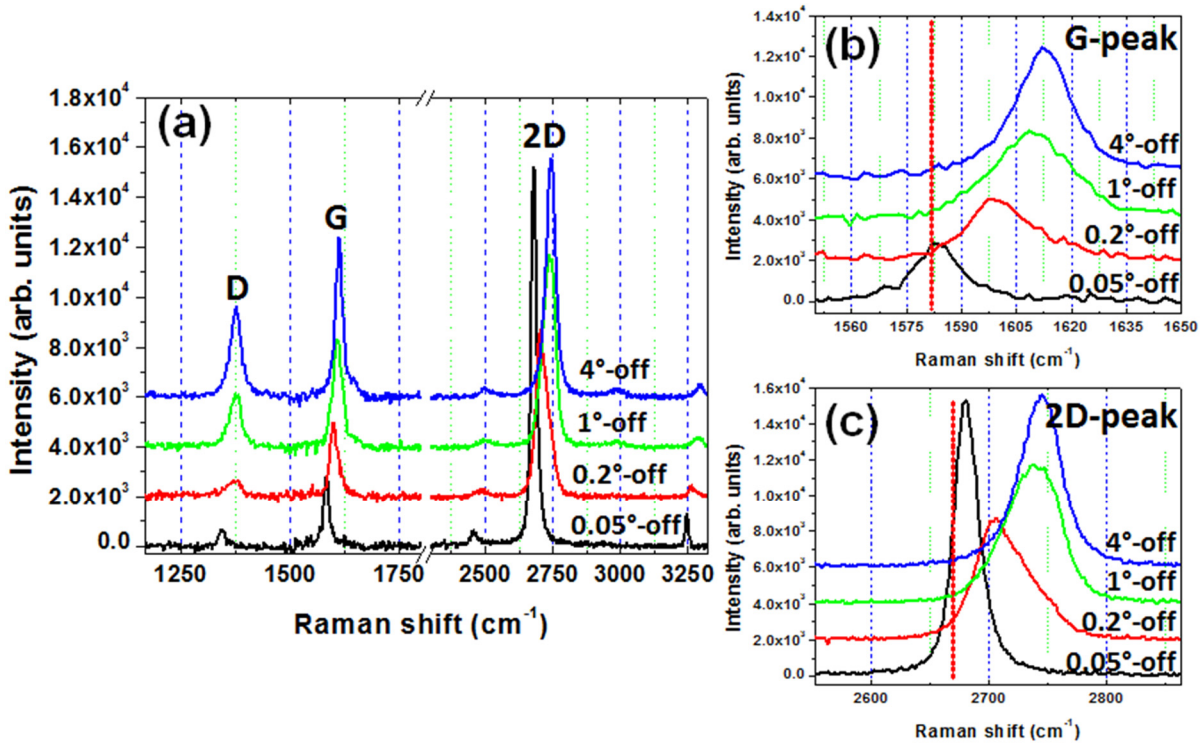

Figure 3. 26: *Raman spectra of the different growth samples, prepared with 100% of H_2 at 1450°C, presented in* ***(a)****, with a zoom-in on the G and the 2D peaks in* ***(b)*** *and* ***(c)*** *respectively. The red line in* ***(b)*** *and* ***(c)*** *represents the reference for exfoliated graphene around 1582 cm^{-1} and 2670 cm^{-1} for the G- and 2D-peak respectively.*

3.2.4.3. Discussion and conclusion

We have shown first observations with AFM, LEED and Raman spectroscopy of the influence of the substrate's miscut angle on the morphology, structure and number of layers of the graphene grown on SiC under two different growth conditions: 17% of H_2 at 1550°C and 100% of

H_2 at 1450°C. In the first case, AFM images reveal that the morphology of the as-grown graphene is barely influenced by the substrate's miscut angle for offcuts between 0.2 and 4°. The difference we notice is a change in the terrace width and a thicker deposition for larger offcuts (1 and 4°), confirmed with Raman spectroscopy. For the substrate with the lowest offcut (0.05°-off), a uniform two-dimensional growth seems more challenging as triangular shapes appear on the large terraces formed by step-bunching. LEED measurements revealed the presence of a buffer layer in addition to the graphene and SiC diffraction spots. However, the diffraction spots of the buffer layer fade away for larger offcuts and completely disappear for the 4°-off sample. We have attributed this behavior to the increase in the deposited thickness since LEED is a surface-sensitive technique. The presence of graphene was confirmed with Raman spectroscopy, which also allowed us to estimate the number of graphene layers. Indeed, the number of layers is slightly increasing for offcuts between 0.05 and 1°off, and a more important increase for the 4°off-substrate (1.5 times more compared to the 1°off-substrate). We also detected an upshift and broadening of the G- and 2D-peak compared to exfoliated graphene. Both the upshift and broadening increase for the two peaks for larger offcuts.

In the second case, for the growth under 100% of H_2 at 1450°C, as expected the morphology and structure of graphene are not similar to the less hydrogenated growths. Graphene presents a two-dimensional growth without the manifestation of triangular clusters for the 0.05°-off sample; instead, wrinkles are detected with AFM and in-plane rotational disorder with LEED. Such observations are associated with a hydrogenated interface and freestanding graphene. However, we suspect the presence of few covalent bonds between graphene and the substrate, but more investigations are required for confirmation. In any case the hydrogenation of the interface is dominating under these growth conditions. Raman spectroscopy uncover some areas without any graphene on the 0.05°-off sample, confirming the challenging growth on this sample. Nevertheless, all samples exhibited G, 2D and D peaks attesting for graphene deposition with disorder. The number of layers estimated with Raman spectroscopy is increasing with the offcut but not exceeding 2.6 MLs for the 4°-off substrate. In addition, same as before, the G and 2D peaks are upshifting towards higher wavenumbers and broadening for substrates with larger offcuts.

In conclusion, both the growth sets for the two amounts of H_2 present different morphologies and different structures, but this is expected based on the previous H_2-Ar study. In addition, both sets show a similar behavior in Raman spectroscopy where the corresponding G and 2D bands seem to upshift for substrates with larger offcuts, associated with a broadening of both peaks in both cases. We will discuss in details these upshifts in **part 3.3**.

3.3. Strain in graphene on SiC: a Raman spectroscopy study

We have studied so far the influence of different parameters on the growth of graphene on SiC by CVD, such as the propane flow, the growth time, the growth temperature, the H_2 amount in the gas mixture and the substrate's miscut angle. The H_2 amount and the miscut angle seem to influence the graphene's properties, since we noticed with Raman spectroscopy a shift occurring for graphene peaks depending on these growth parameters. This shift can rise from different factors, such as a variation of the number of graphene layers and/or the doping concentration and/or the strain within graphene.

Previous studies [118,181] have investigated the influence of the H_2 amount in the gas mixture on the strain in graphene grown on SiC by CVD under H_2. In particular, the work in reference [181] has concluded on the basis of GIXRD that graphene on a hydrogenated interface is more strained than graphene on a buffer layer. In addition, the work in reference [118] allowed to conclude that the sample for which the wrinkles start to appear, when increasing the H_2 amount, is the most strained. Therefore, we suspect in our study a variation of the strain distribution when changing the H_2 amount in the gas mixture.

We will discuss in this part how to assess the strain in graphene with Raman spectroscopy and how to separate the effects of strain from other parameters (doping and graphene thickness) on Raman spectra. Before we examine in details our Raman spectra we will explain the origins of the strain in graphene based on the literature.

3.3.1. Origins of strain in graphene

Different studies attempted to evaluate the strain in graphene grown on the Si-face of SiC [165,181–183]. Yet, the origin of the strain is still a matter of debate, not to mention the inconsistency of the reported lattice parameters of graphene and their evolution with the temperature, which makes the task of estimating the strain even harder.

Ni et al. [165] attribute the strain in the graphene layer to the difference in lattice parameters between the ($6\sqrt{3}\times6\sqrt{3}$) super cell of SiC (31.935 Å, considering a_{SiC} to be 3.073 Å) and the graphene (13×13) super cell (31.928 Å, assuming a_{Gr} to be 2.456 Å). This lattice mismatch is expected to result in a tensile strain. However, the authors add that STM observations revealed that the SiC interface reconstruction does not always maintain its 6×6 periodicity, thus leading to a lattice parameter for the SiC super cell less than 30 Å, and therefore the strain in graphene will be compressive. On the contrary, J. Röhrl et al. [183] excluded completely the strain emanating from the difference in lattice parameters, by considering it negligible. They propose that a compressive strain rises from the difference in thermal expansion coefficients (TEC) between SiC and graphene when cooling down the sample from the growth temperature to room temperature. They also assume that graphene is strain free at the growth temperature. N. Ferralis et al. [159,182] argue that graphene can be either strain free or under tensile strain at the growth temperature, depending on the growth duration. They explain that longer growths will lead to a mechanical

equilibrium between the graphene and the substrate. The resulting strain at room temperature is the difference between the strain at the growth temperature and the compressive strain due to the difference in TEC after cooling down. In these studies, graphene was grown by Si sublimation of the Si-face of SiC under UHV, meaning that graphene is always expected to be associated with the ($6\sqrt{3}\times6\sqrt{3}$) buffer layer. On the other hand, our growth technique, carried out under hydrogen-argon near atmospheric pressures, allows to control the interface properties with the H_2 amount in the gas mixture. In other words, high H_2 amount leads to a hydrogenated interface and disordered graphene, while low H_2 amount results in well-ordered graphene grown on a ($6\sqrt{3}\times6\sqrt{3}$) buffer layer. We believe that this influence on the interface properties will lead to different strain distribution in the two cases. Even though our growth mechanism is not the same as the Si sublimation technique, we can still easily adopt the reasoning considered in the literature [159,165,182,183] for the origin of strain in in graphene.

In our growth conditions, graphene with a buffer layer can be achieved with low H_2 amount in the range of 9% and 33% under 1550°C. In this range, SiC undergoes a surface reconstruction, i.e. the ($6\sqrt{3}\times6\sqrt{3}$) reconstruction evidenced by LEED measurements, which should coincide with the graphene (13×13) super cell as already attested in many studies in the literature [105,165]. If we assume that graphene stretches or contracts to perfectly fit both super cells, strain should depend on the difference in lattice parameter. For this very simple calculation, the difficulty lies in the choice of the lattices parameters. Different values of the graphene relaxed lattice parameter can be found in the literature. Some studies adopt the in-plane lattice parameter of graphite which ranges from 2.456 Å or 2.4589 Å to 2.464 Å [24–26]. For instance, Ni et al. considered 2.456 Å [165] to predict the lattice mismatch. To complete the picture, another factor contributes to the strain in graphene, other than the lattice mismatch: the difference in TEC between SiC and graphene. SiC will undergo a contraction of -0.85%, if we consider 3.107 Å [184,185] and 3.081 Å [166] to be the in-plane lattice parameters at 1823 K (our growth temperature) and 300 K respectively. While for graphene, we will consider the values of graphite, ergo a contraction of -0.1% [183,186,187] when cooling down to room temperature. As a result, upon cooling down, the graphene layer should suffer a contraction of -0.75% due to the difference in TEC. This result matches the work of N. Ferallis et al.[182] and J. Röhrl et al.[183], who estimated a contraction of -0.8% of the graphene layer. Even though their growth temperature is lower than ours, the TECs of SiC and graphite seem steady between high temperatures [186,187]. To summarize, two factors contribute to the development of strain in graphene grown on SiC: the lattice mismatch and the TEC mismatch. As a result, at room temperature the residual strain is the sum of these two mismatches. If we consider the reasoning of N. Ferralis et al. [159,182], graphene can be strained at the growth temperature because of the lattice mismatch with the $6\sqrt{3}$-SiC structure, then when cooling down the graphene layer will undergo a contraction due to the TEC mismatch.

To estimate the strain at the growth temperature we have to consider the lattice parameters at the growth temperature. The 6H-SiC lattice expands from 3.081 Å at room temperature [166] to 3.107 Å at 1550°C [184,185] i.e. our growth temperature. For graphene, we will consider the

parameters of graphite, which expands at 1550°C, resulting in a lattice parameter of 2.470 Å [187]. Accordingly, the lattice mismatch at our growth temperature between the (6√3×6√3)-SiC and the (13×13)-graphene is +0.575% ("+" for tensile strain), and not zero as J. Röhrl et al. [183] have considered. For information, all these parameters are summarized in table 3.4. Accordingly, it is possible to anticipate the strain at room temperature as the sum of the tensile strain (+0.575%) at the growth temperature due to lattice mismatch between the (6√3×6√3)-SiC and (13×13)-graphene and the compressive strain (-0.75%) due to the thermal mismatch, resulting in a compressive strain of -0.18% at room temperature. Note that few discrepancies can rise from these predictions, for instance the tensile strain that we predicted at the growth temperature (+0.575%), can be smaller depending on the growth time, as N. Ferralis et al. [182] suggested. Likewise, it is also possible to predict a contraction of -0.38% for graphite instead of -0.1% when cooling down from reference [187], which will lead to a graphene layer under tensile strain at room temperature.

Table 3. 4: *Literature parameters for SiC and graphene/graphite used in the theoretical predication of the strain.*

Parameters	**Lattice parameters at T_G = 1550°C**	**References**	**TEC mismatch between T_G and 300°K**	**References**
SiC	3.107 Å	[184,185]	-0.85%	[166,184,185]
Graphene/ Graphite	2.470 Å	[187]	-0.1%	[183,186,187]

These strain predictions can be affected by different parameters, mainly the values of lattice parameters and TEC, but also it can be influenced indirectly by the growth parameters, such as the growth temperature, the growth time and the hydrogen amount in the gas mixture [118,181]. For instance, N. Ferralis et al. [159,188] argue that the strain at the growth temperature can be reduced for longer growths by creating a mechanical equilibrium between the SiC and the graphene super cells. Secondly, the growth temperature and the hydrogen amount influence the graphene's structure and the hydrogenation of the interface, which is expected to affect the strain in the following way: when the graphene is grown on a 6√3 structure, for relatively low H_2 % (9% to 33% in our current study), the buffer layer is sharing covalent bonds with the substrate, forcing the graphene layer to be well ordered and under substantial tensile strain at the growth temperature, and thus leading to a minimum value of residual strain at room temperature. When increasing the hydrogen in the gas mixture, hydrogen will replace the covalent bonds of the buffer layer with the substrate and thus hydrogenating the interface and decreasing the influence of the buffer layer on the graphene layer. As a consequence, at high hydrogen amount (75% to 100%), the interface should be hydrogenated and the graphene layer is supposed to grow without a buffer layer and strain free at the growth temperature with different orientations, because it is not bound to the

substrate. Therefore, the only contributor to the strain is the TEC mismatch, which should be equal to -0.75%. This amount of strain cannot stay accumulated and needs to be relieved, this is why for these type of growths (H_2-rich) we observe wrinkles at the surface, which we attribute to a strain relief mechanism [82,113,189]. Other studies attribute strain relaxation to the roughening of step edges [159,188]. For the intermediate case, around 50% of H_2 in the previous set of samples grown at 1550°C (or 32% of H_2 in reference [118] grown at 1450°C), the interface is partially hydrogenated and the buffer layer still exists along with disorder. We believe that in this case the presence of the buffer layer will prevent the graphene layer to relieve strain. This is why the strain is supposed to be at its maximum for the intermediate case.

To conclude, different studies have attempted to estimate the strain in graphene grown on SiC. However, the origins of the strain are still debatable and difficult to predict, mainly because of the different lattice parameters and thermal expansion coefficients reported in the literature for graphene, graphite and SiC. Regardless of these discrepancies, we believe that the best approach is to consider the lattice mismatch between the $(6\sqrt{3}\times6\sqrt{3})$-SiC and the (13×13)-graphene super cell, and the TEC mismatch which adds up when cooling down to room temperature. Different growth parameters can influence the strain in graphene, such as the H_2 amount in the gas mixture. In fact, hydrogen has a direct influence on the interface between SiC and graphene, which affects the strain. Graphene grown with low H_2 % in the gas mixture is more likely to be associated with a buffer layer sharing covalent bonds with the substrate. The strain in this case originates from the difference in lattice parameters between the SiC and graphene super cells, added to the difference in TEC when cooling down the sample. For high H_2 % the interface will be hydrogenated, hence we assume that graphene will grow relaxed at the growth temperature since it is poorly bound to the substrate. At room temperature, due to the difference in TEC the graphene layer will be under tremendous amount of thermoelastic strain. This strain can be slightly relieved with the formation of wrinkles at the surface and/or surface roughening. In the intermediate case of H_2 %, we assume that the graphene layer is under the maximum amount of strain, because the buffer layer is still present and thus preventing any strain relaxation, even though it can be partially hydrogenated.

3.3.2. H_2 influence on strain

In **part 3.2.3**, we have investigated the influence of the H_2 amount in the gas mixture on the growth of graphene on the basis of AFM, LEED and Raman spectroscopy. We came to the conclusion that H_2 influences directly the graphene properties, mainly the morphology, the thickness and the structure. When H_2 is mixed with argon, at low H_2 percentages (9%-33%), a $(6\sqrt{3}\times6\sqrt{3})$ interface reconstruction is manifested, known as the buffer layer, whereas for a high H_2 percentage (75%), graphene is grown with disorder and a hydrogenated interface. For an intermediate amount of H_2 (50%) both structures coexist together. We also detect a shift in the graphene spectra with Raman spectroscopy for the different samples grown with different H_2 amounts. In fact, we suspect that the hydrogenation of the interface can influence the electrical properties of graphene and the strain within the graphene layer, based on our previous discussion on the origins of strain.

We will investigate in this part the reasons behind the Raman shift for the different samples grown with different H_2 amounts. We present in Fig. 3.27 the 2D-frequency as a function of the G-frequency for the different samples. As we previously mentioned, Raman maps with different sizes were carried out for the different samples, therefore for the samples of 9, 17, 25 and 75% of H_2 121 spectra were measured, whereas for the samples 33% and 50% of H_2 905 and 1541 spectra were recorded, respectively. The solid orange line in Fig. 3.27 corresponds to the expected behavior of the 2D-frequency as a function of the G-frequency when a monolayer graphene is under biaxial strain only [90]. The solid magenta line represents the expected behavior of the 2D-frequency as a function of the G-frequency for strain-free graphene with varying density of holes [154]. In this particular study, the dark green ring in Fig. 3.27 represents the reference frequencies at 1582 cm^{-1} and 2688.5 cm^{-1}. These values were recorded experimentally on strain free and undoped graphene on SiC in the same Raman setup for the same laser wavelength as our graphene samples.

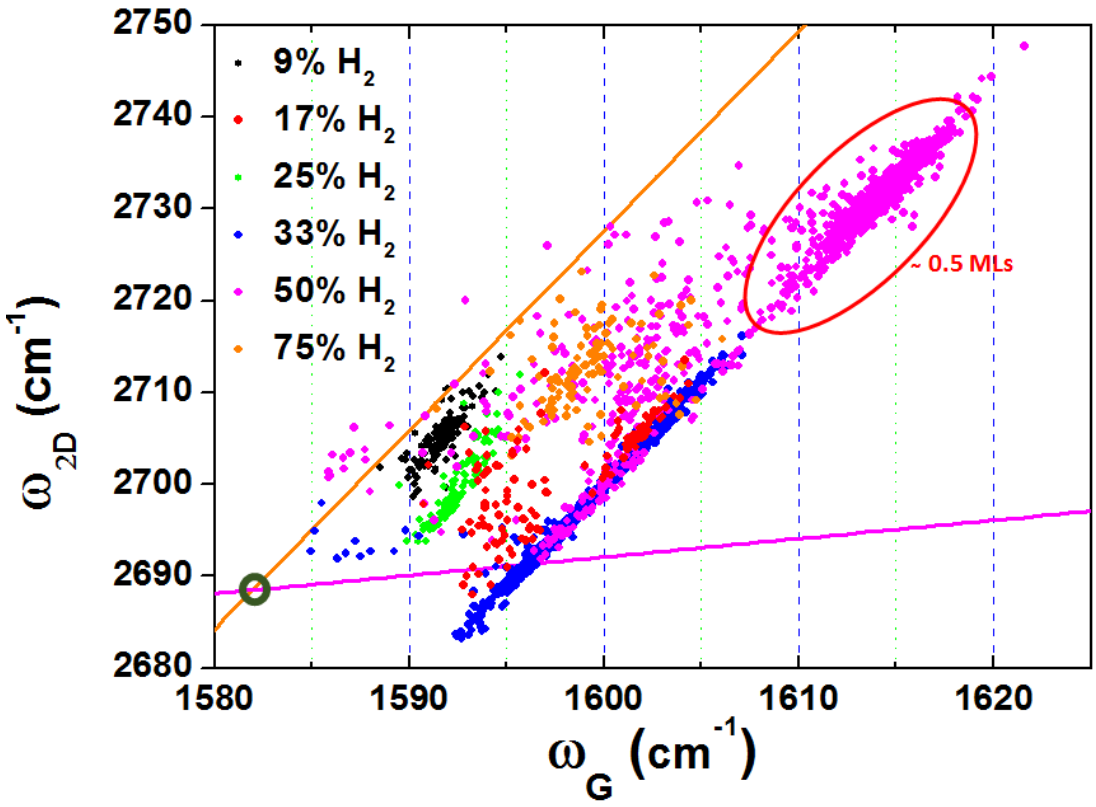

Figure 3. 27: *2D-frequency as a function of the G-frequency for the different samples grown with different H_2 amounts at 1550°C. The solid orange line is the ratio 2D over G when a monolayer of graphene is under strain only. The solid magenta line is the expected behavior for strain-free graphene with varying hole density. The green ring represents the reference position.*

Compared to the reference frequencies (1582 and 2688.5 cm^{-1}) all the samples present upshifted G and 2D peaks, probably because the graphene layer is thicker, more doped and more

strained. It is not easy to quantify the Raman shift due to the different parameters affecting this shift, but we will go through each parameter that can contribute to the shift in order to understand its effects on the Raman spectra. First, the number of layers affects only the 2D-band frequency [141], hence an increase in the number of layers should lead to an upshift of the 2D-band only. On the other hand, two other parameters can influence the shift as well: the carrier density and the strain. To investigate the doping and strain effect we will base our reasoning on the work of Das et al. and Ji. Eun Lee et al. [150,154]. Das et al. [150] have studied the behavior of Raman spectra for doped graphene while controlling the doping concentration by applying a top-gate voltage. In these two mentioned studies, it was found that increasing the carrier density is translated into a more important upshift in the G-band compared to the 2D-band. Accordingly, doping of the graphene film should lead to a horizontal shift in the f(G, 2D) curve. Finally, Ji. Eun Lee et al. [154] demonstrated that a compressive strain will result in a 2D-upshift two times more important than the G-upshift.

We have previously presented the number of graphene layers for the different samples estimated with Raman spectroscopy: for the growths with 9, 25, 33 and 75% of H_2 the number of layers is around 1.4, 1.2, 1 and 2 MLs, respectively. For the growth with 17% of H_2, the calculated number of layers presented a bimodal distribution around 0.5 and 1.3 MLs. Finally, for the 50% H_2-growth the thickness is around 0.5 MLs. We suspect that the non-uniform distribution we detect in Fig. 3.27 rises from the non-uniform distribution of the number of layers for each sample. For example, if we take the 17% H_2-sample (red dots), we see that we have indeed two groups of dots in Fig. 3.27 which correspond to the bimodal distribution of the number of layers. For the 50% H_2 sample (magenta dots), the dots indicated by the red circle correspond to 0.5 MLs, whereas the ones around the blue dots correspond to 1 ML. We can already notice the complicated task of evaluating the shift due to the non-uniform growth on the different samples, but we will attempt to comment the general trends we observe in Fig. 3.27. First, we detect a horizontal shift between the 9%-sample (black dots) and the 33%-sample (blue dots). For this reason, we suspect a variation of the carrier density between these samples. Second, the magenta dots with 0.5 MLs are upshifted both for the G-peak and the 2D-peak. The shift is both vertical and horizontal at the same time suggesting regions under more strain. The 75% H_2-sample appears slightly vertically upshift compared to the other samples, except the 50% H_2-sample. This could be due to the thickness of the graphene layer, since the 75% H_2-sample results mostly in 2 graphene MLs, while the other growths lead to thicknesses less than 1.5 MLs. We also detect a horizontal upshift for the 75% H_2-sample compared to the 9 and 25% H_2-samples, which could be due to a difference in carrier density. Finally, the 33% H_2-sample presents a non-uniform distribution in Fig. 3.27 (blue dots), even though the thickness is mainly around 1 ML, this could rise of a non-uniform distribution of strain across the sample.

In conclusion, it seems difficult to assess the effects of the different parameters on the Raman shift, since we suspect that the different parameters are changing at the same time: the samples are not uniform, with different thicknesses across each sample, in addition to varying carrier density and varying strain distribution. Besides, they are not uniform among each other, where each sample has a number of layers different than the other. For this reason, we cannot suppose any change in strain between the different samples, at least not before we optimize these

growths to enhance the uniformity and second it seems important to have information concerning the carrier density of each sample to correlate with Raman spectroscopy. The 50% H_2-sample seems to have areas under more strain compared to the other samples, but these areas present incomplete layers of graphene (0.5 MLs) and cannot be compared with the others. In addition, because of this non uniformity, we were not able to make the same conclusions as in the references [118,181] that a hydrogenated sample is under more strain than a sample with a buffer layer and that the sample with both structures (the $6\sqrt{3}$ and IRD) should be the most strained.

3.3.3. Substrate's miscut angle influence on strain

We have discussed in **part 3.2.4** on the basis of AFM, LEED and Raman spectroscopy the influence of the substrate's miscut angle on the growth of graphene; in particular, on the morphology, the structure and the thickness of the deposited graphene layer. We also noticed with Raman spectroscopy a shift in the graphene spectra dependent on the substrate's miscut angle. We will discuss in the following the origins of this shift for the two growth conditions we employed for the offcut study: 17% of H_2 at 1550°C and 100% of H_2 at 1450°C. Note that in the offcut study we have not done any map scanning with Raman spectroscopy as it was the case for the hydrogen-argon study, but instead for each sample different spectra were recorded at different regions. The reference frequencies considered for this study are the same as before with G and 2D peaks around 1582 cm^{-1} and 2688.5 cm^{-1} respectively.

3.3.3.1. Growth with 17% of H_2

To better visualize the Raman shift, we present in Fig. 3.28 the 2D-frequency as a function of the G-frequency for the different samples. The solid orange line corresponds to a monolayer graphene under biaxial strain only [90]. The solid magenta line represents strain-free graphene with varying density of holes [154]. The samples seem to present uniform data except for the 1°-off sample (green dots), which presents data points between the red and blue dots but outspread among each other. All the samples present G and 2D peaks upshifted compared to the reference frequencies, probably due to a difference in thickness, carrier density and strain within the graphene layer.

To quantify the Raman shift we will attempt to exclude the least of the causes to find the main contributor to the shift. First, an increase in the number of layers should lead to an upshift of the 2D-band only [141]. If this is the case, we expect to see a vertical evolution of the data in Fig. 3.28 but instead we see both vertical and horizontal evolution due to the simultaneous upshift of the G-band. Besides, the number of layers is only slightly changing for the first three offcuts (0.05, 0.2 and 1°-off). This minor increase in the number of layers is not enough to induce the average 20 cm^{-1}-shift that we detect between the 0.05 and the 1°-off sample, there has to be another parameter contributing to the upshift, either doping or strain. On the other hand, the upshift seems to be more vertical than horizontal between the 1°- and 4°-off samples, which is consistent with the increase in the number of layers from 1.8 MLs to 3 MLs respectively. Therefore, for the 4°-off sample the upshift could be mainly caused by the increase in thickness.

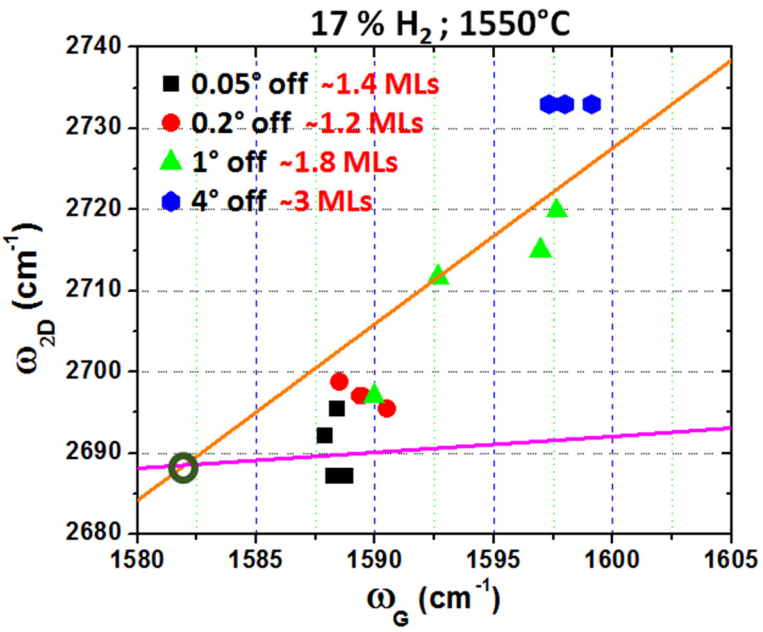

Figure 3. 28: *2D-frequency as a function of the G-frequency for the different samples grown with 17% of H_2 at 1550°C. The solid orange line is the ratio 2D over G when a monolayer of graphene is under strain only. The solid magenta line is the expected behavior for strain-free graphene with varying hole density. The green ring represents the reference position.*

To investigate the doping and strain effect we consider the work of Das et al. and Ji. Eun Lee et al. [150,154]. An increase in the carrier density should lead to a more important upshift in the G-band compared to the 2D-band, hence a more horizontal evolution of the f(G, 2D) curve. In Fig. 3.28, the average G-frequency shifts ~6 cm^{-1} (resp. 10 cm^{-1}) between the 0.05°-off sample and the 1°-off sample (resp. 4°-off sample). Based on the data of Das et al. [150] and if we consider that the G-peak shift originates from doping, for the 6 cm^{-1}-shift of the G-peak, the 2D-peak should barely move, and for the 10 cm^{-1}-shift of the G-peak, the 2D-peak should shift about 8 cm^{-1}, which is not consistent with our results since the 2D-peak shifts 20 cm^{-1} (resp. 43 cm^{-1}) between the 0.05°-off sample and the 1°-off sample (resp. 4°-off sample). We can conclude that the doping effect is small or at least negligible compared to other effects such as the number of layers and compressive strain. Indeed, Ji. Eun Lee et al. [154] have demonstrated that a compressive strain will result in a 2D-upshift two times more important than the G-upshift, which agrees with our observations. Therefore, we can deduce that the upshift we detect is mainly due to an increase in compressive strain with the substrate's offcut. However, since the 4°-off sample is more vertically shifted, the effect of the number of layers on the shift is also important in this last case, probably more important than the strain effect.

Finally, now that we have narrowed down the cause of the upshift to the strain, we can assess the broadening of the peaks in Fig. 3.24(b, c) when the offcut is larger. As we mentioned before, the number of graphene layers is known to influence the 2D-peak width, but not the G-peak width. However, the presence of a non-uniform strain on the same sample, could broaden

both G and 2D peaks. Therefore, it is possible to attribute the broadening of the G and 2D peaks on the high wavenumber side to non-uniform strain distribution when increasing offcuts.

In conclusion, we have attributed the upshift of the G and 2D bands with the offcut to mainly compressive strain, but we cannot rule out completely the effects of doping and the number of layers. Instead, we suspect that the main contributor to the upshift is an increase in compressive strain for the first three samples (0.05, 0.2 and 1°-off), but for the 4°-off sample the increase in thickness appears to be the dominating factor. The carrier density effect is supposed to be minimal compared to the strain and the thickness effects. Further observations related to the peaks FWHM reveal that the strain distribution might not be uniform in the graphene layer and this non-uniformity is increasing with the offcut.

3.3.3.2. Growth with 100% H_2

For the growth with 100% of H_2 at 1450°C, we conducted a similar study as before: to better visualize the upshift we present in Fig. 3.29 the 2D-frequency as a function of the G-frequency for the different samples. The orange solid line corresponds to a monolayer graphene under only strain [90], whereas the solid magenta line represents strain-free graphene with varying density of holes [154].

The 0.05°-off sample data in Fig. 3.29 seem scattered attesting for non-uniform deposition. It is therefore difficult to include this sample in our discussion, but still it cannot be completely excluded. In the following, we will consider the same reasoning as before to explain the upshift of the G and 2D peaks. The upshift in this case is neither horizontal nor vertical, but instead parallel to the solid orange line. As we alluded before, three parameters can influence the upshift of these Raman peaks: the increase in the number of graphene layers, in the doping and the increase in compressive strain. The 2D-peak is shifting 45 cm^{-1} between the 0.2°-off sample and the 4°-off sample. It is not possible for doping to cause this amount of shift, since the 2D-peak barely shifts with doping [150]. It is also not possible to attribute this shift to the increase in number of layers, since in our case we have one extra layer between the 0.2°-off sample and the 4°-off sample. Therefore, we can conclude that while we cannot completely rule out the influence of the increase in number of layers or doping, it is safe to say that the upshift is mainly caused by an increase in compressive strain. Finally, if we consider the broadening of the peaks in Fig. 3.26(b, c), and since the broadening affects both peaks, we can make the same conclusion as before that there is a non-uniformity in the strain distribution along the sample.

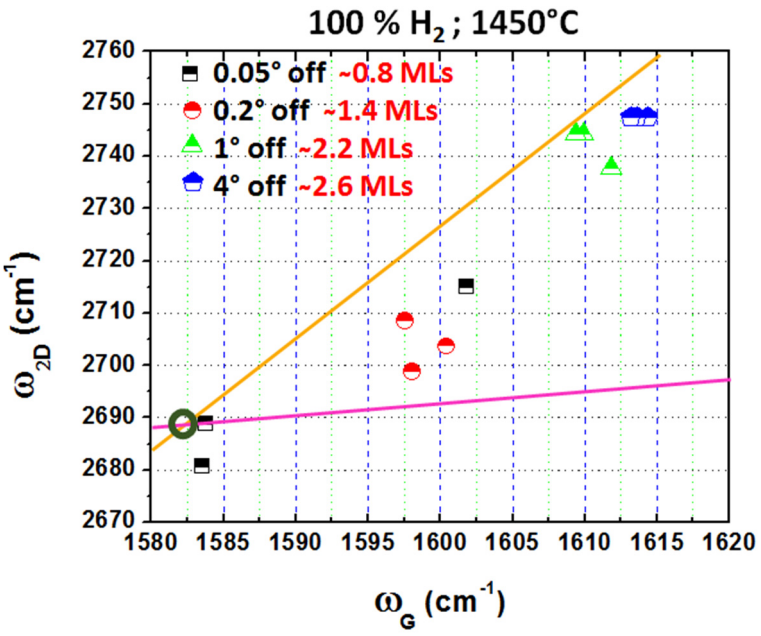

Figure 3. 29: *2D-frequency as a function of the G-frequency for the different samples grown with 100% of H_2 at 1450°C. The solid orange line is the ratio 2D over G when a monolayer of graphene is under strain only. The solid magenta line is the expected behavior for strain-free graphene with varying hole density. The green ring represents the reference position.*

3.3.4. Discussion and conclusion

We have attempted to study the origin of the Raman shift for different samples grown with different H_2 amounts in the gas mixture. However, we believe that the different parameters contributing to the shift such as the carrier density, the thickness and the strain, are changing at the same time, which makes the task of evaluating each parameter nearly impossible. In addition, the samples are not uniform in terms of thickness, where each sample presents different number of layers compared to the others, along with a non-uniform distribution of the thickness across its surface. This non-uniformity will certainly influence the strain, for example the 50% H_2-sample is more strained compared to the other samples, probably because it presents incomplete graphene layers. Tiberj et al. [145] suggested that incomplete graphene layers can be strained because they are bound to the SiC substrate and unable to relieve strain, based on STM measurements.

For all these reasons, it is complicated to compare the samples to one another and understand the Raman shift. Further studies are required to enhance the uniformity of such samples and electrical measurements are necessary to deduce the carrier density of each sample. At this point, we cannot make any affirmative conclusions for this set of samples. Nevertheless, we were able to point out few observations, such as a possible variation in the carrier density among the samples with the different H_2 amount. If we assume that a negative charge transfer can occur from the substrate to the graphene layers when a buffer layer is grown [105], hydrogenating the interface will definitely have an influence on this charge transfer. In fact, when we are increasing the

hydrogen amount in the gas mixture for the growth of graphene, we are introducing more hydrogen at the interface and replacing the buffer layer's shared bonds with the substrate, hence probably reducing the charge transfer. In addition, we expect a hole doping from the atmosphere [19,154], which is usually compensated by the negative charge transfer from the substrate. Now if we are considering that the negative charge transfer is being reduced when increasing the H_2 amount, we therefore expect an increase in the hole density, associated with an upshift of the corresponding Raman G-peak.

Regarding the substrate's miscut angle, we have also discussed the influence of this parameter on the growth of graphene. To do so, we have considered different SiC substrates with different miscut angles ranging between 0.05, 0.2, 1 and 4°. We also considered two sets of samples grown for the same duration and with the same propane flow rate, but under different amounts of H_2 and different temperatures to influence the hydrogenation of the interface. In other words, the first set was grown with 17% of H_2 at 1550°C to promote the formation of a buffer layer, whereas the second set was grown with 100% of H_2 at 1450°C, to instigate the hydrogenation of the interface and minimize the effects of the buffer layer. Our goal was to remove completely the buffer layer and replace it with Si-H bonds at the interface to create two extreme cases between the two grown sets. We were able to achieve that and the Si-H bonds are dominant in the second case, since we observed wrinkles and disorder with AFM, LEED and Raman, associated with a hydrogenated interface. Further Raman investigations revealed an upshift of the G and 2D peaks for substrates with larger offcuts, which we attributed to an increase in compressive strain with the offcut. Even though this upshift can also be emanating from an increase in the number of layers and doping, we demonstrated that their contribution is minor compared to the strain contribution. We summarize these results in Fig. 3.30 for the two graphene sets.

In Fig. 3.30, besides the 0.05°-off sample, the 100% H_2-samples seem to have G and 2D peaks more upshifted compared to those of the 17% H_2-samples. This upshift is less likely to be caused by the variation in the number of layers because the thickness is more or less the same for the two set of samples. For example, the 0.2°-off sample presents 1.2 MLs for the 17% H_2-growth and 1.4 MLs for the 100% H_2-growth. In addition, the 4°-off sample presents 3 MLs for the 17% H_2-growth, but 2.6 MLs for the 100% H_2-growth. One would expect higher 2D values for the 4°-off sample grown with 17% of H_2, but this is not the case in Fig. 3.30. Therefore, we believe that the reason behind the more important upshift for the 100% H_2-samples is mainly due to more important compressive strain. This difference in compressive could be rising from the two different origins of strain, either from the difference in lattice parameters for the 17% H_2-case or from the thermal mismatch for the 100% H_2-case. As we have discussed in **part 3.3.1**, the samples grown with low H_2 amount are expected to be associated with a buffer layer. The presence of a buffer layer leads to an intrinsic strain due to the lattice mismatch between the $(6\sqrt{3}\times6\sqrt{3})$ SiC super cell and the (13×13) graphene super cell, in addition to the thermoelastic strain due to the thermal expansion mismatch between SiC and graphene. The addition of both of these strains will lead to a weaker strain compared to the case dominated by the thermoelastic strain only when the sample

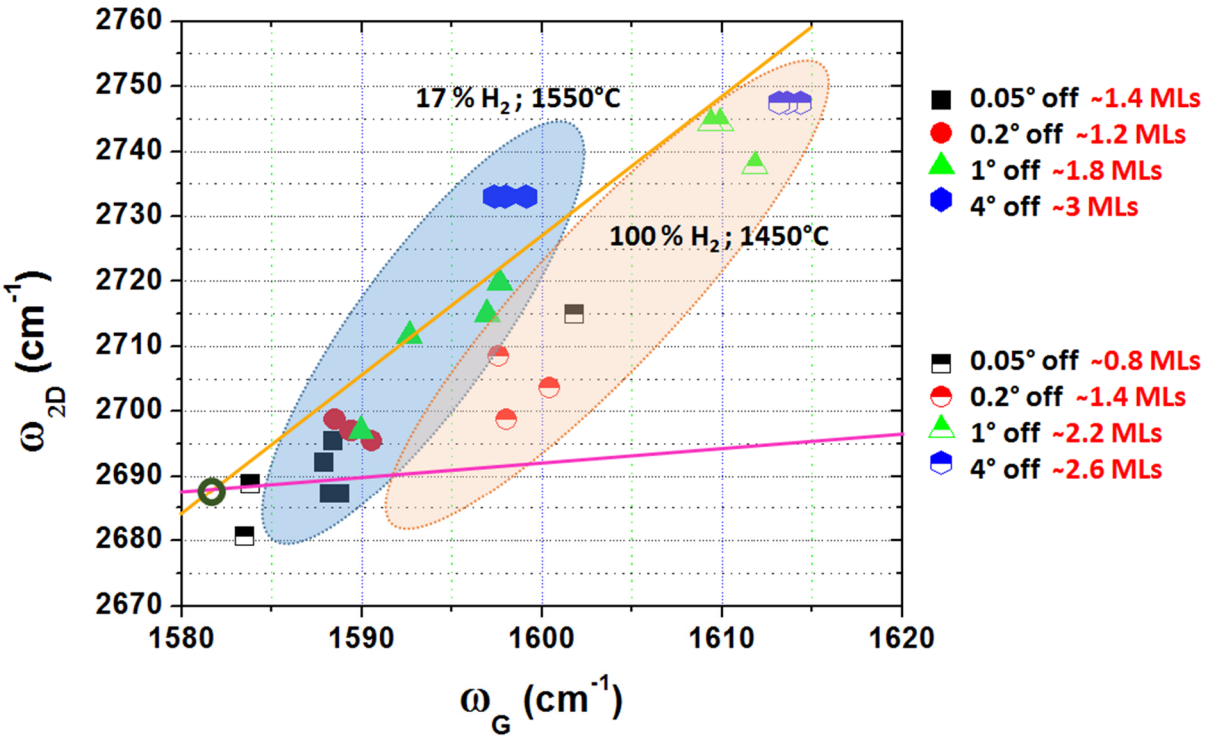

Figure 3. 30: *2D-frequency as a function of the G-frequency for the different samples grown with 17% of H_2 at 1550°C (blue zone) and with 100% of H_2 at 1450°C (pink zone).*

is grown with important H_2 amounts. In fact, when the sample is grown with high H_2 %, the graphene is supposed to grow relaxed at the growth temperature since it is poorly bound to the substrate. Then, when cooling down, thermal strain will accumulate and lead to important compressive strain at room temperature.

The second important observation we made previously was that both the G and 2D peaks become wider for larger offcuts in both growth conditions. Since this behavior is occurring for both peaks, we attributed it to a non-uniform strain distribution across the sample, which is increasing when the offcut is larger. We will attempt in the following to explain why the compressive strain is increasing with the offcut for the same growth conditions and why the strain is supposed to be non-uniform. The reasonable approach is to ascribe this behavior to the varying parameters when the substrate's offcut is changing, which is the step density. In fact, larger offcuts imply smaller and more frequent steps. For example, the 0.2°-off substrate (Fig. 3.23(b)) exhibits a step edge every ~ 200 nm, whereas the 4°-off substrate (Fig. 3.23(d)) presents a step edge every ~ 50 nm. We believe that this increase in step density is behind the increase in compressive strain in the graphene sheet. In addition, if we distinguish between two areas on the surface of the sample: the step terrace and the proximity of the step edge, we can attribute the non-uniform strain distribution to the presence of these two different areas. Indeed, a Raman study have shown that graphene on SiC is under a lot more strain at step edges than on the terraces [190]. Therefore, increasing the step density for larger offcuts increases the step edge density i.e. the area under

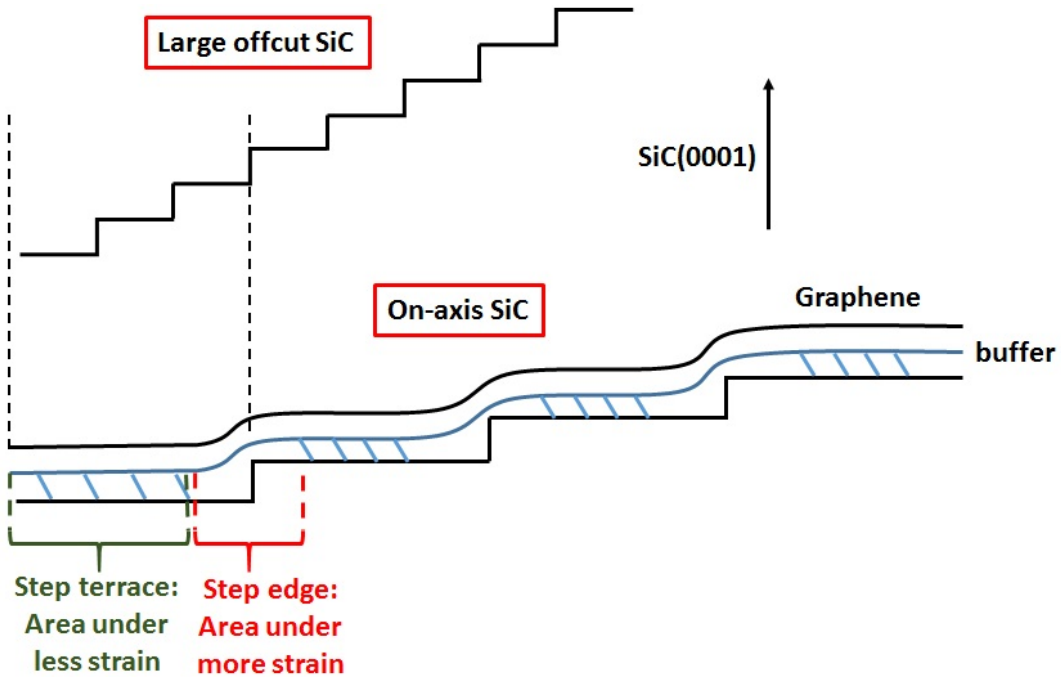

Figure 3. 31: *Schematic illustration showing the step density for on-axis and off-axis SiC substrates, and the strain distribution.*

more strain, resulting in a more strained sample. We illustrate the strain distribution in Fig. 3.31 and the difference between substrates with two different offcuts, for the case of graphene on a buffer layer. This behavior seems to be the opposite of what is usually expected for heteroepitaxies where the relaxation of the strain is supposed to happen at the step edges.

So far, we have correlated the increase in compressive strain to the increase in step density with the offcut, but we have not discussed the reason behind the presence of more strain at the step edges. In a previous study [191] we assessed this issue for the growth under 17% H_2, i.e. graphene with a buffer layer. We assumed that the buffer layer encounters some difficulties to bond to the substrate around the step edges, therefore around these areas the strain coming from the lattice mismatch does not exist and the dominating strain is thermoelastic strain. This could be the reason behind more important strain at the step edges. However, investigating the second graphene set grown with 100% H_2, in conditions promoting the hydrogenation of the buffer layer and minimizing its effects, the thermoelastic strain is dominating along the whole surface, therefore our previous reasoning is not valid in this case. There must be another reason for the increase in strain and the non-uniform strain distribution. If we go back to the Raman estimation of the graphene thickness, we notice that each sample presents a decimal number of layers, probably due to the presence of extra layers or patches of multilayers of graphene. The AFM topographic images do not reveal the presence of such patches but if we examine the phase image we can uncover such areas.

We show in Fig. 3.32, AFM phase images of the 0.2 and 1°-off samples prepared with 17% of H_2 at 1550°C. As we can see in Fig. 3.32(a), there are regions with darker contrast between two

adjacent steps, indicated by red arrows, attesting for extra graphene patches in these areas. Same for the 1°-off samples, presented in Fig. 3.32(b), we can discern areas with different contrasts. The difference is not as obvious as the previous sample but we suspect a non-uniform distribution of the number of layers. Concerning the samples grown with 100% of H_2 at 1450°C, we show an example in Fig. 3.32(c) of the phase image of the 0.2°-off sample. We can see in the phase image few areas with darker contrast, indicated by white arrows, which we attribute to extra graphene patches. We correlate this non-uniform thickness distribution, due to extra graphene patches at step edges or between steps, to the non-uniform strain distribution. It is possible that the areas with extra patches (in the step edge region) are more strained than the areas with less graphene layers (at the step terrace). The higher strain for thicker graphene areas could be due to an increase of the strain with the increase in the number of layers. This could explain the broadening of both of the G and 2D peaks in the Raman spectra. If it was only the 2D-peak that was broadening, we would have attributed it to the non-uniform thickness, but in fact the G-peak is broadening as well, meaning that the non-uniform thickness is leading to a non-uniform strain distribution and affecting both G and 2D peaks. Now when the offcut is increasing, the morphology is not changing with the offcut, only the terraces are getting smaller and the density of step edges is increasing. Therefore, we assume that the density of the areas under more strain will increase as well with the

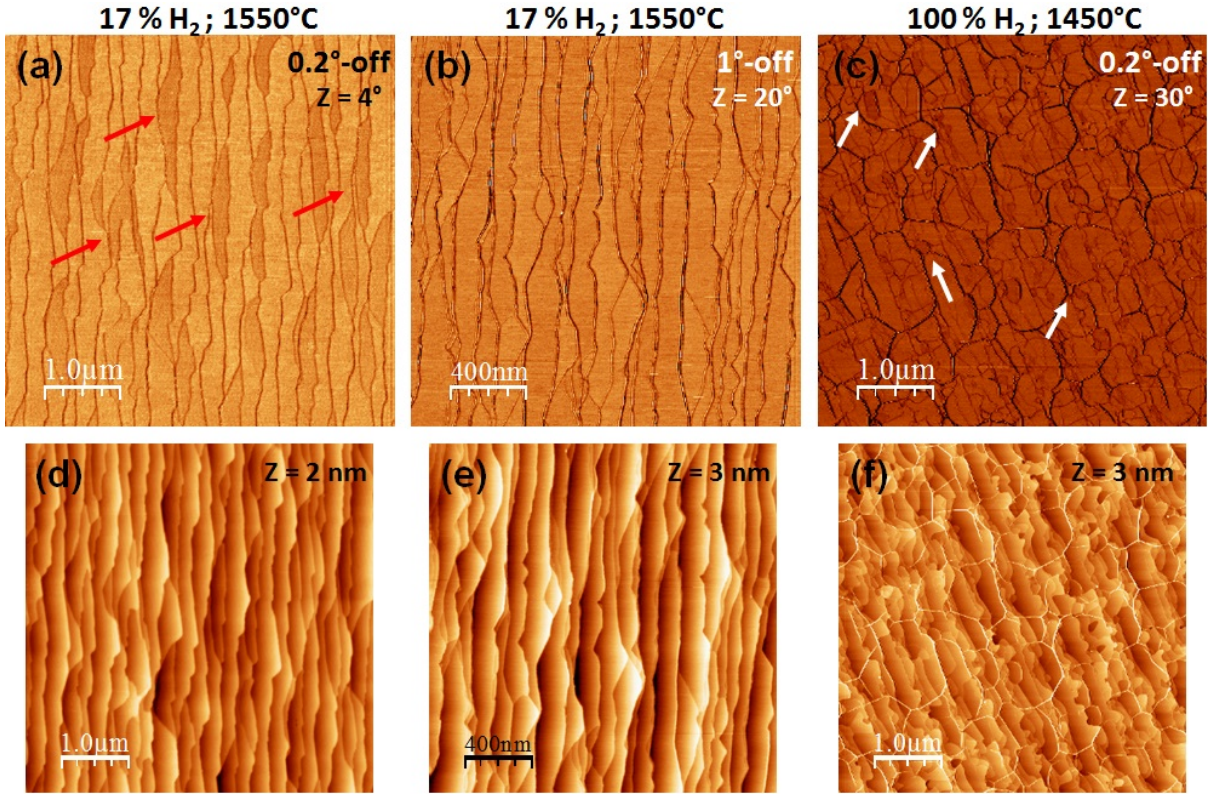

***Figure 3. 32: (a)** and **(c)** 5×5 µm² and **(b)** 2×2 µm² AFM phase images of the different growths: **(a)** 17% H_2 at 1550°C on the 0.2°-off substrate, **(b)** 17% H_2 at 1550°C on the 1°-off substrate and **(c)** 100% H_2 at 1450°C on the 0.2°-off substrate. **(d)** to **(f)** the corresponding topographic images.*

offcut, which explains the higher compressive strain for larger offcuts detected with Raman spectroscopy.

As a conclusion, we have studied the influence of the substrate's miscut angle on the growth of graphene under two different growth conditions: 17% and 100% H_2. In terms of morphology, the growth seems more challenging on the on-axis substrates, regardless of the H_2 amount in the gas mixture. From these two offcut sets we noticed that the 100% H_2-samples are more strained than the 17% H_2-samples, which we attributed to the dominating thermoelastic strain in the case of the 100% H_2-growths. In addition, we detected an increase in compressive strain for larger offcuts, which we attributed to the increase of the step-edge density with the offcut. In fact, the non-uniform strain distribution made us distinguish between two areas of different strain amounts along the surface: the step-terrace and the step-edge. We noticed that in the area of the step-edge we are very likely to have extra graphene patches, regardless of the H_2 amount, leading to non-uniform thickness distribution and affecting the strain distribution. This non-uniformity becomes more important for larger offcuts, since the step-edge density is increasing. We first assumed that this non-uniformity rises from different origins of strain (lattice mismatch and thermal expansion mismatch) for the buffer layer case. However, this non-uniformity exists as well in the case of the hydrogenated interface, when the thermoelastic strain is dominating across the whole surface, which led us to consider the step edges as areas where graphene is under more strain because it is thicker. In all cases, regardless of the origin of the strain, the ideal offcut for the growth of graphene on SiC seems to be around 0.2° for the 17% and 100% H_2 growth conditions. In this case the strain is minimal, which does not jeopardize the mobility of charge carriers, the growth is two dimensional and uniform; and the number of layers is close to a single layer of graphene.

3.4. Optimized growths and performances

Graphene is known for its remarkable electrical properties, especially its improved charge carrier mobility, yet so far we have not mentioned the electrical properties of our graphene since we were focusing on the growth parameters. It was important to discuss the role of each of the growth parameters, because once we understand which parameter will affect what, it will be possible to better control the growth and produce uniform graphene, since we suppose that the non-uniformity has a bad influence on the electrical properties of graphene. We present in this part our attempts to make the graphene growth more uniform.

First, we believe that the substrate's miscut angle has a direct influence on the charge carrier mobility. A study done by C. Dimitrakopoulos et al. [192] on graphene grown by Si sublimation of SiC (0001), revealed that the mobility is reduced for substrates with larger offcuts. The carrier mobility was recorded on Hall bars in the direction perpendicular to the step edges. They also illustrated the decreasing mobility with the decreasing width of the SiC terraces (i.e. for larger offcuts). This seems reasonable since the charge carriers are less likely to be scattered by any defects on flat surfaces with large terraces. Besides, as we have demonstrated before, substrates with larger offcuts induce a more important strain to graphene, which could also reduce the mobility. Therefore, it is better to aim for substrates with lower offcuts for applications requiring important carrier mobility. However, other issues rise when considering on-axis substrates. As we have seen previously, it can be challenging to achieve two-dimensional and uniform growth on low offcut substrates, whether under 17% H_2 or 100% H_2. In fact, the growth on the 0.05°off-substrate under 17% H_2 led to the manifestation of triangular clusters, whereas the growth under 100% H_2 was not uniform as some areas presented no signs of graphene deposition with Raman spectroscopy. Even for the 0.09°off substrate presented in **part 3.2.3**, the growth was not uniform. AFM and Raman spectroscopy revealed areas without any graphene, see Fig. 3.19(c) for the 25% H_2-growth or Fig. 3.20(d) for the 17% H_2-growth.

For all the previous reasons, we slightly modified our growth conditions to optimize the growth on on-axis substrates. We mainly increased the growth time to 15 minutes instead of 5 minutes, but we also changed the temperature between 1550 and 1600°C, and the H_2 amount between 17% and 25%. The propane flow rate was kept at 5 sccm, and the pressure at 800 mbars. We compare in Fig. 3.33 the 5-minute growth and the 15-minute growth on the 0.05°-off substrate. Fig. 3.33(a) was previously commented: it presents graphene grown with 17% of H_2 at 1550°C for 5 minutes. Triangular shapes were detected and identified with Raman spectroscopy as graphene. In contrast, Fig. 3.33(b) presents a uniform growth, smaller steps and less triangular features (we can still detect one or two triangular patterns with AFM). This latter was grown with 25% of H_2 at 1600°C for 15 minutes. We assume that the longer growth time has allowed graphene to cover the whole surface and not just nucleate at the terraces. The terraces are narrower in Fig. 3.33(b), probably due to the two-dimensional graphene deposition, but still they reach 1.5 microns in width, which is not bad for transport measurements. XPS measurements, shown in Fig. 3.33(c), reveal a graphene peak for both of the samples, slightly shifted in binding energy. We had to normalize the

spectra to the corresponding SiC peak, to be in the same intensity range, since they were recorded in different sessions. Nevertheless, the ratio sp^2/sp^3 is more or less the same for both spectra: 0.99 for the black curve and 0.98 for the red one, which means that the number of deposited graphene layers is the same for both samples. Therefore, since we estimated 1.4 MLs with Raman spectroscopy for the 5-minute growth, we assume that we also have something around one layer of graphene for the 15-minute growth. This result contradicts what we previously presented in **part 3.2.1**, which is that the deposition should increase with the growth time. However, it is important to keep in mind that for the growth time study we used substrates with larger offcuts (around 0.45°), which promote faster and more important deposition. In this case, for a lower offcut (0.05°) the longer growth has increased the coverage of the surface and not the number of layers.

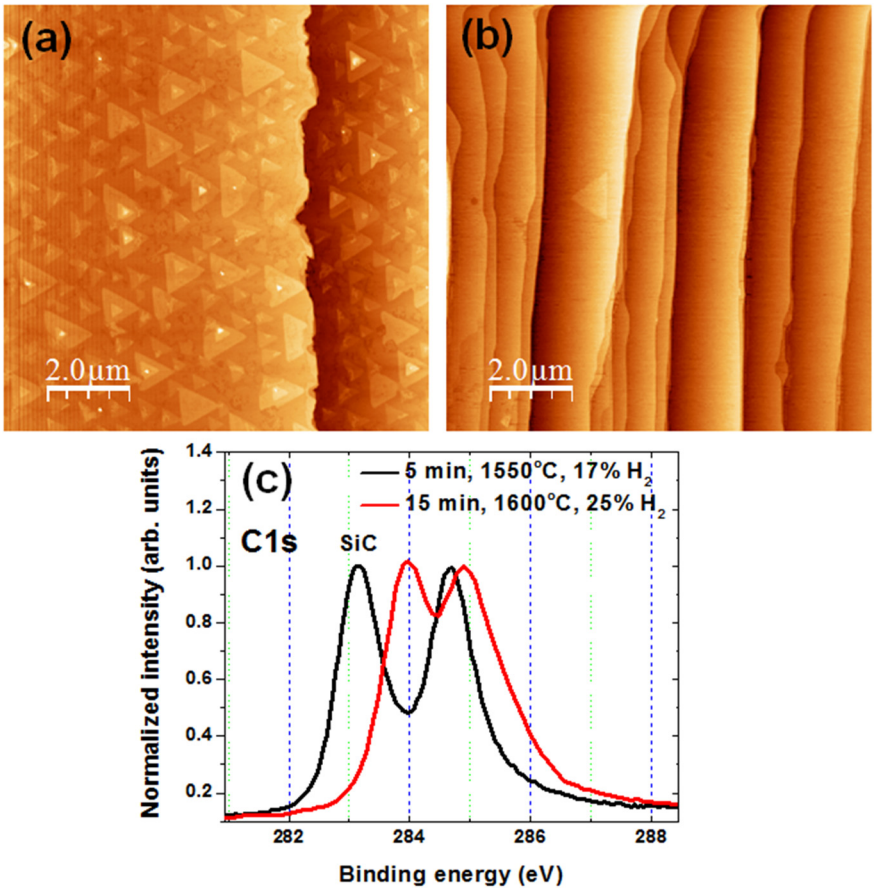

Figure 3. 33: *10×10 µm² AFM images of graphene grown on SiC (0001) 0.05°-off under two different conditions:* ***(a)*** *1550°C, 5 min and 17% of H_2;* ***(b)*** *1450°C, 15 min and 25% of H_2.* ***(c)*** *Corresponding C1s core-level spectra.*

We also demonstrate a uniform graphene growth on a 0.07°-off substrate with AFM and Raman spectroscopy. The Raman measurements were carried out by Timotée Journot in the lab LMP Leti. The graphene growth was carried out with 25% of H_2 at 1600°C, 5 sccm of propane for 15 minutes on a ¼ of 2''-substrate, 0.07°-off. We show AFM images of different areas of the substrate in Fig. 3.34(a-c), which appear to be homogeneous, attesting for the uniform graphene growth. We also recorded Raman spectra in different areas, confirming the presence of graphene and a uniform coverage, see Fig. 3.34(d). The spectra in Fig. 3.34(d) were recorded at different positions, as we can see in the inset of Fig. 3.34(d), then the number of layers was calculated by dividing the G-peak area to that of a HOPG reference. The estimated number of layers is around 0.9 and 1 ML, except for few positions with 0.7 and 0.8 MLs, mainly at the edges of the substrate. In addition, the 2D peaks of the different spectra can be fitted with a single Lorentzian suggesting the presence of a graphene monolayer across the substrate [119]. This proves that for substrates with a small offcut, the deposition is more likely to remain around one graphene layer for 15 minutes of growth.

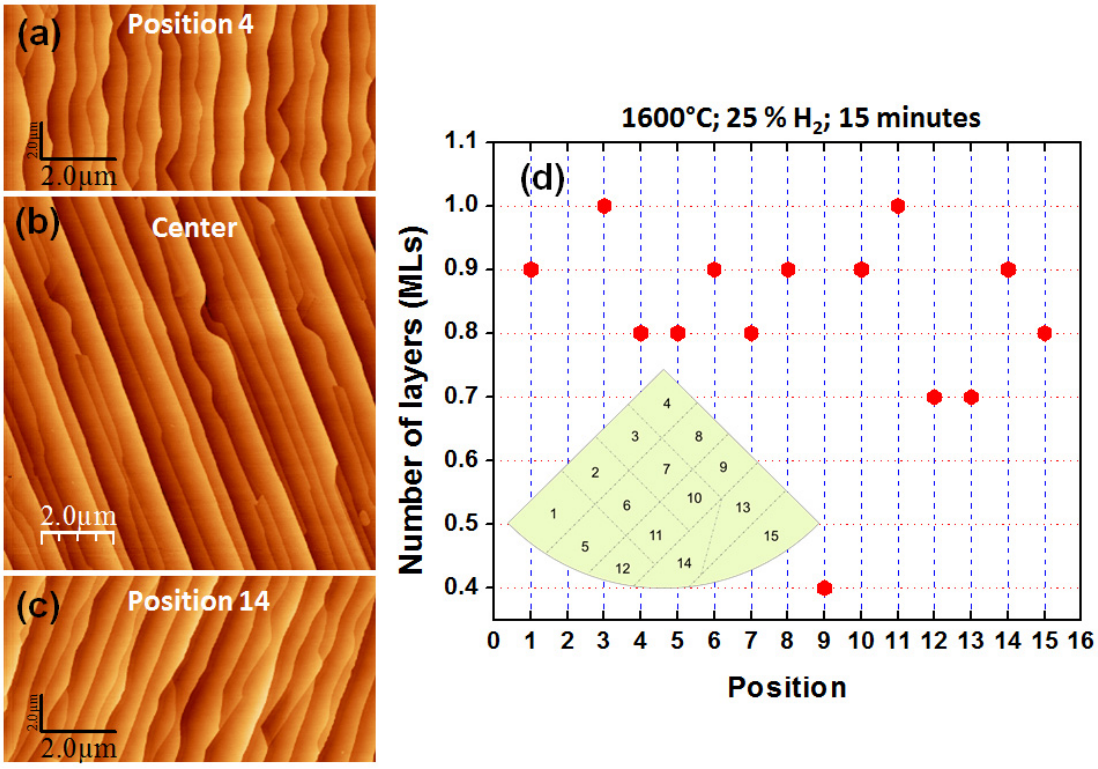

***Figure 3. 34: (a)** to **(c)** 10×10 µm² AFM images taken from different areas of graphene grown on ¼ of 2''-SiC, 0.07°-off at 1600°C, for 15 minutes and under 25% of H_2. **(d)** The estimated number of layers calculated from Raman spectra recorded at different areas of the sample.*

Electrical measurements

The growth on on-axis substrates under these modified conditions (i.e. 25% H_2, 15 minutes, 1600°C) seems promising, allowing a uniform coverage of graphene with a thickness around one layer. Hall Effect and resistivity measurements were conducted with the four-probe Van der Pauw technique on graphene grown on semi-insulating SiC substrate (0.08°-off) under these growth conditions, uncovering interesting electrical properties. An AFM image of the grown sample is shown in Fig. 3.35(a). The sample presents straight steps 600 nm-wide, with few steps exhibiting rough edges indicated by a white arrow, which we believe is a strain relaxation mechanism [159,188]. The phase image shows few areas of different contrasts, which can be extra layers, but they are not dominant. Van der Pauw patterns were processed on a 1×1 cm^2-sample to measure the carrier mobility and sheet resistance (see **part 2.3.6** in **chapter 2** for details on the processing). The average sheet resistance is 3387 Ω/□, the graphene is n-doped with an average sheet carrier density of 1.1×10^{12} cm^{-2} and a mobility of 1708 cm^2/V.s measured at 300 K. The electrical measurements are summarized at the end in table 3.5.

For comparison, Hall Effect measurements were also carried out on the sample presented in Fig. 3.35(b), grown with 17% of H_2, for 5 minutes and at 1550°C.

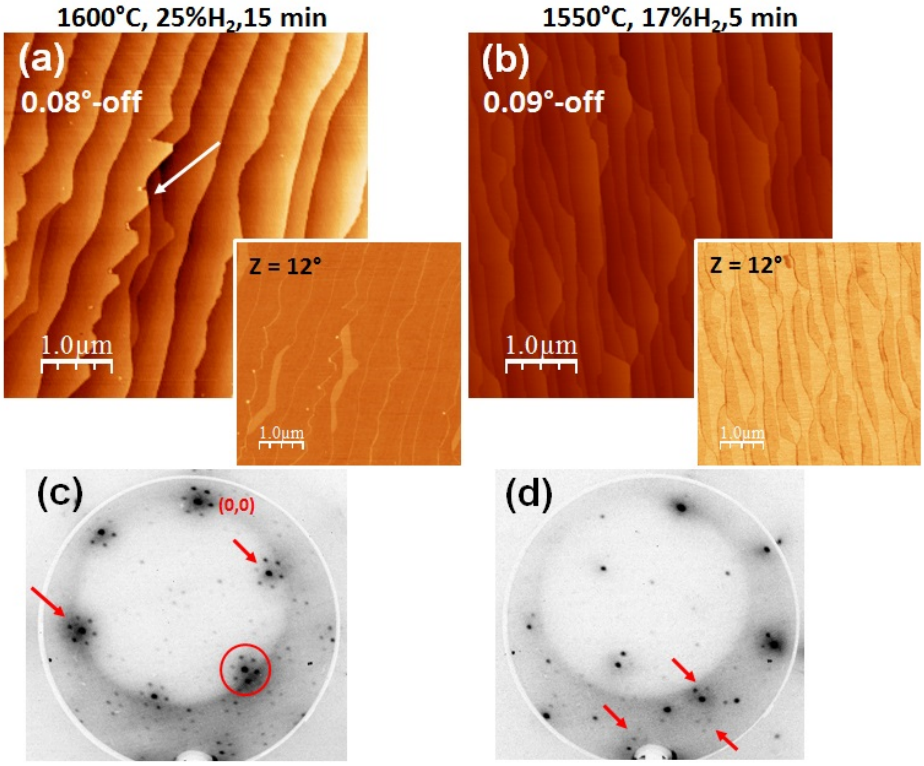

Figure 3. 35: *5×5 µm² AFM topographic and phase images of two different samples grown with two different growth conditions:* ***(a)*** *0.08°-off sample prepared with 25% of H_2 at 1600°C for 15 minutes.* ***(b)*** *0.09°-off sample prepared with 17% of H_2 at 1550°C for 5 minutes.* ***(c)*** *and* ***(d)*** *The corresponding LEED images taken at an electron energy of 140 eV.*

The measurements revealed different results: p-doped graphene with an average carrier density of 4.7×10^{12} cm^{-2}, a mobility of 1707 $cm^2/V.s$ and a sheet resistance of 771 Ω/□ measured at 300 K. The p-doping is expected to be caused by moisture from the atmosphere [19,154]. Despite the obvious non-uniform thickness in the phase image (inset of Fig. 3.35(b)) the mobility does not seem to be affected and the sheet resistance is relatively low, compared to the 15-minute sample, which appears to be more uniform in thickness (see phase image in inset of Fig. 3.35(a)). However, we believe that the higher sheet resistance is not related to the surface uniformity but rather to the buffer layer. In fact, if we look at the corresponding LEED patterns in Fig. 35(c, d), we notice that the buffer layer diffraction spots (indicated by red arrows and circles) are more manifested in Fig. 3.35(d) for the 15-minute growth.

Similar observations can be made by examining the XPS C1s core-level presented in Fig. 3.36 for the two samples. The buffer layer peaks seem to be more intense for the 15-minute growth sample (red curve), creating the extra shoulder at the higher binding energy side. We suspect that the buffer layer is not the same in two cases: for the 5- and 15-minute growths. It might be possible that even if we detect signs of the buffer in the case of 5-minute growths, and because of the presence of hydrogen in the gas mixture, Si-H bonds exist at the same time with the buffer layer, creating a "hydrogenated" buffer layer. In other words, the buffer layer exists and shares bonds with the silicon from the substrate, but at the same time hydrogen bonds as well with the silicon from the substrate. When we increase the temperature and the growth time, it is probable that under the influence of the longer times at high temperature, hydrogen will desorb from the interface allowing new bonds between the buffer layer and the substrate. This is why signs of the buffer layer are more noticeable for the longer growths with XPS and LEED. This could be the reason for the higher sheet resistance and the shift towards higher binding energy in XPS, since the buffer layer was always thought to be detrimental for the graphene's electrical properties.

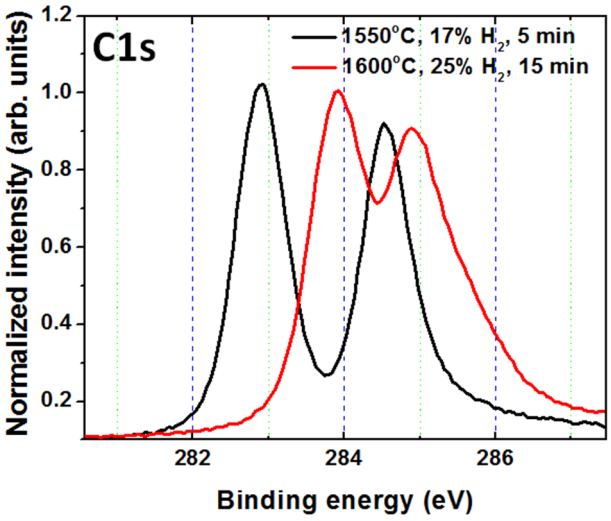

Figure 3. 36: *C1s core-level spectra of the two growth prepared with 17% of H_2 at 1550°C for 5 minutes (black curve) and under 25% of H_2 at 1600°C for 15 minutes (red curve).*

Also, it explains the electron doping, since more bonds with the substrate will lead to more electron transfer from the substrate to the graphene layer. Yet we suppose along with other studies [37,41,105,179] that the charges will be trapped at the interface, explaining the reduced charge carrier density on the 15-minute growth samples.

Before we summarize, Hall Effect measurements were also carried out on growths under 100% of H_2 for 5 minutes at 1450°C. Although the sheet resistance is low (~ 600 Ω/□), the graphene is strongly p-doped (~ 8×10^{12}) and the mobility around 1000 $cm^2/V.s$. This structure does not present any buffer layer and the graphene is expected to be freestanding. However, this could be the reason of the excessive p-doping, since no electrons can migrate from the substrate to compensate the effect of the hole doping. To summarize, in attempts to have good carrier mobility we considered low-offcut substrates for their wide terraces, which we believe promotes good transport properties. However, the growth on low-offcut substrates is challenging, since graphene seems to nucleate on the terraces or grows in a non-uniform way. We attempted to increase the growth time and temperature to assess this problem, which seemed promising at first, allowing to grow uniform graphene on a ¼ of a 2'' substrate, with a homogeneous deposition around 1 ML. However, we suspect that for longer growth times, hydrogen tend to desorb from the interface and more bonds will form with the substrate, leading to n-doped graphene and high sheet resistance in the order of 3000 Ω/□. This result can be problematic if we want to use graphene as a contact or an electrode, which requires low sheet resistance. On the bright side, even though the 5-minute growth under 17% H_2 seems not so homogenous in terms of graphene thickness, the carrier mobility is around 1700 $cm^2/V.s$ at 300 K for p-doping. The transport could be occurring on the terraces with complete graphene layers. We attribute the enhanced mobility to the presence of H_2 at the interface along with the buffer layer. In fact, we believe that this is one of the advantages of our technique compared to Si sublimation, since we are able to introduce H_2 at the interface during the growth and control the electrical properties of the graphene layer, leading to enhanced mobility compared to the Si sublimation technique [80]. To this end, although the results seem dispersed, the wide range of observations allows us to control the doping of the graphene layer, the sheet resistance and the carrier density. Therefore, depending on the application, whether for metrology or electronic uses (as an electrode or channel) we can adapt our growth conditions to fit the required need.

In conclusion, if we compare the results in table 3.5, we can deduce that the carrier mobility depends strongly on the carrier density as well as the sheet resistance. The first sample (**S1**) presents high sheet resistance compared to the others, but because of the reduced electron density, the mobility is around 1700 $cm^2/V.s$ at 300 K. The second sample (**S2**) in table 3.5 has a lower sheet resistance but higher carrier density (p-type), which leads to a similar mobility as the first sample. And finally, the third sample (**S3**) is highly p-doped with lower sheet resistance and mobility. We attribute the difference in doping type and levels of the graphene layer to the hydrogenation of the buffer layer: for a less hydrogenated buffer layer, electrons will migrate from the substrate to the graphene layer (**S1**), whereas for a hydrogenated interface (**S2** and **S3**), the

electrons migration is reduced and the graphene layer is more affected by the hole doping coming from the surrounding atmosphere (moisture or other).

Table 3. 5: *Electrical measurement recorded at 300 K on different graphene samples*

Growth conditions	**Carrier density (cm^{-2})**	**Doping type**	**Sheet resistance (Ω/□)**	**Mobility ($cm^2/V.s$)**
S1: 25% H_2; 15 minutes; 1600°C	~1.1×10^{12}	Electrons	~3000	~1708
S2: 17% H_2; 5 minutes; 1550°C	~4.7×10^{12}	Holes	~770	~1707
S3: 100% H_2; 5 minutes; 1450°C	~8×10^{12}	Holes	~600	~1000

3.5. General conclusion

In this chapter we presented a wide range of results starting with thermodynamic calculations, then going through the different growth parameters and their influence on the graphene growth, to reach finally optimized graphene growths with different characteristics. First, we started by attempting to understand the different parameters contributing to the graphene growth on SiC. We were able to confirm experimentally that propane is the main source for carbon in our growth conditions, by conducting a set of annealing experiments of SiC under H_2 or H_2+Ar. The annealing without any propane did not result in the formation of graphene. On the other hand, the annealing of SiC under pure argon has led to the formation of graphene by Si sublimation, but to make this possible, we had to completely change our usual growth conditions, by decreasing the total pressure and increasing the temperature and the growth duration. In order to understand the reason behind the inability to sublimate silicon under H_2 we had to do some thermodynamic calculations with the help of a software known as FactSage, which consists of calculating the concentration of species reacting together, while minimizing the Gibbs free energy of the system. These calculations revealed that considering Si sublimation under H_2 is not relevant. In fact, H_2 reacts with SiC and creates molecules containing C-H bonds, Si-H bonds or both C-Si bonds. However, the C-gases have vapor pressures much more important than the Si-gases, which is not likely to lead to any excess of carbon at the surface to form graphene. In contrast, the annealing under only argon creates an opposite effect, leading to Si-species with vapor pressures higher than the C-species, which will lead to a carbon residue at the surface and form graphene. This led us to the conclusion that under our growth conditions of H_2+Ar, the propane is the main contributor to the growth. The SiC etching can also be a contributor, but quantifying its contribution seems a difficult task.

In a second part, we concentrated on the different growth parameters, to understand their influence on the growth. We believe that understanding the role of each of the growth parameters will lead to an optimized graphene sample. Different parameters influence the growth of graphene, such as the growth duration and the propane flow. The growth duration allows to control the deposited thickness of graphene, especially under 100% of H_2, because under 17% of H_2 the variation of the number of layers with the time seems less important. This is not the case for the propane flow, which seems to influence the number of graphene layers regardless of the H_2 amount. In addition to these parameters, the growth temperature seems to also have an influence on the morphology, the thickness and the structure of graphene.

We also investigated the effect of the hydrogen amount in our H_2 + Ar gas mixture on the growth. The hydrogen amount influences the graphene morphology, thickness and structure. Low hydrogen amount leads to the formation of a $(6\sqrt{3}\times6\sqrt{3})$ buffer layer. In contrast, high hydrogen amount leads to graphene with wrinkles at the surface and disorder due to the absence of the buffer layer. In fact, we expect that hydrogen bonds with the silicon from the substrate and prevents the buffer layer from forming. Yet this effect can be reduced with the temperature, which has a direct influence on the hydrogenation of the interface. A high temperature will provoke the desorption

of the hydrogen from the interface and promote the formation of the buffer layer. Therefore it is important to introduce the right amount of H_2 for the right temperature. In addition, we discussed the strain in our graphene layers depending on the growth conditions. We suspected from previous studies that when the graphene is grown with a buffer layer, the strain at room temperature will be at its minimum. In this case, the strain is the sum of a tensile strain developed at the growth temperature and a compressive strain occurring upon cooling doing. The tensile strain is due to the lattice mismatch between the ($6\sqrt{3}\times6\sqrt{3}$) SiC and the (13×13) graphene super cells, whereas the compressive strain is a thermoelastic strain due to the difference in thermal expansion coefficients between SiC and graphene. In the case of high H_2 amount in the gas mixture, only the thermal strain is present, leading to a maximum strain at room temperature. However, we investigated the set of samples grown with different H_2 amounts with Raman spectroscopy to examine any strain variation, but the study seemed complicated. The different samples presented different thicknesses among each other, along with a non-uniform thickness for each sample. In addition, we noticed that the carrier density might be changing as well from one sample to another. These observations made the study difficult and almost impossible.

We also studies the influence of the substrate's miscut angle on the growth of graphene. Substrates with a very small offcut (0.05°off) seem challenging for the growth of graphene during 5 minutes since they do not allow a homogeneous growth, whether it was performed with 17% of H_2 or 100%. The growth becomes more uniform for offcuts starting from 0.2°-off, and no important morphological and structural differences rise for larger offcuts, mainly the terrace widths decrease when the offcut is larger. On the other hand, Raman spectroscopy investigations revealed that substrates with larger offcuts induce an important strain to the graphene layer, with a non-uniform strain distribution across the sample, whether they were grown with 17% of H_2 or 100%. In addition, for these set of growths we noticed that the samples grown with 100% of H_2 appear to be more strained than the samples grown with 17% of H_2. We attribute this behavior to the hydrogenation of the interface in the case of 100% of H_2, which will lead to strain-free graphene at the growth temperature since it is poorly bound to the substrate. As a result, important thermoelastic strain will accumulate when cooling down. Further investigations have led us to propose that the presence of extra patches of graphene at step edges or between steps could be areas with more strain than the step-terrace area. This explains the non-uniform strain distribution and the increase in strain for larger offcuts. In fact, when the offcut is larger the step-edge density will be larger as well, leading to more areas with more strain and thus increasing the total strain of the sample. In conclusion, the ideal offcut seems to be around 0.2°-off, resulting in a minimum strain and uniform growth.

Finally, we were able to improve the growth on on-axis substrates by increasing the growth duration to 15 minutes and the temperature to 1600°C. This led to good electron mobility (~1700 $cm^2/V.s$) but high sheet resistance (around 3000 Ω/□) which is not ideal for electronic applications. Nevertheless, we realized that even though the growth is not uniform for the 5-minute growth carried out with 17% of H_2, the mobility is also good and in the same range as before, but

this time the sheet resistance is smaller and the type of doping is hole-doping. This can be enhanced by other means with post-growth treatments to reduce the hole-doping. Overall, we were able to produce both n-doped and p-doped graphene, which allows us to invest our graphene in different applications. To conclude, we believe that our approach allows a better control of the buffer layer with mainly the hydrogen amount and the temperature. With the right amount of H_2 in the gas mixture we can minimize the effects of the buffer layer by having a partially hydrogenated buffer layer, which we believe has a good influence on the mobility of our graphene samples.

Chapter 4

Graphene and III-nitrides

In chapter 4, we will study materials other than SiC, mainly III-nitrides. Combining graphene with III-nitrides is very appealing for different applications in the electronics and optoelectronics markets. Indeed, according to the literature, some studies have already employed graphene as transparent electrodes for GaN and other materials [10,22], and also as a contact for AlGaN based electron devices [23]. It could be also beneficial to combine graphene with AlN-based devices, which allows us to integrate graphene with the developed markets of UV and visible LEDs as well as laser diodes [193–195], but also for power electronics [196,197]. In addition, this can also create new applications for graphene devices with AlN as an insulator on a back-gate.

In a previous study, graphene direct growth on nitrides was proven to be possible [103], where graphene layers were grown on AlN templates on Si (111). However, the graphene quality was not optimized since the growth temperature of graphene was limited to the melting point of silicon (1414°C), whereas the optimal growth temperature of graphene on SiC is generally around 1550°C. In this chapter, we present our attempts of growing graphene on bulk AlN, AlN templates on SiC and sapphire and AlGaN templates on sapphire, with a similar approach than on SiC. Prior to the growth of graphene, we investigate the effects of high temperature annealing on different nitride materials. The goal of this pre-growth step is to assess the behavior of such substrates under high temperatures, which was found to be both beneficial and destructive for the nitride substrates, having a direct influence on the morphology and the crystalline quality. Finally, we present first results of AlN growth on graphene on SiC. Our study is based on AFM, XPS, LEED observations and in some cases Raman spectroscopy.

4.1. Experimental details

In the following paragraphs we will present the experimental details employed for the annealing of the nitride substrates and the graphene growth conditions, along with the different substrates used for the different studies.

4.1.1. Nitrides templates and substrates

The III-nitrides materials used here were mainly AlN: bulk AlN and AlN templates grown on SiC and sapphire, but also AlGaN templates on sapphire. The bulk AlN substrate was a 1'' substrate, which we cleaved into ~5×5 mm^2 samples for the annealing and graphene growth studies. The templates were grown in CRHEA by Julien Brault and Yvon Cordier in MBE systems equipped with ammonia (NH_3) as the nitrogen source. Prior to the growth on SiC, the SiC surface was annealed in H_2 in order to prepare the surface with a step-like morphology. Different AlN thicknesses were considered, ranging between 100 and 240 nm for SiC, and around 120 nm for sapphire. For more details on the AlN growth on sapphire please refer to reference [123]. The AlN layers grown on SiC and sapphire had the Al-polarity, as observed with reflection high-energy electron diffraction (RHEED) at the end of the growth process. AlGaN layers were also prepared in a MBE reactor: first a GaN buffer layer was grown on a sapphire substrate, followed by an AlN layer growth, 100 to 200 nm-thick, then AlGaN layers were deposited with a thickness of 500 nm and different aluminum contents, for more information please refer to reference [198,199]. Here as well, the samples are cleaved into 5×5 mm^2 pieces. The substrates and templates used are shown in Fig. 4.1 and listed in table 4.1. Few defects appear at the surface of the different templates such as polishing scratches (Fig. 4.1(a)), etching pits (inset of Fig. 4.1(e)), aggregates as white objects (Fig. 4.1(b, d-g)) and no signs of the atomic steps in Fig. 4.1(a, d-g).

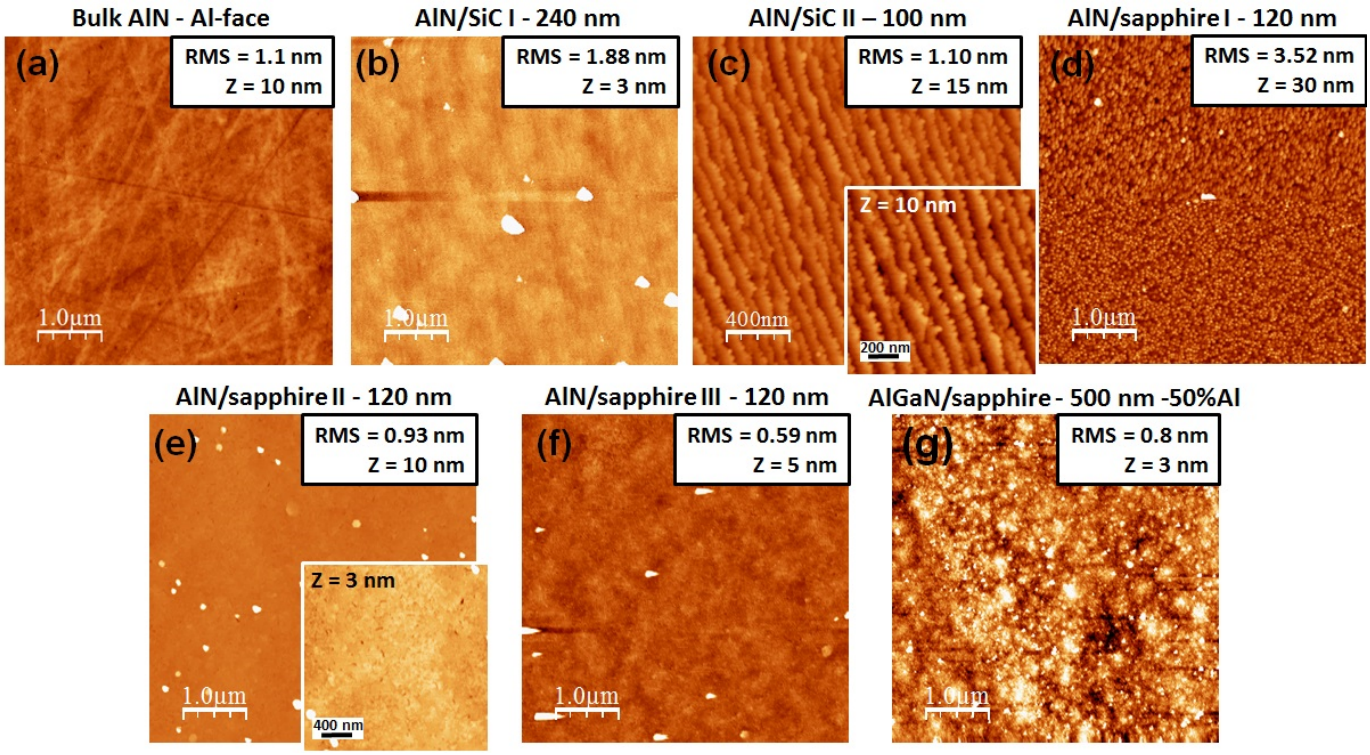

Figure 4. 1: *5×5 µm² AFM topographic images (except for* ***(c)*** *2×2 µm²) of the different templates used in this chapter. Inset of* ***(c)*** *and* ***(e)*** *are 1×1 µm² and 2×2 µm² images respectively.*

4.1.2. Nitrides annealing and graphene growth

The annealing process had different purposes: it can be considered as a preliminary study before the growth of graphene, but also as an approach to prepare the surface for III-V regrowth and in our case for graphene growth (epi-ready surface), especially in the case of bulk AlN. The annealing can also be helpful to highlight and understand the defects in the AlN templates and enhance the crystalline quality of AlN grown on SiC and sapphire. In fact, important lattice and thermal expansion coefficients mismatches (TEC) exist between the different materials. The in-plane mismatches are: AlN/sapphire lattice mismatch of 13% and TEC mismatch of 44%; AlN/6H-SiC lattice mismatch 0.9% and TEC mismatch of 0% [200,201]. These important mismatches between AlN and sapphire are the reason behind the important density of threading dislocations [123], hence a high-temperature annealing study seems interesting, even independently of the graphene growth study. As low-temperature annealing (1150-1250°C) had little effect, we aimed for higher temperatures between 1350 and 1650°, at pressures between 50 and 800 mbars, depending on the substrate (bulk AlN or AlN templates). The annealing was carried out under a mixture of H_2 and N_2, with different percentages, at a total gas flow rate changing between 6 slm and 16 slm [104]. The argon in the gas mixture was replaced by N_2, because we believe that N_2 helps to stabilize the surface, based on preliminary annealing tests, even if the decomposition of N_2 is low [202]. The annealing and graphene growth conditions are summarized in table 4.1 for the different AlN substrates.

Table 4. 1: *Summary of the substrates and the annealing/growth conditions.*

Sample	AlN/AlGaN thickness	Annealing	Graphene growth attempts
Bulk AlN		1000-1400°C; 50-200 mbars; N_2 + H_2	1350°C; 800 mbars; N_2; 17 sccm C_3H_8
AlN/SiC I	240 nm	1450°C; 800 mbars; N_2 + H_2	1450 -1550°C; 800 mbars; N_2; 2-10 sccm C_3H_8
AlN/SiC II	100 nm	1350°C; 800 mbars; N_2	1350-1450°C; 800 mbars; N_2; 10-17 sccm C_3H_8
AlN/sapphire I + II	120 nm	1450°C; 800 mbars; N_2 + H_2	1450°C; 800 mbars; N_2; 2-10 sccm C_3H_8
AlN/sapphire III + IV*	120 nm	1350-1650°C; 800 mbars; N_2	No attempts/just annealing for the crystalline quality
AlGaN/sapphire	500 nm	1250-1450°C; 800 mbars; N_2	1350°C; 800 mbars; N_2; 2-10 sccm C_3H_8

*Note that we only presented an AFM image of the template III in Fig. 4.1, because both templates have similar morphologies.

The graphene epitaxy doesn't differ much from that on SiC, but instead of a hydrogen-argon mixture, we applied a hydrogen-nitrogen mixture with a 6 to 16 slm flow rate, depending on the study, but in most cases only nitrogen was used as the carrier gas. Hydrogen can be very reactive at high temperatures, this is why we avoided using it for the growth. The growth process is presented in Fig. 4.2. As we can see, the annealing step was not employed in this case, mainly because the AlN surfaces already presented steps resulting from the morphology of SiC, or to avoid any major effects to the surface with the high temperature annealing. Therefore, only in the case of bulk AlN, the previously annealed samples were used for the graphene growth, whereas for the AlN templates the annealing and graphene growth studies were carried out on two different set of samples. The III-nitride sample is exposed to the carrier gas during the temperature ramp. Then propane with a flow rate of 2 to 17 sccm is introduced for 5 minutes when the growth temperature is reached. After the deposition, the propane flow rate is cut-off and the sample is cooled down under the carrier gas. The growth temperatures range between 1350 and 1550°C, at 800 or 900 mbars.

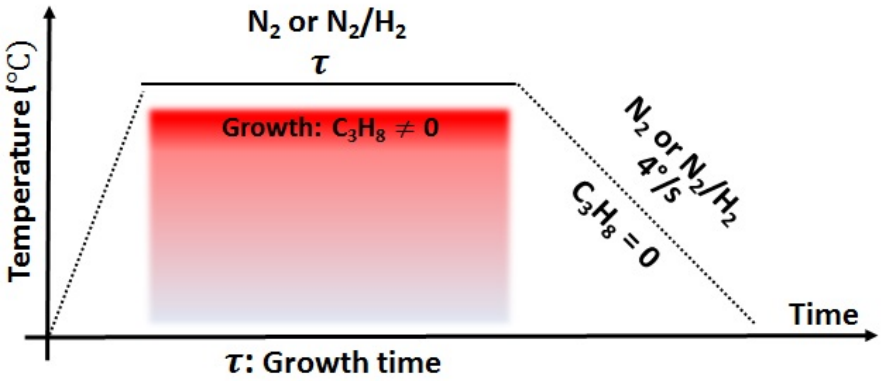

Figure 4. 2: *Schematic representation of the growth process of graphene on III-nitrides.*

4.2. Bulk AlN: annealing and graphene growth

4.2.1. Annealing of the Al-face of bulk AlN

First, we started by annealing the Al-face of bulk AlN at different temperatures, in order to find the right temperature to enhance the morphology of the surface. The annealing temperatures ranged between 1100 and 1500°C, at 200 mbars, for 5 minutes, with a gas mixture of 50% H_2 (8 slm) and 50% N_2 (8 slm). For the study on bulk AlN, the total gas mixture was 16 slm for the annealing and 10 slm for the growth of graphene. The surface before any treatment is shown in Fig. 4.3(a), where we can see polishing scratches and no atomic steps. The annealing at 1100°C (Fig. 4.3(b)) does not seem to have any effect on the morphology. We start seeing some changes at 1300°C (Fig. 4.3(c)) where the polishing scratches seem to be reduced and etching pits start to appear. The pits seem to be aligned together, which is why we attribute them to polishing scratches etched during the annealing process. A more obvious change in morphology appears at 1400°C (Fig. 4.3(d)) where atomic steps appear on the surface. In this latter image, we can still detect a polishing scratch appearing as a brighter line. However, the surface is mostly dominated by atomic steps with rough edges. The roughness of the surface has slightly increased compared to the reference image in Fig. 4.3(a). Increasing the temperature to 1500°C (Fig. 4.3(e)) results in a rougher surface (RMS of 3.1 nm) but with straighter steps compared to Fig. 4.3(d).

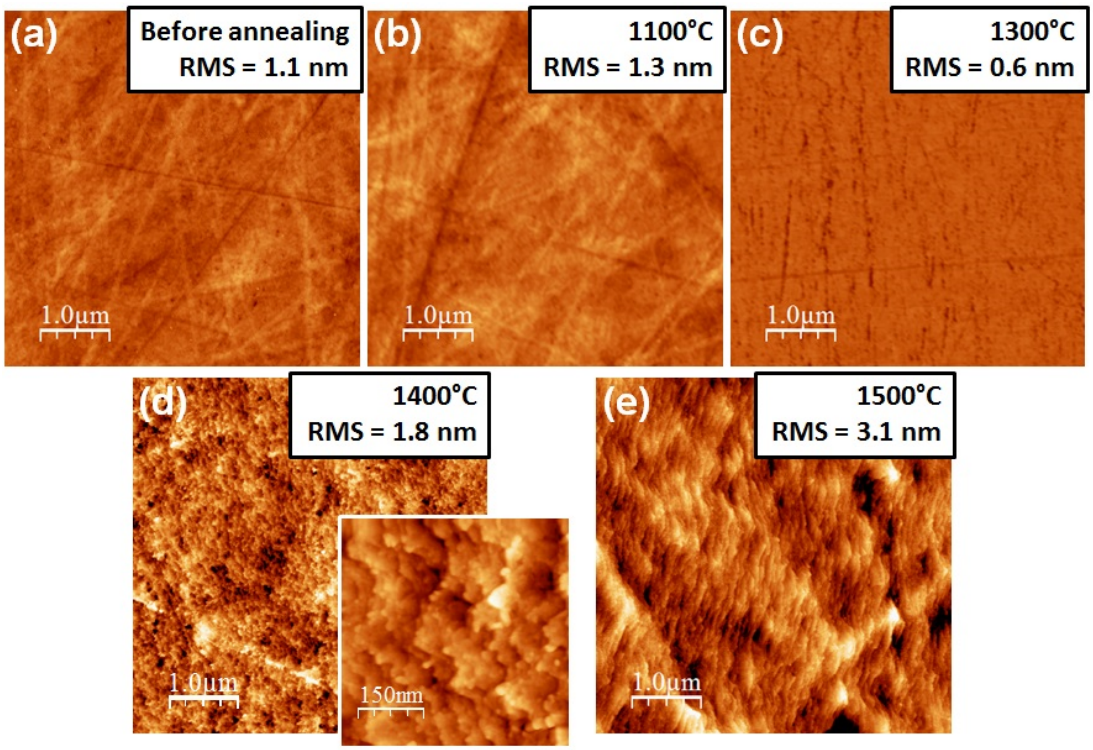

Figure 4. 3: *5×5 µm² AFM images of the Al-face of bulk AlN presenting the reference surface before annealing in* ***(a)*** *and the annealed samples at different temperatures:* ***(b)*** *1100°C,* ***(c)*** *1300°C,* ***(d)*** *1400°C and* ***(e)*** *1500°C. Inset of* ***(d)*** *is a 0.75×0.75 µm². The annealing conditions are: 200 mbars, 5 minutes and 50% H_2 (8 slm) + 50% N_2 (8 slm). The AFM z-scale is 10 nm.*

Therefore, temperatures of 1400 and 1500°C appear interesting for surface-preparation and graphene growth, allowing the manifestation of atomic steps without too much roughening the surface. However, we will consider 1400°C in the following while changing other annealing parameters.

We show in Fig. 4.4 the optimization of the annealing conditions on the Al-face, by decreasing the total pressure and increasing the hydrogen amount, for 5 minutes of annealing. The first two AFM images in Fig. 4.4(a, b) are the reference image and the annealing at 1400°C and 200 mbars, which we previously presented in Fig. 4.3(d). Reducing the annealing pressure to 50 mbars (Fig. 4.4(c)), under a gas mixture of 50% H_2 + 50% N_2, enhances the morphology compared to Fig. 4.4(b), since the steps in the former case appear straighter. The morphology even gets better and more regular when the H_2 percentage is increased to 75% (Fig. 4.4(d)), accompanied with an increase in roughness to 4 nm. After this step, no scratches can be detected but instead well-defined atomic steps dominate the surface. The change of the morphology is ascribed to an increase of the etching rate when decreasing the annealing pressure and increasing the hydrogen amount in the gas mixture. Note that the annealing under the same conditions but at 1300°C gives similar results, but with steps slightly narrower. In Fig. 4.4(d), the AlN surface morphology is similar to AlN layers grown on chemico-mechanically polished bulk AlN (see fig. 11(c) in reference [203]). This leads us to the conclusion that our optimized annealing conditions can be an interesting surface

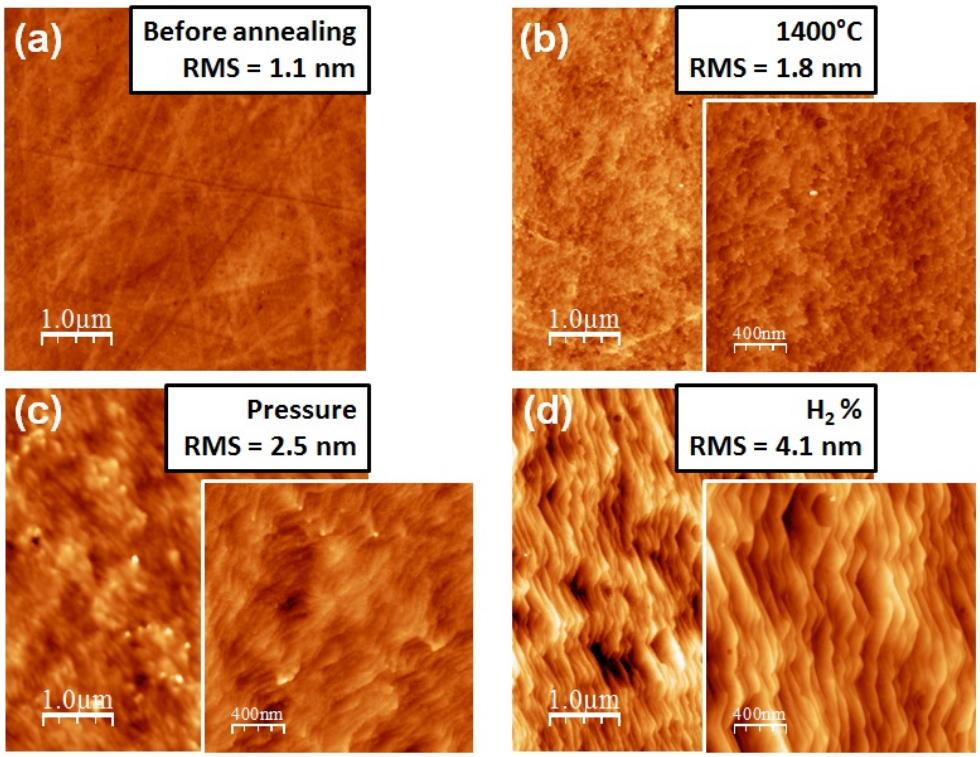

Figure 4. 4: *5×5 µm² AFM images of the reference surface in* ***(a)*** *and the annealed samples at* ***(b)*** *1400°C, 200 mbars and 50% H_2,* ***(c)*** *1400°C, 50 mbars and 50% H_2,* ***(d)*** *1400°C, 50 mbars and 75% H_2. Figures in Inset are 2×2 µm² images. The AFM z-scale is 25 nm.*

preparation process and a complement for mechanical and chemico-mechanical polishing of bulk AlN substrates.

For the growth of graphene, since we suspect that the growth gives better results at 800 mbars from our previous experience on SiC [101], we had to anneal AlN substrates with different gas mixtures at 800 mbars to choose the right combination for the growth of graphene. We show in Fig. 4.5 the different gas combinations that we applied at 800 mbars, 1400°C, for 5 minutes. Note that these samples were not previously annealed. Fig. 4.5(b) for the annealing with 50% H_2 + 50% N_2, displays important etching pits at the surface, which led us to decrease the hydrogen amount and increase the N_2 in the gas mixture. As we can see in Fig. 4.5(c, d) no important changes occur. Therefore, for the growth of graphene we will apply a gas flow of 100% N_2 instead of the 50% H_2 + 50% N_2 combination.

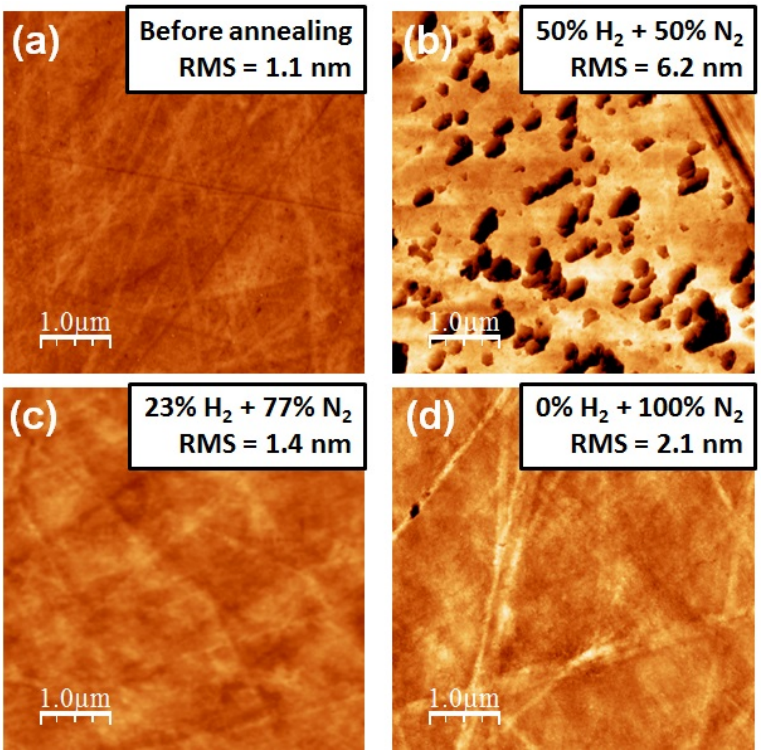

Figure 4. 5: *5×5 µm² AFM images of the Al-face of bulk AlN presenting the reference surface before annealing in* ***(a)*** *and the annealed samples at 1400°C and 800 mbars with different H_2 amounts:* ***(b)*** *50% H_2 + 50% N_2,* ***(c)*** *23% H_2 + 77% N_2,* ***(d)*** *0% H_2 + 100% N_2. AFM z-scale is 25 nm.*

4.2.2. Annealing of the N-face of bulk AlN

A similar study was carried out on the N-face of bulk AlN, but the surface preparation step of this face was more challenging since the N-face presented a lot of defects such as open pits and polishing scratches before any annealing treatment, see Fig. 4.6(a). Nevertheless, we attempted different annealing conditions on this particular face. At first, we applied the optimized conditions

of annealing that we previously employed on the Al-face, i.e. 1400°C, 50 mbars, 5 minutes, and 75% H_2 + 25% N_2, see Fig. 4.6(b). With these conditions, the scratching pits seem to disappear, but the surface seems to get rougher and the open pits wider. For this reason, we attempted to reduce the hydrogen amount to reduce the etching. But even with 23% of H_2 in the gas mixture (Fig. 4.6(c)) the etching effect on the morphology is important. The best solution is an annealing with 100% of N_2 without any H_2 in the gas mixture (Fig. 4.6(d)), but we can still see marks of the polishing scratches and no signs of the atomic steps. We also tried to manipulate the pressure and the temperature, but without any success of enhancing the morphology. We can deduce that for the N-face, the initial state of the surface dominated by defects and open pits limits any improvements of the morphology.

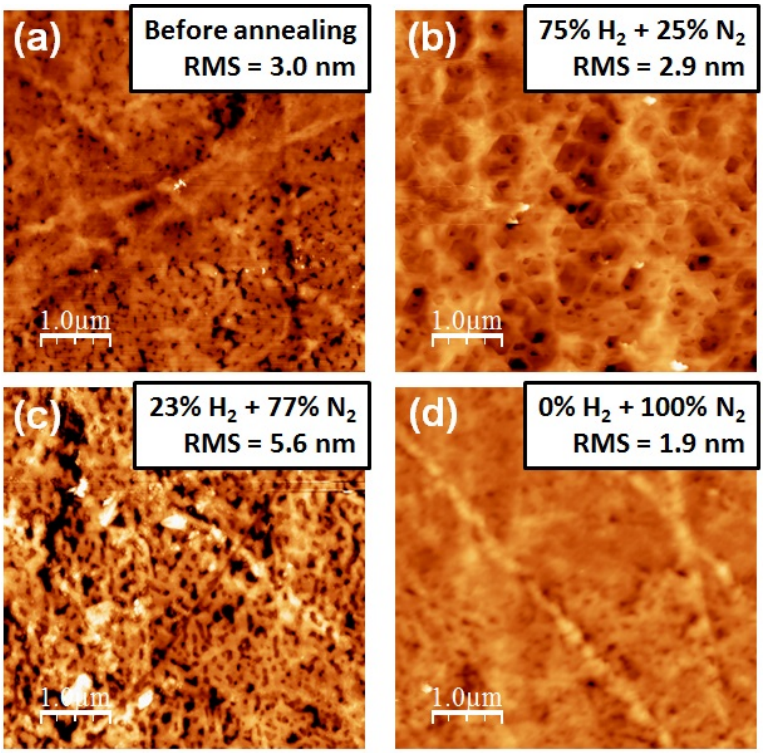

Figure 4. 6: *5×5 µm² AFM images of the N-face of bulk AlN presenting the reference surface before annealing in* ***(a)*** *and the annealed samples at 1400°C and 50 mbars with different H_2 amounts:* ***(b)*** *75% H_2 + 25% N_2,* ***(c)*** *23% H_2 + 77% N_2,* ***(d)*** *0% H_2 + 100% N_2. AFM z-scale is 25 nm.*

To summarize, we have tried to anneal both the Al- and N-face of bulk AlN, in an attempt of reducing the polishing scratches and enhancing the morphology of the sample. The annealing of the Al-face with 75% of H_2 and 25% of N_2 at 50 mbars has led to the appearance of well-defined atomic steps without any polishing scratches, due to the etching effect of hydrogen at high temperatures (1300-1400°C). However, the attempts of enhancing the N-face of bulk AlN have failed, due to the poor initial state of the surface before any treatment. Now that we have studied the effect of high temperature annealing under H_2 + N_2 of bulk AlN, we can investigate the growth of graphene on such substrates.

4.2.3. Graphene growth on bulk AlN

Graphene growth on nitrides was first attempted on bulk AlN, which can be used as a model for the growth of graphene on nitrides. For this part, we have used AlN substrates already annealed and prepared with the optimized annealing conditions, because of the limited availability of bulk AlN samples. We adopted the growth conditions employed for the growth of graphene on AlN templates on Si(111) from reference [103], i.e. 1350°C, 800 mbars, 6 minutes of 17 sccm of propane, but 100% N_2 instead of 50% H_2 + 50% N_2. We present in Fig. 4.7(a) the graphene growth attempt on the Al-face. However, no pronounced changes in the morphology are detected compared to the annealed sample (Fig. 4.4(d)), but the atomic steps seem less defined after the graphene growth attempt in Fig. 4.7(a). Interestingly, we can observe the formation of wrinkles on the back face of the same sample (N-face in Fig. 4.7(b)) similar to those found on graphene on SiC. These wrinkles suggest the possibility of having graphene on the nitrogen face, even though this face was facing the sample holder. For this reason, another sample was placed upside down, having the N-face exposed to the incoming gas and the Al-face towards the sample holder. While no difference is observed on the Al-face (Fig. 4.7(c)) compared to Fig. 4.7(a), we can clearly see the wrinkles who appear to be more stretched out among each other in Fig. 4.7(d) compared to Fig. 4.7(b). This structure with wrinkles is usually found on the C-face SiC [81,189] and on the Si-face under special conditions [17,18]. It is known that this kind of morphology is usually

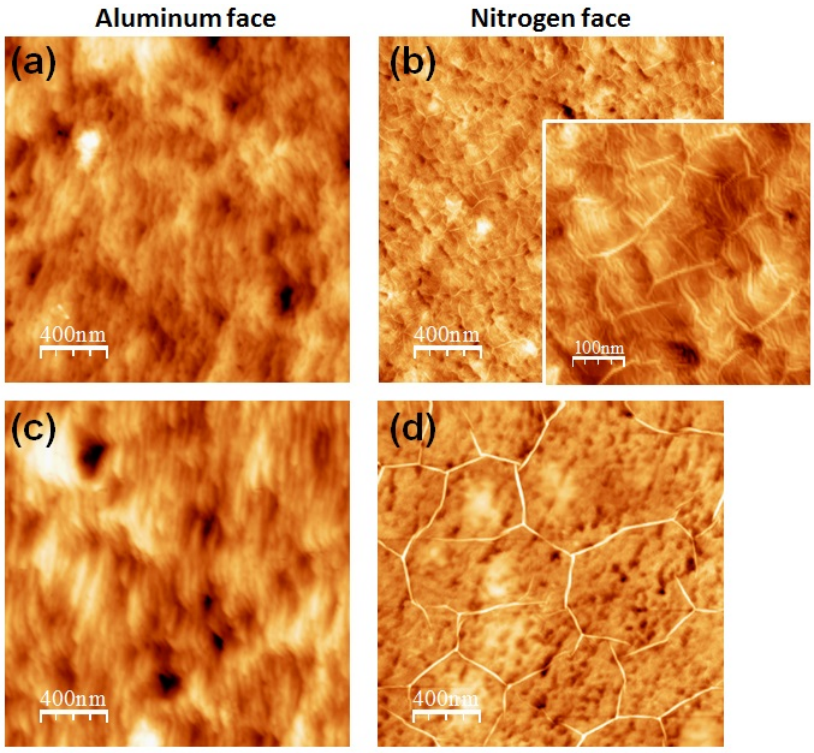

Figure 4. 7: *2×2 µm² AFM images of different growth attempts at 1350°C and 800 mbars with 17 sccm of C_3H_8:* ***(a, b)*** *when the Al-face is up and* ***(c, d)*** *when the N-face is up. Inset of* ***(b)*** *is a 0.5×0.5 µm² AFM image. AFM z-scale is 15 nm for* ***(a)*** *and* ***(c)****, and 10 nm for* ***(b)*** *and* ***(d)****.*

associated with in-plane rotational disorder within the graphene sheet, as we have previously discussed in the previous chapter [81,82].

For confirmation of graphene deposition, we examined these samples with XPS and Raman spectroscopy. The corresponding C1s core-level is presented in Fig. 4.8 for the graphene growth attempt when the N-face was exposed to the coming gas ("N-face up"). The spectra in the inset represent the growth attempt when the Al-face was exposed to the gas ("Al-face up"). Regardless of the orientation of the sample during the growth, the black curves represent the spectra recorded on the Al-face, whereas the red curves represent the spectra measured on the N-face. We also show the XPS spectra of the N-and Al-face before any treatment (green and blue curves) and the spectra of the annealed samples before the growth of graphene (orange and pink). The orange and magenta curves correspond to the annealed sample from Fig. 4.4(d). Note that since in this chapter were are dealing with AlN, i.e. an insulating material, the flood gun (electron gun) was used during the XPS measurements, to eliminate or reduce any charging effects of the sample's surface.

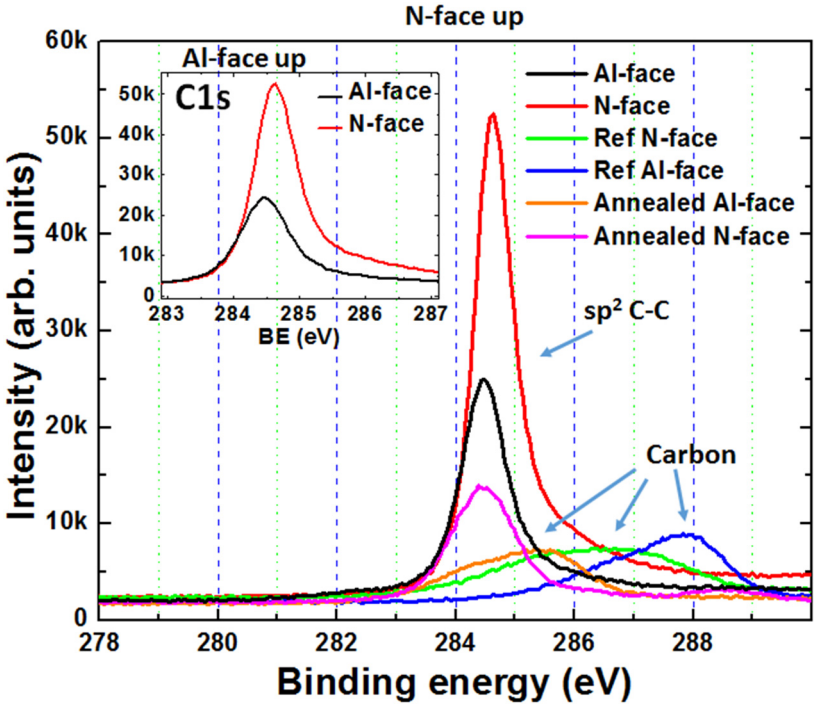

Figure 4. 8: *C1s core-level spectra of the Al-face and the N-face before and after the graphene growth attempts at 1350°C and 800 mbars with 17 sccm of C_3H_8, when the N-face was up (or Al-face up in inset).*

In Fig. 4.8, we can detect a large carbon signature on the AlN substrate (reference samples), which is attributed to a contamination on the surface. After the annealing, the carbon peaks of the annealed samples (orange and magenta) are shifted towards lower binding energies with respect to those of the references. In addition, the carbon peak on the N-face is more intense and narrower after the annealing and appears to be shifted towards the sp^2-carbon peak, indicating the beginning

of a carbon/graphene deposition, possibly from the CVD chamber (which is made of graphite). For the black and red curves, we detect peaks at 284.5 eV, on both N and Al faces after the growth attempt of graphene, in both cases when the N-face is up or when the Al-face is up during growth. We attribute these peaks to a graphitic phase deposition since they are at the vicinity of the sp^2 carbon-carbon binding energy observed for graphene on SiC [86,101,105]. However, no matter which face was up during the growth, the sp^2-peak is always more intense on the N-face than on the Al-face.

To further complete our investigations, we carried out Raman measurements. Fig. 4.9 displays Raman spectra for the two samples presented in Fig. 4.7. The first sample had the Al-face exposed to the incoming gas flow while the N-face was facing the sample holder (presented in Fig. 4.7(a, b)), which corresponds to Fig. 4.9(a). The second sample had the N-face up during the graphene growth attempt (Fig. 4.7(c, d)) and is presented in Fig. 4.9(b). In both cases, both of the AlN polarities have been analyzed by Raman spectroscopy. The spectra measured on the Al-face are represented by the black curves in Fig. 4.9(a, b), whereas the N-face spectra are represented by the red curves. All spectra display the signature of graphene/graphite, i.e. the D, G and 2D modes, but also the D' and D+D' modes, around 1350, 1582, 2700, 1625 and 2900 cm^{-1} respectively [119,160]. The presence of the D and D' peaks implies the presence of defects, for more details on these peaks please refer to **Appendix A**. The same features were detected on FLG grown on AlN on Si (111) templates [103]. For samples grown on the Al-face, the G-peak FWHM ranges between 50 and 55 cm^{-1}, while the 2D-band is barely detected since it presents a low-intensity peak. These observations for the Al-face are usually detected on amorphous or highly disordered sp^2-carbon [141]. In contrast, for graphene grown on the N-face, the G-peak is narrower with FWHM ranging between 21 and 28 cm^{-1}, attesting for the better graphene quality on the N-face compared to the

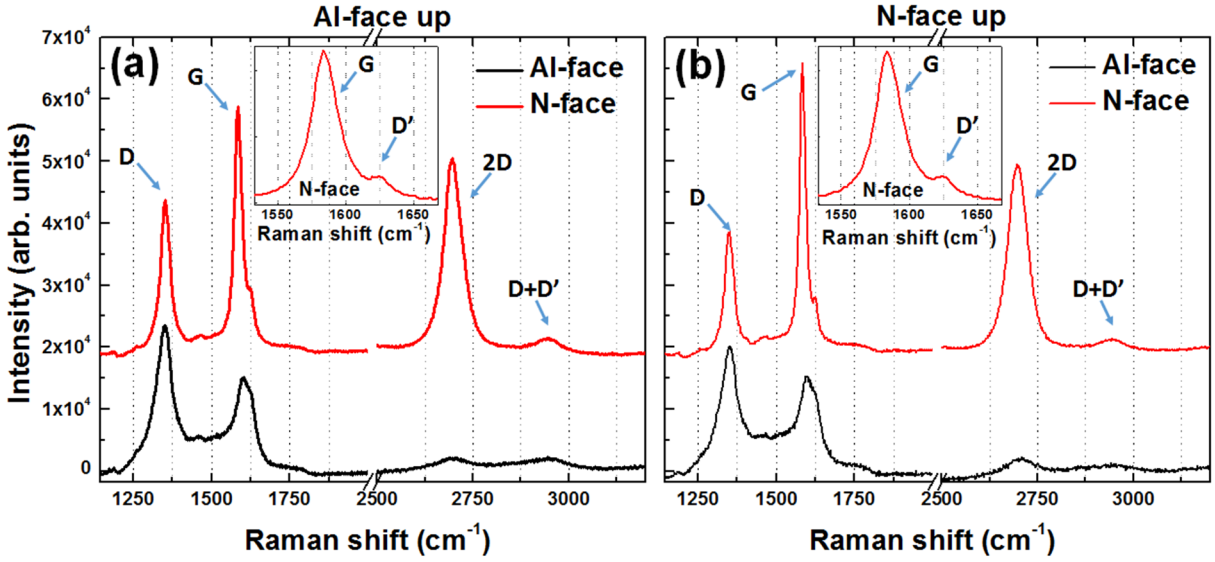

Figure 4. 9: *Raman spectra of the Al-face and N-face of the graphene growth attempts at 1350°C and 800 mbars with 17 sccm of C_3H_8, when the Al-face was up in* ***(a)*** *and when the N-face was up in* ***(b)****. Figures in the inset are a zoom-in on the G-band.*

Al-face. We also detect the 2D-peak on the N-face with FWHM ranging between 43 and 60 cm^{-1}. In addition, the G-peak seems to be more intense on the N-face when the N-face is up during the growth, which is reasonable since it is facing the gas flow of propane.

The G peak integrated intensity normalized to the one of a reference HOPG sample ranges from 0.1 up to 0.6 on the N-face and is around 0.2 on the Al-face, regardless of which face was exposed to the gas flow during the graphene growth attempt. As a first approximation, we can compare these values to those calculated for graphene on SiC, where a single graphene layer corresponds to a G/HOPG ratio around 0.03. Hence, these values imply that few layers and/or multilayers of graphene (FLG/MLG) have been grown. However, we cannot estimate the number of layers with the same formula used for graphene on SiC, since AlN is a different material. In fact, the formula for the calculation of the number of graphene layers was developed for graphene on SiC by combining μ-Raman spectroscopy with μ-transmission measurements in the following way: a low-noise photodiode was placed behind the SiC substrate (on which graphene ribbons were grown) in the same Raman spectroscopy setup, then by doing optical transmission maps and point by point measurements along with the Raman measurements, one can deduce the optical extinction of the bare SiC substrate and of single- and bi-layer graphene and correlate them to the corresponding Raman spectra [146]. Therefore, a similar study should be done on graphene on AlN to precisely calculate the number of deposited graphene layers. Until then, we can deduce that when the G/HOPG ratio is important, more graphene layers have been deposited on the AlN substrate. To this end, even if more statistics are needed to conclude for sure, these observations seem to be compatible with the XPS analysis suggesting that the growth is favored on the N-face more than on the Al-face, even if the N-face is against the substrate holder. We suspect in this latter case, that the propane is able to reach the N-face placed on the sample holder, or it is possible that the sample holder is also a source of carbon.

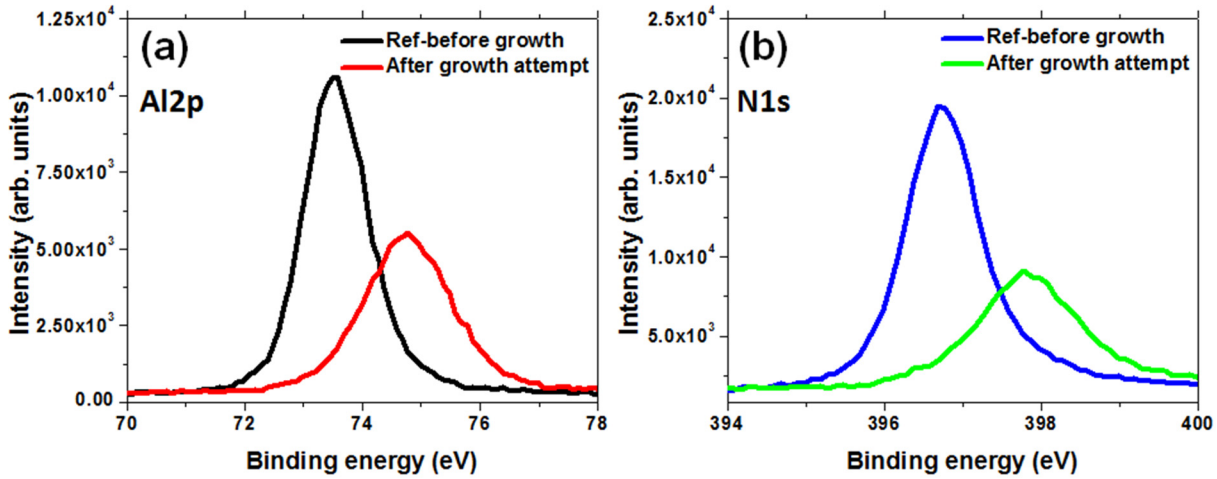

Figure 4. 10: (a) *Al2p and* ***(b)*** *N1s core-level spectra of the N-face when this latter was up during the graphene growth attempt.*

To pinpoint the number of deposited graphene layers we investigated in more details XPS spectra. For example, we examined the Al2p and N1s core-level spectra measured on the N-face after the graphene growth attempt, when the N-face was up (sample in Fig. 4.7(d)). We show these spectra in Fig. 4.10. As we can see after the growth attempt, the Al2p and N1s peaks are almost 50% attenuated but not extinguished. For an excitation energy Al Kα of 1486 eV, N1s and Al2p electrons have kinetic energies around 1100 and 1400 eV respectively, which leads to electrons with IMFP in graphite of ~19 Å (for N1s electrons) and ~24 Å (for Al2p electrons) [133], i.e. corresponding to 5 and 6 graphene layers. Therefore, since we can still detect the AlN signal through the deposited graphene with XPS and knowing the IMFP of the electrons in graphite, we assume that the number of graphene layers is around 5 monolayers or less, but we cannot rule out the presence of thicker layers in some regions. Now concerning the binding energies in Fig. 4.10, we notice that the peaks are upshifted after the growth attempt. This could be because the electrons are being slowed down by the graphene overlayer on their way out of the sample, but more investigations are required to confirm this assumption.

Further investigations reveal that the ratio of peak intensities D/G, which is inversely proportional to the domain size of graphene (see **Appendix A**), is found to be 0.2-0.6 on the N-face and 1.6-1.9 on the Al-face. Thus, using I(D)/I(G) we can deduce that the crystallite size is between 10 and 14 nm on the Al-face, whereas on the N-face it is at least two times larger [204]. In addition, in the case of the Al-face, the I(D')/I(D) is found to be close to 3.5, which points towards boundary defects [121]. On the other hand, on the N-face, the I(D')/I(D) ratio is found to be higher, between 4 and 6. This suggests that there are two types of defects: boundary and vacancy defects [121].

4.2.4. Conclusion

In summary, we have presented in this part the graphene growth attempts on bulk AlN. Starting with already annealed bulk AlN samples, the growth was carried out at 1350°C, 800 mbars, under 100% of N_2 and 17 sccm of propane. AFM images reveal no substantial changes of the Al-face when attempting to grow graphene compared to the annealed sample. On the other hand, the deposition is characterized by the manifestation of wrinkles on the N-face, even when this face is placed against the sample holder. We suspect that propane is able to reach the N-face, or that carbon is coming from the graphite substrate holder. XPS measurements confirm the presence of sp^2 graphene on both faces. However, further investigations with Raman spectroscopy revealed the presence of defects, especially on the Al-face where the deposition is supposed to be amorphous and/or with small disordered sp^2-carbon domains. Compared to our previous study [103], the graphene grown with the same conditions at 1350°C seems better in terms of quality on AlN templates on Si (111), than on the Al-face of bulk AlN. On the other hand, the graphene grown on the N-face of bulk AlN is more developed with larger domains and important deposition, with Raman spectra and domain sizes similar to those in reference [103] for graphene grown at 1350°C. Comparing the growth on the N-face and the Al-face of bulk AlN, the graphene signatures in both XPS and Raman are more intense on the N-face than on the Al-face, attesting for a more favored

growth on the N-face. In all cases, we suspect important deposition of few or multilayers of graphene, which we suspect to be around 5 MLs based on XPS measurements, but we cannot rule out the possibility of having thicker graphene areas. This is not necessarily a drawback if we want to use graphene as a low-resistivity electrode since Bae et al. [10] have demonstrated that increasing the thickness of the deposited graphene will reduce its sheet resistance.

We assume that the favored growth on the N-face is due to rougher surfaces on the N-face (RMS = 3 nm) compared to the Al-face (RMS = 1.1 nm) prior to any treatment. This difference in roughness and also the presence of defects may partly explain the more efficient growth on the N-face, but more investigations are required to understand this difference in growth. In addition, by combining the observations of AFM, XPS and Raman spectroscopy, we point out certain similarities in the growth mechanism on the C-face of SiC and on the N-face of AlN. On the C-face of SiC, FLG films are characterized by a large number of layers with rotational disorder and by the presence of wrinkles on the surface [81,90,189]. Similarly, in this work, we observed wrinkles and a more important carbon deposition on the N-face of AlN, and even though we have not done any LEED measurements, Raman spectroscopy reveals an important D peak which implies the presence of disorder within the FLG layers on both N and Al faces. Finally, the results seem promising but future work should concentrate on enhancing the graphene quality by investigating other growth parameters, or considering other surface preparation methods for the Al-face. In addition, electrical measurements are necessary to assess the graphene electrical properties, especially since in the present study the samples were not big enough to process Van der Pauw patterns for the electrical measurements. However, we did detect a current flow when placing two electrical probes on the samples surface after graphene growth attempt, which confirms the deposition of conductive graphene layers on AlN.

4.3. AlN templates on SiC (0001)

4.3.1. AlN/SiC templates annealing

In this part, we will discuss the annealing of AlN layers grown by MBE on SiC templates. The AlN is 240 nm-thick with aluminum as the polarity. We show in Fig. 4.11 AFM images of the AlN/SiC template (template I) prior to any annealing. In the 5×5 µm^2 AFM image (Fig. 4.11(a)) we can detect some 3D clusters, which appear in some areas of the sample. The origin of these clusters could be either from the annealing of the SiC prior to the AlN growth and/or from the growth of AlN itself. In Fig. 4.11(b) we can discern a step-like morphology, probably due to the initial morphology of SiC prior to the AlN growth. The goal of the annealing is to test whether the AlN layers can withstand the high temperature required for the graphene growth, but also to see if we can enhance the sample's surface.

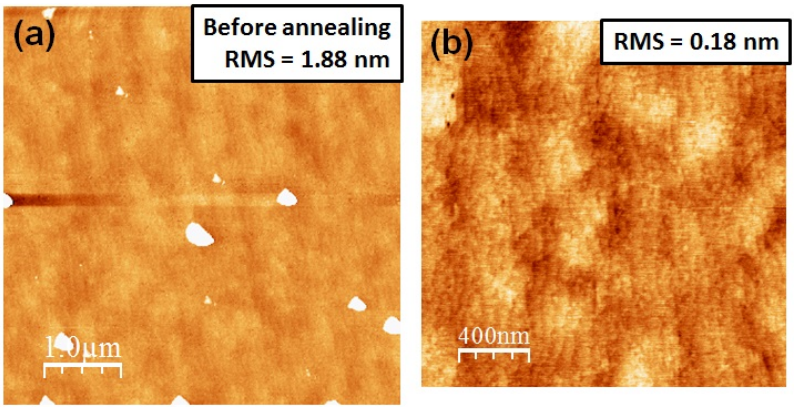

Figure 4. 11: (a) *5×5 µm^2 AFM image of the 240 nm-thick AlN layer grown on SiC (AFM z-scale: 3 nm).* ***(b)*** *2×2 µm^2 AFM image (AFM z-scale: 1.5 nm)*

The AlN/SiC template was exposed to different gas mixtures at 1450°C and 800 mbars, for 5 minutes, as we present in Fig. 4.12. Unlike the previous part, the total gas mixture was set to 6 slm in this part, instead of 16 slm as it was in the case of bulk AlN. We also changed another parameter for this particular study: the position of the sample in the reactor. The sample was placed towards the back of the reactor, precisely 1.5 cm more than the usual position. We do not usually change this position as it is already optimized, we only changed it for the study on AlN templates since it seemed to be giving better results. This parameter will be referred to as X in the following; here X is set at 40 mm instead of the usual position at 25 mm.

The annealing under 0% H_2 + 100% N_2 in Fig. 4.12(b) does not seem to have any effect on the surface compared to the reference surface in Fig. 4.12(a). In addition, we can still detect few 3D clusters when doing a larger scale image (inset of Fig. 4.12(b)). Similarly, for the annealing under 50% H_2 + 50% N_2 (Fig. 4.12(c)), the surface remains unchanged, where atomic steps still appear and few 3D objects can be detected when scanning large areas with AFM. However, increasing the hydrogen to 100% (Fig. 4.12(d)) leads to the formation of open etching pits as well as 3D objects. This can be explained by considering that H_2 is etching the surface and the etched

material is being re-deposited on the surface to form 3D aggregates. These first results show that the surface of the AlN layers on SiC is quite stable under N_2 + H_2 at 1450°C as long as we avoid putting too much hydrogen in the gas mixture. Therefore, this AlN on SiC substrate can be a good candidate for the growth of graphene at high temperatures.

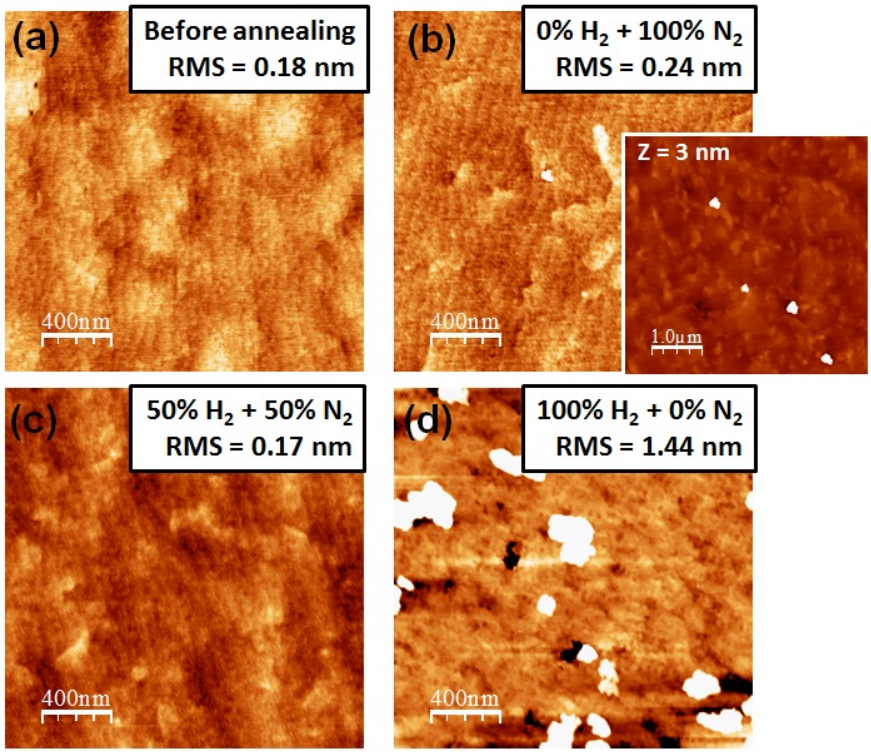

Figure 4. 12: *2×2 µm² AFM images of* ***(a)*** *the reference image before any annealing,* ***(b)*** *to* ***(d)*** *the annealed AlN/SiC samples at 1450°C, 800 mbars, 5 minutes with different gas mixtures:* ***(b)*** *0% H_2 + 100% N_2,* ***(c)*** *50% H_2 + 50% N_2,* ***(d)*** *100% H_2 + 0% N_2. Inset of* ***(b)*** *5×5µm². AFM z-scale is 1.5 nm, except for* ***(d)*** *z = 3 nm.*

With these annealing attempts we showed that the AlN morphology is stable at 1450°C under specific conditions, but we did not enhance the surface quality in any way. In fact, the objective of the annealing is to remove the 3D objects while leading to the formation of well-defined atomic steps with wide terraces, without creating etching pits. For this reason, we tried to increase the temperature to 1550°C under 50% H_2 + 50% N_2, see Fig. 4.13(b). The annealing at 1550°C reveals small etching pits, see Fig. 4.13(c). The increase in temperature has increased the etching but did not enhance the surface quality. It seems that our objective is complicated to reach with this AlN template. We will have to settle for the annealing at 1450°C under 100% of N_2 or with low amount of H_2. Now that we have examined the different AlN layer morphologies at high temperatures and with different gas mixtures, it is possible to study the growth conditions of graphene since the AlN layer seems to be stable at 1450°C under 100% of N_2 and 50% H_2 + 50% N_2.

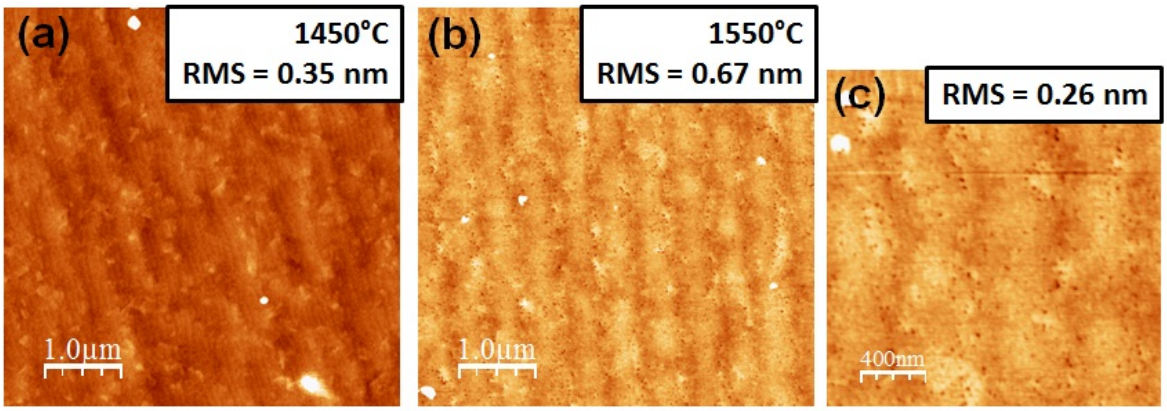

Figure 4. 13: *5×5 µm² AFM images of the annealing with 50% H_2 + 50% N_2 at* ***(a)*** *1450°C and* ***(b)*** *1550°C.* ***(c)*** *The corresponding 2×2 µm² AFM image of* ***(b)****. AFM z-scale is 3 nm.*

4.3.2. Graphene growth on AlN/SiC templates

For the growth of graphene, we first considered the 240 nm-thick AlN on SiC template (template I). The substrate was found to be stable at 1450°C, 800 mbars with 100% of N_2. Therefore, we applied these conditions while adding propane for 5 minutes for the growth of graphene. Our first attempts were done at X = 25 mm, which is the usual position of the sample in the reactor. However, as we can see in Fig. 4.14(a), the growth with 2 sccm of propane revealed small pits across the surface, probably due to etching or AlN decomposition. Adding 5 sccm of

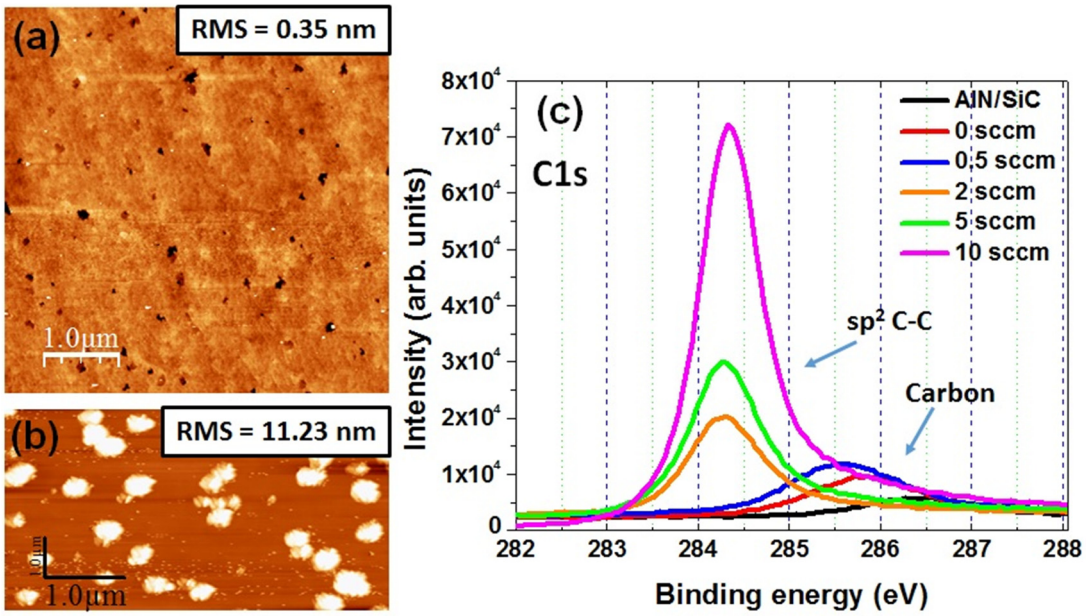

Figure 4. 14: *5×5 µm² AFM images of graphene grown at 1450°C with* ***(a)*** *2 sccm (z = 3 nm) and* ***(b)*** *5 sccm of propane (z = 50 nm).* ***(c)*** *The corresponding C1s core-level spectra of the different growth with different propane amounts.*

propane leads to areas with over deposition as we can see in Fig. 4.14(b). It could be either that 5 sccm of propane is already too much for the growth of graphene on AlN templates, or an issue related to the growth kinetics, which can be solved by increasing the temperature or the total pressure. It is probably the latter reason, since the growth is accumulated in certain regions and not uniformly distributed on the surface.

Investigating the C1s core-level of the samples grown with different propane flow rates, presented in Fig. 4.14(c) adds interesting information. The black curve represents the reference sample before any annealing or growth attempt, while the red one is a regular annealing without any propane. These two spectra are in the vicinity of amorphous carbon, but the red curve is slightly shifted towards lower binding energies. Adding only 0.5 sccm of propane to the gas mixture (blue curve) results also in a small shift towards lower binding energies, without any noticeable increase in the peak's intensity. These shifts could be a beginning of carbon/graphene deposition, making the sample slightly more conductive than the reference sample, with less charging effects. When increasing the propane flow rate to 2 sccm, the corresponding peak (orange curve) is more intense than the previous one and appears at 284.3 eV in the vicinity of sp^2-graphene. Increasing the amount of propane to 5 sccm and 10 sccm leads to an increase in the intensity of the corresponding peak, especially for the 10 sccm-sample. We can conclude from these observations that 2 sccm of propane is enough to deposit carbon/graphene and that increasing the propane flow rate increases the deposition but in a non-uniform way since the 5 sccm-growth AFM image reveals areas of over deposition. Since we are limited in terms of temperature we considered only 2 sccm of propane for the growth of graphene and placed the sample at X = 40 mm in an attempt to avoid or minimize the formation of open pits on the surface.

Interestingly the growth seems better at X = 40 mm as we can see in Fig. 4.15(a), always at 1450°C and 100% N_2. The growth in Fig. 4.15(a) shows no marks of open pits compared to the AFM image in Fig. 4.14(a). Note that the scan area is not the same for both images, but still open pits should be detectable in a 2×2 μm^2-area, if they are present. We also tried different pressures: 800 mbars (Fig. 4.15(a)) and 900 mbars (Fig. 4.15(b)) as the total pressure in an attempt to enhance the uniformity of the deposition. The growth at 900 mbars in Fig. 4.15(b) presents the same morphology as in Fig. 4.15(a) without any difference detected. We compare the C1s core-level spectra of these two growths and the growth at X = 25 mm in Fig. 4.15(c). No noticeable difference is detected between the peak of the growth at X = 40 mm (red curve) and that of the growth at X = 25 mm (orange curve) at 800 mbars, whereas the peak corresponding to the 900 mbars-growth (blue curve) seems slightly upshifted in intensity. These observations confirm that it is possible to place the sample at X = 40 mm without compromising the deposition while enhancing the morphology. We assume that when we place the sample towards the back of the reactor the thermodynamics and hydrodynamics of the growth change. It is complicated to really assess these parameters, but it is possible to attribute the change to a reduced exposure to the incoming gases. In fact, the gases have to undergo a longer distance at the high temperature before they reach the

sample, which could initiate chemical reactions and the decomposition of propane before arriving to the sample.

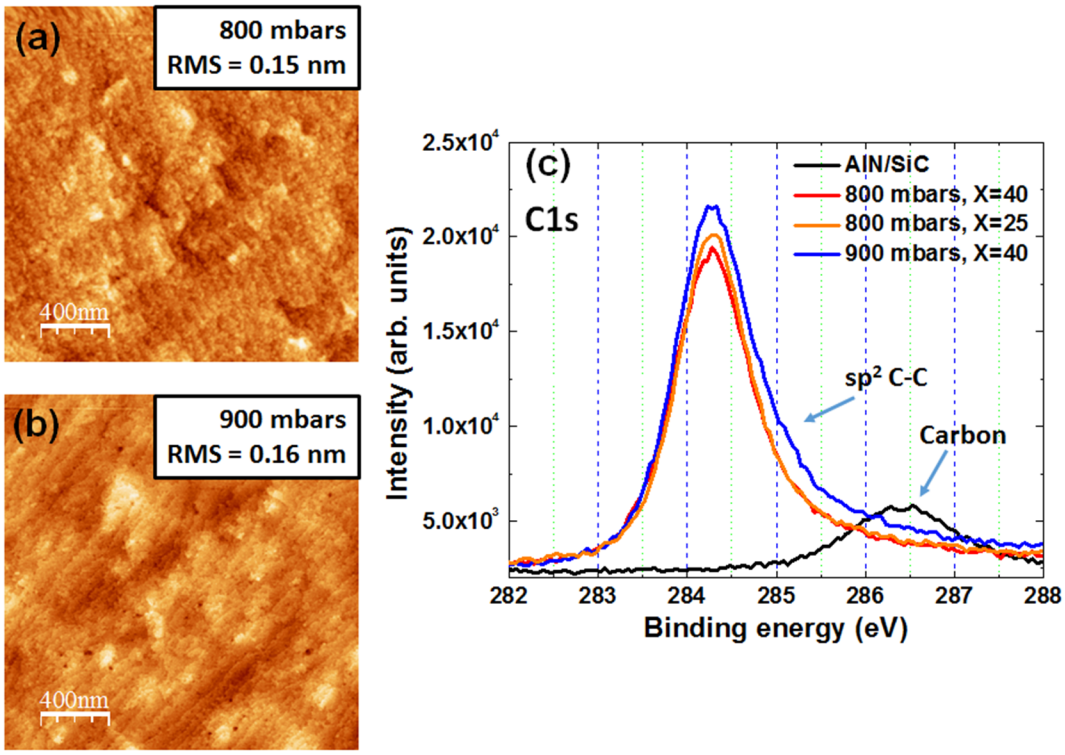

Figure 4. 15: *2×2 µm² AFM images of graphene grown at 1450°C with 2 sccm of propane at* ***(a)*** *800 mbars and* ***(b)*** *900 mbars. AFM z-scale is 1.5 nm.* ***(c)*** *The corresponding C1s core-level spectra of the different growths.*

We also did LEED measurements to uncover the structure of the grown graphene on AlN. The graphene growth was done at 900 mbars, 100% of N_2, for 5 minutes under 2 sccm of propane, at 1450°C presented in Fig. 4.16(a) and at 1550°C presented in Fig. 4.16(b). The growth at 1550°C seems stable but we notice the appearance of an open pit, indicated by a white arrow in Fig. 4.16(b). The corresponding LEED images are presented in Fig. 4.16(c, d). We notice the presence of graphitic rings which suggests that the graphene is disordered. We also perceive the diffraction spots of AlN, which we can identify when comparing the diffraction patterns to a reference AlN/SiC shown in the inset of Fig. 4.16(c). We can make the same observations in Fig. 4.16(d) for the growth at 1550°C, but in this case the elongated shapes appear to be shorter. It could be a sign that graphene starts to become more ordered at the higher temperature. We also notice that the graphene lattice is oriented at a 30°-angle with respect to the AlN lattice, which is similar to the growth of graphene on SiC (0001).

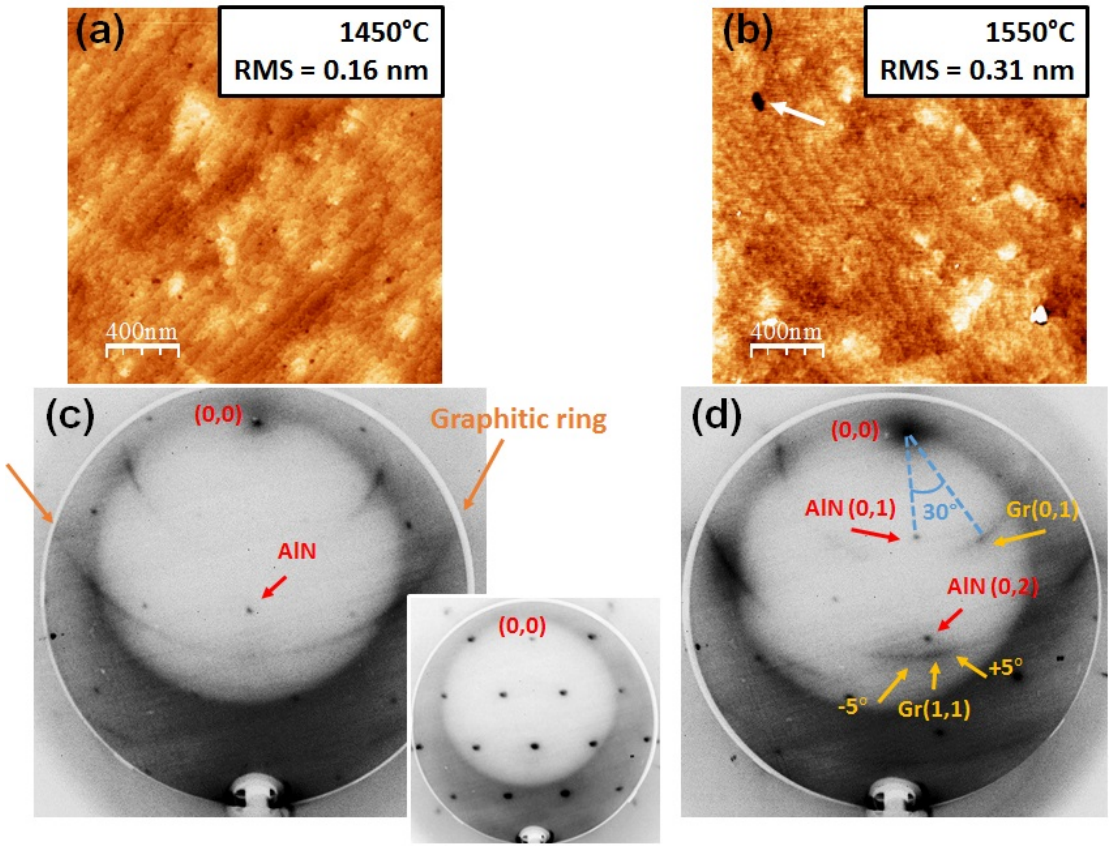

Figure 4. 16: *2×2 μm² AFM images of graphene grown at* ***(a)*** *1450°C and* ***(b)*** *1550°C, with 2 sccm of propane at 900 mbars. AFM z-scale is 1.5 nm.* ***(c)*** *and* ***(d)*** *the corresponding LEED diffraction patterns taken at an electron energy of 160 eV. AlN/SiC reference presented in the inset of* ***(c)****.*

To complete our study, we attempted to do Raman measurements on each of the samples in two different regions. However, Raman investigations revealed areas without any graphene for both samples, as we can see in Fig. 4.17, without the subtraction of the AlN/SiC template signal. Even with the SiC background signal, we should be able to see the 2D-peak or at least a low intensity peak around 2700 cm^{-1} (similar to the case of the Al-face on bulk AlN), but no signs of the 2D-band can be detected. These observations are not in agreement with XPS, but the spot widths of the two techniques are not the same: the spot width of the laser for Raman measurements is around 400 nm, whereas the spot width of the X-ray gun in XPS is around 400 microns. Therefore, it might be possible that graphene does not cover the whole surface.

To summarize this part, we were able to deposit a graphitic phase on the AlN/SiC templates. We tested different growth parameters such as the propane flow rate, the sample's position in the reactor, the temperature and the total pressure. Based on AFM and XPS observations, our first deduction was that the best position to conserve the sample's surface quality is at X = 40 mm, i.e. 15 mm more than the usual position. The ideal propane flow rate for the

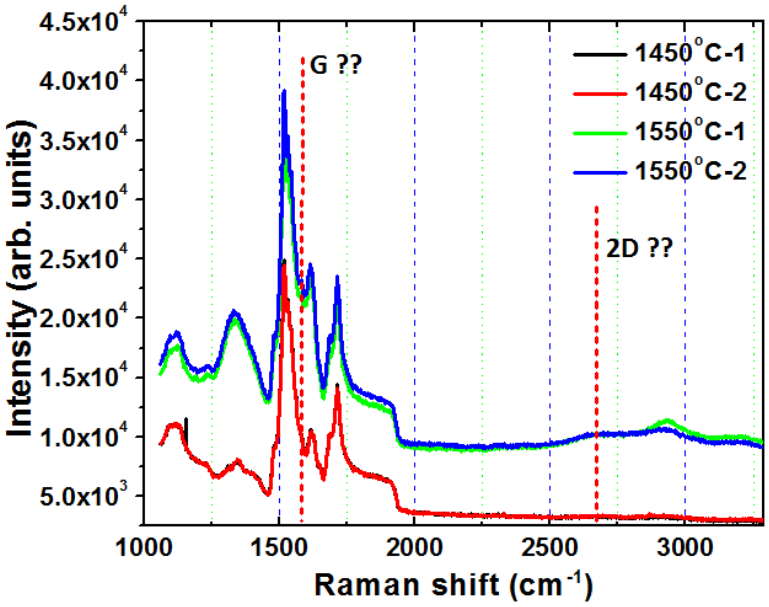

Figure 4. 17: *Raman spectra of the graphene growth attempts at 1450 and 1550°C. The spectra were vertically shifted for clarity.*

growth of graphene is 2 sccm, since at 5 sccm the growth is not uniform and over deposition features appear on the surface. No important differences appear when increasing the total pressure to 900 mbars, nor when increasing the temperature to 1550°C. However, at 1550°C some open pits start to appear, therefore it is possible to consider this temperature as the limit for the growth of graphene on AlN. LEED measurements revealed that the graphene is disordered, but we suspect that it is less disordered at 1550°C compared to 1450°C. It also seems to have a favored orientation at a 30°-angle with respect to the AlN lattice at 1550°C, which is similar to the growth of graphene on SiC (0001). Nevertheless, Raman measurements revealed areas without any graphene, for both of the samples grown at 1450 and 1550°C. We suspect that these areas are not dominant, since Raman is a more local technique with a laser spot width of 400 nm. In contrast, XPS and LEED, which have a larger spot size, confirm the presence of a graphene or a graphitic phase, based on the presence of a sp^2-carbon peak in XPS spectra and graphitic rings in LEED patterns, along with diffraction spots for the 1550°C-growth corresponding to graphene. In conclusion, it is important to do wider scans with Raman spectroscopy, but so far it seems that the graphene deposition is not uniform and not covering the whole sample's surface.

So far we have shown that the growth of graphene on AlN is possible, but the growth is not optimized. The disorder and the possibility of having incomplete graphene layers can be very detrimental for the electrical properties of graphene. Therefore, we attempted to grow graphene on another AlN/SiC template (template II), but this time the AlN layer is thinner (about 100 nm) and the SiC substrate was annealed under H_2 prior to the growth of AlN [205]. In addition, the SiC substrate is 4°-off axis in this case, whereas the previous SiC substrate was 0.2°-off. We show an AFM image of the AlN surface before any annealing or graphene attempts in Fig. 4.18(a). The

surface presents well-defined steps and a higher RMS of 1.1 nm compared to the previous template (cf. Fig. 4.11(b)). In addition, a smaller scale AFM image (inset of Fig. 4.18(a)) reveals rough step edges. The higher RMS in this case could be due to the off-axis SiC substrate and to the fact that the AlN layer is not as thick as in the previous case, thus making it more influenced by the morphology of the SiC substrate. In addition, the crystalline quality of the AlN film, examined with XRD, seems better on the AlN/SiC template I, having a lower ω-scan FWHM of the (0004) reflection (~0.17°) compared to that of the AlN/SiC template II (~0.38°).

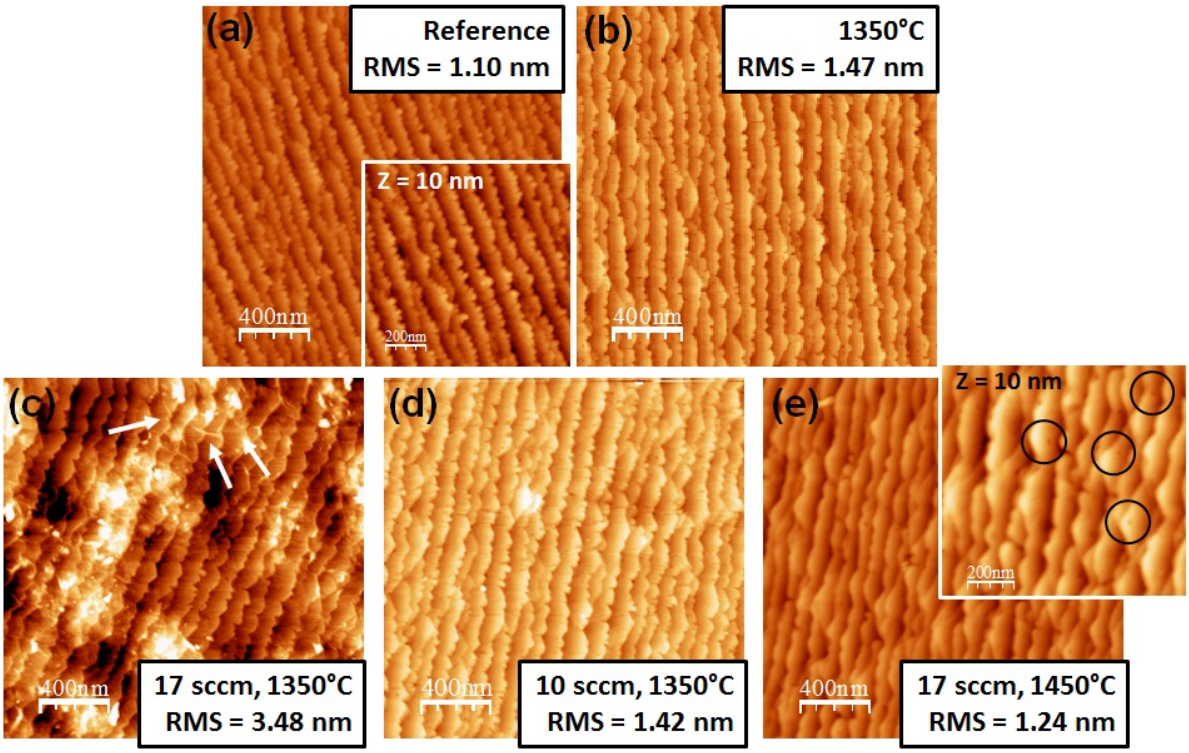

Figure 4. 18: *2×2 μm² AFM images of **(a)** 100 nm AlN on SiC, **(b)** 5-min annealing at 1350°C, **(c)** graphene growth attempt at 1350°C with 17 sccm of propane, **(d)** graphene growth at 1350°C with 10 sccm of propane and **(e)** graphene growth at 1450°C with 17 sccm of propane. Inset of **(a)** and **(e)** are 1×1 μm² AFM images. AFM z-scale: 15 nm.*

The first annealing and graphene growth attempts were carried out in similar conditions than before: 1350°C, 100% N_2 (10 slm), 800 mbars, X = 25 mm. The 5-minute annealing is shown in Fig. 4.18(b), where no clear changes appear with respect to the reference image, we only notice an increase in the RMS. For the growth of graphene, similarly to bulk AlN, 17 sccm of propane and 6 minutes of growth were required to deposit graphene, see Fig. 4.18(c). As we can see in this AFM image, brighter regions appear, which we suspect to be graphene over deposition areas. We also detect few wrinkles in these areas, indicated by white arrows in Fig. 4.18(c), which we attribute to a graphitic phase deposition. To make the deposition more uniform, we considered two solutions: reducing the propane flow rate to 10 sccm at 1350°C (Fig. 4.18(d)) and increasing the growth temperature to 1450°C for 17 sccm of propane (Fig. 4.18(e)). In Fig. 4.18(d) we do not see

the over deposition areas nor the wrinkles. The surface resembles the reference morphology in Fig. 4.18(a), therefore it is hard to say if we have a graphitic deposition or not. Also in Fig. 4.18(e) for the growth at 1450°C, no over deposition nor wrinkles can be detected, but instead the morphology looks slightly better since the step edges seem to be smooth and not rough as in the reference image in Fig. 4.18(a). This could be a sign of graphene deposition, which covers the AlN steps. We also detect some point-like defects indicated by black circles in the 2×2 μm^2 AFM image shown in the inset of Fig. 4.18(e). These points are very small and barely discernable, they could be either dislocations or from the high temperature growth of graphene. However, from first observations the higher temperature seems to have improved the uniformity of the growth compared to Fig. 4.18(c).

We examined the C1s core-level spectra of the annealed sample and the growth samples, as presented in Fig. 4.19. The annealed sample (red curve) presents an intense carbon peak at 286.9 eV, probably due to carbon contamination from the reactor, but surprisingly the peak did not shift towards lower binding energy compared to the reference peak, as it was the case for the previous substrate and the bulk AlN. It might be possible that for this substrate a higher temperature is required to obtain a graphitic deposition by just annealing. The peak corresponding to the growth at 1350°C with 10 sccm of propane (blue curve) is more intense than the reference peak and appears in the vicinity of sp^2-graphene at 284.9 eV, whereas the 17 sccm growth at 1350°C (orange curve) results in a peak even more intense and at 284.6 eV. These observations suggest that increasing the propane flow rate increases the graphene deposition and makes the sample more conductive, resulting in a sp^2-peak at lower binding energies. Finally, our attempt to make the growth more uniform by increasing the temperature to 1450°C for 17 sccm of propane

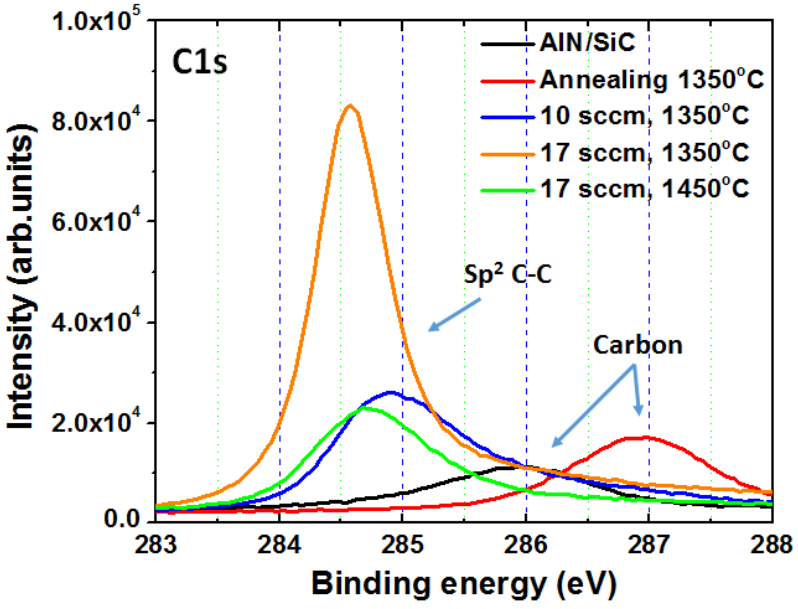

Figure 4. 19: *C1s core-level spectra of the annealed sample and the graphene growth samples, prepared at 1350 and 1450°C at 800 mbars and 100% of N_2.*

is represented by the green curve appearing at 284.7 eV. Unfortunately, the peak is reduced in intensity compared to the orange and the blue peaks, leading us to the conclusion that this could be not the best approach to make the deposition more uniform if we want to achieve a thick graphene deposition.

We completed the study with Raman spectroscopy, presented in Fig. 4.20. All the spectra reveal the signature of graphene with defects, i.e. the D, G, D', 2D and D+D' modes around 1350, 1582, 1625, 2700 and 2900 cm^{-1} respectively [119,160]. The sample grown at 1350°C presented in Fig. 4.20(a) displays Raman spectra which are similar, but a difference in intensities rises when scanning different regions of the sample. The reason behind this difference in intensity can be due to the presence of regions with a thicker deposition, as already observed with AFM (see Fig. 4.18(c)). The I(D)/I(D') ratio is found to be close to 3.5 which again points towards boundary defects [121]. And by using I(D)/I(G) [204], the crystallite size is found to be between 12 and 30 nm. On the other hand, for the sample grown at 1450°C, Raman measurements presented in Fig. 4.20(b) reveal that the sample is mainly covered by poor quality graphene, represented by the blue spectrum, similar to that observed on the aluminum face of bulk AlN. Other areas present a better graphene quality, represented by the green spectrum in Fig. 4.20(b), but unfortunately, the poor quality areas are dominant. No Raman measurements were done on the 10 sccm-growth. We can conclude that even though AFM first observations suggest that the growth is more uniform at 1450°C, where no over deposition features appear, Raman spectroscopy reveal areas with poor quality graphene. In contrast, the growth at 1350°C presents uniform graphene in terms of quality but some areas of different thicknesses. This leads us to the conclusion that increasing the temperature is probably not the best solution for a good uniform growth. Perhaps the growth time should be increased as well when increasing the temperature.

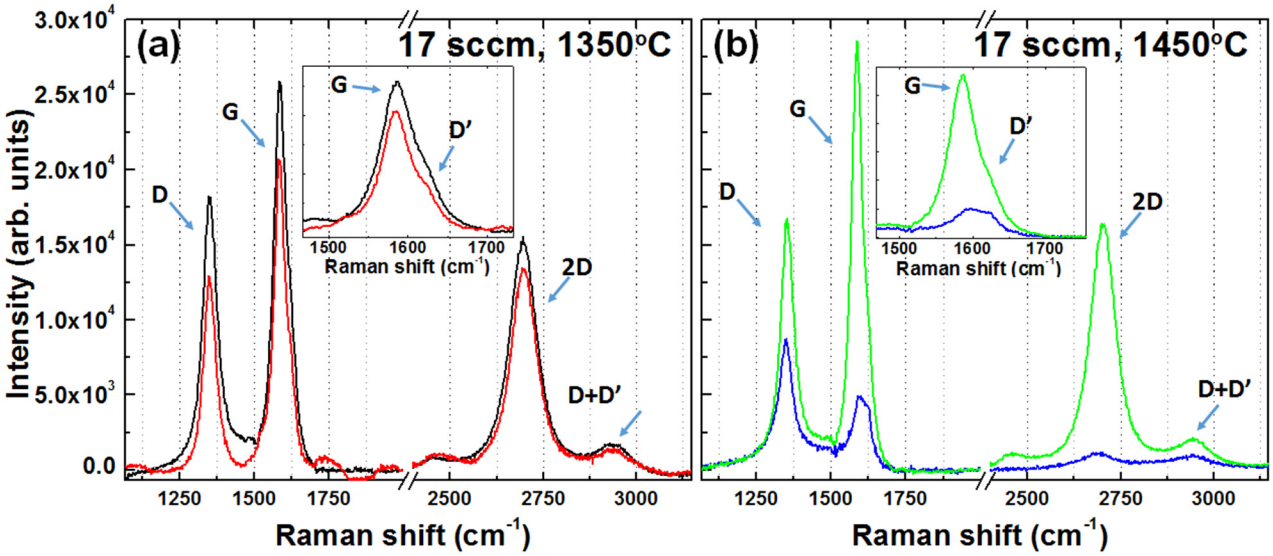

Figure 4. 20: *Raman measurements of different areas of the* ***(a)*** *1350°C-growth and* ***(b)*** *1450°C-growth. The two figures have the same vertical scale. Figures in the inset are a zoom-in on the G-peak.*

4.3.3. Conclusion

As a conclusion, we have attempted to grow graphene on AlN grown on SiC templates. Prior to the growth of graphene, annealing tests were done at 1350 and 1450°C to see if the AlN surface can withstand the high temperature required for the graphene growth and to try to enhance the AlN morphology. A first substrate was studied with a 240 nm-thick AlN layer. The AlN was found to be stable under a gas mixture with low hydrogen amount at 1450°C (less or equal to 50% of the total gas mixture). For the growth of graphene we explored different growth parameters to optimize the growth conditions, such as the propane flow, the total pressure and the sample's position in the reactor. The best growth conditions were found to be with 2 sccm of propane for 5 minutes at 1450°C, 800 or 900 mbars and at a position X = 40 mm, i.e. 15 mm more than the usual position. XPS and LEED revealed the deposition of a graphitic phase, by exhibiting the sp^2-carbon peak with XPS and graphitic rings with LEED. This latter observation with LEED suggests that the graphene consists of disordered domains, but we suspect that the growth at 1550°C slightly reduces the disorder amount. Despite this promising observations, Raman spectroscopy, which is more local, uncovered areas without any graphene. Therefore, we conclude that the growth is not uniform and that graphene does not cover the whole surface of the sample, but we suspect that the areas with graphene present a better quality when grown at 1550°C instead of 1450°C.

For this reason, the growth of graphene was studied on another template with a 100 nm-thick AlN layer grown on an off-axis SiC substrate and a special H_2-annealing of the SiC substrate prior to the growth of AlN. This substrate can be more promising for applications using the AlN as a back-gate since it is thinner than the previous case. The growth of graphene on this substrate seemed different, requiring more propane as high as 17 sccm at 1350°C, similar to the growth on bulk AlN. This latter growth presented areas of over deposition but Raman spectroscopy revealed a uniform graphene growth in terms of quality with the presence of boundary defects. Our attempts of having a more uniform growth in terms of thickness were not very successful. We attempted to reduce the propane flow rate to 10 sccm at 1350°C, which resulted in a less intense sp^2-graphene peak in XPS. We also attempted to increase the temperature to 1450°C for 17 sccm of propane. Even though the morphology seems uniform with AFM, Raman spectroscopy unveiled areas with poor quality graphene. We also attempted to study the influence of the growth duration, but we do not present any results here since the effects are similar to the increase in the propane flow rate. In fact, when we do a growth longer than 5 minutes (e.g. 8 minutes) we will obtain areas with over deposition similar to what we observed for a growth with too much propane.

So far the growth of graphene on AlN/SiC templates seems promising but challenging, requiring a more thorough study of the different growth parameters to enhance the graphene's uniformity and quality. In addition, the growth of graphene seems very dependent on the substrate itself, since different substrates required different propane amounts for the growth to take place. We believe that this rises from the different preparation of the AlN layers and mainly from the different morphology. The first AlN/SiC template presented a lower RMS but a higher step density, thus requiring only 2 sccm of propane to grow graphene, whereas the second template

presented a higher RMS but lower step density and required 10 to 17 sccm of propane to grow graphene. Therefore, the growth appears to be dependent on the step density, which seems normal since a higher step density presents more nucleation sites for the graphene growth.

4.4. AlN templates on sapphire (0001)

4.4.1. AlN/sapphire templates annealing

The most common substrate for the growth of AlN is sapphire owing to its low cost, therefore our study would be incomplete if we do not consider such substrates for the growth of graphene. Similarly to before, it is important to monitor the behavior of the AlN layer at high temperatures in the range of the graphene growth. Hence, our first approach would be to investigate the effects of high temperature annealing on the morphology of AlN layers grown on sapphire.

Our second approach revolves around the high temperature annealing effect on the crystalline quality of the epitaxial AlN layers. In fact, since sapphire is a low cost substrate it is attractive for the growth of AlN, but on the other hand, due to important difference in lattice parameters, high density of threading dislocations emerge within the AlN epitaxial layer. We conducted a study to improve the structure of AlN and reduce the dislocations density [123].

For the following studies different templates of AlN on sapphire were used, but the thickness of the AlN layer is always 120 nm. The difference between the substrates is in the growth conditions of the epitaxial AlN layer, mainly in the growth temperature.

4.4.1.1. Annealing effect on the morphology

The first annealing attempts were carried out at 1450°C and 800 mbars, for 5 minutes with a gas mixture of 6 slm (N_2 + H_2); the sample is placed at X = 40 mm. The AlN layer was grown by MBE at 900°C, with a nucleation layer grown at 500°C. The reference morphology before any annealing is shown in Fig. 4.21(a). As we can see, the initial surface before any annealing is already rough (RMS = 3.5 nm). Annealing the sample with 100% of N_2 (Fig. 4.21(b)) in the gas mixture results in a small decrease in the roughness, but no obvious improvements in the morphology. We also detect some aggregates (white features on AFM images) at the surface, either from the growth of AlN before any annealing or from the re-deposition of etched AlN. Adding hydrogen to the gas mixture even degrades the morphology as we can see in Fig. 4.21(c), more aggregates appear and the RMS increases to 6 nm. As to the 100% H_2-annealing presented in Fig. 4.21(d), no white objects appear and the RMS is about 3 nm.

We attempted to study another AlN template on sapphire (template II), prepared with slightly different conditions: the AlN layer was grown at 1000°C and the nucleation layer at 400°C. XRD measurements reveal that the crystalline quality of the AlN/sapphire template I is better with a ω-scan FWHM of the (0002) reflection around 0.036°, whereas the AlN/sapphire template II presents a ω-scan FWHM of the (0002) reflection around 0.17°. The initial morphology seems slightly better than before, see Fig. 4.22(a). The surface is less rough (RMS = 0.93 nm) than the previous template, but aggregates still appear from the growth of AlN. We can also detect some very small open pits in the 2×2 μm^2-AFM image (figure in inset). The annealing at 100% N_2 shown in Fig. 4.22(b) seems to enlarge the open pits, but the RMS has slightly decreased. The expansion of the open pits is not very encouraging and represents a limitation for the growth of graphene. Adding hydrogen to the gas mixture leads to wider pits and rougher surfaces with a higher RMS, see Fig. 4.22(c, d).

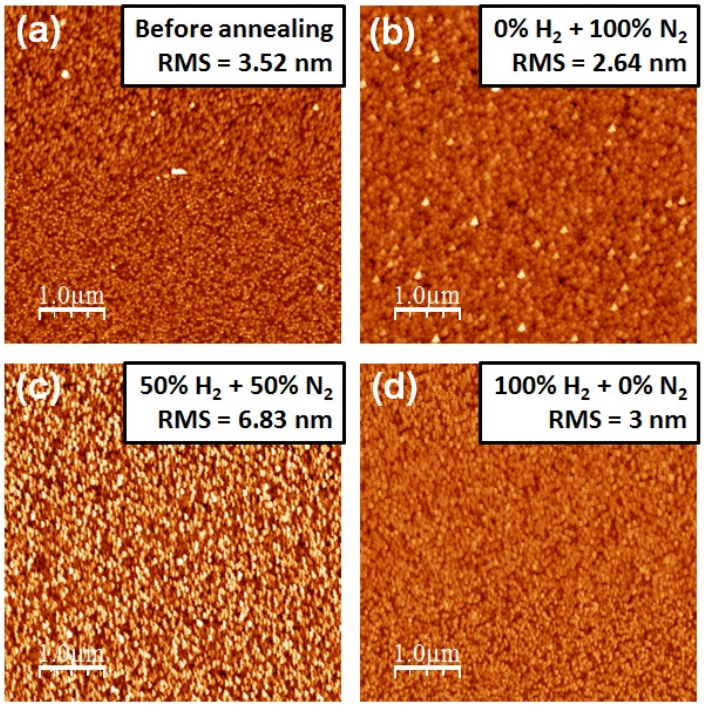

Figure 4. 22: *5×5 µm²-AFM images of the different annealing at 1450°C for different gas mixtures:* ***(a)*** *the reference AlN/sapphire template I,* ***(b)*** *0% H_2 + 100% N_2,* ***(c)*** *50% H_2 + 50% N_2 and* ***(d)*** *100% H_2 + 0% N_2. The AFM z-scale is 30 nm for all the samples.*

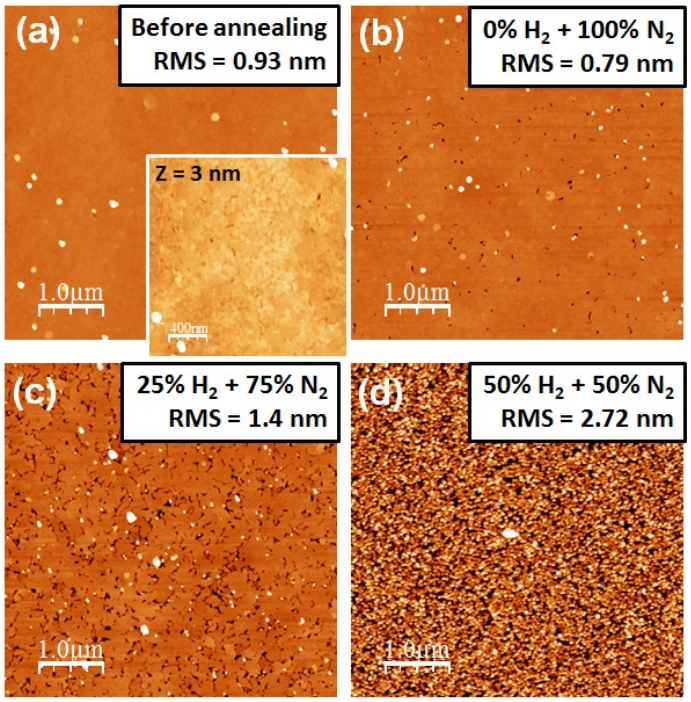

Figure 4. 21: *5×5 µm²-AFM images of the different annealing at 1450°C for different gas mixtures:* ***(a)*** *the reference AlN/sapphire template II,* ***(b)*** *0% H_2 + 100% N_2,* ***(c)*** *25% H_2 + 75% N_2 and* ***(d)*** *50% H_2 + 50% N_2. Inset of* ***(a)*** *is a 2×2 µm²-AFM image.*

The annealing of the AlN/sapphire templates does not seem to enhance the morphology and the surface quality of the AlN film, but the surface is more or less stable when annealing with 100% of N_2 at 1450°C. Therefore, it is better to use N_2 when attempting to grow graphene or for other annealing purposes. We will present in the following the annealing effects on the crystalline structure of AlN grown on sapphire.

4.4.1.2. Annealing effect on the crystallinity

For this particular study [123] two AlN/sapphire templates were prepared with two different growth conditions: templates III and IV, but we will refer to them as S1 and S2 as they are presented in reference [123]. The difference between the two templates is the temperature of the nitridation step: 940°C for S1 and 900°C for S2. Then the nucleation layer growth step is the same for both samples, carried out at 400°C and finally the 120 nm-AlN layer was deposited at 940°C for S1 and 900°C for S2. The annealing of the samples was conducted in the CVD reactor and the XRD study was carried out by Maud Nemoz at CRHEA.

The annealing temperatures ranged between 1350 and 1650°C for 6 minutes at 800 mbars with 6 slm of N_2 in the gas mixture. The annealing time effect was also studied, by annealing one sample for 5 minutes at first then annealing it again for extra 15 minutes. We also attempted flash annealing, meaning that the temperature was increased to reach the annealing temperature

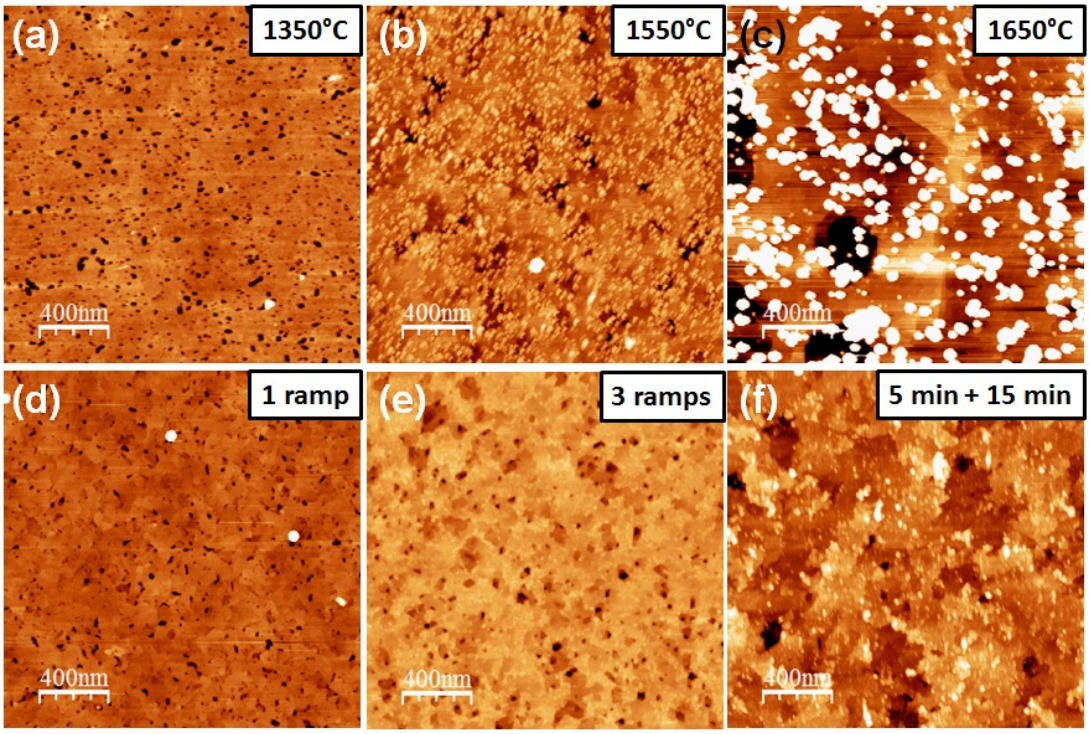

Figure 4. 23: *2×2 µm²-AFM images of the annealed samples of the S2 template at* ***(a)*** *1350°C,* ***(b)*** *1550°C and* ***(c)*** *1650°C.* ***(d)*** *to* ***(f)*** *annealing at 1550°C for different annealing times:* ***(d)*** *1 temperature ramp (no plateau),* ***(e)*** *3 temperature ramps and* ***(f)*** *two-step annealing, the first for 5 min then for 15 min. The AFM z-scale is 10 nm, except for* ***(a)*** *and* ***(d)*** *where it is 5 nm.*

(1550°C), followed by an immediate decrease to the room temperature. We did this for one sample and for another sample we did three successive ramps from room temperature to 1550°C and back to room temperature each time. We show AFM images of some of the annealed samples of the S2 template in Fig. 4.23. Even for the annealing at 1350°C (Fig. 4.23(a)), the surface is covered with open pits due to the decomposition of AlN. Increasing the annealing temperature increases the width of these pits with the addition of aggregates appearing as well, as we can see in Fig. 4.23(b) at 1550°C. In this latter AFM image, the surface is covered with aggregates, probably due to the re-deposition of AlN. The aggregates and the open pits become even bigger at 1650°C, presented in Fig. 4.23(c). This behavior is normal, since for higher temperatures the AlN is expected to decompose even more.

We have also investigated the effects of successive temperature ramps to 1550°C followed instantly by cooling down to room temperature, without any temperature plateau. We show AFM images of these annealing experiments in Fig. 4.23(d, e). This technique has led to less aggregates at the surface compared to the annealing at 1550°C for 5 minutes in Fig. 4.23(b), but the morphology does not seem to be better as we still observe important amount of open pits. In addition, the surface appears rougher after the 3-ramp annealing compared to the 1-ramp annealing. Finally, we tried to do two successive annealing at 1550°C, first for 5 minutes and second for 15 minutes to investigate the annealing time effect on the crystalline structure. The morphology resembles slightly the annealing in Fig. 4.23(b), but with less aggregates at the surface. The RMS of the annealed samples as a function of the temperature are summarize in Fig. 4.24. The RMS trend is the same for both prepared templates S1 and S2: it slightly decreases for the annealing at 1350°C compared to the as-grown sample, then it starts to increase when

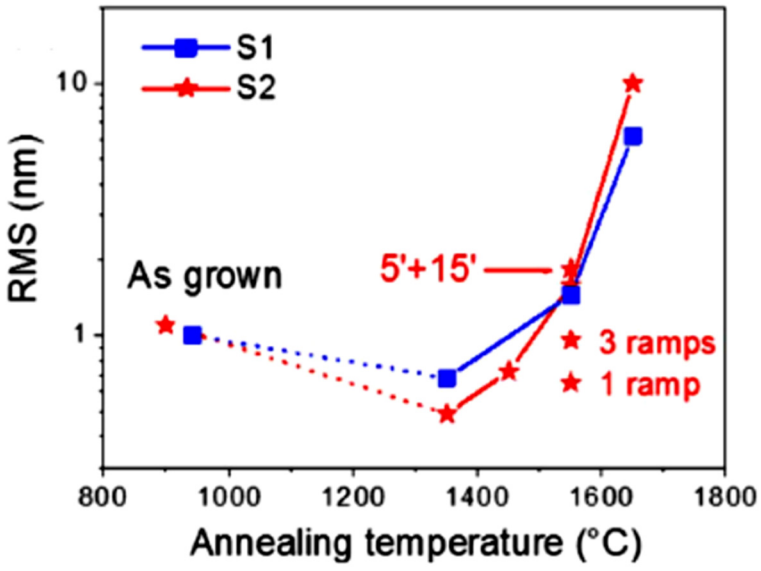

Figure 4. 24: *RMS data collected from AFM images as a function of the annealing temperature and annealing time for the two different AlN/sapphire templates.*

increasing the temperature, reaching a maximum for 1650°C. Both of the ramp-annealing have RMS around that of the 1450°C-annealing, with the 3-ramp annealing having a slightly higher RMS than the 1-ramp annealing, which seems normal. Interestingly the RMS of the two-time annealing (5+15 minutes) is close to that of the one-time annealing for 5 minutes at 1550°C.

Now that we have examined the influence of the high temperature annealing on the morphology, we can investigate its influence on the crystalline quality, which is the true goal of this study. Thorough investigations were done with XRD to reveal any changes in the structural quality of the AlN layer. We present the ω-scan FWHM of the 0002 symmetric reflection and the 10-11 skew symmetric reflection as a function of the annealing temperature in Fig. 4.25(a, b), for the two set of samples. These parameters reflect the tilt and twist angles of the AlN crystals, in other words the structural quality of the AlN film. For both the 0002 and the 10-11 reflections, the ω-scan FWHM decreases when the annealing temperature increases. For the substrate S1, the ω-scan FWHM of both reflections decreases as well when the annealing time is increasing. For example, the FWHM is smaller for the 3-ramp annealing compared to the 1-ramp annealing at 1550°C. Whereas the two-step annealing (5 + 15 minutes) at 1550°C seems to be as efficient as the 5-minute annealing at 1650°C. The decrease of the ω-scan FWHM of the 0002 symmetric reflection and the 10-11 skew symmetric reflection with the increase in the annealing temperature suggests that the annealing has a positive influence on the structural quality of the AlN layer, which improves for higher annealing temperatures.

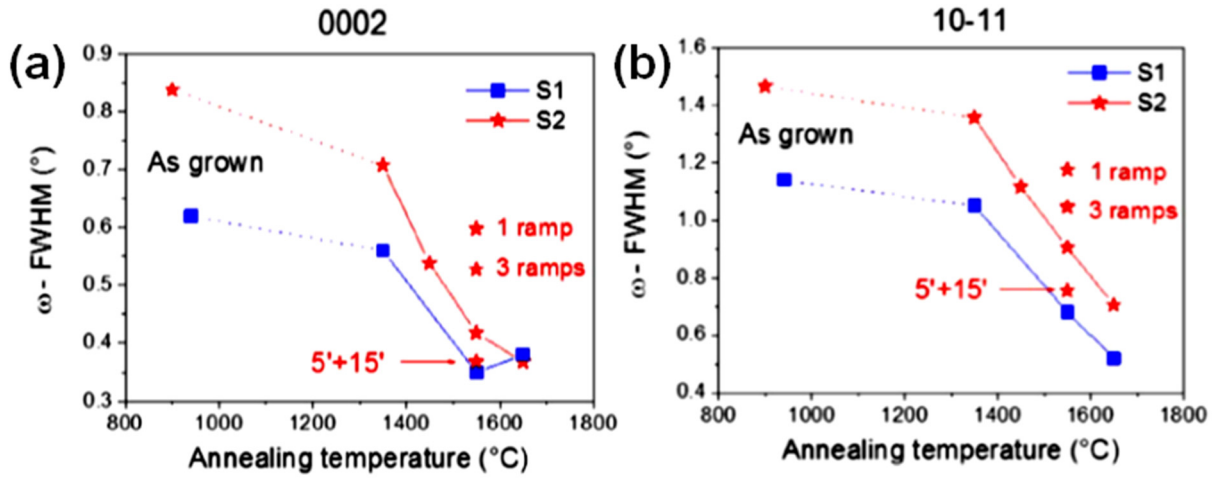

Figure 4. 25: *ω-scan FWHM as a function of the annealing temperature for the* ***(a)*** *0002 symmetric reflection and the* ***(b)*** *10-11 skew reflection. The disconnected points in these two graphs represent the as-grown S1 and S2 templates.*

Further investigations revealed that the annealing also affects the threading dislocation density, which decreases when increasing the annealing temperature as confirmed with TEM, see reference [123]. Therefore, we can deduce from Fig. 4.23 that the best sample is the one annealed at 1650°C for 5 minutes, but the two-time annealing (5 + 15 minutes) has a similar influence on the structural quality. In addition, if we combine these observations with the previous AFM and

RMS-trend observations, we can add that the best tradeoff is to consider the two-step annealing at 1550°C instead of the 5-minute annealing at 1650°C. Because as we can see, the two-step annealing at 1550°C is less destructive to the surface than the 5-minute annealing at 1650°C, while having the same influence on the structural quality.

We can compare this work to the literature where we can find studies that also attempted to enhance the crystalline quality of AlN grown on sapphire by doing high temperature annealing [206,207]. However, in these studies the authors adopted other techniques to grow their AlN layer, for example in reference [206] they grew a nucleation layer with MOVPE, 100 to 1000-nm thick at 1150 and 1200°C, whereas in our case the nucleation layer is 5 nm-thick grown at a temperature around 400°C. In the second reference [207] 170 to 340 nm-thick AlN layers were grown by sputtering at 650°C. The AlN layers prepared in these studies presented better crystalline quality than the templates with a 5 nm-thick buffer layer that we show here. Two annealing approaches were considered, the first: annealing under N_2 + CO at 1500-1750°C for 2 hours [206]; the second: annealing under N_2 atmosphere at 1600-1700°C for 1 hour while placing two AlN templates face-to-face to suppress the thermal decomposition of AlN [207]. If we compare our XRD data [123] to theirs [206,207] for similar AlN thicknesses and regardless of the initial crystalline quality of the AlN layer, our annealing at 1650°C for 5 minutes seems to have positive effects on the crystalline quality in the same order of magnitude as in these studies [206,207]. In contrast, their approaches have led to an enhanced morphology associated with the manifestation of steps and terraces, which we failed to achieve. But in fact, their annealing is done for longer times and higher temperatures than in our case, hence it seems that longer annealing times are crucial to observe any enhancements of the morphology. In our study we did try to do face-to-face annealing for shorter times (5 to 15 minutes) but did not succeed to enhance the surface's quality. In conclusion, our annealing conditions enhanced the crystalline quality with effects as important as the annealing methods we find in the literature, but we failed in enhancing the morphology. Therefore, for future attempts we can try to optimize our annealing conditions based on these studies, possibly by using propane with small amounts along with N_2, since carbon seems to have a positive effect on the morphology or by optimizing the face-to-face annealing by increasing the annealing time.

4.4.2. Conclusion on the annealing of AlN/sapphire templates

To summarize, we have attempted to anneal epitaxial AlN layers on sapphire (0001). Regardless of the annealing conditions, the AlN morphology does not seem to be stable at temperatures as high as 1350°C and more, whether under a mixture of N_2 + H_2 or under a pure N_2 gas mixture. The annealing seems to initiate the decomposition of AlN, where pits appear at the surface along with aggregates, which we attribute to the decomposition and re-deposition of the AlN. This decomposition increases with the temperature as the pits get wider and the aggregates larger. We attempted to reduce the morphology deterioration by doing a shorter annealing with only the temperature ramp without any annealing plateau. The temperature-ramp annealing at 1550°C appears to be less destructive than the continuous 5-minute annealing at 1550°C, but still

pits dominate the surface. This inability of the AlN layer to withstand high temperature makes it a bad candidate for the growth of graphene, which can lead to poor quality graphene in terms of structural and electrical properties. However, the annealing has other benefits, such as enhancing the structural quality, i.e reducing the threading dislocation density. In fact, an XRD study completed with TEM has shown that the annealing of AlN layers grown on sapphire has a direct and positive influence on the structural quality. The ω-scan FWHM of the 0002 symmetric reflection and the 10-11 skew symmetric reflection, which is related to the tilt and twist of the AlN crystals and due to threading dislocations, decreases when increasing the annealing temperature and the annealing time, thus suggesting an improvement in the structural quality. By comparing the XRD data, we came to the conclusion that a longer annealing at 1550°C has similar effects to a shorter annealing at 1650°C, but at the same time the lower-temperature annealing is less damaging to the surface, which seems a good tradeoff.

4.4.3. Graphene growth on AlN/sapphire templates

As we have demonstrated previously, the AlN templates on sapphire are not the best candidates for the growth of graphene, because of the important decomposition of AlN at 1350 and 1450°C. Nevertheless, we carried out few growth attempts to see how the templates behave under propane and if the deposition of graphene is possible.

The growth was conducted on the AlN/sapphire template I previously presented in Fig. 4.21(a), at 1450°C, 800 mbars, for 5 minutes with 6 slm of N_2 and varying propane flows; the sample was placed at X = 25 mm, the usual position. We show the AFM image of the growth with 2 sccm of propane in Fig. 4.26(a), with the corresponding C1s core-level spectrum in Fig. 4.26(b), along with other spectra for different propane flow rates. The morphology of the sample is very rough as expected, but the XPS spectra follow the same trend we observed on AlN/SiC when

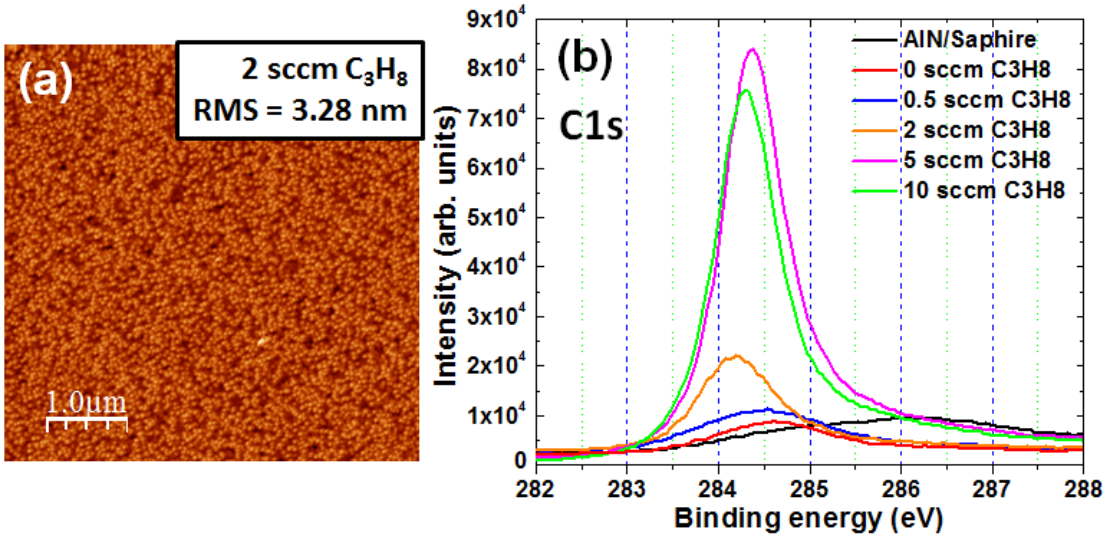

Figure 4. 26: (a) *5×5 µm² AFM image of the growth attempt of graphene with 2 sccm of propane at 1450°C.* ***(b)*** *C1s core-level spectra of the different growth attempts with different propane flow rates. AFM z-scale is 30 nm.*

changing the propane flow rate. The reference peak (black curve) appears at 286.4 eV, while the annealed sample's peak (red curve) appears at 284.8 eV, i.e. shifted towards a lower binding energy suggesting the beginning of a graphitic deposition. Increasing the propane flow rate results in a larger shift towards lower binding energies and an increase in the peaks intensities. For example, the 2 sccm-growth peak is at 284.2 eV in the vicinity of sp^2-graphene. Adding 5 sccm of propane (green spectrum) leads to the manifestation of a peak at 284.4 eV, with a noticeable increase in intensity, suggesting an increase in the graphitic deposition. Same for the 10 sccm-growth, the peak is intense but not as intense as the 5 sccm-growth peak. We presume that it should be more intense, but the signal might be saturated due the increase in deposition compared to the short probing depth of the XPS technique.

If we go back to the 5 sccm-growth peak, it seems more upshifted compared to the 2 sccm-growth peak. We assume that this is related to the increase in the graphitic layer thickness, which could create a difference in the transferred charge density (from the substrate) between the lowest graphene layer and the topmost layer, resulting in a less significant charge transfer to the topmost layer and leading to an upshift in XPS, as suggested in reference [105]. The second interesting observation for this peak, is that if we compare it to the 5 sccm-growth on the AlN/SiC in Fig. 4.14(b), we notice that the peak is more intense in the case of the growth on AlN/sapphire, which suggests a more important deposition in this latter case for the same propane amount. We attribute this observation to a rougher surface of the AlN grown on sapphire compared to AlN grown on SiC, which could be the main factor influencing the deposition of graphene/graphite. Other factors might rise, such as the presence of defects and dislocations in the case of AlN on sapphire.

Our second attempt of growing graphene was on the AlN/sapphire template II previously presented in Fig. 4.22(a), which initially seemed better than the previous template, but exhibited small pits prior to any annealing or growth attempt. We present in Fig. 4.27 AFM images of the annealing and graphene growth attempt with similar conditions as before but for X = 40 mm. As we can see in Fig. 4.27(b) the morphology becomes very rough after the growth attempt with 2 sccm of propane, compared to the annealed sample image in Fig. 4.27(a). Also, important amount of pits appear at the surface along with aggregates in Fig. 4.27(b). The surface gets even rougher with 5 sccm of propane (Fig. 4.27(c)). The increase of the roughness and of the density of pits can be ascribed to different reasons: it could be due to a non-uniform graphitic deposition, or to etching and/or surface reconstruction under the influence of hydrogen emanating from the propane. Regardless of the reason, the growth of graphene seems very challenging, since by adding propane we inflict a lot of damage on the morphology of the AlN film. Even though the surface is too much damaged, XPS spectra presented in Fig. 4.27(d) attest for a graphitic deposition with 2 sccm of propane and more importantly with 5 sccm of propane. Surprisingly the reference peak seems also in the vicinity of sp^2-carbon for reasons that are not clear to us.

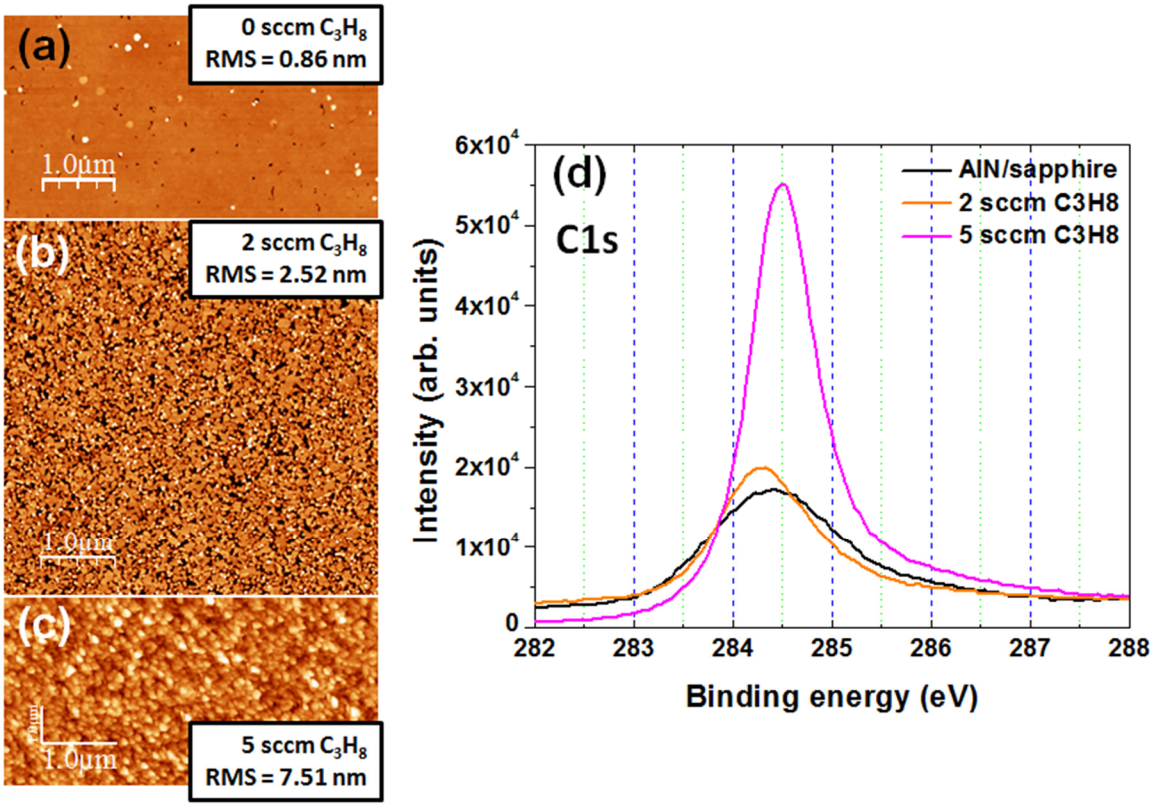

Figure 4. 27: *5×5 µm² AFM images of the annealed sample at 1450°C in* ***(a)*** *and the growth attempts of graphene with* ***(b)*** *2 sccm of propane and* ***(c)*** *5 sccm of propane.* ***(d)*** *C1s core-level spectra of the different growth attempts. AFM z-scale: 10 nm for* ***(a)*** *and* ***(b)****, but 50 nm for* ***(c)****.*

4.4.4. Conclusion on the graphene growth on AlN/sapphire templates

We have studied in this part the possibility of growing graphene on epitaxial AlN on sapphire. The initial state of the surface, either very rough or covered with defects and open pits, made the task very difficult. The AlN cannot withstand the high temperature required for the growth of graphene, nor the exposure to propane, even though we detect a graphitic deposition when adding propane to the gas mixture. Therefore, it seems important to first optimize the growth of the AlN layer on sapphire before attempting to grow graphene. Another solution would be to adopt other methods for the annealing of the AlN film similar to those found in the literature [206,207], since these studies have demonstrated that it is possible to obtain a step-like morphology for AlN on sapphire for the right annealing conditions. On the other hand, the annealing study of such templates has revealed that even though the annealing is destructive to the surface, it can be very beneficial for the structural quality of the AlN layer and to reduce the threading dislocations densities. This opens a new path for our objective, one can do homoepitaxy of AlN on the annealed AlN samples, possibly enhancing the morphology of the AlN film, which will be helpful for the growth of better quality graphene.

4.5. Graphene growth on AlGaN templates

Another interesting material to combine with graphene is AlGaN, which will open new markets and applications for graphene as a thin transparent and/or low-resistivity electrode. However, growing graphene directly on AlGaN with CVD is not an easy task because gallium in the AlGaN film is very likely to evaporate at the growth temperature of graphene. For this reason, we did few tests to find the maximum temperature that we can reach for this particular study. In Fig. 4.28, we present two annealing attempts without any propane to study the effect of the temperature on the AlGaN film.

Note that we studied three different AlGaN on sapphire templates, with different aluminum composition: 50% Al, 65% Al and 75% Al. The results were the same for all the substrates with similar observations with AFM and XPS, hence we will only present the study done on the 50% Al-template with a 500 nm-thick AlGaN layer. The initial morphology of this substrate shown in Fig. 4.28(a), does not seem to be smooth, with a lot of aggregates appearing at the surface, probably from the growth of the AlGaN film. The first annealing was done at 1250°C with 10 slm of N_2 at 800 mbars for 5 minutes, presented in Fig. 4.28(b). The annealing seems to slightly enhance the morphology by reducing the RMS and removing the aggregates from the surface.

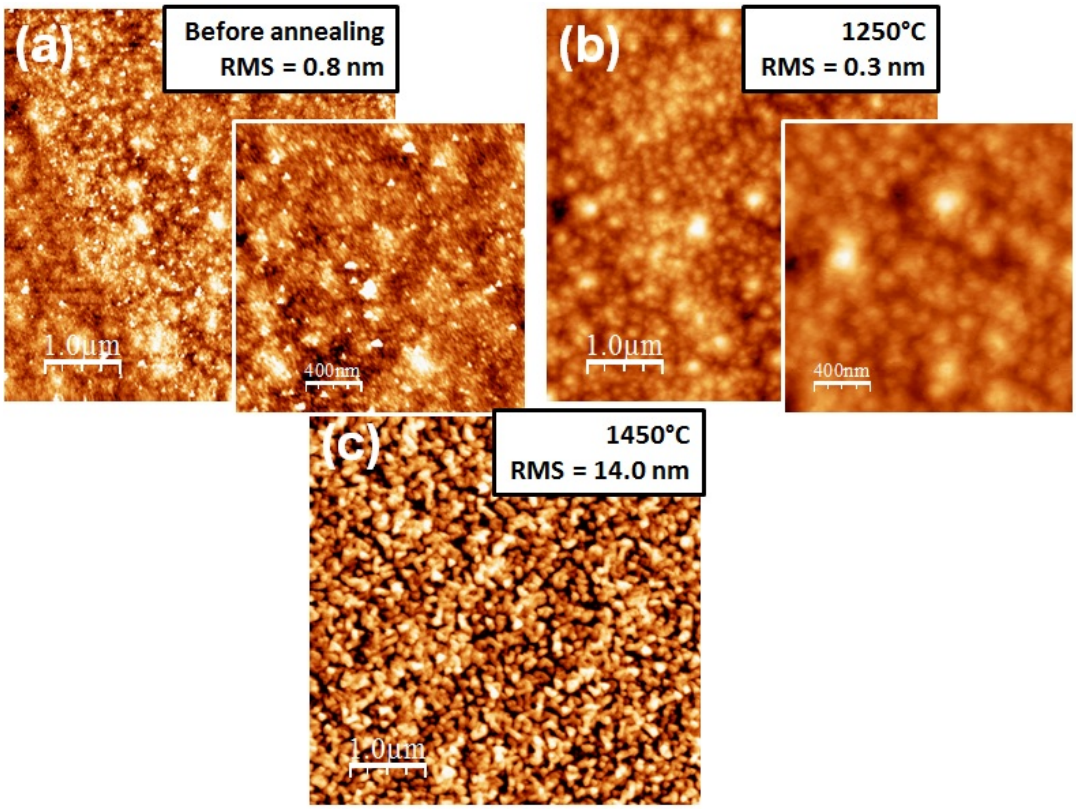

Figure 4. 28: *5×5 µm² AFM images of the reference sample in* ***(a)*** *and the annealed samples at* ***(b)*** *1250°C and* ***(c)*** *1450°C. Figures in inset are 2×2 µm² AFM images. AFM z-scale is 3 nm except for* ***(c)*** *where the z-scale is 50 nm.*

The second annealing was carried out at 1450°C, but as we can see in Fig. 4.28(c) the morphology is severely damaged: important pits appear at the surface and the RMS rises to 14 nm. We attributed this behavior to the thermal decomposition of the AlGaN film. To this end, we cannot attempt to grow graphene at 1450°C as we did in the previous studies. For this reason, we attempted the graphene growth at a lower temperature, i.e. 1350°C.

For the growth of graphene we employed the annealing conditions at 1350°C, but by adding propane to the gas mixture, always for 5 minutes with 100% of N_2 at 800 mbars. We considered different propane flow rates as we present in Fig. 4.29. We show in Fig. 4.29(a) the growth attempt with 2 sccm of propane, where important open pits appear across the surface. The roughness has increased compared to the reference AFM image in Fig. 4.28(a), but the surface seems less damaged than with the annealing at 1450°C in Fig. 4.28(c). Since the propane flow rate is low, the surface resembles a regular annealing without any propane. We then increased the propane flow rate to 5 sccm (Fig. 4.29(c)), which resulted in a completely different morphology. We do not see the open pits, but instead we see a surface covered with wrinkles forming very small domains along with regions with brighter contrast indicated by white arrows. The presence of wrinkles can be a sign of graphene deposition, and the bright regions suggest over deposition in some areas, similarly to what we observed previously on the AlN/SiC template II. To limit this non-uniform deposition we can try to increase the temperature, but this did not work so well for the AlN/SiC template; this is why we lowered slightly the propane flow rate to 3.5 sccm. As we can see in Fig. 4.29(b), the morphology remains the same but with less brighter regions, which still appear but less frequently and are smaller in size. What is interesting for these three samples with the different propane flow rates is that we only see a damaged surface for the 2 sccm of propane, while for the other two growth attempts, no open pits can be detected as if increasing the propane amount has led to the reduction of the AlGaN film decomposition/etching. The reason for this behavior is not clear to us, but a recent study has shown that annealing AlN on sapphire under N_2 + CO helps

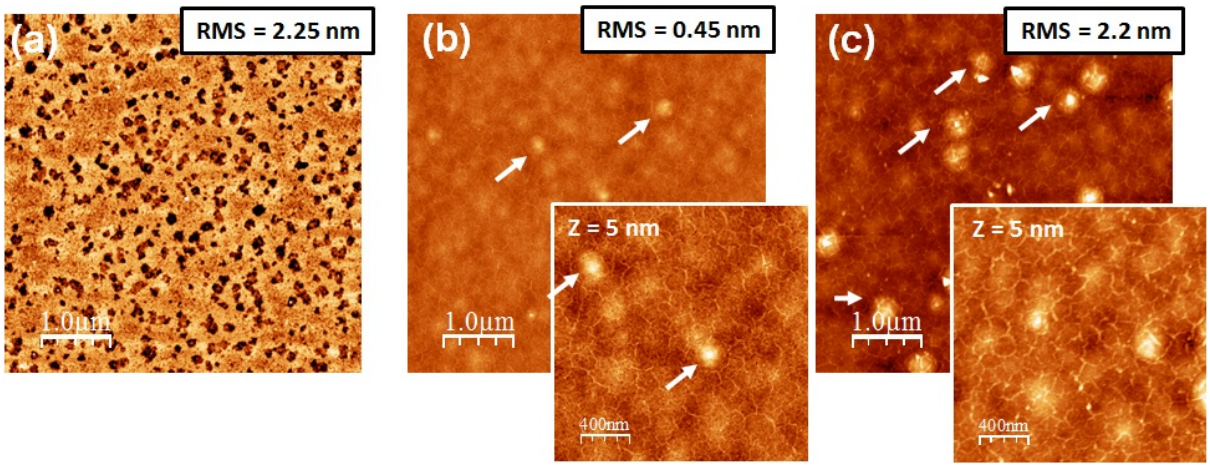

Figure 4. 29: *5×5 µm² AFM images of the growth attempts at 1350°C with 100% of N_2 and different propane flow rates:* ***(a)*** *2 sccm,* ***(b)*** *3.5 sccm and* ***(c)*** *5 sccm. Figures in inset are 2×2 µm² AFM images. AFM z-scale is 10 nm except for the figures in the inset.*

to improve the morphology of the AlN film [206]. We do not know the exact role of carbon in the surface enhancing process, but this could be a reason why we don't see a damaged surface for 3.5 and 5 sccm of propane. However, this approach did not work when we attempted to grow graphene on AlN on sapphire templates as we have seen before, possibly because the N_2 + propane mixture has to be optimized depending on the quality of the AlN film.

The graphitic phase deposition, was confirmed with XPS by examining the C1s core-level measured on the different samples, presented in Fig. 4.30. The reference peak i.e. the sample before any annealing, appears at 284.7 eV. The growth with 2 sccm of propane presents a peak at 284.4 eV, slightly downshifted compared to the reference peak, suggesting the beginning of a graphitic phase deposition. Increasing the propane flow rate to 3.5, 5 and 10 sccm, results in an increase of the carbon peak intensity as expected. Surprisingly, the growth at 5 sccm of propane exhibits a peak aligned with the reference peak and less intense than that of the 3.5 sccm-growth. It is possible that for 5 sccm of propane, the X-ray gun has excited areas with a less graphitic deposition. Or another possibility could be that the AlGaN samples are not uniform: since we work with cleaved samples, it is very possible that one sample comes from the center of the AlGaN template and the other from the edge of the template. On the other hand, the peaks of the 3.5 and 10 sccm-growths are at 284.5 eV, which is in the vicinity of sp^2-graphene. Therefore, it is reasonable to conclude that 3.5 sccm seems a good amount of propane to deposit a graphitic phase in the sp^2-configuration.

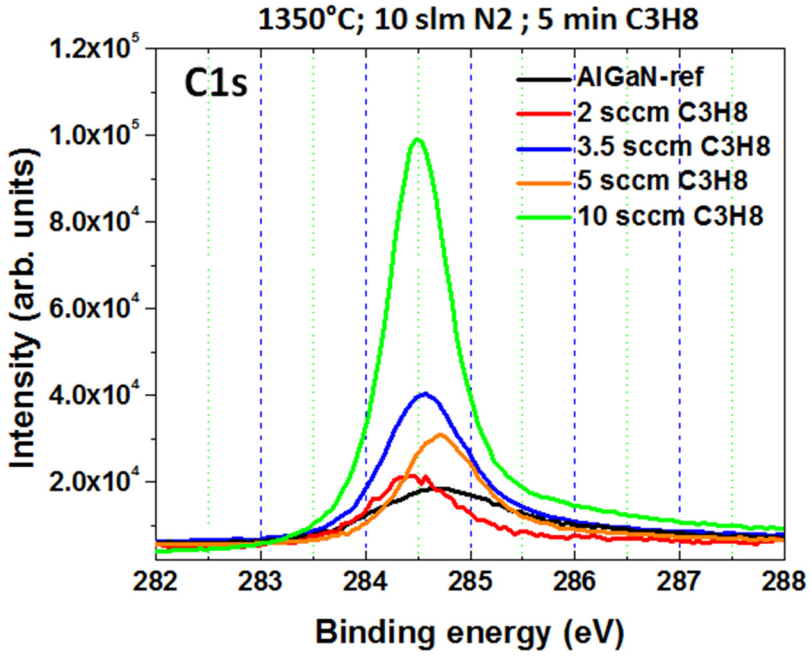

Figure 4. 30: *C1s core-level spectra of the different growth attempts with different propane flow rates. The spectra are aligned at the same baseline.*

We also examined other core-level peaks with XPS for the 3.5 sccm-growth such as Ga3d, Al2p, N1s and O1s, see Fig. 4.31. After the graphene growth attempt, all the peaks are downshifted compared to the reference peak, suggesting an increase in the sample's conductivity, probably due to the deposition of graphene. We notice a decrease in the intensity of the Ga3d peak (Fig. 4.31(a)) accompanied with an increase in the intensity of the other peaks. This decrease can be attributed to the deposition of graphene and/or to the sublimation of gallium. In fact, if gallium is evaporating faster than aluminum, an excess of aluminum will form at the surface, which explains the increase in the peak intensity in Fig. 4.31(b) after the graphene growth attempt. In addition, the Al2p peak of the as-grown sample seems to be different than the reference peak, where an asymmetric shape appears towards higher binding energy suggesting the manifestation of a new component, possibly due to new bonds with the aluminum of the sample. The asymmetric shape is in the vicinity of the binding energy of Al_2O_3 (around 74.5 eV) [208–210], associated with an increase in the intensity of the O1s peak. It seems that aluminum oxide has formed beneath the carbon layer, possibly oxygen migrating from the sapphire substrate through defects and cavities under the influence of the high temperature, or from the residual oxygen doping of the as-grown AlGaN layer (usually

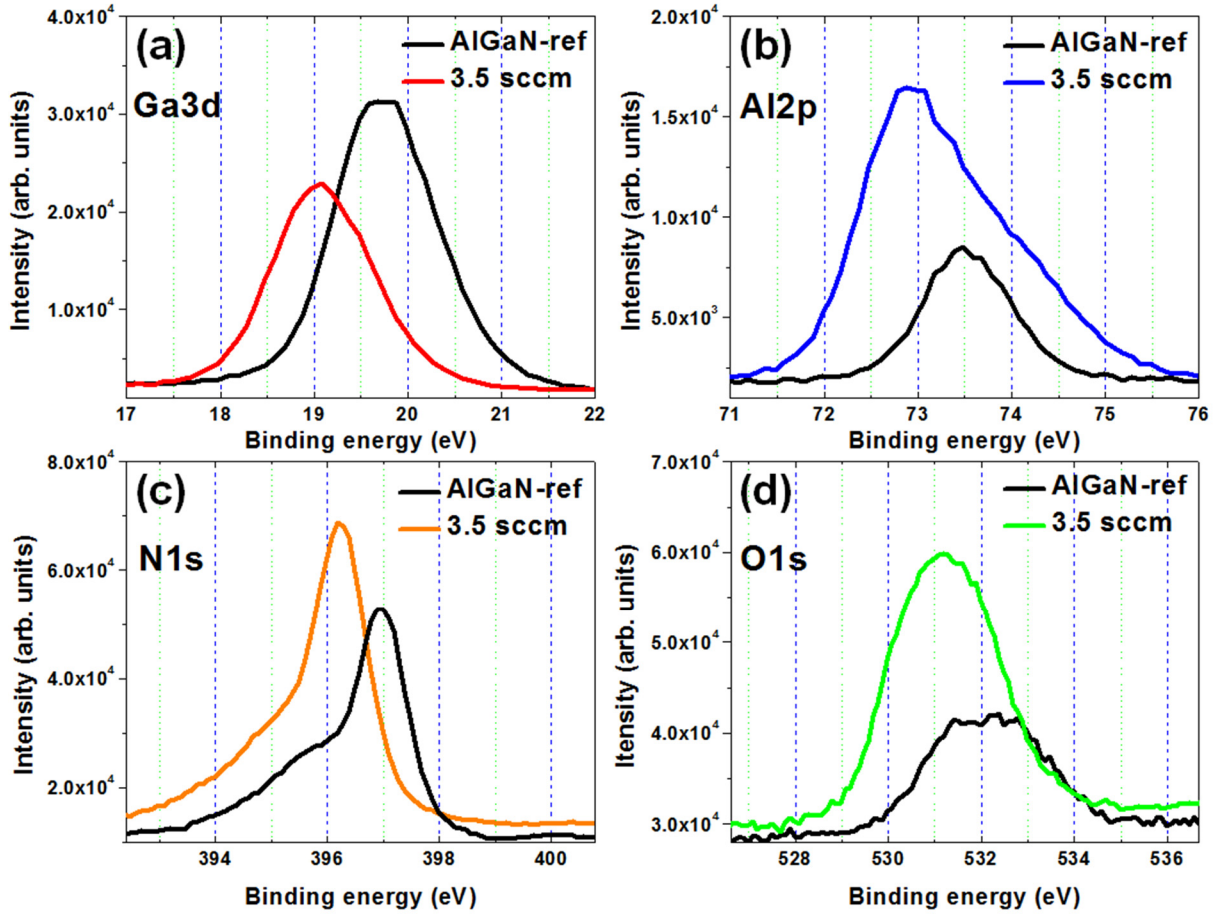

Figure 4. 31: *Different core-levels for the 3.5 sccm-grown sample at 1350°C with 100 % of N_2.* ***(a)*** *Ga3d core-level,* ***(b)*** *Al2p core-level,* ***(c)*** *N1s core-level and* ***(d)*** *O1s core-level.*

several $10^{18}/cm^3$ according to secondary ion mass spectrometry measurements). However, XPS is not enough to make affirmative conclusions at this stage, other techniques such as TEM are necessary to look into the structure beneath the carbon layer.

Finally, before we conclude, we show in Fig. 4.32, AFM and XPS observations carried out on the 65% Al-composition template, on which the same study was conducted. In fact, for each growth or annealing two samples were placed in the reactor, one of the 50% Al-composition template and the other of the 65% Al-composition template. AFM and XPS measurements reveal the same observations made on the previous template.

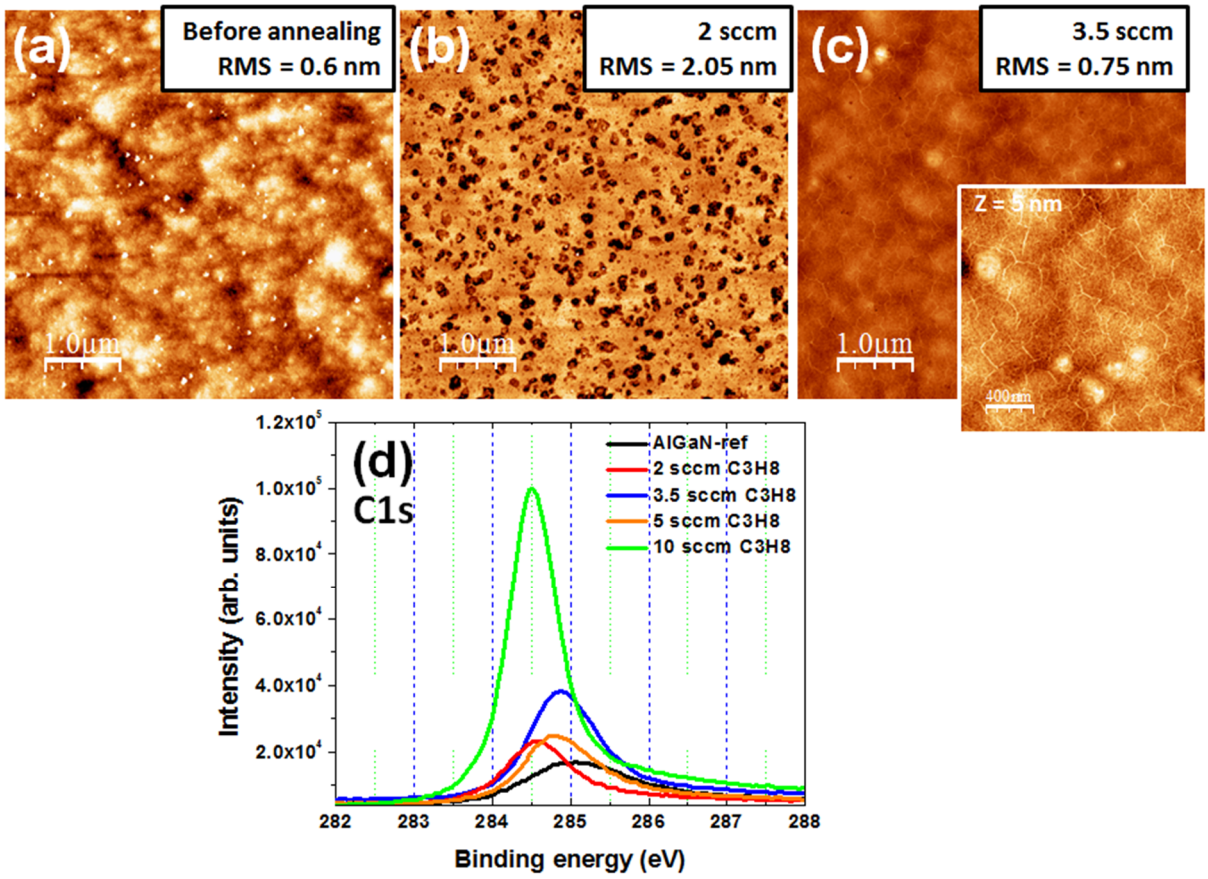

Figure 4. 32: *5×5 µm² AFM images of the reference sample with 65% Al-composition in* ***(a)*** *and the growth attempts at 1350°C with 100% of N_2 and different propane flow rates:* ***(b)*** *2 sccm and* ***(c)*** *3.5 sccm.* ***(d)*** *C1s core-level spectra of the different growth attempts with different propane flow rates. The spectra are aligned at the same baseline.*

To summarize, we have presented preliminary results on the growth of graphene on AlGaN templates on sapphire. The AlGaN film is not very stable at high temperatures in the range of 1350 and 1450°C, even under 100% of N_2. However, the morphology does not appear to be damaged when attempting to grow graphene with 3.5 sccm of propane. We suspect the deposition of graphene or of a graphitic phase since wrinkles appear at the surface, which we usually attribute to disordered graphene. In addition, a sp^2-carbon peak appears in the C1s core-level spectrum of

the as-grown sample. On the other hand, we suspect some changes occurring to the AlGaN layer, since the corresponding core-levels reveal a decrease in the gallium concentration accompanied with an increase of the nitrogen, oxygen and aluminum contents, along with the manifestation of an asymmetric shape in the Al2p core-level spectrum compared to the reference sample. However, XPS is not enough to truly understand these phenomena, other techniques are needed such as TEM, XRD or GIXRD.

So far we have shown that it is possible to deposit a graphitic phase on AlGaN grown on sapphire, but to confirm that this phase is really graphene Raman spectroscopy is required, along with electrical measurements to assess the graphene's electrical properties. In addition, it is important to investigate the properties of the AlGaN layer, because of we intend to use it later in a HEMT device, we cannot risk deteriorating its quality. Therefore, these first results seem promising, but more investigations are required. On a side note, we attempted to do some LEED measurements, but we were not able to detect any diffraction patterns at all. The reason behind this behavior is very likely to be related to the electrical properties of the template. In fact, we usually don't detect any diffraction patterns with LEED when the substrate is an insulator.

4.6. AlN growth attempt on graphene/SiC

The growth of graphene on AlN, whether bulk or template, is promising but challenging and very dependent on the initial surface quality and morphology of the AlN template or substrate, which adds more difficulties to our objective. An alternative route would be to grow AlN on the optimized graphene on SiC. We present in this part preliminary results of AlN growth attempts by MBE on graphene/SiC. This work is complementary to a study carried out by Timotée Journot at the lab LMP Leti on the growth of GaN on graphene on SiC by MOVPE, where the graphene samples are provided by us.

The graphene was grown by CVD on SiC (0001) 1°-off at 1550°C and 800 mbars, with 33% of H_2 + 67% of Ar and 5 sccm of propane, for 5 minutes. We show in Fig. 4.33 AFM images of the graphene layer grown on SiC. The morphology is typical of a graphene growth on SiC under low H_2-amount in the gas mixture. The terraces are 60 to 120 nm-wide with heights between 0.6 and 2 nm characteristic of graphene on SiC and step-bunching. We also notice some extra features between adjacent steps, indicated by a red arrow in Fig. 4.33(b), associated with different contrasts in the corresponding phase image in Fig. 4.33(c) and attributed to extra graphene layers.

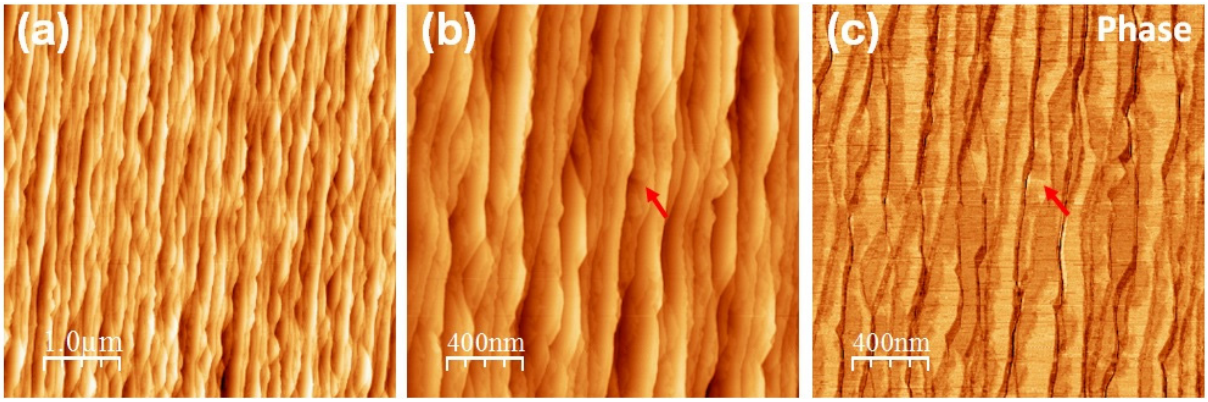

Figure 4. 33: *AFM images of the graphene growth on SiC:* ***(a)*** *5×5 µm², **(b)** 2×2 µm² and **(c)** the corresponding phase image. Z-scale = 3 nm and 10° for the topographic and phase images respectively.*

The AlN growth was carried out in an MBE system with 200 sccm of NH_3 as the nitrogen source (total pressure less than 10^{-5} Torrs) and an aluminum flow resulting in a growth rate of 100 nm/h. The growth was monitored with RHEED; a 4.6 nm nominal thickness AlN layer was grown on three samples: the first at 700°C on a graphene sample, the second at 900°C on another graphene sample and the third at 900°C on a bare SiC sample for comparison. It is our intention to grow such a thin AlN layer to assess the early stages of the deposition and to be able to characterize the graphene after the AlN growth.

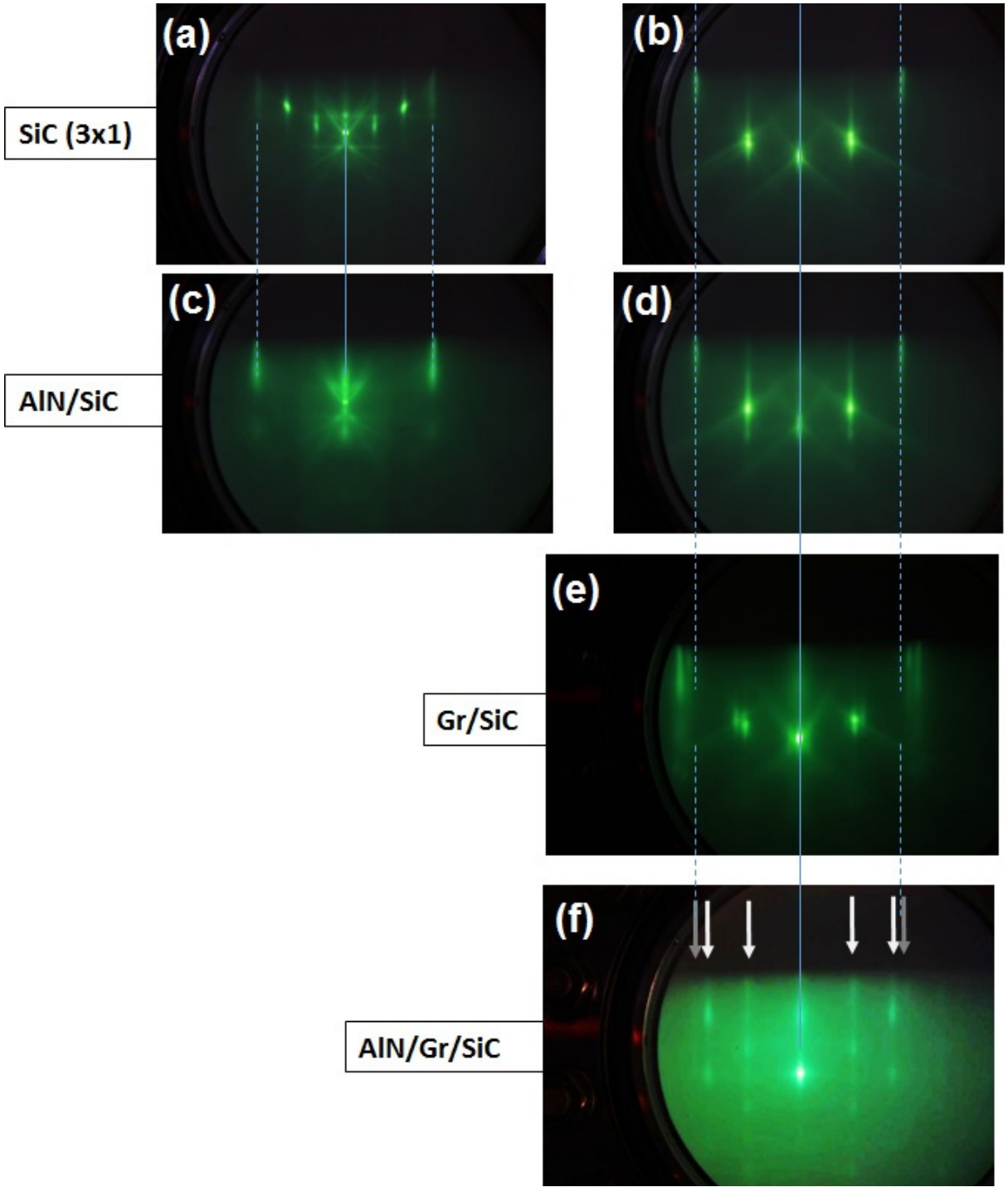

Figure 4. 34: (a, b) *RHEED patterns recorded on the two main azimuths of (3x1) reconstructed surface of SiC before growth of AlN and after in* ***(c, d)****.* ***(e)*** *RHEED pattern of Graphene on SiC along one azimuth before the growth of 4.6 nm of AlN and after in* ***(f)****.*

As shown in the RHEED patterns in Fig.4.34(a-d), the growth of AlN on SiC is smooth (streaky patterns with sharp lines) and the distance between the main diffraction lines is kept unchanged due to tiny lattice mismatch between both crystal lattices. Note that RHEED and LEED are two similar surface techniques based on electron diffraction with few differences. LEED relies on low-energy electrons, usually with a normal incidence, to probe the surface, whereas RHEED consists of high-energy electrons but at a grazing incidence with respect to the sample. The grazing incidence leads to diffraction patterns in the form of streaks, but when the surface is rough diffraction spots may appear as well. Fig. 4.34(e) shows the diffraction pattern for graphene grown on SiC. The growth of AlN (Fig. 4.34(f)) results in the apparition of new diffraction lines indicate by arrows. The intensity of the lines is modulated, indicating a rougher surface. Also, the brighter lines indicated by white arrows do not align with the ones of AlN grown on SiC; only weak lines appear at such a location indicated by the grey arrows. This indicates that AlN with different lattice parameters and/or different in-plane orientations has been grown on graphene.

We present in Fig. 4.35 AFM images of the corresponding three AlN growth attempts. Fig. 4.35(a) represents the growth on the bare SiC substrate, where we can still distinguish the direction of the SiC steps. We also notice in the 1×1 μm^2 AFM image (figure in inset) the grain structure of the AlN, which suggests that the growth is columnar at the early stages. In Fig. 4.35(b, c), for the growth on graphene, the structure is not the same as in Fig. 4.35(a), we can no longer discern the SiC steps nor the columnar growth of AlN. No noticeable difference is detected between the two graphene samples: we can detect on both samples aggregates (white features) and dendrite-shape features, which we can attribute to the AlN deposition.

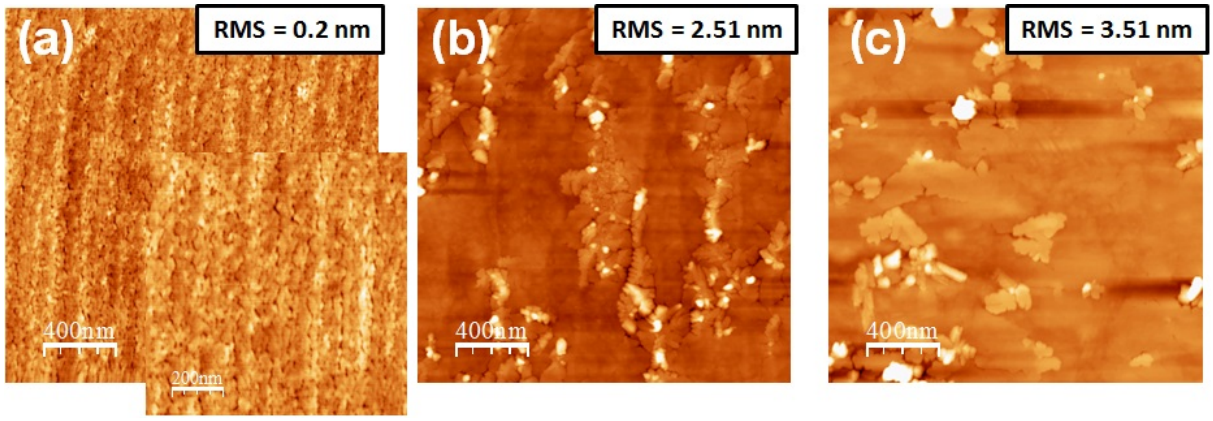

Figure 4. 35: *2×2 μm^2 AFM images of the AlN growth attempts:* ***(a)*** *at 900°C on bare SiC (z = 3 nm),* ***(b)*** *at 700°C on graphene (z = 25 nm) and* ***(c)*** *at 900°C on graphene (z = 25 nm). Inset of* ***(a)*** *is a 1×1 μm^2 AFM image.*

To evaluate the state of the graphene after the growth of AlN, Raman spectroscopy measurements were carried out by Timotée Journot at LMP Leti before and after the growth. We present in Fig. 4.36 the graphene/SiC substrate before the AlN growth (black curve), and the spectra recorded on the two graphene samples after the AlN growth at 700°C (red and blue curves)

and at 900°C (orange and magenta curves). The two curves for each AlN/Gr/SiC sample represent two spectra recorded in two different regions of the sample. All the spectra present D, G and 2D peaks around 1360, 1590 and 2730 cm^{-1} respectively. Regardless of the peaks positions, they seem aligned with the reference peak before the AlN growth, which confirms that graphene is still present after the growth of AlN, without any changes regarding its properties. This result is encouraging since it demonstrates that the graphene layer is able to withstand the growth conditions of the AlN layer, without undergoing any changes in strain or doping.

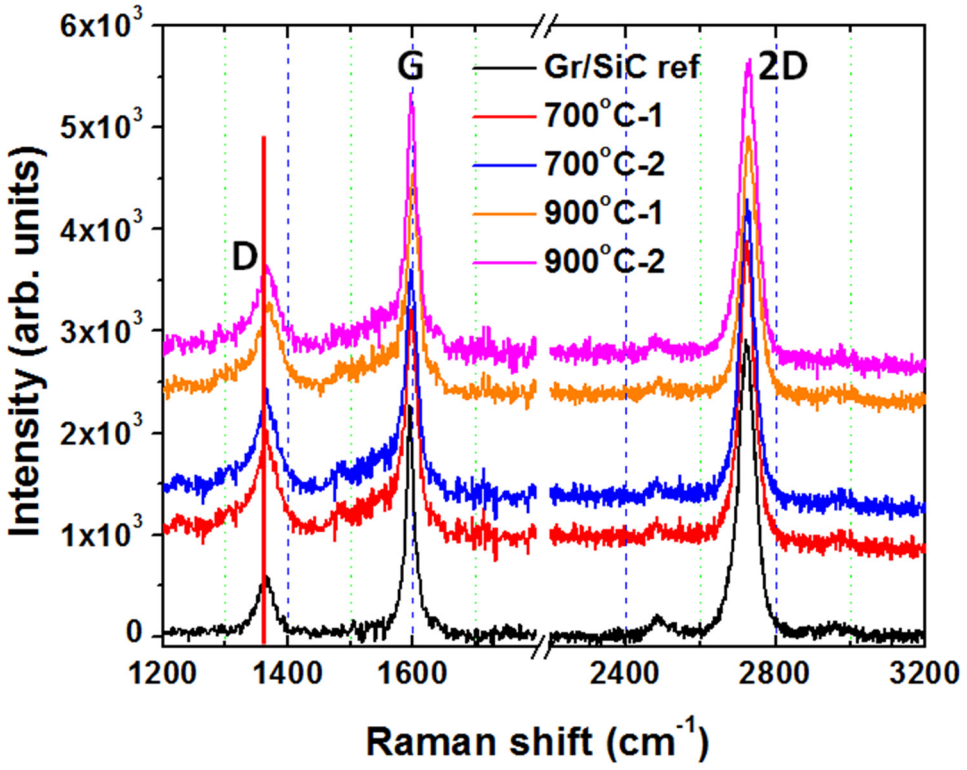

Figure 4. 36: *Raman spectra of the graphene/SiC substrates before and after the AlN growth attempts. The spectra are vertically shifted for clarity.*

In addition, we carried out LEED measurements on the three samples after the AlN growth attempts, presented in Fig. 4.37. We can see in Fig. 4.37(a) the diffractions spots of AlN and SiC that are aligned together due to the close lattice constants of the two materials. In contrast, in Fig. 4.37(b, c) the diffraction patterns are very weak, but we detect large diffraction spots and elongated rings for the two samples, indicated by white arrows. The large diffractions spots indicate the presence of different lattice parameters while the diffractions rings suggest that the grains of AlN are probably disordered, which is consistent with the RHEED observations made previously.

The presence of dendrite-shape patterns on graphene indicates that the latter AlN growth is much more efficient than on bare SiC. However, the AlN nucleates and grows with no particular in-plane orientation on the graphene; even if the RHEED pattern indicates the presence of lines in

Fig. 4.34(f), their intensity is modulated. This can be an advantage as well as a drawback, since AlN is supposed to be growing without any shared bonds with the graphene layer, which prevents the formation of defects due to the difference of lattice constants. On the other hand, the AlN is found to be disordered, which we can attribute to the AlN nucleation at step edges where we suppose to have extra graphene layers. A question can arise from this observation: will the AlN growth be better in the absence of extra graphene layers?

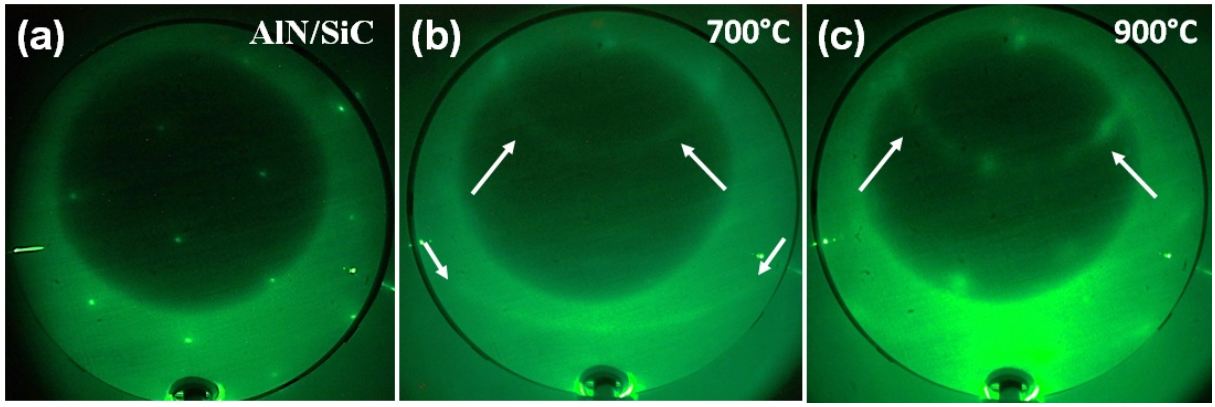

Figure 4. 37: *LEED patterns of the AlN growth attempts on* ***(a)*** *SiC and on graphene at* ***(b)*** *700°C and* ***(c)*** *900°C, taken at an electron energy of 120 eV.*

In summary, we were able to grow a thin layer of AlN on graphene previously grown on SiC, without compromising the graphene layer as confirmed with Raman spectroscopy. AFM images reveal dendrite-shape features, which we can attribute to the deposition of AlN. On the other hand, RHEED and LEED patterns suggest that the AlN layer is very likely to be disordered with different in-plane orientations. We suspect that this behavior is related to the initial morphology of graphene, which presents extra layers at the step edges. We should consider in the future to optimize the graphene growth, for example by increasing the growth time as we have shown in **chapter 3**. It is also important to grow thicker AlN layers to see if the AlN quality is enhanced or not.

4.7. General conclusion

In this chapter we have considered the growth of graphene on III-nitrides. It seems interesting to combine graphene with nitrides such as AlN and AlGaN devices, as both materials have a lot of potential and can lead to interesting applications. We first studied bulk AlN for the growth of graphene. Before any growth attempt, it was important to prepare the surface of AlN since it presented polishing scratches and no atomic steps. The annealing of the Al-face was successful, resulting in a smooth surface with atomic steps and no signs of the polishing scratches. In contrast, the annealing of the N-face of bulk AlN was not very successful because of the initial state of the N-face. Before any annealing, the N-face presented a rough surface with open pits, defects and scratches, whereas the Al-face was much smoother, with only scratches appearing at the surface. This could explain why the annealing had a positive effect on the Al-face but a destructive effect on the N-face. After having prepared an epi-ready AlN surface, the growth attempts of graphene were carried out on the Al-face at 1350°C. Surprisingly, AFM images uncovered wrinkles on the N-face after the growth of graphene, even though this face was placed against the sample holder. Further investigations with XPS and Raman spectroscopy revealed that the growth of graphene seems more favored on the N-face than on the Al-face, with a deposition around 5 MLs of graphene on the N-face, even if the Al-face is exposed to the incoming gases. In addition, Raman spectroscopy unveiled the presence of defects on both faces, along with poor graphene quality on the Al-face, which is suspected to be highly disordered or amorphous. We attributed the favored graphene growth on the N-face to the surface roughness and to the presence of defects, but it is also probably related to the chemical and surface energy properties of the N-face. In fact, the growth on bulk AlN can be compared to the growth on bulk SiC, since graphene grows faster on the N- and C-face, with the presence of wrinkles and disorder, compared to the Al- and Si-face of AlN and SiC respectively.

The growth seems promising, but the AlN market today is more based on AlN templates since it is cheaper and easier to grow AlN on SiC, Si and sapphire instead of growing bulk AlN. Therefore, it seems reasonable to attempt to grow graphene on AlN templates if we want to integrate graphene into the AlN market. For this reason, we considered also for our study AlN on SiC and sapphire templates. First, 240 nm-AlN layers were grown on 0.2°off-SiC, then annealed at temperatures as high as 1450 and 1550°C, and with different gas mixtures of N_2 + H_2, in order to assess the stability of the AlN in the range of the graphene growth conditions. The AlN was found to withstand high temperatures but under N_2 atmosphere or with H_2 not exceeding 50% of the gas mixture. In addition, for the growth of graphene, we tested different growth parameters such as the propane flow rate, the total pressure and the sample's position in the reactor. We were able to confirm the presence of a graphitic phase with XPS and LEED, by detecting the sp^2-carbon peak in XPS and elongated shapes with LEED usually associated with disordered graphene. Unfortunately, Raman spectroscopy revealed areas without any graphitic deposition, which led us to study another template with a different AlN thickness. The second template consisted of a 100 nm-AlN layer grown on a 4°-off SiC substrate. Growth attempts were successful at 1350°C

and 1450°C, but it was necessary to increase the propane flow rate to 10 and 17 sccm, whereas for the previous template only 2 sccm of propane were enough. Graphene deposition was confirmed with XPS and Raman spectroscopy. However, the growth at 1450°C presented areas of poor graphene quality. On the other hand, the growth at 1350°C with 17 sccm seemed more uniform in terms of graphene quality, but presented defects and different deposited thicknesses as it was observed with Raman spectroscopy and AFM. Therefore, we should explore in the future other growth parameters as more optimization is required to enhance the uniformity of the graphene growth. On the other hand, we can also focus on optimizing first the AlN templates before the growth of graphene since this latter seems very dependent on the AlN template: for example, the second template required more propane to initiate a graphitic deposition. We believe that this can be attributed to the step density, which was more important on the first AlN template.

Sapphire is also a commonly used substrate for the growth of AlN, therefore we studied AlN/sapphire templates with a 120 nm-thick AlN layer. We studied two templates, but neither of them was stable under the annealing conditions, due to their initial morphology dominated by defects and open pits. The surface becomes even worse when adding propane to the gas mixture. It seems that it is important to first optimize the growth of AlN on sapphire before the growth of graphene, or consider AlN layers prepared by other methods such as MOVPE. Other alternatives can be to optimize the annealing process, since it is possible to find in the literature studies who succeeded on enhancing the AlN surface quality by adding a carbon source with the N_2 or by doing a face-to-face annealing. On the other hand, we also did an XRD study which revealed that annealing such templates under different temperatures and annealing time has a positive and direct influence on the structural quality of the AlN epitaxial film.

In conclusion, graphene growth on bulk AlN was not very successful on the Al-face where amorphous or highly disordered graphene was detected, but it is a lot better on the N-face with crystallite sizes reaching 30 nm. We also demonstrated that it is possible to grow graphene on AlN/SiC templates, but the growth was very dependent on the AlN layer requiring different propane flow rates for the different templates. Nevertheless, for the right growth conditions we were able to grow graphene with grain sizes reaching 30 nm, similar to the N-face of bulk AlN. In addition, Raman spectroscopy revealed that all the graphene films presented defects, either boundary defects or vacancy defects (or both). On the other hand, the graphene growth on AlN/sapphire templates was found to be limited by the surface quality of the AlN layer. Even though the crystalline quality of the sapphire templates is comparable to the SiC templates, the initial morphology is not the same. AlN on SiC presented a step-like morphology, whereas AlN on sapphire presented a columnar-structure with the presence of open pits (for the template II). We believe that this difference is related to the large mismatches between AlN and sapphire compared to AlN and SiC, which have almost the same structure and the same in-plane lattice parameters.

Last but not least, we investigated the growth of graphene on AlGaN templates prepared on sapphire, with different aluminum composition ranging between 50% and 75%. The growth of graphene was done at 1350°C with a propane flow rate of 3.5 sccm, associated with the

manifestation of wrinkles detected with AFM and the sp^2-carbon peak recorded with XPS. The growth of graphene seems possible, but further investigations with XPS led us to suspect the oxidation of the aluminum beneath the graphene layer, possibly by oxygen migration from the substrate or oxygen diffusion from the residual doping of the AlGaN layer under the influence of the high temperature. Further examinations with other techniques are required to confirm this hypothesis.

Finally, we considered another approach to combine graphene and AlN by growing AlN on graphene/SiC substrates. A very recent study has shown that it is possible to deposit a thin layer of AlN on graphene by MBE without deteriorating the graphene layer nor changing its properties. In contrast, the AlN layer appears to be disordered as observed with RHEED and LEED. These first results of this alternative approach are encouraging and worth exploring even more.

To conclude, we have demonstrated the direct growth of graphene or a graphitic phase from an external carbon source on different III-V nitride templates. The task is challenging since the growth of graphene requires a relatively high temperature, which is not ideal for the nitride films. But this is not the only issue to tackle, since the deposited graphene is not of high quality, with defects and disorder. Hence, different topics need to be assessed and new approaches to be considered if the graphene is required for electronic applications. Work is still in progress to evaluate the properties of the graphene layer, in addition to growth attempts on AlGaN templates for HEMT applications.

Summary & perspectives

The interest in graphene has been growing since the Eureka of Noveselov and Geim in 2004 after uncovering its exceptional electrical properties. Since then, different elaboration techniques were developed to synthesize graphene such as exfoliation from graphite, Si sublimation from SiC substrates, CVD on metal and direct growth on SiC with an external carbon source. Some of these methods date as far back as the 1970s, but continued to be developed, while other approaches such as the direct growth emerged more recently, around 2010, inspired from the CVD growth on metal.

Our research group at CRHEA was also intrigued by graphene and motivated to develop a personalized elaboration technique for graphene in a homemade CVD reactor. They considered the direct growth by CVD with an external carbon source to obtain graphene layers on SiC (0001) under different atmospheres: pure hydrogen or pure argon or a combination of both gases. In particular, the growth with a mixture of hydrogen and argon produced high quality graphene on SiC, which was invested in the metrology of the electrical resistance since it outperformed the existing quantum Hall effect devices. In addition, this latter approach allowed the tuning of the electrical properties of graphene by modifying the growth conditions. Despite these appealing results, a thorough exploration of this technique was still needed, which was the main trigger for the work of this thesis.

The major part of this work revolves around the growth of graphene on SiC (0001) by CVD. Our objective was in a first place to shed the light on this growth technique and second to optimize the growth of graphene while assessing some of the unsolved and unclear issues of the growth, starting with understanding the thermodynamics of our growth method compared to the Si sublimation approach. For this reason, we conducted annealing attempts of SiC under H_2 and H_2 + Ar, completed with thermodynamic simulations. These studies have led us to the conclusion that it is not possible to consider Si sublimation under H_2, since the SiC substrate in this case produces carbon-species in the gas phase a lot more than silicon-species. On the contrary, when annealing SiC under argon, SiC decomposes to generate mainly silicon-species in the gas phase, which leads to an excess of carbon at the surface and forms graphene. Therefore, for the case with H_2, propane is necessary as the main source of carbon for the growth of graphene.

After the thermodynamic study, we were motivated to explore the different growth parameters to understand their role in the graphene growth and how they influence the graphene properties. For instance, we investigated the effects of the growth duration, the propane flow rate and the growth temperature on the deposition of graphene.

Another interesting parameter is the hydrogen amount in the gas mixture, having important effects on the growth of graphene regarding the morphology and the structure. To understand the role of H_2 in the growth, we conducted a thorough study based on AFM, LEED, Raman spectroscopy and XPS. Depending on the hydrogen amount in the gas mixture, the structure of graphene can be modified between graphene associated with a buffer layer and free-standing graphene with in-plane rotational disorder. The reason behind this behavior is related to the intercalation of hydrogen at the interface between the graphene layer and the SiC as we have discussed in the manuscript. Based on previous studies and the literature, we expected that these two graphene structures have an influence on the strain within the graphene layer. For this reason, we carried out a Raman study to emphasize the role of H_2 on the strain, but unfortunately, the strain variation was mainly due to non-uniformities in thickness, which made the study complicated. Nevertheless, this study has revealed a carrier density variation with the H_2 amount.

We were also interested in investigating the influence of the substrate's miscut angle on the graphene growth, since it is usually neglected in the literature, but has a direct influence on the growth as we have demonstrated in the manuscript. For this study, we considered the growth of graphene on substrates having different miscut angles. The graphene growth on the 0.05°-off substrate seemed challenging and not uniform. On the other hand, the growth appears to be easier on the 0.2, 1 and 4°-off substrates, resulting in uniform graphene. The only difference we noticed was a thicker deposition for off-axis substrates. Raman spectroscopy also revealed an increase in the strain for larger offcuts, which can be attributed to an increase in the step density with the offcut, but also to the increase in thickness.

Finally, we combined the different growth parameters to produce uniform graphene on a large scale on SiC with high carrier mobility, around 1700 $cm^2/V.s$ at 300 K. We also demonstrated the possibility of having different carrier types (electrons or holes) depending on the growth parameters, which gives us a wide range of applications where we can invest our graphene.

Since the growth of graphene depends mainly on the external carbon source, we extended the graphene growth to III-nitrides semiconductors, which may allow us to integrated graphene into new markets with new applications. Our objective was to adapt our growth technique to grow graphene on bulk AlN and AlN templates on SiC and sapphire prepared with MBE. Prior to the graphene growth, we conducted annealing studies on the different substrates and templates to enhance the AlN surface quality and to assess its behavior under high temperatures required for the growth of graphene. We were successful in improving the surface quality in most cases, except for the AlN films on sapphire which were not stable at high temperatures. On the other hand, the high temperature annealing was found to have a positive effect on the crystalline quality of the

AlN films. The growth of graphene was evidenced on all the AlN templates based on AFM, XPS, LEED and Raman spectroscopy. However, the graphene layer presented defects and disorder in some cases and was found to be favored on the N-face of bulk AlN compared to the Al-face of the same sample and on thinner AlN layers grown on previously prepared SiC substrates. We also attempted to grow graphene on AlGaN templates prepared on sapphire with MBE. The deposition of a graphitic phase was identified with AFM and XPS, but we suspect that the AlGaN film has been altered by the graphene growth attempts as evidenced with XPS. Finally, we considered an alternative route to combine graphene with AlN, by growing AlN with MBE on graphene on SiC. First results seem promising, since the AlN growth was proven to be possible, but it might be consisting of disordered domains based on RHEED and LEED measurements. In addition, the graphene layer was found keep its properties after the AlN growth as evidenced with Raman spectroscopy.

In conclusion, our growth approach has been proven to be reliable, allowing to produce uniform graphene on a large scale (1/4 of 2'' SiC substrate). We were able to assess few issues such as the reduced carrier mobility for graphene on SiC (0001) and the growth of extra graphene layers on step edges. Our results can be enhanced even more, but compared to the Si sublimation technique of the Si-face of SiC, we were able to reduce the formation of extra layers and enhance the charge carrier mobility by increasing the growth time and slightly modifying the gas mixture and the growth temperature. In addition, since we have demonstrated that it is possible to intercalate hydrogen at the interface during the growth, we can try to find the right H_2 amount for the right growth conditions to produce "quasi-freestanding graphene" which will probably have a positive effect on the carrier mobility. At the same time, we should focus our efforts on preparing uniform samples for the H_2-set study, to complete this work and understand the H_2 effect on the strain. We were also able to uncover unclear matters regarding the substrate's miscut angle. In fact, at the beginning we used to optimize the growth on a certain substrate and then apply the same growth conditions to another substrate, only to find that the results are not the same due to the variation of the miscut angle between the two different substrates. After studying the influence of the substrate's miscut angle, we now understand how to optimize the growth on the different substrates and which growth parameter should be modified to adapt to the different offcut.

This work has explored in details different aspects of the growth of graphene and has brought a wealth of information concerning the growth process. Now that we understand the role of the different growth parameters we can anticipate the behavior of the growth and improve even more the uniformity and the charge carrier mobility. The benefit of this technique is that it relies on an external carbon source, allowing to grow graphene directly on the substrate of interest for different applications, for example on SiC or AlN for electronics with field effect transistors and AlN as a gate insulator. We were also interested in combining graphene with AlGaN for HEMT applications, but the task seems challenging since the AlGaN layer is not stable at high temperatures. Work is still in progress to improve this and to complete it with electrical measurements to evaluate the properties of graphene grown on nitrides. On the other hand, we can

also try to optimize the growth of AlN on graphene on SiC for similar applications such as transistors with a top gate.

Finally, I just like to add that this work not only contributed to the progress of research on the direct growth technique but also contributed to the advancements of research in different areas through different projects and collaborations, where we provided graphene samples for many objectives such as metrology studies, the growth of GaN on graphene, the study of graphene nanometric islands, the study of graphene thermal properties, the growth of silicene on graphene and other projects.

Appendix A

Double resonance, D, D' and disorder

As we have mentioned in **chapter 2**, the defect-induced D-peak originates from zone boundary phonons, around the Brillouin zone corners K (or K'), activated by double resonance [139,141]. The same process can occur intra-valley i.e. double resonance within the same cone K (or K'), resulting in the D'-peak, appearing for defected graphite/graphene [143,144]. The double resonance involves four virtual transitions: i) a laser induced transition of an electron-hole pair. ii) electron-phonon scattering with an exchanged momentum q. iii) defect scattering or electron-phonon scattering with an exchanged momentum $-q$. iv) electron-hole recombination [139], see Fig. C1(a, b). The 2D (~2700 cm^{-1}) and 2D' (3240 cm^{-1}) peaks are the second order of the D and D' peaks respectively [140,141]. Other peaks might appear due to defects in graphene around 2450 cm^{-1} noted as D+D'' and around 2940 cm^{-1} noted as D+D', due to a combination between the D phonon and other phonons [120,121,144]. The intensity ratio I(D')/I(D) can give an idea on the type of defects, whether they are boundary defects, vacancy defects or both [121,144]. It is worth noting that not all defects give rise to the D peak, it is therefore important to try to find other peak alterations, such as an increase in FWHM or decrease in intensity. In addition, The integrated intensity A(D)/A(G) ratio was found to be proportional to the crystallite size L_a for a laser line wavelength λ_l in nanometers, although it is preferred to be calculated with I(D)/I(G) for highly disorder samples, in order to decouple the intensity from the FWHM. The following relationship expresses L_a for lightly disordered samples [204]:

$$L_a(nm) = (2.4 \times 10^{-10})\lambda_l^4 \times \frac{A_G}{A_D} \qquad \text{(C.1)}$$

The I(D)/I(G) relation combined with other observations can be used to assess the disorder within the graphene sheet [141,144]. However, it can be complicated, for example I(D)/I(G) will increase for increasing disorder, the D' peak will appear and all the peaks broaden. For high disorder, the broadening of the G and D' peaks will appear as one line. It is then better to consider one G peak at ~1600 cm^{-1} instead of ~1580 cm^{-1}. On the other hand, in the case of amorphous sp^2 carbon, the I(D)/I(G) ratio will decrease, the G-peak will downshift to 1510 cm^{-1}, and the second-order bands will be replaced with a small bump. In this case, the presence of the D-peak will indicate order. Other observations can be made: when changing the laser's wavelength the G-peak position will be affected for disordered graphene [141,144].

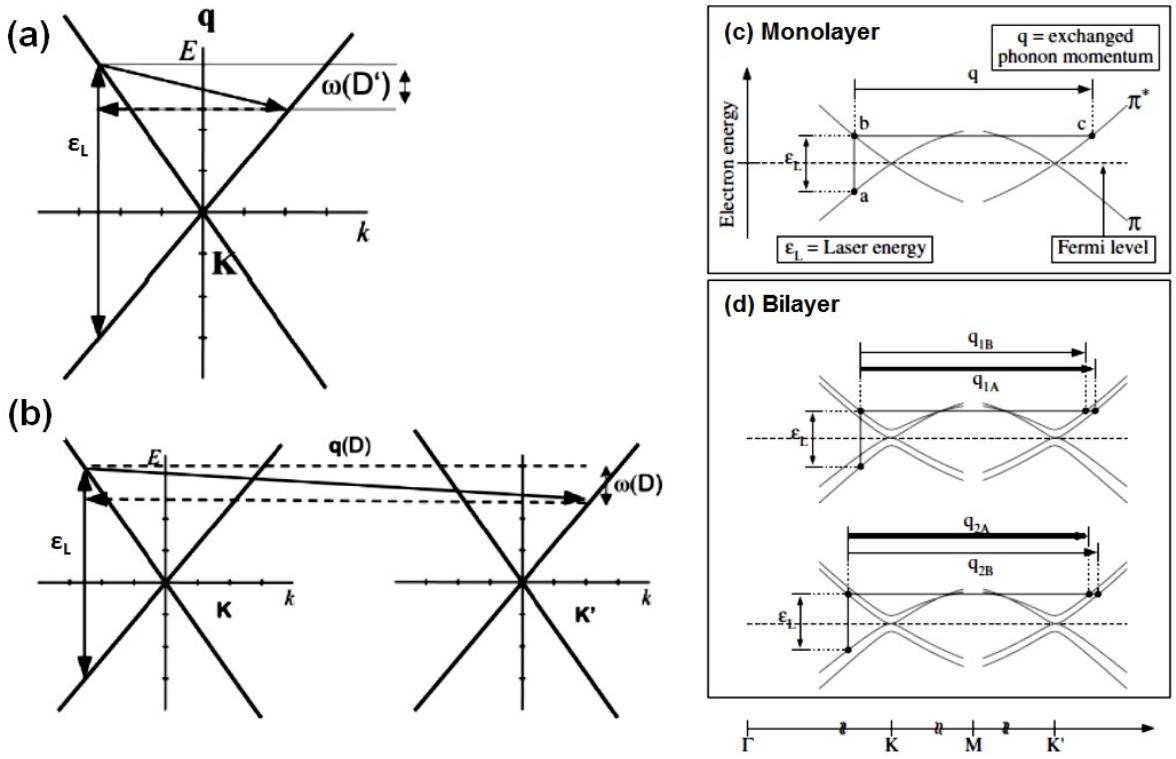

Figure C.1: *Double resonance scheme occurring* ***(a)*** *intra-valley for the D'-peak and* ***(b)*** *inter-valley for the D-peak [141]. Double resonance for the 2D-peak* ***(c)*** *in a monolayer and* ***(d)*** *in a bilayer [120].*

2D-peak and thickness

Investigating the 2D-peak can also be fruitful, especially for information regarding the graphene thickness. The 2D-peak in bulk graphite presents two components D_1 and D_2 [143], 1/4 and 1/2 the intensity of the G-peak. In contrast, the 2D-peak of a single layer of graphene can be fitted with a single Lorentzian. This is not the case for bilayer-graphene and thicker, where the 2D-peak will split into four components as a response to the splitting of the band structure for bilayer-graphene [37,38]. The 2D-peak for bilayers is also upshifted compared to single-layer graphene and will increase even more with the number of layers [119]. This upshift only occurs to the 2D-peak, while the G peak's frequency is barely influenced by the increase in the number of layers. The reason behind the splitting of the 2D peak is explained by Ferrari et al. [119] and presented in Fig. C1(c, d), taken from reference [119]. The incident radiation induces two most probable transitions, then due to electron-phonon scattering all electron bands are coupled amongst them, resulting in four processes consisting of phonons with momenta q_{1A}, q_{1B}, q_{2A} and q_{2B}. The corresponding processes for holes and for the less intense optical transitions are not presented, but they are associated with momenta similar to q_{1A}, q_{1B}, q_{2A} and q_{2B}. These four wave-vectors correspond to phonons with different frequencies, leading to four different peaks in the Raman spectrum for bilayer-graphene. Therefore the upshift and the splitting of the 2D-peak can be employed to determine the number of layers.

References

[1] P.R. Wallace, The Band Theory of Graphite, Phys. Rev. 71 (1947) 622–634. doi:10.1103/PhysRev.71.622.

[2] A.J. Van Bommel, J.E. Crombeen, A. Van Tooren, LEED and Auger electron observations of the SiC(0001) surface, Surf. Sci. 48 (1975) 463–472. doi:10.1016/0039-6028(75)90419-7.

[3] K.S. Novoselov, A.K. Geim, S.V. Morozov, D. Jiang, Y. Zhang, S.V. Dubonos, I.V. Grigorieva, A.A. Firsov, Electric Field Effect in Atomically Thin Carbon Films, Science. 306 (2004) 666–669. doi:10.1126/science.1102896.

[4] C. Berger, Z. Song, T. Li, X. Li, A.Y. Ogbazghi, R. Feng, Z. Dai, A.N. Marchenkov, E.H. Conrad, P.N. First, W.A. de Heer, Ultrathin Epitaxial Graphite: 2D Electron Gas Properties and a Route toward Graphene-based Nanoelectronics, J. Phys. Chem. B. 108 (2004) 19912–19916. doi:10.1021/jp040650f.

[5] C. Berger, Z. Song, X. Li, X. Wu, N. Brown, C. Naud, D. Mayou, T. Li, J. Hass, A.N. Marchenkov, E.H. Conrad, P.N. First, W.A. de Heer, Electronic Confinement and Coherence in Patterned Epitaxial Graphene, Science. 312 (2006) 1191–1196. doi:10.1126/science.1125925.

[6] Y.-M. Lin, C. Dimitrakopoulos, K.A. Jenkins, D.B. Farmer, H.-Y. Chiu, A. Grill, P. Avouris, 100-GHz Transistors from Wafer-Scale Epitaxial Graphene, Science. 327 (2010) 662–662. doi:10.1126/science.1184289.

[7] P.W. Sutter, J.-I. Flege, E.A. Sutter, Epitaxial graphene on ruthenium, Nat. Mater. 7 (2008) 406–411. doi:10.1038/nmat2166.

[8] A. Reina, X. Jia, J. Ho, D. Nezich, H. Son, V. Bulovic, M.S. Dresselhaus, J. Kong, Large Area, Few-Layer Graphene Films on Arbitrary Substrates by Chemical Vapor Deposition, Nano Lett. 9 (2009) 30–35. doi:10.1021/nl801827v.

[9] Qingkai Yu, Jie Lian, Sujitra Siriponglert, Hao Li, Yong P. Chen, and Shin-Shem Pei, Graphene segregated on Ni surfaces and transferred to insulators, Appl. Phys. Lett. 93 (2008) 113103. doi:10.1063/1.2982585.

[10] S. Bae, H. Kim, Y. Lee, X. Xu, J.-S. Park, Y. Zheng, J. Balakrishnan, T. Lei, H. Ri Kim, Y.I. Song, Y.-J. Kim, K.S. Kim, B. Özyilmaz, J.-H. Ahn, B.H. Hong, S. Iijima, Roll-to-roll production of 30-inch graphene films for transparent electrodes, Nat. Nanotechnol. 5 (2010) 574–578. doi:10.1038/nnano.2010.132.

[11] E. Moreau, F.J. Ferrer, D. Vignaud, S. Godey, X. Wallart, Graphene growth by molecular beam epitaxy using a solid carbon source, Phys. Status Solidi A. 207 (2010) 300–303. doi:10.1002/pssa.200982412.

[12] J. Hwang, V.B. Shields, C.I. Thomas, S. Shivaraman, D. Hao, M. Kim, A.R. Woll, G.S. Tompa, M.G. Spencer, Epitaxial growth of graphitic carbon on C-face SiC and Sapphire by chemical vapor deposition (CVD), J. Cryst. Growth. 312 (2010) 3219–3224. doi:10.1016/j.jcrysgro.2010.07.046.

[13] W. Strupinski, K. Grodecki, A. Wysmolek, R. Stepniewski, T. Szkopek, P.E. Gaskell, A. Grüneis, D. Haberer, R. Bozek, J. Krupka, J.M. Baranowski, Graphene Epitaxy by Chemical Vapor Deposition on SiC, Nano Lett. 11 (2011) 1786–1791. doi:10.1021/nl200390e.

[14] K.I. Bolotin, K.J. Sikes, Z. Jiang, M. Klima, G. Fudenberg, J. Hone, P. Kim, H.L. Stormer, Ultrahigh electron mobility in suspended graphene, Solid State Commun. 146 (2008) 351–355. doi:10.1016/j.ssc.2008.02.024.

[15] K.S. Novoselov, V.I. Fal'ko, L. Colombo, P.R. Gellert, M.G. Schwab, K. Kim, A roadmap for graphene, Nature. 490 (2012) 192–200. doi:10.1038/nature11458.

[16] A. Al-Temimy, C. Riedl, U. Starke, Low temperature growth of epitaxial graphene on SiC induced by carbon evaporation, Appl. Phys. Lett. 95 (2009) 231907. doi:10.1063/1.3265916.

[17] A. Michon, S. Vézian, A. Ouerghi, M. Zielinski, T. Chassagne, M. Portail, Direct growth of few-layer graphene on 6H-SiC and 3C-SiC/Si via propane chemical vapor deposition, Appl. Phys. Lett. 97 (2010) 171909. doi:10.1063/1.3503972.

[18] A. Michon, S. Vézian, E. Roudon, D. Lefebvre, M. Zielinski, T. Chassagne, M. Portail, Effects of pressure, temperature, and hydrogen during graphene growth on SiC(0001) using propane-hydrogen chemical vapor deposition, J. Appl. Phys. 113 (2013) 203501. doi:10.1063/1.4806998.

[19] B. Jabakhanji, A. Michon, C. Consejo, W. Desrat, M. Portail, A. Tiberj, M. Paillet, A. Zahab, F. Cheynis, F. Lafont, F. Schopfer, W. Poirier, F. Bertran, P. Le Fèvre, A. Taleb-Ibrahimi, D. Kazazis, W. Escoffier, B.C. Camargo, Y. Kopelevich, J. Camassel, B. Jouault, Tuning the transport properties of graphene films grown by CVD on SiC(0001): Effect of in situ hydrogenation and annealing, Phys. Rev. B. 89 (2014) 085422. doi:10.1103/PhysRevB.89.085422.

[20] F. Lafont, R. Ribeiro-Palau, D. Kazazis, A. Michon, O. Couturaud, C. Consejo, T. Chassagne, M. Zielinski, M. Portail, B. Jouault, F. Schopfer, W. Poirier, Quantum Hall resistance standards from graphene grown by chemical vapour deposition on silicon carbide, Nat. Commun. 6 (2015) 6806. doi:10.1038/ncomms7806.

[21] R. Ribeiro-Palau, F. Lafont, J. Brun-Picard, D. Kazazis, A. Michon, F. Cheynis, O. Couturaud, C. Consejo, B. Jouault, W. Poirier, F. Schopfer, Quantum Hall resistance standard in graphene devices under relaxed experimental conditions, Nat. Nanotechnol. 10 (2015) 965–971. doi:10.1038/nnano.2015.192.

[22] G. Jo, M. Choe, C.-Y. Cho, J.H. Kim, W. Park, S. Lee, W.-K. Hong, T.-W. Kim, S.-J. Park, B.H. Hong, Y.H. Kahng, T. Lee, Large-scale patterned multi-layer graphene films as transparent conducting electrodes for GaN light-emitting diodes, Nanotechnology. 21 (2010) 175201. doi:10.1088/0957-4484/21/17/175201.

[23] G. Fisichella, G. Greco, F. Roccaforte, F. Giannazzo, Current transport in graphene/AlGaN/GaN vertical heterostructures probed at nanoscale, Nanoscale. 6 (2014) 8671–8680. doi:10.1039/C4NR01150C.

[24] P. Trucano, R. Chen, Structure of graphite by neutron diffraction, Nature. 258 (1975) 136–137. doi:10.1038/258136a0.

[25] J.S. Kukesh, L. Pauling, Graphite, Am. Mineral. 35 (1950) 125–125.

[26] Y. Baskin, L. Meyer, Lattice Constants of Graphite at Low Temperatures, Phys. Rev. 100 (1955) 544–544. doi:10.1103/PhysRev.100.544.

[27] J. Hass, W.A. de Heer, E.H. Conrad, The growth and morphology of epitaxial multilayer graphene, J. Phys. Condens. Matter. 20 (2008) 323202. doi:10.1088/0953-8984/20/32/323202.

[28] S. Latil, L. Henrard, Charge Carriers in Few-Layer Graphene Films, Phys. Rev. Lett. 97 (2006) 036803. doi:10.1103/PhysRevLett.97.036803.

[29] M.I. Katsnelson, Graphene: carbon in two dimensions, Mater. Today. 10 (2007) 20–27. doi:10.1016/S1369-7021(06)71788-6.

[30] G.W. Semenoff, Condensed-Matter Simulation of a Three-Dimensional Anomaly, Phys. Rev. Lett. 53 (1984) 2449–2452. doi:10.1103/PhysRevLett.53.2449.

[31] F.D.M. Haldane, Model for a Quantum Hall Effect without Landau Levels: Condensed-Matter Realization of the "Parity Anomaly," Phys. Rev. Lett. 61 (1988) 2015–2018. doi:10.1103/PhysRevLett.61.2015.

[32] K.S. Novoselov, A.K. Geim, S.V. Morozov, D. Jiang, M.I. Katsnelson, I.V. Grigorieva, S.V. Dubonos, A.A. Firsov, Two-dimensional gas of massless Dirac fermions in graphene, Nature. 438 (2005) 197–200. doi:10.1038/nature04233.

[33] A.K. Geim, K.S. Novoselov, The rise of graphene, Nat. Mater. 6 (2007) 183–191. doi:10.1038/nmat1849.

[34] Y. Zhang, Y.-W. Tan, H.L. Stormer, P. Kim, Experimental observation of the quantum Hall effect and Berry's phase in graphene, Nature. 438 (2005) 201–204. doi:10.1038/nature04235.

[35] K.S. Novoselov, Z. Jiang, Y. Zhang, S.V. Morozov, H.L. Stormer, U. Zeitler, J.C. Maan, G.S. Boebinger, P. Kim, A.K. Geim, Room-Temperature Quantum Hall Effect in Graphene, Science. (2007). doi:10.1126/science.1137201.

[36] F. Varchon, R. Feng, J. Hass, X. Li, B.N. Nguyen, C. Naud, P. Mallet, J.-Y. Veuillen, C. Berger, E.H. Conrad, L. Magaud, Electronic Structure of Epitaxial Graphene Layers on SiC: Effect of the Substrate, Phys. Rev. Lett. 99 (2007) 126805. doi:10.1103/PhysRevLett.99.126805.

[37] A. Bostwick, T. Ohta, J.L. McChesney, K.V. Emtsev, T. Seyller, K. Horn, Eli Rotenberg, Symmetry breaking in few layer graphene films, New J. Phys. 9 (2007) 385. doi:10.1088/1367-2630/9/10/385.

[38] E. McCann, Asymmetry gap in the electronic band structure of bilayer graphene, Phys. Rev. B. 74 (2006) 161403. doi:10.1103/PhysRevB.74.161403.

[39] E. McCann, V.I. Fal'ko, Landau-Level Degeneracy and Quantum Hall Effect in a Graphite Bilayer, Phys. Rev. Lett. 96 (2006) 086805. doi:10.1103/PhysRevLett.96.086805.

[40] E.V. Castro, K.S. Novoselov, S.V. Morozov, N.M.R. Peres, J.M.B.L. dos Santos, J. Nilsson, F. Guinea, A.K. Geim, A.H.C. Neto, Biased Bilayer Graphene: Semiconductor with a Gap Tunable by the Electric Field Effect, Phys. Rev. Lett. 99 (2007) 216802. doi:10.1103/PhysRevLett.99.216802.

[41] T. Ohta, A. Bostwick, J.L. McChesney, T. Seyller, K. Horn, E. Rotenberg, Interlayer Interaction and Electronic Screening in Multilayer Graphene Investigated with Angle-Resolved Photoemission Spectroscopy, Phys. Rev. Lett. 98 (2007) 206802. doi:10.1103/PhysRevLett.98.206802.

[42] J.B. Oostinga, H.B. Heersche, X. Liu, A.F. Morpurgo, L.M.K. Vandersypen, Gate-induced insulating state in bilayer graphene devices, Nat. Mater. 7 (2008) 151–157. doi:10.1038/nmat2082.

[43] J. Hass, F. Varchon, J.E. Millán-Otoya, M. Sprinkle, N. Sharma, W.A. de Heer, C. Berger, P.N. First, L. Magaud, E.H. Conrad, Why Multilayer Graphene on 4H-SiC (000-1) Behaves Like a

Single Sheet of Graphene, Phys. Rev. Lett. 100 (2008) 125504. doi:10.1103/PhysRevLett.100.125504.

[44] J.M.B. Lopes dos Santos, N.M.R. Peres, A.H. Castro Neto, Graphene Bilayer with a Twist: Electronic Structure, Phys. Rev. Lett. 99 (2007) 256802. doi:10.1103/PhysRevLett.99.256802.

[45] R.R. Nair, P. Blake, A.N. Grigorenko, K.S. Novoselov, T.J. Booth, T. Stauber, N.M.R. Peres, A.K. Geim, Fine Structure Constant Defines Visual Transparency of Graphene, Science. 320 (2008) 1308–1308. doi:10.1126/science.1156965.

[46] K.S. Kim, Y. Zhao, H. Jang, S.Y. Lee, J.M. Kim, K.S. Kim, J.-H. Ahn, P. Kim, J.-Y. Choi, B.H. Hong, Large-scale pattern growth of graphene films for stretchable transparent electrodes, Nature. 457 (2009) 706–710. doi:10.1038/nature07719.

[47] F. Bonaccorso, Z. Sun, T. Hasan, A.C. Ferrari, Graphene photonics and optoelectronics, Nat. Photonics. 4 (2010) 611–622. doi:10.1038/nphoton.2010.186.

[48] Kunook Chung, Hyeonjun Beak, Youngbin Tchoe, Hongseok Oh, Hyobin Yoo, Miyoung Kim, and Gyu-Chul Yi, Growth and characterizations of GaN micro-rods on graphene films for flexible light emitting diodes, APL Mater. 2 (2014) 092512. doi:10.1063/1.4894780.

[49] Z. Sun, T. Hasan, F. Torrisi, D. Popa, G. Privitera, F. Wang, F. Bonaccorso, D.M. Basko, A.C. Ferrari, Graphene Mode-Locked Ultrafast Laser, ACS Nano. 4 (2010) 803–810. doi:10.1021/nn901703e.

[50] Jahan M. Dawlaty, Shriram Shivaraman, Jared Strait, Paul George, Mvs Chandrashekhar, Farhan Rana, Michael G. Spencer, Dmitry Veksler, and, Yunqing Chen, Measurement of the optical absorption spectra of epitaxial graphene from terahertz to visible, Appl. Phys. Lett. 93 (2008) 131905. doi:10.1063/1.2990753.

[51] A.R. Wright, J.C. Cao, C. Zhang, Enhanced Optical Conductivity of Bilayer Graphene Nanoribbons in the Terahertz Regime, Phys. Rev. Lett. 103 (2009) 207401. doi:10.1103/PhysRevLett.103.207401.

[52] F. Xia, T. Mueller, Y.-M. Lin, A. Valdes-Garcia, P. Avouris, Ultrafast graphene photodetector, Nat. Nanotechnol. 4 (2009) 839–843. doi:10.1038/nnano.2009.292.

[53] Y. Kang, H.-D. Liu, M. Morse, M.J. Paniccia, M. Zadka, S. Litski, G. Sarid, A. Pauchard, Y.-H. Kuo, H.-W. Chen, W.S. Zaoui, J.E. Bowers, A. Beling, D.C. McIntosh, X. Zheng, J.C. Campbell, Monolithic germanium/silicon avalanche photodiodes with 340 GHz gain–bandwidth product, Nat. Photonics. 3 (2009) 59–63. doi:10.1038/nphoton.2008.247.

[54] F. Wang, Y. Zhang, C. Tian, C. Girit, A. Zettl, M. Crommie, Y.R. Shen, Gate-Variable Optical Transitions in Graphene, Science. 320 (2008) 206–209. doi:10.1126/science.1152793.

[55] M. Liu, X. Yin, E. Ulin-Avila, B. Geng, T. Zentgraf, L. Ju, F. Wang, X. Zhang, A graphene-based broadband optical modulator, Nature. 474 (2011) 64–67. doi:10.1038/nature10067.

[56] X. Wang, L. Zhi, N. Tsao, Ž. Tomović, J. Li, K. Müllen, Transparent Carbon Films as Electrodes in Organic Solar Cells, Angew. Chem. Int. Ed. 47 (2008) 2990–2992. doi:10.1002/anie.200704909.

[57] Junbo Wu, Héctor A. Becerril, Zhenan Bao, Zunfeng Liu, Yongsheng Chen, and, Peter Peumans, Organic solar cells with solution-processed graphene transparent electrodes, Appl. Phys. Lett. 92 (2008) 263302. doi:10.1063/1.2924771.

[58] I. Meric et al., High-Frequency Performance of Graphene Field Effect Transistors with Saturating IV-characteristics 15–18 (IEEE Electron Devices Society, 2011).

[59] A. Tzalenchuk, S. Lara-Avila, A. Kalaboukhov, S. Paolillo, M. Syväjärvi, R. Yakimova, O. Kazakova, T.J.B.M. Janssen, V. Fal'ko, S. Kubatkin, Towards a quantum resistance standard based on epitaxial graphene, Nat. Nanotechnol. 5 (2010) 186–189. doi:10.1038/nnano.2009.474.

[60] L. Liao, Y.-C. Lin, M. Bao, R. Cheng, J. Bai, Y. Liu, Y. Qu, K.L. Wang, Y. Huang, X. Duan, High-speed graphene transistors with a self-aligned nanowire gate, Nature. 467 (2010) 305–308. doi:10.1038/nature09405.

[61] L. Liao, J. Bai, R. Cheng, Y.-C. Lin, S. Jiang, Y. Qu, Y. Huang, X. Duan, Sub-100 nm Channel Length Graphene Transistors, Nano Lett. 10 (2010) 3952–3956. doi:10.1021/nl101724k.

[62] A.S. Mayorov, R.V. Gorbachev, S.V. Morozov, L. Britnell, R. Jalil, L.A. Ponomarenko, P. Blake, K.S. Novoselov, K. Watanabe, T. Taniguchi, A.K. Geim, Micrometer-Scale Ballistic Transport in Encapsulated Graphene at Room Temperature, Nano Lett. 11 (2011) 2396–2399. doi:10.1021/nl200758b.

[63] C.R. Dean, A.F. Young, I. Meric, C. Lee, L. Wang, S. Sorgenfrei, K. Watanabe, T. Taniguchi, P. Kim, K.L. Shepard, J. Hone, Boron nitride substrates for high-quality graphene electronics, Nat. Nanotechnol. 5 (2010) 722–726. doi:10.1038/nnano.2010.172.

[64] J. Cai, P. Ruffieux, R. Jaafar, M. Bieri, T. Braun, S. Blankenburg, M. Muoth, A.P. Seitsonen, M. Saleh, X. Feng, K. Müllen, R. Fasel, Atomically precise bottom-up fabrication of graphene nanoribbons, Nature. 466 (2010) 470–473. doi:10.1038/nature09211.

[65] M.Y. Han, B. Özyilmaz, Y. Zhang, P. Kim, Energy Band-Gap Engineering of Graphene Nanoribbons, Phys. Rev. Lett. 98 (2007) 206805. doi:10.1103/PhysRevLett.98.206805.

[66] D.C. Elias, R.R. Nair, T.M.G. Mohiuddin, S.V. Morozov, P. Blake, M.P. Halsall, A.C. Ferrari, D.W. Boukhvalov, M.I. Katsnelson, A.K. Geim, K.S. Novoselov, Control of Graphene's Properties by Reversible Hydrogenation: Evidence for Graphane, Science. 323 (2009) 610–613. doi:10.1126/science.1167130.

[67] R.R. Nair, W. Ren, R. Jalil, I. Riaz, V.G. Kravets, L. Britnell, P. Blake, F. Schedin, A.S. Mayorov, S. Yuan, M.I. Katsnelson, H.-M. Cheng, W. Strupinski, L.G. Bulusheva, A.V. Okotrub, I.V. Grigorieva, A.N. Grigorenko, K.S. Novoselov, A.K. Geim, Fluorographene: A Two-Dimensional Counterpart of Teflon, Small. 6 (2010) 2877–2884. doi:10.1002/smll.201001555.

[68] A.A. Balandin, Thermal properties of graphene and nanostructured carbon materials, Nat. Mater. 10 (2011) 569–581. doi:10.1038/nmat3064.

[69] See supporting data on science online of K.S. Novoselov et al., Science. 306 (2004) 666–669.

[70] K.S. Novoselov, A. Mishchenko, A. Carvalho, A.H.C. Neto, 2D materials and van der Waals heterostructures, Science. 353 (2016) aac9439. doi:10.1126/science.aac9439.

[71] F. Withers, O. Del Pozo-Zamudio, A. Mishchenko, A.P. Rooney, A. Gholinia, K. Watanabe, T. Taniguchi, S.J. Haigh, A.K. Geim, A.I. Tartakovskii, K.S. Novoselov, Light-emitting diodes by band-structure engineering in van der Waals heterostructures, Nat. Mater. 14 (2015) 301–306. doi:10.1038/nmat4205.

[72] P. Blake, P.D. Brimicombe, R.R. Nair, T.J. Booth, D. Jiang, F. Schedin, L.A. Ponomarenko, S.V. Morozov, H.F. Gleeson, E.W. Hill, A.K. Geim, K.S. Novoselov, Graphene-Based Liquid Crystal Device, Nano Lett. 8 (2008) 1704–1708. doi:10.1021/nl080649i.

[73] Y. Hernandez, V. Nicolosi, M. Lotya, F.M. Blighe, Z. Sun, S. De, I.T. McGovern, B. Holland, M. Byrne, Y.K. Gun'Ko, J.J. Boland, P. Niraj, G. Duesberg, S. Krishnamurthy, R. Goodhue, J. Hutchison, V. Scardaci, A.C. Ferrari, J.N. Coleman, High-yield production of graphene by liquid-phase exfoliation of graphite, Nat. Nanotechnol. 3 (2008) 563–568. doi:10.1038/nnano.2008.215.

[74] D.R. Dreyer, R.S. Ruoff, C.W. Bielawski, From Conception to Realization: An Historial Account of Graphene and Some Perspectives for Its Future, Angew. Chem. Int. Ed. 49 (2010) 9336–9344. doi:10.1002/anie.201003024.

[75] H.C. Schniepp, J.-L. Li, M.J. McAllister, H. Sai, M. Herrera-Alonso, D.H. Adamson, R.K. Prud'homme, R. Car, D.A. Saville, I.A. Aksay, Functionalized Single Graphene Sheets Derived from Splitting Graphite Oxide, J. Phys. Chem. B. 110 (2006) 8535–8539. doi:10.1021/jp060936f.

[76] I. Forbeaux, J.-M. Themlin, J.-M. Debever, Heteroepitaxial graphite on 6H-SiC (0001) Interface formation through conduction-band electronic structure, Phys. Rev. B. 58 (1998) 16396–16406. doi:10.1103/PhysRevB.58.16396.

[77] A. Charrier, A. Coati, T. Argunova, F. Thibaudau, Y. Garreau, R. Pinchaux, I. Forbeaux, J.-M. Debever, M., Sauvage-Simkin, and J.-M. Themlin, Solid-state decomposition of silicon carbide for growing ultra-thin heteroepitaxial graphite films, J. Appl. Phys. 92 (2002) 2479–2484. doi:10.1063/1.1498962.

[78] I. Forbeaux, J.-M. Themlin, J.-M. Debever, High-temperature graphitization of the 6H-SiC (0001) face, Surf. Sci. 442 (1999) 9–18. doi:10.1016/S0039-6028(99)00891-2.

[79] T. Seyller, K.V. Emtsev, K. Gao, F. Speck, L. Ley, A. Tadich, L. Broekman, J.D. Riley, R.C.G. Leckey, O. Rader, A. Varykhalov, A.M. Shikin, Structural and electronic properties of graphite layers grown on SiC(0 0 0 1), Surf. Sci. 600 (2006) 3906–3911. doi:10.1016/j.susc.2006.01.102.

[80] K.V. Emtsev, A. Bostwick, K. Horn, J. Jobst, G.L. Kellogg, L. Ley, J.L. McChesney, T. Ohta, S.A. Reshanov, J. Röhrl, E. Rotenberg, A.K. Schmid, D. Waldmann, H.B. Weber, T. Seyller, Towards wafer-size graphene layers by atmospheric pressure graphitization of silicon carbide, Nat. Mater. 8 (2009) 203–207. doi:10.1038/nmat2382.

[81] F. Varchon, P. Mallet, L. Magaud, J.-Y. Veuillen, Rotational disorder in few-layer graphene films on 6H-SiC (000-1): A scanning tunneling microscopy study, Phys. Rev. B. 77 (2008) 165415. doi:10.1103/PhysRevB.77.165415.

[82] L.B. Biedermann, M.L. Bolen, M.A. Capano, D. Zemlyanov, R.G. Reifenberger, Insights into few-layer epitaxial graphene growth on 4H-SiC (000-1) substrates from STM studies, Phys. Rev. B. 79 (2009) 125411. doi:10.1103/PhysRevB.79.125411.

[83] C. Riedl, U. Starke, J. Bernhardt, M. Franke, K. Heinz, Structural properties of the graphene-SiC(0001) interface as a key for the preparation of homogeneous large-terrace graphene surfaces, Phys. Rev. B. 76 (2007) 245406. doi:10.1103/PhysRevB.76.245406.

[84] E. Pallecchi, F. Lafont, V. Cavaliere, F. Schopfer, D. Mailly, W. Poirier, A. Ouerghi, High Electron Mobility in Epitaxial Graphene on 4H-SiC(0001) via post-growth annealing under hydrogen, Sci. Rep. 4 (2014). doi:10.1038/srep04558.

[85] J. Baringhaus, M. Ruan, F. Edler, A. Tejeda, M. Sicot, A. Taleb-Ibrahimi, A.-P. Li, Z. Jiang, E.H. Conrad, C. Berger, C. Tegenkamp, W.A. de Heer, Exceptional ballistic transport in epitaxial graphene nanoribbons, Nature. 506 (2014) 349–354. doi:10.1038/nature12952.

[86] C. Riedl, C. Coletti, T. Iwasaki, A.A. Zakharov, U. Starke, Quasi-free Standing Epitaxial Graphene on SiC by Hydrogen Intercalation, Phys. Rev. Lett. 103 (2009). doi:10.1103/PhysRevLett.103.246804.

[87] Transfer of graphene layers grown on SiC wafers to other substrates and their integration into field effect transistors, Appl. Phys. Lett. 95 (2009) 202101. doi:10.1063/1.3263942.

[88] J. Kim, H. Park, J.B. Hannon, S.W. Bedell, K. Fogel, D.K. Sadana, C. Dimitrakopoulos, Layer-resolved graphene transfer via engineered strain layers, Science. 342 (2013) 833–836. doi:10.1126/science.1242988.

[89] Luxmi, N. Srivastava, G. He, R.M. Feenstra, P.J. Fisher, Comparison of graphene formation on C-face and Si-face SiC {0001} surfaces, Phys. Rev. B. 82 (2010) 235406. doi:10.1103/PhysRevB.82.235406.

[90] C. Bouhafs, V. Darakchieva, I.L. Persson, A. Tiberj, P.O.Å. Persson, M. Paillet, A.-A. Zahab, P. Landois, S. Juillaguet, S. Schöche, M. Schubert, R. Yakimova, Structural properties and dielectric function of graphene grown by high-temperature sublimation on 4H-SiC(000-1), J. Appl. Phys. 117 (2015) 085701. doi:10.1063/1.4908216.

[91] J. M. Blakely, J. S. Kim, and H. C. Potter, Segregation of Carbon to the (100) Surface of Nickel, J. Appl. Phys. 41 (1970) 2693–2697. doi:10.1063/1.1659283.

[92] J.C. Shelton, H.R. Patil, J.M. Blakely, Equilibrium segregation of carbon to a nickel (111) surface: A surface phase transition, Surf. Sci. 43 (1974) 493–520. doi:10.1016/0039-6028(74)90272-6.

[93] B. Lang, A LEED study of the deposition of carbon on platinum crystal surfaces, Surf. Sci. 53 (1975) 317–329. doi:10.1016/0039-6028(75)90132-6.

[94] T.A. Land, T. Michely, R.J. Behm, J.C. Hemminger, G. Comsa, STM investigation of single layer graphite structures produced on Pt(111) by hydrocarbon decomposition, Surf. Sci. 264 (1992) 261–270. doi:10.1016/0039-6028(92)90183-7.

[95] I.V. Makarenko, A.N. Titkov, Z. Waqar, P. Dumas, E.V. Rut'kov, N.R. Gall', Structural properties of a monolayer graphite film on the (111)Ir surface, Phys. Solid State. 49 (2007) 371–376. doi:10.1134/S106378340702031X.

[96] H. Ueta, M. Saida, C. Nakai, Y. Yamada, M. Sasaki, S. Yamamoto, Highly oriented monolayer graphite formation on Pt(1 1 1) by a supersonic methane beam, Surf. Sci. 560 (2004) 183–190. doi:10.1016/j.susc.2004.04.039.

[97] S. Marchini, S. Günther, J. Wintterlin, Scanning tunneling microscopy of graphene on Ru(0001), Phys. Rev. B. 76 (2007) 075429. doi:10.1103/PhysRevB.76.075429.

[98] J. Coraux, A.T. N'Diaye, C. Busse, T. Michely, Structural Coherency of Graphene on Ir(111), Nano Lett. 8 (2008) 565–570. doi:10.1021/nl0728874.

[99] X. Li, W. Cai, J. An, S. Kim, J. Nah, D. Yang, R. Piner, A. Velamakanni, I. Jung, E. Tutuc, S.K. Banerjee, L. Colombo, R.S. Ruoff, Large-area synthesis of high-quality and uniform graphene films on copper foils, Science. 324 (2009) 1312–1314. doi:10.1126/science.1171245.

[100] L. Banszerus, M. Schmitz, S. Engels, J. Dauber, M. Oellers, F. Haupt, K. Watanabe, T. Taniguchi, B. Beschoten, C. Stampfer, Ultrahigh-mobility graphene devices from chemical vapor deposition on reusable copper, Sci. Adv. 1 (2015) e1500222. doi:10.1126/sciadv.1500222.

[101] M. Portail, A. Michon, S. Vézian, D. Lefebvre, S. Chenot, E. Roudon, M. Zielinski, T. Chassagne, A. Tiberj, J. Camassel, Y. Cordier, Growth mode and electric properties of graphene and graphitic phase grown by argon-propane assisted CVD on 3C-SiC/Si and 6H-SiC, J. Cryst. Growth. 349 (2012) 27–35. doi:10.1016/j.jcrysgro.2012.04.004.

[102] M. Portail, A. Michon, S. Vézian, D. Lefebvre, S. Chenot, A. Ouerghi, M. Zielinski, T. Chassagne, Y. Cordier, CVD Growth of Graphene on 2'' 3C-SiC/Si Templates: Influence of Substrate Orientation and Wafer Homogeneity, Mater. Sci. Forum. 717–720 (2012) 621–624. doi:10.4028/www.scientific.net/MSF.717-720.621.

[103] A. Michon, A. Tiberj, S. Vézian, E. Roudon, D. Lefebvre, M. Portail, M. Zielinski, T. Chassagne, J. Camassel, Y. Cordier, Graphene growth on AlN templates on silicon using propane-hydrogen chemical vapor deposition, Appl. Phys. Lett. 104 (2014) 071912. doi:10.1063/1.4866285.

[104] R. Dagher, S. Matta, R. Parret, M. Paillet, B. Jouault, L. Nguyen, M. Portail, M. Zielinski, T. Chassagne, S. Tanaka, J. Brault, Y. Cordier, A. Michon, High temperature annealing and CVD growth of few-layer graphene on bulk AlN and AlN templates, Phys. Status Solidi A. (2017) n/a-n/a. doi:10.1002/pssa.201600436.

[105] K.V. Emtsev, F. Speck, T. Seyller, L. Ley, J.D. Riley, Interaction, growth, and ordering of epitaxial graphene on SiC{0001} surfaces: A comparative photoelectron spectroscopy study, Phys. Rev. B. 77 (2008) 155303. doi:10.1103/PhysRevB.77.155303.

[106] U. Starke, C. Riedl, Epitaxial graphene on SiC(0001) and SiC (000-1) : from surface reconstructions to carbon electronics, J. Phys. Condens. Matter. 21 (2009) 134016. doi:10.1088/0953-8984/21/13/134016.

[107] U. Starke, J. Schardt, J. Bernhardt, M. Franke, K. Reuter, H. Wedler, K. Heinz, J. Furthmüller, P. Käckell, F. Bechstedt, Novel Reconstruction Mechanism for Dangling-Bond Minimization: Combined Method Surface Structure Determination of SiC(111)-(3×3), Phys. Rev. Lett. 80 (1998) 758–761. doi:10.1103/PhysRevLett.80.758.

[108] U. Starke, J. Schardt, J. Bernhardt, M. Franke, K. Heinz, Stacking Transformation from Hexagonal to Cubic SiC Induced by Surface Reconstruction: A Seed for Heterostructure Growth, Phys. Rev. Lett. 82 (1999) 2107–2110. doi:10.1103/PhysRevLett.82.2107.

[109] M. Sabisch, P. Krüger, J. Pollmann, Ab initio calculations of structural and electronic properties of 6H-SiC(0001) surfaces, Phys. Rev. B. 55 (1997) 10561–10570. doi:10.1103/PhysRevB.55.10561.

[110] J. Borysiuk, R. Bożek, W. Strupiński, A. Wysmołek, K. Grodecki, R. Stępniewski, J.M. Baranowski, Transmission electron microscopy and scanning tunneling microscopy investigations of graphene on 4H-SiC(0001), J. Appl. Phys. 105 (2009) 023503. doi:10.1063/1.3065481.

[111] S. Forti, K.V. Emtsev, C. Coletti, A.A. Zakharov, C. Riedl, U. Starke, Large-area homogeneous quasifree standing epitaxial graphene on SiC(0001): Electronic and structural characterization, Phys. Rev. B. 84 (2011) 125449. doi:10.1103/PhysRevB.84.125449.

[112] J. Hass, R. Feng, J.E. Millán-Otoya, X. Li, M. Sprinkle, P.N. First, W.A. de Heer, E.H. Conrad, C. Berger, Structural properties of the multilayer graphene/4H-SiC system as determined by surface x-ray diffraction, Phys. Rev. B. 75 (2007) 214109. doi:10.1103/PhysRevB.75.214109.

[113] G.F. Sun, J.F. Jia, Q.K. Xue, L. Li, Atomic-scale imaging and manipulation of ridges on epitaxial graphene on 6H-SiC(0001), Nanotechnology. 20 (2009) 355701. doi:10.1088/0957-4484/20/35/355701.

[114] J.K. Hite, M.E. Twigg, J.L. Tedesco, A.L. Friedman, R.L. Myers-Ward, C.R. Eddy, D.K. Gaskill, Epitaxial graphene nucleation on C-face silicon carbide, Nano Lett. 11 (2011) 1190–1194. doi:10.1021/nl104072y.

[115] J. Robinson, X. Weng, K. Trumbull, R. Cavalero, M. Wetherington, E. Frantz, M. LaBella, Z. Hughes, M. Fanton, D. Snyder, Nucleation of Epitaxial Graphene on SiC(0001), ACS Nano. 4 (2010) 153–158. doi:10.1021/nn901248j.

[116] A. Michon, E. Roudon, M. Portail, D. Lefebvre, S. Vézian, Y. Cordier, A. Tiberj, T. Chassagne, M. Zielinski, Graphene/SiC Interface Control Using Propane-Hydrogen CVD on 6H-SiC(0001) and 3C-SiC(111)/Si(111), Mater. Sci. Forum. 711 (2012) 253–257. doi:10.4028/www.scientific.net/MSF.711.253.

[117] A. Michon, E. Roudon, M. Portail, B. Jouault, S. Contreras, S. Chenot, Y. Cordier, D. Lefebvre, S. Vézian, M. Zielinski, T. Chassagne, J. Camassel, Structural and Electrical Properties of Graphene Films Grown by Propane/Hydrogen CVD on 6H-SiC(0001), Mater. Sci. Forum. 717–720 (2012) 625–628. doi:10.4028/www.scientific.net/MSF.717-720.625.

[118] A. Michon, L. Largeau, A. Tiberj, J.R. Huntzinger, O. Mauguin, S. Vézian, D. Lefebvre, F. Cheynis, F. Leroy, P. Müller, T. Chassagne, M. Zielinski, M. Portail, X-Ray Diffraction and Raman Spectroscopy Study of Strain in Graphene Films Grown on 6H-SiC(0001) Using Propane-Hydrogen-Argon CVD, Mater. Sci. Forum. 740–742 (2013) 117–120. doi:10.4028/www.scientific.net/MSF.740-742.117.

[119] A.C. Ferrari, J.C. Meyer, V. Scardaci, C. Casiraghi, M. Lazzeri, F. Mauri, S. Piscanec, D. Jiang, K.S. Novoselov, S. Roth, A.K. Geim, Raman Spectrum of Graphene and Graphene Layers, Phys. Rev. Lett. 97 (2006) 187401. doi:10.1103/PhysRevLett.97.187401.

[120] M.A. Pimenta, G. Dresselhaus, M.S. Dresselhaus, L.G. Cançado, A. Jorio, R. Saito, Studying disorder in graphite-based systems by Raman spectroscopy, Phys. Chem. Chem. Phys. 9 (2007) 1276–1290. doi:10.1039/B613962K.

[121] A. Eckmann, A. Felten, A. Mishchenko, L. Britnell, R. Krupke, K.S. Novoselov, C. Casiraghi, Probing the Nature of Defects in Graphene by Raman Spectroscopy, Nano Lett. 12 (2012) 3925–3930. doi:10.1021/nl300901a.

[122] A. Leycuras, Growth of CVD Thin Films and Thick LPE 3C SiC in a Specially Designed Reactor, Mater. Sci. Forum. 338–342 (2000) 241–244. doi:10.4028/www.scientific.net/MSF.338-342.241.

[123] M. Nemoz, R. Dagher, S. Matta, A. Michon, P. Vennéguès, J. Brault, Dislocation densities reduction in MBE-grown AlN thin films by high-temperature annealing, J. Cryst. Growth. 461 (2017) 10–15. doi:10.1016/j.jcrysgro.2016.12.089.

[124] http://www.tankeblue.com/index_en.html.

[125] http://www.qualitymaterial.net/sic-crystal.html.

[126] I. Horcas, R. Fernández, J.M. Gómez-Rodríguez, J. Colchero, J. Gómez-Herrero, A.M. Baro, WSXM: A software for scanning probe microscopy and a tool for nanotechnology, Rev. Sci. Instrum. 78 (2007) 013705. doi:10.1063/1.2432410.

[127] J.C. Byers, P. Tamiasso-Martinhon, C. Deslouis, A. Pailleret, O.A. Semenikhin, Atomic Force Microscopy Studies of Carbon Nitride (CNx) Films Deposited on a Conducting Polymer Substrate, J. Phys. Chem. C. 114 (2010) 18474–18480. doi:10.1021/jp103795c.

[128] K.D. O'Nei, O.A. Semenikhin, AFM Phase Imaging of Electropolymerized Polybithiophene Films at Different Stages of Their Growth, J. Phys. Chem. C. 111 (2007) 14823–14832. doi:10.1021/jp074076u.

[129] S. N. Magonov, D. Darrell H. Reneker, Characterization of Polymer Surfaces with Atomic Force Microscopy, Annu. Rev. Mater. Sci. 27 (1997) 175–222. doi:10.1146/annurev.matsci.27.1.175.

[130] F. J. Ferrer, E. Moreau, D. Vignaud, D. Deresmes, S. Godey, and X. Wallart, Initial stages of graphitization on SiC(000-1), as studied by phase atomic force microscopy, J. Appl. Phys. 109 (2011) 054307. doi:10.1063/1.3560896.

[131] K. Emtsev, Electronic and structural characterizations of unreconstructed SiC{0001} surfaces and the growth of graphene overlayers, Dissertation, Friedrich-Alexander-Universität Erlangen-Nürnberg, 2009.

[132] S. Hüfner, Photoelectron Spectroscopy: Principles and Applications, Springer Science & Business Media, 2013.

[133] S. Tanuma, C.J. Powell, D.R. Penn, Calculations of electron inelastic mean free paths, Surf. Interface Anal. 37 (2005) 1–14. doi:10.1002/sia.1997.

[134] D.J. Gardiner, P.R. Graves, Practical Raman Spectroscopy, Springer Science & Business Media, 2012.

[135] S. Reich, C. Thomsen, Raman spectroscopy of graphite, Philos. Trans. R. Soc. Lond. Math. Phys. Eng. Sci. 362 (2004) 2271–2288. doi:10.1098/rsta.2004.1454.

[136] R.P. Vidano. ,D.B. Fischbach, Observation of Raman band shifting with excitation wavelength for carbons and graphites, 39 (1981) 341. doi:http://dx.doi.org/10.1016/0038-1098(81)90686-4.

[137] F. Tuinstra and J. L. Koenig, Raman Spectrum of Graphite, J. Chem. Phys. 53 (1970) 1126–1130. doi:10.1063/1.1674108.

[138] A.C. Ferrari, J. Robertson, Interpretation of Raman spectra of disordered and amorphous carbon, Phys. Rev. B. 61 (2000) 14095–14107. doi:10.1103/PhysRevB.61.14095.

[139] C. Thomsen, S. Reich, Double Resonant Raman Scattering in Graphite, Phys. Rev. Lett. 85 (2000) 5214–5217. doi:10.1103/PhysRevLett.85.5214.

[140] A.C. Ferrari, D.M. Basko, Raman spectroscopy as a versatile tool for studying the properties of graphene, Nat. Nanotechnol. 8 (2013) 235–246. doi:10.1038/nnano.2013.46.

[141] A.C. Ferrari, Raman spectroscopy of graphene and graphite: Disorder, electron–phonon coupling, doping and nonadiabatic effects, Solid State Commun. 143 (2007) 47–57. doi:10.1016/j.ssc.2007.03.052.

[142] I. Pócsik, M. Hundhausen, M. Koós, L. Ley, Origin of the D peak in the Raman spectrum of microcrystalline graphite, J. Non-Cryst. Solids. 227–230, Part 2 (1998) 1083–1086. doi:10.1016/S0022-3093(98)00349-4.

[143] R.J. Nemanich, S.A. Solin, First- and second-order Raman scattering from finite-size crystals of graphite, Phys. Rev. B. 20 (1979) 392–401. doi:10.1103/PhysRevB.20.392.

[144] L.G. Cançado, A. Jorio, E.H.M. Ferreira, F. Stavale, C.A. Achete, R.B. Capaz, M.V.O. Moutinho, A. Lombardo, T.S. Kulmala, A.C. Ferrari, Quantifying Defects in Graphene via

Raman Spectroscopy at Different Excitation Energies, Nano Lett. 11 (2011) 3190–3196. doi:10.1021/nl201432g.

[145] A. Tiberj, J.-R. Huntzinger, J. Camassel, F. Hiebel, A. Mahmood, P. Mallet, C. Naud, J.-Y. Veuillen, Multiscale investigation of graphene layers on 6H-SiC(000-1), Nanoscale Res. Lett. 6 (2011) 171. doi:10.1186/1556-276X-6-171.

[146] N. Camara, J.-R. Huntzinger, G. Rius, A. Tiberj, N. Mestres, F. Pérez-Murano, P. Godignon, J. Camassel, Anisotropic growth of long isolated graphene ribbons on the C face of graphite-capped 6H-SiC, Phys. Rev. B. 80 (2009) 125410. doi:10.1103/PhysRevB.80.125410.

[147] F Fromm, M H Oliveira Jr, A Molina-S´anchez, M Hundhausen, J M J Lopes, H Riechert, L Wirtz, and T Seyller, Contribution of the buffer layer to the Raman spectrum of epitaxial graphene on SiC(0001). http://iopscience.iop.org/1367-2630/15/4/043031/media (accessed March 10, 2017).

[148] T. Schumann, M. Dubslaff, M.H. Oliveira, M. Hanke, J.M.J. Lopes, H. Riechert, Effect of buffer layer coupling on the lattice parameter of epitaxial graphene on SiC(0001), Phys. Rev. B. 90 (2014) 041403. doi:10.1103/PhysRevB.90.041403.

[149] A. Tiberj, J.R. Huntzinger, N. Camara, P. Godignon, J. Camassel, Raman spectrum and optical extinction of graphene buffer layers on the Si-face of 6H-SiC, ArXiv12121196 Cond-Mat. (2012). http://arxiv.org/abs/1212.1196 (accessed March 10, 2017).

[150] A. Das, S. Pisana, B. Chakraborty, S. Piscanec, S.K. Saha, U.V. Waghmare, K.S. Novoselov, H.R. Krishnamurthy, A.K. Geim, A.C. Ferrari, A.K. Sood, Monitoring dopants by Raman scattering in an electrochemically top-gated graphene transistor, Nat. Nanotechnol. 3 (2008) 210–215. doi:10.1038/nnano.2008.67.

[151] J. Yan, Y. Zhang, P. Kim, A. Pinczuk, Electric Field Effect Tuning of Electron-Phonon Coupling in Graphene, Phys. Rev. Lett. 98 (2007) 166802. doi:10.1103/PhysRevLett.98.166802.

[152] M. Kalbac, A. Reina-Cecco, H. Farhat, J. Kong, L. Kavan, M.S. Dresselhaus, The Influence of Strong Electron and Hole Doping on the Raman Intensity of Chemical Vapor-Deposition Graphene, ACS Nano. 4 (2010) 6055–6063. doi:10.1021/nn1010914.

[153] S. Pisana, M. Lazzeri, C. Casiraghi, K.S. Novoselov, A.K. Geim, A.C. Ferrari, F. Mauri, Breakdown of the adiabatic Born–Oppenheimer approximation in graphene, Nat. Mater. 6 (2007) 198–201. doi:10.1038/nmat1846.

[154] J.E. Lee, G. Ahn, J. Shim, Y.S. Lee, S. Ryu, Optical separation of mechanical strain from charge doping in graphene, Nat. Commun. 3 (2012) 1024. doi:10.1038/ncomms2022.

[155] T.M.G. Mohiuddin, A. Lombardo, R.R. Nair, A. Bonetti, G. Savini, R. Jalil, N. Bonini, D.M. Basko, C. Galiotis, N. Marzari, K.S. Novoselov, A.K. Geim, A.C. Ferrari, Uniaxial strain in graphene by Raman spectroscopy: G peak splitting, Gr"uneisen parameters, and sample orientation, Phys. Rev. B. 79 (2009) 205433. doi:10.1103/PhysRevB.79.205433.

[156] J. Zabel, R.R. Nair, A. Ott, T. Georgiou, A.K. Geim, K.S. Novoselov, C. Casiraghi, Raman Spectroscopy of Graphene and Bilayer under Biaxial Strain: Bubbles and Balloons, Nano Lett. 12 (2012) 617–621. doi:10.1021/nl203359n.

[157] Z.H. Ni, T. Yu, Y.H. Lu, Y.Y. Wang, Y.P. Feng, Z.X. Shen, Uniaxial Strain on Graphene: Raman Spectroscopy Study and Band-Gap Opening, ACS Nano. 2 (2008) 2301–2305. doi:10.1021/nn800459e.

[158] G. Grimvall, Thermophysical Properties of Materials, Elsevier, 1999.

[159] N. Ferralis, Probing mechanical properties of graphene with Raman spectroscopy, J. Mater. Sci. 45 (2010) 5135–5149. doi:10.1007/s10853-010-4673-3.
[160] D. Graf, F. Molitor, K. Ensslin, C. Stampfer, A. Jungen, C. Hierold, L. Wirtz, Spatially Resolved Raman Spectroscopy of Single- and Few-Layer Graphene, Nano Lett. 7 (2007) 238–242. doi:10.1021/nl061702a.
[161] A.U. MacRae, Low-Energy Electron Diffraction, Science. 139 (1963) 379–388. doi:10.1126/science.139.3553.379.
[162] Y. Chung, Practical Guide to Surface Science and Spectroscopy, Academic Press, 2001.
[163] F. Jona, J.A.S. Jr, W.S. Yang, Low-energy electron diffraction for surface structure analysis, Rep. Prog. Phys. 45 (1982) 527. doi:10.1088/0034-4885/45/5/002.
[164] E. Bauer, Interpretation of Low-Energy Electron Diffraction Patterns of Adsorbed Gases, Phys. Rev. 123 (1961) 1206–1208. doi:10.1103/PhysRev.123.1206.
[165] Z.H. Ni, W. Chen, X.F. Fan, J.L. Kuo, T. Yu, A.T.S. Wee, Z.X. Shen, Raman spectroscopy of epitaxial graphene on a SiC substrate, Phys. Rev. B. 77 (2008) 115416. doi:10.1103/PhysRevB.77.115416.
[166] A. Bauer, J. Kräußlich, L. Dressler, P. Kuschnerus, J. Wolf, K. Goetz, P. Käckell, J. Furthmüller, F. Bechstedt, High-precision determination of atomic positions in crystals: The case of 6H- and 4H-SiC, Phys. Rev. B. 57 (1998) 2647–2650. doi:10.1103/PhysRevB.57.2647.
[167] I. Sanc, Graphite 2H, (1990).
[168] L. Van der Pauw, A Method of Measuring the Resistivity and Hall Coefficient on Lamellae of Arbitrary Shape., Philips Tech. Rev. 20 (1958) 220–224.
[169] L. Van der Pauw, A method of measuring specific resistivity and Hall effect of discs of arbitrary shape, Philips Res. Rep. 13 (1958) 1–9.
[170] B.L. VanMil, K.-K. Lew, R.L. Myers-Ward, R.T. Holm, D.K. Gaskill, C.R. Eddy Jr., L. Wang, P. Zhao, Etch rates near hot-wall CVD growth temperature for Si-face 4H-SiC using H2 and C3H8, J. Cryst. Growth. 311 (2009) 238–243. doi:10.1016/j.jcrysgro.2008.11.030.
[171] E. Neyret, L. Di Cioccio, E. Blanquet, C. Raffy, C. Pudda, T. Billon, J. Camassel, SiC In-Situ Pre-Growth Etching: A Thermodynamic Study, Mater. Sci. Forum. 338–342 (2000) 1041–1044. doi:10.4028/www.scientific.net/MSF.338-342.1041.
[172] SGTE. Thermodynamic properties of inorganic materials compiled by SGTE. In: Martienssen W, editor. Landolt-Börnstein – numerical data and functional relationships in science and technology. Berlin, Heidelberg: Springer-Verlag; 2004. p. 140.
[173] M.D. Allendorf, C.F. Melius, Theoretical study of the thermochemistry of molecules in the silicon-carbon-hydrogen system, J. Phys. Chem. 96 (1992) 428–437. doi:10.1021/j100180a080.
[174] M.D. Allendorf, C.F. Melius, Theoretical study of thermochemistry of molecules in the silicon-carbon-chlorine-hydrogn system, J. Phys. Chem. 97 (1993) 720–728. doi:10.1021/j100105a031.
[175] Rocabois P, Chatillon C, Bernard C. Mass spectrometry experimental investigation and thermodynamic calculation of the Si–C–O system and SixCyOz fibre stability. In: Naslain R, Lamon J, Doumeingts D, editors. High temp. ceramic matrix composites. Abington, Cambridge CB16AH, UK: Woodhead Pub. Ltd., Abington Hall; 1993. p. 93–100.
[176] http://www.factsage.com/.

[177] M.D. Allendorf, Equilibrium Predictions of the Role of Organosilicon Compounds in the Chemical Vapor Deposition of Silicon Carbide, J. Electrochem. Soc. 140 (1993) 747. doi:10.1149/1.2056152.

[178] c. D. Stinespring and J. C. Wormhoudt, Surface studies relevant to silicon carbide chemical vapor deposition, J. Appl. Phys. 65 (1989) 1733–1742. doi:10.1063/1.342947.

[179] T. Ohta, A. Bostwick, T. Seyller, K. Horn, E. Rotenberg, Controlling the Electronic Structure of Bilayer Graphene, Science. 313 (2006) 951–954. doi:10.1126/science.1130681.

[180] S. Doniach, M. Sunjic, Many-electron singularity in X-ray photoemission and X-ray line spectra from metals, J. Phys. C Solid State Phys. 3 (1970) 285. doi:10.1088/0022-3719/3/2/010.

[181] A. Michon, L. Largeau, O. Mauguin, A. Ouerghi, S. Vézian, D. Lefebvre, E. Roudon, M. Zielinski, T. Chassagne, M. Portail, Graphene growth using propane-hydrogen CVD on 6H-SiC(0001): temperature dependent interface and strain, Phys. Status Solidi C. 9 (2012) 175–178. doi:10.1002/pssc.201100225.

[182] N. Ferralis, R. Maboudian, C. Carraro, Evidence of Structural Strain in Epitaxial Graphene Layers on 6H-SiC(0001), Phys. Rev. Lett. 101 (2008) 156801. doi:10.1103/PhysRevLett.101.156801.

[183] J. Röhrl, M. Hundhausen, K.V. Emtsev, T. Seyller, R. Graupner, L. Ley, Raman spectra of epitaxial graphene on SiC(0001), Appl. Phys. Lett. 92 (2008) 201918. doi:10.1063/1.2929746.

[184] A. Taylor, R.M. Jones, Silicon Carbide - A High Temperature Semiconductor, in: Pergamon Press, Oxford, London, New York, Paris, 1960: p. 147.

[185] C.A. and E. of the L.V. III/17A-22A-41A1b, Silicon carbide (SiC), lattice parameters, thermal expansion, in: O. Madelung, U. Rössler, M. Schulz (Eds.), Group IV Elem. IV-IV III-V Compd. Part B - Electron. Transp. Opt. Prop., Springer Berlin Heidelberg, 2002: pp. 1–11. doi:10.1007/10832182_600.

[186] D.K.L. Tsang, B.J. Marsden, S.L. Fok, G. Hall, Graphite thermal expansion relationship for different temperature ranges, Carbon. 43 (2005) 2902–2906. doi:10.1016/j.carbon.2005.06.009.

[187] N. Mounet, N. Marzari, First-principles determination of the structural, vibrational and thermodynamic properties of diamond, graphite, and derivatives, Phys. Rev. B. 71 (2005) 205214. doi:10.1103/PhysRevB.71.205214.

[188] N. Ferralis, J. Kawasaki, R. Maboudian, C. Carraro, Evolution in surface morphology of epitaxial graphene layers on SiC induced by controlled structural strain, Appl. Phys. Lett. 93 (2008) 191916. doi:10.1063/1.3028091.

[189] G. Prakash, M.A. Capano, M.L. Bolen, D. Zemlyanov, R.G. Reifenberger, AFM study of ridges in few-layer epitaxial graphene grown on the carbon-face of 4H–SiC, Carbon. 48 (2010) 2383–2393. doi:10.1016/j.carbon.2010.02.026.

[190] J.A. Robinson, C.P. Puls, N.E. Staley, J.P. Stitt, M.A. Fanton, K.V. Emtsev, T. Seyller, Y. Liu, Raman Topography and Strain Uniformity of Large-Area Epitaxial Graphene, Nano Lett. 9 (2009) 964–968. doi:10.1021/nl802852p.

[191] R. Dagher, B. Jouault, M. Paillet, M. Bayle, L. Nguyen, M. Portail, M. Zielinski, T. Chassagne, Y. Cordier, A. Michon, CVD growth of graphene on SiC (0001): influence of substrate offcut, Mater. Sci. Forum. (2017) 731. doi:10.4028/www.scientific.net/MSF.717-720.621.

[192] C. Dimitrakopoulos, A. Grill, T.J. McArdle, Z. Liu, R. Wisnieff, D.A. Antoniadis, Effect of SiC wafer miscut angle on the morphology and Hall mobility of epitaxially grown graphene, Appl. Phys. Lett. 98 (2011) 222105. doi:10.1063/1.3595945.

[193] Y. Taniyasu, M. Kasu, T. Makimoto, An aluminium nitride light-emitting diode with a wavelength of 210 nanometres, Nature. 441 (2006) 325–328. doi:10.1038/nature04760.

[194] K. Itaya, M. Onomura, J. Nishio, L. Sugiura, S. Saito, M. Suzuki, J. Rennie, S. Nunoue, M. Yamamoto, H. Fujimoto, Y. Kokubun, Y. Ohba, G. Hatakoshi, M. Ishikawa, Room Temperature Pulsed Operation of Nitride Based Multi-Quantum-Well Laser Diodes with Cleaved Facets on Conventional C-Face Sapphire Substrates, Jpn. J. Appl. Phys. 35 (1996) L1315–L1317. doi:10.1143/JJAP.35.L1315.

[195] M.S. Shur, R. Gaska, Deep-Ultraviolet Light-Emitting Diodes, IEEE Trans. Electron Devices. 57 (2010) 12–25. doi:10.1109/TED.2009.2033768.

[196] M. Qi, G. Li, S. Ganguly, P. Zhao, X. Yan, J. Verma, B. Song, M. Zhu, K. Nomoto, H. (Grace) Xing, D. Jena, Strained GaN quantum-well FETs on single crystal bulk AlN substrates, Appl. Phys. Lett. 110 (2017) 063501. doi:10.1063/1.4975702.

[197] G. Li, B. Song, S. Ganguly, M. Zhu, R. Wang, X. Yan, J. Verma, V. Protasenko, H. Grace Xing, D. Jena, Two-dimensional electron gases in strained quantum wells for AlN/GaN/AlN double heterostructure field-effect transistors on AlN, Appl. Phys. Lett. 104 (2014) 193506. doi:10.1063/1.4875916.

[198] J. Brault, B. Damilano, A. Kahouli, S. Chenot, M. Leroux, B. Vinter, J. Massies, Ultra-violet GaN/Al0.5Ga0.5N quantum dot based light emitting diodes, J. Cryst. Growth. 363 (2013) 282–286. doi:10.1016/j.jcrysgro.2012.11.015.

[199] J.-Y. Duboz, N. Grandjean, F. Omnès, J.-L. Reverchon, M. Mosca, Solar blind detectors based on AlGaN grown on sapphire, Phys. Status Solidi C. 2 (2005) 964–971. doi:10.1002/pssc.200460603.

[200] F.A. Ponce, B.S. Krusor, J.S. Major, W.E. Plano, D.F. Welch, Microstructure of GaN epitaxy on SiC using AlN buffer layers, Appl. Phys. Lett. 67 (1995) 410–412. doi:10.1063/1.114645.

[201] F.A. Ponce, J.S. Major, W.E. Plano, D.F. Welch, Crystalline structure of AlGaN epitaxy on sapphire using AlN buffer layers, Appl. Phys. Lett. 65 (1994) 2302–2304. doi:10.1063/1.112724.

[202] B. Beaumont, P. Gibart, J.P. Faurie, Nitrogen precursors in metalorganic vapor phase epitaxy of (Al,Ga)N, J. Cryst. Growth. 156 (1995) 140–146. doi:10.1016/0022-0248(95)00296-0.

[203] A. Rice, R. Collazo, J. Tweedie, R. Dalmau, S. Mita, J. Xie, Z. Sitar, Surface preparation and homoepitaxial deposition of AlN on (0001)-oriented AlN substrates by metalorganic chemical vapor deposition, J. Appl. Phys. 108 (2010) 043510. doi:10.1063/1.3467522.

[204] M.E. L. G. Cançado, K. Takai, and T. Enoki Y.A. Kim, and H. Mizusaki, A. Jorio, L. N. Coelho, R. Magalhães-Paniago, and M. A. Pimenta, General equation for the determination of the crystallite size La of nanographite by Raman spectroscopy, Appl. Phys. Lett. 88 (2006) 163106. doi:10.1063/1.2196057.

[205] H. Nakagawa, S. Tanaka, I. Suemune, Self-Ordering of Nanofacets on Vicinal SiC Surfaces, Phys. Rev. Lett. 91 (2003) 226107. doi:10.1103/PhysRevLett.91.226107.

[206] H. Miyake, G. Nishio, S. Suzuki, K. Hiramatsu, H. Fukuyama, J. Kaur, N. Kuwano, Annealing of an AlN buffer layer in N2–CO for growth of a high-quality AlN film on sapphire, Appl. Phys. Express. 9 (2016) 025501. doi:10.7567/APEX.9.025501.

[207] H. Miyake, C.-H. Lin, K. Tokoro, K. Hiramatsu, Preparation of high-quality AlN on sapphire by high-temperature face-to-face annealing, J. Cryst. Growth. 456 (2016) 155–159. doi:10.1016/j.jcrysgro.2016.08.028.

[208] M. Zhu, P. Chen, R.K.Y. Fu, W. Liu, C. Lin, P.K. Chu, AlN thin films fabricated by ultra-high vacuum electron-beam evaporation with ammonia for silicon-on-insulator application, Appl. Surf. Sci. 239 (2005) 327–334. doi:10.1016/j.apsusc.2004.05.287.

[209] P.H. Bolt, E. ten Grotenhuis, J.W. Geus, F.H.P.M. Habraken, The interaction of thin NiO layers with single crystalline α-Al2O3(11$\bar{2}$0) substrates, Surf. Sci. 329 (1995) 227–240. doi:10.1016/0039-6028(95)00063-1.

[210] B.R. Strohmeier, Characterization of an Activated Alumina Claus Catalyst by XPS, Surf. Sci. Spectra. 3 (1994) 141–146. doi:10.1116/1.1247775.